University of Sheffield

Spatio-temporal dynamics of glacial erosion in high Alpine catchments

William Jonathan Wenban

A thesis submitted in partial fulfilment of the
requirements for the degree of
Doctor of Philosophy

The University of Sheffield
Department of Geography

1st May 2024

Abstract

The impact of glaciation leaves a distinct signature in mountain landscapes. These high relief environments, with heterogeneous long-profiles comprised of complex features and landforms like large topographic steps, overdeepened basins and adverse slopes, are unique to the influences of glacial erosion and differ markedly to fluvial landscapes. Complex topography within high alpine catchments occupied by today's glaciers is suggestive of strong spatial variability in the efficacy of glacial erosion, yet the specific rates and reasons behind this remain poorly understood and raise questions regarding the role of glacial erosion in balancing tectonic uplift to maintain topographic steady-state. A novel inventory of contemporary icefalls in upper catchments across Switzerland is compiled which shows a strong correlation to climate gradients, suggestive of a disconnect in regions of effective erosion over time and signifies their potential importance in the long-term landscape evolution of glacial catchments. A numerical landscape evolution model is then used to explore the spatio-temporal variability of glacial erosion under different climate conditions and to test the impact of different numeric erosion laws. The pre-existing topography and positioning of the catchment in the wider basin is found to be a dominant control on the patterns and rates of glacial erosion, which has the potential to differ significantly between glacial and interglacial states or to remain relatively similar depending on catchment characteristics. Choice of erosion law also has a substantial impact on the strength of erosion occurring across the catchment and demonstrates the need for improved empirical constraints. Finally, a unique method of luminescence thermochronometry is applied to bedrock samples from the field to derive a novel time-series of exhumation rates spanning the past 100 ka, which is used to infer patterns of glacial erosion that broadly agree with the modelled outcomes. Collectively, high alpine catchments are shown to be highly dynamic and as regions of longest ice residency time, are responsible for maintaining a long-term dynamic equilibrium of the landscape through orders of magnitude changes in erosion according to topographic features and climate conditions.

Acknowledgements

The metaphor ‘standing on the shoulders of giants’ is commonly applied to academia and this thesis is no exception. Looking back over the past few years there are many people who have helped me along this research journey and provided another rung in the ladder to reach those shoulders.

Firstly, I gratefully acknowledge the University of Sheffield Hossein Farmy Scholarship for funding this research and I would like to sincerely thank my supervisors Darrel Swift and Ed Rhodes for their expert wisdom and guidance along the way, it’s been quite the rollercoaster and you both helped me cling on and ride out the bumpier parts! Thank you also to Simon Cook for some great conversations and encouragement along the way. I will particularly cherish the fond memories of time spent in the field with Darrel and Simon amongst others and hope for more of those moments in the future.

For my own fieldwork I am indebted to my good friend Rosie Huck for accompanying me to Switzerland in 2021 amongst ever changing Covid travel restrictions to endure some big hikes carrying heavy backpacks full of rocks. It was an immense effort without which some of the most exciting results of the thesis would not have been possible. Thank you also to Stuart Lane and Floreana Marie Miesen for hosting us at their research camp at Otemma for a couple of days during this trip. I’m grateful to Remy Veness who also joined me in 2022 to access samples in the upper summit reaches of Otemma. These field excursions were incredibly fun and successful thanks to you all and have created lasting memories as well as research outputs.

Numerical modelling was a brand-new field to me at the start of this research and the source of many headaches. Thank you to Ann Rowan who initially got me setup with iSOSIA and provided some troubleshooting advice over email in the following years. I am very thankful to Vivi Pedersen and Gustav Jungdal-Olesen for giving up a week of their time to allow me to visit Aarhus and learn their ways of iSOSIA, as well as provide continuous email and video call support thereafter with so much enthusiasm and friendliness. Thank you also to Fabio Magrani who provided some troubleshooting help and advice over email.

I am deeply grateful to Nathan Brown who has been so friendly and forthcoming, likewise providing time for me to visit and learn his ways. Nathan’s TL method is incredibly exciting, and I’m honoured to have been the first piece of major research it has been applied to outside of his own PhD several years ago. I see enormous potential in its

application across a range of situations and hope to maintain contact and see the method grow in the future.

Thank you to all the wider staff in the Sheffield Geography department, who provided insightful comments during informal conversations or presentations. Especially thank you to the lab team (Rob Ashurst, Paul Allard & Cari Littler) for always being on hand to help with lab and fieldwork things, a truly great bunch of people.

Thank you to all my friends that have kept me going, especially in these last few months when I've retreated into a deep hole to write the thesis, thanks for checking up on me and instigating fun outings to the Peaks or pubs!

To my girlfriend Bella, thank you for enduring the last few years of my (sometimes unhealthy) relationship with this PhD, it's been as hard on you as it has for me, and your support has been everything.

Finally, thank you to my parents and family, who provide unending love and support in everything I do.

Table of Contents

List of Figures

List of Tables

List of abbreviations

DEM	Digital Elevation Model
ELA	Equilibrium Line Altitude
GP	Glacial Period
IG	Interglacial
LGM	Last Glacial Maximum
LGP	Last Glacial Period
LIA	Little Ice Age
QELA	average Quaternary Equilibrium Line Altitude
SGI	Swiss Glacier Inventory
TLT	Thermoluminescence Thermochronometry

Chapter 1

Introduction

1.1 General Introduction and Rationale

Mountain environments across earth have been shaped and reshaped through many successive glacial and interglacial cycles, making the landscapes we see today a complex palimpsest of change driven by a multitude of environmental forces.

Alpine landscapes that have undergone significant glaciation are distinct in their appearance – a high relief environment of deep U-shaped valleys beneath steep, jagged peaks, with a complex heterogenous profile linking the two (Figure 1.1a). This is in contrast to predominantly fluvial environments, which comprise of smooth concave longitudinal valley profiles, starting in steeper upper headwaters and finishing in flatter lower reaches, interrupted by the occasional knickpoint along the way (Figure 1.1b).

Despite this obvious and visually impressive glacial signature, obtaining quantitative data on where, how and why glaciers act to erode the land with specific intensity remains a difficult and elusive task due to the composite interaction of different processes – both glacial and non-glacial – as well as the timescales involved. However, with ever-improving technologies and techniques, it is possible to delve further into the intricacies of these processes with the aim of shedding a little more light on how glaciers act to evolve mountain topography through time.

Previous work on the efficacy of glacial erosion has been focused largely on a few key landforms such as cirques at the head of the catchment (e.g. Anders et al., 2010; Mîndrescu & Evans, 2014; Evans et al., 2015; Barr & Spagnolo, 2015; Crest et al., 2017; Evans, 2021) and overdeepened basins in the trunk valleys or forelands (e.g. Cook & Swift, 2012; Patton et al., 2016; Haeberli et al., 2016; Magrani et al., 2020), whilst other major landforms such as bedrock riegel ridges (e.g. Steinemann et al., 2021) and icefall steps (e.g. MacGregor et al., 2000; Jiskoot et al., 2017) have received relatively little attention, despite potentially holding equally valuable information about glacial valley evolution. Looking at the dynamism of the catchment and long-profile as a whole is only now starting to be explored using higher-order numerical models that can account for more elements of the highly

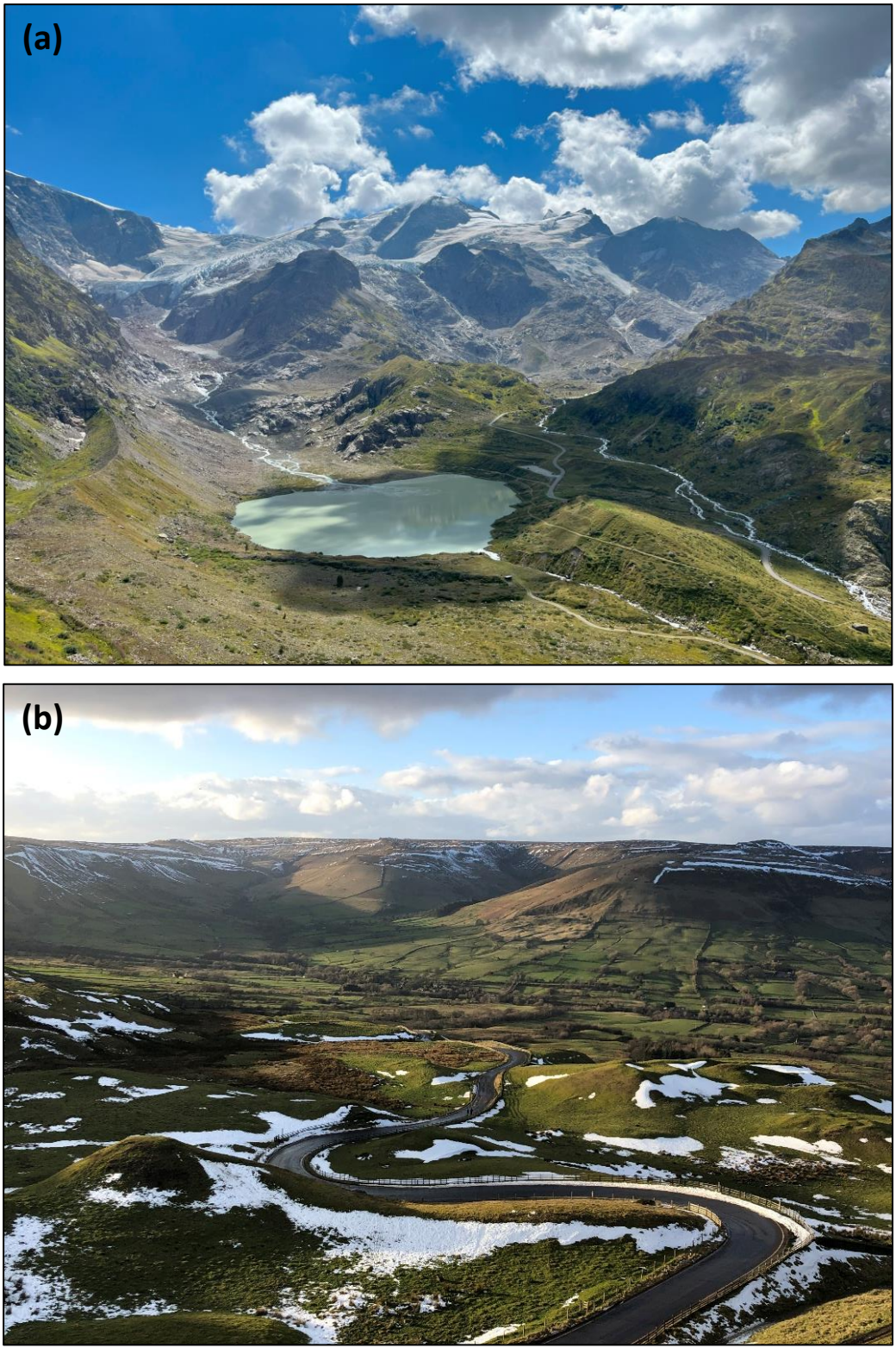

Figure 1.1: Examples of contrasting glacially and fluvially-dominated landscapes. **(a)** View of Steingletscher, Switzerland, with high relief peaks connected to the valley via steep slopes and cliffs, also containing adverse ridges and a large overdeepening occupied by a lake. **(b)** View of Edale valley in the Peak District, UK, lower in relief with smoother graded topography and hillsides incised by concave fluvial valleys.

variable ice dynamics experienced in these regions (e.g. Liebl et al., 2021).

The motivation for this thesis is to explore and quantify the spatial and temporal patterns of glacial erosion that are qualitatively apparent from the landforms they create at the individual high alpine catchment scale. Recently, advances in numerical modelling capabilities have permitted the simulation of the impacts of large-scale glaciation of entire mountain ranges over whole glacial cycles (e.g. Seguinot et al., 2018; Seguinot & Delaney, 2021). However, currently such models are limited to coarse (> 500 m) resolutions and as such, lack the detail to explore processes operating on smaller landforms in the upper catchments occupied by today's glaciers. Here, in the high topography regions where ice occupation time is at its longest, a number of questions have been asked about the ability of glaciation to rapidly denude the landscape and suppress the effects of tectonic uplift (Brozović et al., 1997), which will be discussed later in this chapter (section 1.2.3). Consequently, this thesis aims to address this lack of higher-resolution data by applying a combination of modern techniques – namely GIS-based topographic analysis of icefalls as a major landform, numerical landscape evolution modelling of different climate and erosion scenarios and a novel application of thermoluminescence thermochronometry that has the ability to constrain a rich exhumation history of bedrock samples from the field. This multi-faceted approach provides new insights into the efficacy of glacial erosion at smaller catchment scales over the timeframe of the last glacial period. The research presented here is specifically focused on the Swiss Alps and in two particular field sites – Glacier d'Otemma and Triftgletscher – but it is believed the findings and discussions generated will be broadly applicable to similar glaciated alpine landscapes worldwide.

The following sections will present an overview of the current knowledge and literature for the key fields of research and topics addressed in this thesis; starting with a brief summary of glaciation in the Swiss Alps (1.2.1), followed by an overview of the impact of glaciation on alpine landscapes (1.2.2) and discussions on the ability of glacial erosion to counter uplift (1.2.3) before finally, a review of the challenges in constraining the dynamics of glacial erosion (1.2.4). After this context, the specific aims and objectives of the thesis will be defined (1.3) and the overall thesis structure will be laid out (1.4).

1.2 Context

1.2.1 Glacial and Interglacial Variability in the Swiss Alps

In order to explore the impacts glacial erosion has on mountain topography, it is important to have an initial understanding of the history of glaciation in the study region, both from a wider perspective after initial orogenic formation, and in more detail over the most recent glacial period, which is the main timeframe of focus for this thesis.

The Swiss Alps comprises the central region of the wider European Alps, an approximately 1000 km long orogenic belt formed towards the end of the Cretaceous and into the Tertiary (Fitzsimons & Veit, 2001). Continental collision between the European and Adriatic plates drove tectonic formation of the Alps and established the main drainage organisation following the major tectonic structures, with the majority of mountain building occurring during the period of 25-15 Ma (Valla et al., 2021). Stable isotope palaeoaltimetry data suggests the present-day high elevation of the Alps had been established by the mid-Miocene (ca. 15 Ma) (Campani et al., 2012).

Cooling of the global climate into the Quaternary brought about the start of a complex history of glaciation in the Alps and with it, major geomorphic changes. Compilations of data from sediment records, geomorphological mapping and various radiometric dating methods (e.g. luminescence, radiocarbon etc.) documents at least 15 major glacial advances out into the Swiss foreland during the Quaternary (Schlüchter, 2004). Thermochronometric data proposes a two to three-fold increase in exhumation rates for the Western and Central Alps since 2 Ma, attributed to a combination of intense glacial erosion and tectonic slab detachment (Fox et al., 2016). However, evidence from cosmogenic nuclide dating and apatite He thermochronometry has presented the case for limited erosion within the mountain valleys (~0.1 km/Ma) during the period of early glaciation in the Plio-Pleistocene, followed by an abrupt signal of more intense valley incision at 1 km/Ma following the mid-Pleistocene climate transition (Valla et al., 2021). At this time, approximately 1 Ma, changes in orbital eccentricity brought about a global climate shift, switching the periodicity of glaciations from short (40 ka) and limited extent to longer (100 ka) and greater extents. Such strong cyclicity in glacial and interglacial conditions would have driven geomorphic change and landscape evolution in the Alps through the interplay of powerful environmental forces from fluvial and glacial action under variable climates.

Evidence of glacial activity – tills, moraines, glacio-fluvial deposits – furthest from the Alps in the Swiss foreland has been interpreted as the so-called Most Extensive Glaciation (MEG), believed to have occurred after the first Quaternary glaciations but before the most recent interglacial (Eemian) and glacial (Würmian) periods (Schlüchter, 2004). Recent sediment dating from the northern Swiss foreland has attributed the MEG to an age of approximately 500 ± 100 ka (Dieleman et al., 2022), thus after the dramatic climate shift of the mid-Pleistocene transition.

The last glacial period (LGP), known as the Würmian in the Alps, comprised the period from approximately 115 ka until the start of the current Holocene period ~11 ka. A thorough review of the chronology and field evidence of glaciation in the Alps during this time is given by Ivy-Ochs et al. (2008) and will only be summarised here. A variety of evidence from radiocarbon, cosmogenic and luminescence dating as well as sediment and pollen analysis indicates climate during the LGP was still quite variable with a series of colder stadials and warmer interstadials. Consequently, glaciers in the Alps would have been in a constant state of flux, extending down into the main trunk valleys during the colder stadials and retreating back into tributary valleys during the interstadials. This evidence from different techniques has presented a broad view of approximate timing and conditions of the changing climate– such as pollen analysis revealing a broad distribution of boreal forest during the first temperate interstadial – but the exact impact on the extent of glaciation has been difficult to constrain, particularly during the early Würmian, as much of the evidence will have been overridden by subsequent ice advances and activity. Moreover, field data shows significant regional differences within the Alps, with sedimentation evidence and U/Th dating from the Eastern Alps suggesting glaciers did not extend down into the main alpine valleys during the early Würmian, whilst luminescence dating in the Swiss Alps implies there was extension out into the foreland (Ivy-Ochs et al., 2008 and references therein), potentially a reflection of strong climate and/or precipitation gradients across the Alps.

Conversely, there is a wealth of evidence to document the most recent major extension of glaciers out into the lowlands during the late Würmian at approximately 30 ka, known as the Last Glacial Maximum (LGM) (Figure 1.2), before subsequent warming and retreat from approximately 20 ka onwards. The LGM is widely considered to be the most extensive period of glaciation during the Würmian, with much of the pre-existing valley sediment fills being eroded once more (Muller, 1999). But once again, the timing of advances and subsequent retreat appears to be asynchronous across the Alps (Ivy-Ochs, 2015). This variability is also captured within numerical models of the last glacial cycle and can be

explained as a result of differences in glacier dynamics due to topography alone (Seguinot et al., 2018), since regional differences in climate were not included in these models but would likely further add to the disparity in timings of equilibrium at maximum extent, followed by retreat. For the northern Swiss Alps, cosmogenic dating of erratic boulders from terminal moraine assemblages show moraine stabilisation at approximately 21 ka, followed by abandonment from retreat by ~19 ka (Ivy-Ochs et al., 2004).

Warming during the Lateglacial (~20 ka onwards) resulted in a slight rise in equilibrium line altitudes (ELA), which subsequently exposed large portions of the lowland piedmont lobes to intense ablation and thus rapid down wasting and retreat of the major valley glaciers, which likely became stagnant as a result (Ivy-Ochs, 2015). What followed was a series of small stadial and interstadial climate oscillations to once again give a sequence of readvances and retreats, starting with an Alpine-wide readvance during the Gschnitz stadial (17-16 ka), which was likely a response to the Europe-wide cooling induced from the Heinrich-1 event (Ivy-Ochs et al., 2006) – where vast quantities of ice calving from the North American Laurentide Ice Sheet into the Atlantic Ocean subsequently affected thermohaline circulations and climate.

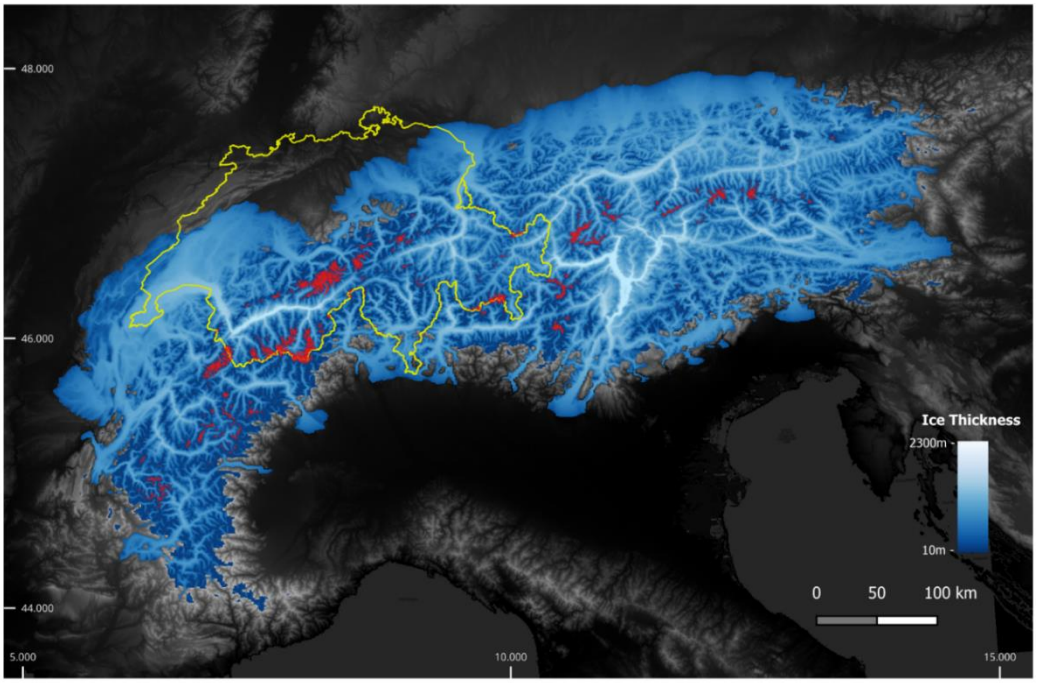

Figure 1.2: The Central European Alps (with Switzerland highlighted in yellow) at LGM ice extent modelled by Višnjević et al. (2020), with modern day glaciers from RGI 6.0 (2017) shown in red.

Cosmogenic, sedimentological and palaeobotanical evidence shows that by the start of the Bølling–Allerød interstadial period (14.69-12.89 ka), ice had ceased to flow across the high mountain passes in the Alps and that eventually the main tributary valleys had also become ice-free during this warmer interstadial (Ivy-Ochs, 2015). A final major readvance several kilometres from cirque basins would then occur in response to the Younger Dryas (12.9 – 11.7 ka) – an abrupt cold climate event triggered by a disruption to the Atlantic meridional overturning circulation (Ivy-Ochs, 2015). In some regional cases readvances persisted into the early Holocene (c. 10.5 ka)(e.g. Schimmelpfennig et al., 2014) from limited cold oscillations, reflecting the climate instability during this time.

The Holocene interglacial period marked the onset of a substantial shift in climate to warmer conditions that did not favour glacial expansion. Instead, periodic recession occurred with radiocarbon dating from the fossilised remains of trees found melting-out of present day glaciers suggesting at least twelve distinct retreat phases during the Holocene, with glaciers likely fluctuating around their equivalent 1985 extent and climate conditions permitting tree growth at altitudes higher than today (Joerin et al., 2006). Ice core data from a dome in the Eastern Alps at 3500 m elevation has been dated to ~5.9 ka, interpreted to mean it was likely ice-free prior to this, during the warm Holocene climate optimum (~9-5 ka), when all but the highest summits (i.e. >4000 m) likely lost their ice cover (Bohleber et al., 2020). Aside from some brief intervals (e.g. ~8.85-8.4 ka) where smaller glaciers capable of quick responses to change may have advanced slightly, the majority of glaciers in the Alps will have remained well behind their late 19th century extents during the predominantly warm and dry conditions of most of the Holocene (Ivy-Ochs et al., 2009).

From 3.3 ka onwards climate cooled and facilitated more widespread advance until a warmer interruption during Roman times (~2.1 ka – 200 AD), during which recession beyond mid-20th century extents occurred. Following from this, a cooler period often termed the 'Little Ice Age' (LIA) ran from approximately 1300 to 1850 AD and resulted in a series of advances that can be traced to the 14th, 17th and 19th centuries, with the last being the most substantial and stabilising by ~1850 (Holzhauser et al., 2005; Ivy-Ochs et al., 2009). LIA extents are well preserved and easily documented today with the presence of large moraines some kilometres from present termini and dramatic valley trimlines frequently found hundreds of metres above the current ice surface (Figure 1.3).

The above overview is but a brief summary of the glacial history of the Alps. It is clear the Alps has a long and complex history of fluctuations in climate and subsequent glacial and interglacial conditions. Only the major changes have been summarised here and are

also presented in Figure 1.4 for an illustrative overview. The intricacies of all the climate variability is beyond the scope of this study and indeed, as aforementioned, difficult to constrain owing to lack of preserved environmental evidence due to the power and extent of the LGM ice masses essentially 'wiping the slate clean'. Even during the comparatively short Holocene period from ~11 ka onwards there has been substantial variation in environmental conditions and glacial extent, with only the key events having been summarised here. The constant switching between large glacial advances and retreats over the last ~100 ka brought with it great geomorphic power that shaped and re-shaped the landscape, leaving behind the environmental clues with which we gain insights into the history of the mountains. The LGM and LIA extents provide good, well-constrained situations of comparatively large and smaller glacial activity respectively, from which we can construct steady-state scenarios and test our understanding of the impact of glaciation on the landscape. These scenarios will form the foundation of numerical landscape evolution modelling presented later in Chapter 3.

The following section will go into more detail on the impacts of glacial erosion on the landscape and how this differs from fluvial activity.

Figure 1.3: Field photo from Triftgletscher in 2021. The prominent boulder-strewn LIA moraine is present in the foreground, some 2.5 km from the present-day ice and ~300 m above the valley floor. The LIA trimline on the valley side is visible in the background (white dashed line).

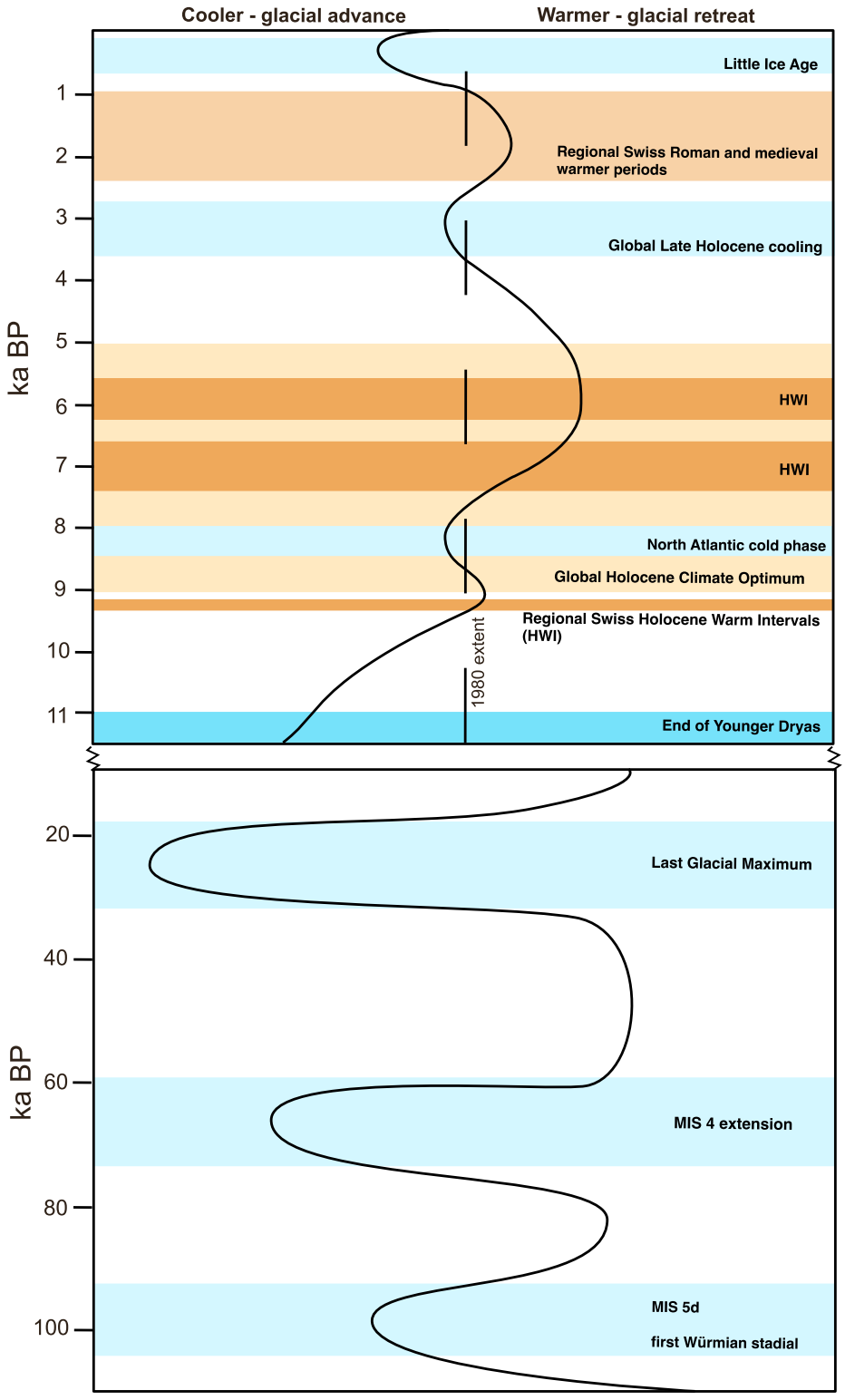

Figure 1.4: Idealised illustrative diagram to show the broad trends in climate changes over the last glacial period and the Holocene (not to scale between periods). Based off the review and reconstructions by Ivy-Ochs et al. (2008, 2009).

1.2.2 Differences in Fluvial and Glacial Impacts on Alpine Landscapes

The impact of glaciation on mountain morphology is readily apparent when comparing the longitudinal profiles of a fluvially dominated and glacially dominated catchment (Figure 1.5). The fluvial longitudinal profile extends in a smooth concave fashion, decreasing in gradient with distance downstream, whilst the glacial profile takes a more convex form and is far more heterogenous, with multiple regions of rapidly changing gradients – overdeepened basins, large steps and adverse slopes. Such heterogeneity is suggestive of substantial spatial variability in glacial erosion across the landscape.

The stream power law is a well devised and common approach to quantifying the erosive power of a given river by taking into account various metrics of the river channel and basin, such as channel slope, width and discharge (Anderson & Anderson, 2010). Currently there

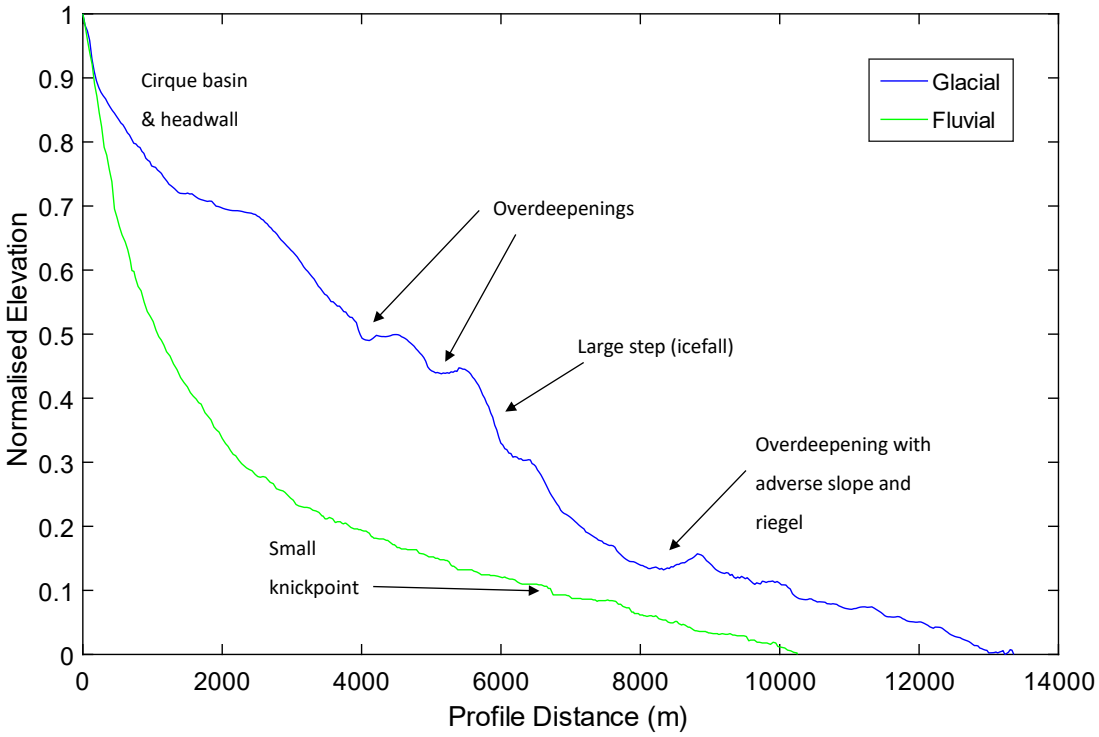

Figure 1.5: Example longitudinal profiles from a fluvial valley in Sierra Nevada, Spain (N37°10', W2°22') and a glacial valley in the French Alps (N45°53' E6°56'), demonstrating the significant difference of their forms. The fluvial profile is smooth and concave, steep in the head and flatter in the lower reaches. The glacial profile is highly heterogenous and more convex in form with multiple significant landforms, suggesting a strong spatial forcing of erosion.

are no equivalent widely accepted analytical approaches for glaciers, though recent work has begun to develop theoretical models that can use ice flow scaling laws to output sliding velocity (and subsequently erosion) based off climatic and topographic parameters (Deal & Prasicek, 2021). Challenges remain, however, largely due to the difficulty in accurately constraining specific glacier characteristics like ice volume and basal sliding (see section 1.2.4), but also due to the fact these ice dynamics vary non-linearly along the profile and in a near constant state of transience according to changes in climate. Hence, the varied longitudinal profiles and landforms of glacial catchments can be seen as evidence of this spatio-temporal non-linearity.

Whether rivers or glaciers are more effective agents of erosion is a long-held debate that spans back to the early years of the study of glaciology in the mid-late 19th century, when there was much discussion over the degree to which glaciers modified alpine valleys – an overview of the main voices and opinions is well provided by Harbor (1989). Today, modern techniques such as GIS and remote sensing permit wide-reaching analyses of geomorphology to provide a wealth of evidence for the impact of these processes on the landscape. Studies across different mountain ranges in the USA directly comparing glaciated and non-glaciated basins has presented evidence for glacial erosion outpacing fluvial (Brocklehurst & Whipple, 2002; Naylor & Gabet, 2007), with the significantly larger size of lower glacial valleys indicating 2-4 times more material removed than in the purely fluvial basins, but with much less pronounced differences in smaller catchments or higher up in the headwaters (Montgomery, 2002). More recently, numerical modelling to devise 'steady-state' glacial profiles and compare them to equivalent fluvial scenarios has suggested glaciers are able to balance the rate of uplift with rates of erosion on lower slope gradients than fluvial profiles, implying that glaciers are more efficient at erosion (Prasicek et al., 2020).

Conversely, in-situ measurements of erosion rates of glacial headwall and valley sides from terrestrial cosmogenic nuclide concentrations in the Himalaya have been shown to be significantly lower than nearby rates of fluvial incision (Heimsath & McGlynn, 2008; Seong et al., 2009). In New Zealand, analysis of sediment yields across glaciated and non-glaciated basins in the Southern Alps showed that glacial cover exerted no detectable influence, with the greatest control being mean annual precipitation (Hicks et al., 1990). Nonetheless, a global comparison of fluvial and glacial erosion rates by Koppes & Montgomery (2009) has shown considerable overlap between the two, suggesting both are capable of denudation at a rate necessary to maintain equilibrium with tectonic uplift. The difference, rather, is that

rates of fluvial erosion have been shown to have little variation over longer million-year timescales, whilst substantial variation is present in the data for glacial erosion over these periods (Koppes & Montgomery, 2009) – once again demonstrating the important spatio-temporal aspect brought about by the sensitivity of glaciation to climate fluctuations. High rates of glacial erosion measured today appear to be a result of a transient response to climate warming, with rates much diminished when averaged over longer timescales, such as on the scale of glacial-interglacial cycles (Gabet et al., 2008). Ultimately Koppes & Montgomery (2009) suggest that tectonics are the primary governing force on rates of both fluvial and glacial erosion over these long timescales, with occasional periods of rapid change in response to other forcings, like sudden changes in climate as we see today. This balance of tectonic and climatic forcing in driving rates and patterns of denudation is a long and ongoing debate explored in the following section.

1.2.3 The Potential for Glacial Erosion to Balance Mountain Uplift

The formation and evolution of mountains is the result of the complex interaction of climate and tectonic processes driving different changes that impact the landscape. The dominant force – whether tectonic uplift drives subsequent changes in regional climate, or climate change brings about greater uplift through enhanced erosion from glacial activity causing lithospheric unloading – was a matter of considerable debate throughout the 19th and 20th centuries and culminated in a seminal paper by Molnar & England (1990) – 'Late Cenozoic Uplift of Mountain Ranges and Global Climate Change: Chicken or Egg?'. In the paper, the authors reject the long-held hypothesis that tectonic uplift was the predominant cause of mountain climate changes in the late Cenozoic era, arguing instead that global changes to a more volatile climate with lower temperatures accentuated mountain building processes through an isostatic response to rapid erosion from glacial activity. Evidence of a worldwide acceleration in erosion and sediment flux during the Pliocene and Pleistocene (Herman et al., 2013) certainly gives credence to this theory given that climate transitions tend to be globally synchronous in nature, whilst tectonic activity is usually more localised. Indeed, studies in the Swiss Alps have deduced that the current patterns of uplift at a rate of ~2-2.5 mm a^{-1} cannot be accounted for with mantle-driven tectonic processes, but instead correlate well to patterns of surface denudation; thus, a significant portion of the uplift is

assigned to lithospheric adjustment to surface unloading from predominantly glacial erosion (Champagnac et al., 2009; Sternai et al., 2019).

Others have argued that the impact of glaciation could not induce significant isostatic response and instead glacial erosion acts to locally increase relief in some regions, whilst actively curtailing it in others. Specifically, it has been suggested that glaciation may limit peak heights and relief through spatially focused erosion at higher elevations around and above the ELA (Whipple et al., 1999). This line of argument was introduced by a landmark study from Brozović et al. (1997), where a topographic analysis of the Himalayas found highly similar mean elevations of basins and catchment hypsometry – i.e. the relationship between land area and elevation – despite regional differences in uplift and erosion rates. Instead, the regional trends in hypsometry were closely correlated with the current extent of glaciation and in particular, snowline elevations. A strong hypsometric maxima was present around and above the average Quaternary ELA position, with about half of the distribution of topographic elevation confined between the altitudes of 4000-5000 m. Thus, the suggestion is that intense glacial erosion focused in this region acts to impose an upper limit on the height of the topography, such that the height of mountain ranges are a function of the altitude window of glaciation and ELA rather than rates of tectonic uplift. The very high altitudes of the Himalaya are therefore suggested to be a function of their low latitude, requiring greater heights before temperatures are cool enough for glacial activity to occur and begin to rapidly denude the summits. In contrast, higher latitude orogens such as the Alaska Range have lower limits for glaciation and hence do not reach the same peak elevations. Similar trends were found for the Andes mountain range, with peak elevations decreasing poleward (Montgomery et al., 2001) and from a comparison of glaciated and non-glaciated basins in the Sierra Nevada, California, USA, with headward erosion focused above the ELA (Brocklehurst & Whipple, 2002). An analysis of the Cascades Range, Washington, USA, found a trend of peak heights being consistently situated less than 600 m above cirques – suggested here as the position of the long-term average Quaternary ELA – regardless of large regional gradients in precipitation and fluvial erosion (Mitchell & Montgomery, 2006). Here, the term ‘glacial buzzsaw’ was used to encapsulate this hypothesis of glaciers’ ability to plane off mountain summits at consistent regional elevations through spatially and temporally focused erosion from the ELA upwards, with particular emphasis on the cirque regions.

Numerous studies have provided similar further supporting evidence for the glacial buzzsaw hypothesis including from the north-western USA (Foster et al., 2008), European

Alps (Anders et al., 2010; Sternai et al., 2011), Kamchatka (Barr & Spagnolo, 2014) and on a wider global scale (Egholm et al., 2009; Mitchell & Humphries, 2015) (Figure 1.6). Notable outliers are present though, such as so-called 'Teflon peaks', which are higher than normal for the surrounding landscape and comprised of particularly steep, smooth and hard rock that has resisted glacial and peri-glacial erosion (Anderson, 2005; Foster et al., 2008; Ward et al., 2012). Volcanic peaks present another key exception, in that they are likely capable of growth at a rate that outpaces glacial erosion (Egholm et al., 2009; Barr & Spagnolo, 2014). Evidence has also suggested that a threshold limit on rock uplift rate may determine the applicability of the glacial buzzsaw, such that in scenarios of particularly rapid uplift, vertical subglacial incision may outpace lateral headwall erosion and thus cirque wall relief would grow rather than be diminished (Brocklehurst & Whipple, 2007; Foster et al., 2008).

The glacial buzzsaw hypothesis is not universally accepted, however. Mitchell & Humphries' (2015) study on the global applicability of the buzzsaw using GIS analysis of cirque floor altitudes attracted two separate responses criticising flaws in the methodology (e.g. analysing only ice-free cirques) and pointed to a frequently overlooked alternative

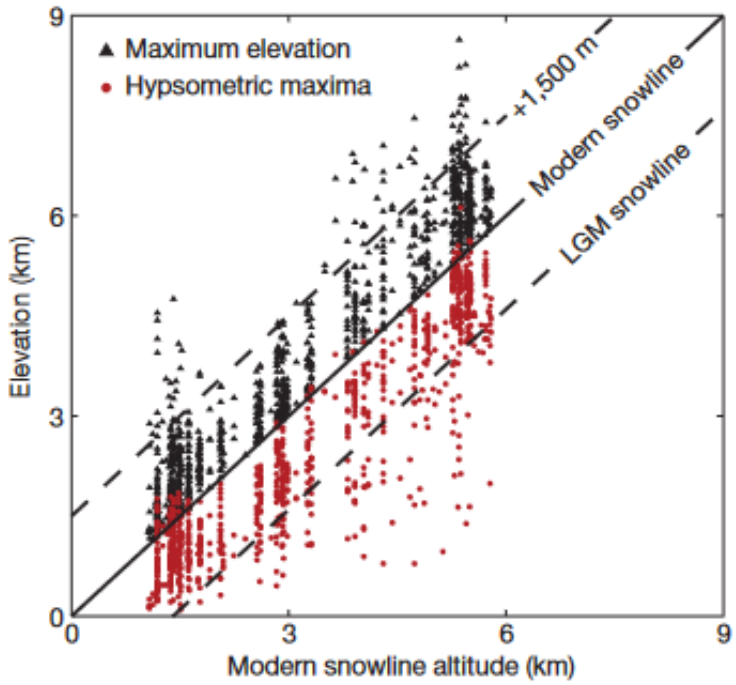

Figure 1.6: The correlation of maximum elevation, hypsometric maxima and snowline altitudes has been used by many to promote the glacial buzzsaw hypothesis. The data here from Egholm et al. (2009) shows that most peaks are less than 1500 m above the current snowline and that the hypsometric maxima of the corresponding landscape tends to be between the current snowline and the LGM snowline – i.e. the region of intense erosion. Figure from Egholm et al. (2009).

hypothesis that cirques may simply be cut into pre-existing topography (Evans et al., 2015; Robl et al., 2015). The counterargument here is that cirques are positioned a set distance beneath summits as an inevitable artefact of their formation occurring in the valley heads near the summits – i.e. the birthplace of glaciers. This was suggested from topographic analysis of the Romanian Carpathian mountains where no evidence was found for significant glacially-induced lowering of summits and ridges (Mîndrescu & Evans, 2014).

Arguably, the idea that erosion is most effective above the ELA is somewhat flawed given that colder temperatures and lack of moisture is not conducive to the current understanding of the mechanisms of how glaciers erode (see next section). Rather, expectations would place the most effective erosion further down the valley where ice is thicker, warmer, faster and frequently producing meltwater (Cook & Swift, 2012; Hall & Kleman, 2014; Swift et al., 2015). Moreover, recent work from Lai & Anders (2020, 2021) has argued that basal thermal regime enacts a first order control on erosion, with different climatic conditions giving variable thermal regimes, despite otherwise very similar ELAs. Indeed, cold-based ice in the accumulation zone has been suggested to be up to 16 times less erosive than warmer ice below the ELA, potentially enabling glaciers to protect summits and permit continued growth rather than limit them (Godon et al., 2013). Moreover, field evidence from detrital thermochronometry in Patagonia has indicated a stronger erosional signal below the LGM ELA (Falkowski et al., 2021), whilst cosmogenic nuclide measurements from the Pyrenees show low rates of ridge lowering outpaced by cirque growth during deglaciating and interglacial periods (Crest et al., 2017).

The fixed window of enhanced erosion presented by the glacier buzzsaw hypothesis appears to contain theoretical flaws then, given that the ice dynamics conducive to effective erosion (more details in the next section) will be spatially variable over time with changing climates and topography. Field studies have suggested cirques erode headward over time and likely dominate landscape evolution in the initial stages of glaciation (Brocklehurst & Whipple, 2002; Oskin & Burbank, 2005; Naylor & Gabet, 2007; Scherler, 2014), which has been reproduced by numerical models (MacGregor et al., 2009; Shuster et al., 2011). But bedrock steps (icefalls) and overdeepenings further down the profile suggest a strong focusing of erosion in these regions also. These features have been replicated in numeric models using a simple linear erosion law coupled with sliding (MacGregor et al., 2000; Anderson et al., 2006), but as a result they occur passively in-situ around regions of high ice flux like confluences or the ELA. More dynamic behaviour of such features, like headward retreat, has been suggested from some field evidence (Shuster et al., 2011; Brown, 2017),

but is only seen in models using more non-linear approaches and including more complex elements of ice dynamics such a hydrological processes (Herman et al., 2011; Liebl et al., 2021) to more reliably account for the variability in ice dynamics within the catchment over time. This non-linear behaviour is not well constrained though and necessitates further study.

In the next section I will review the current understanding of the mechanisms of glacial erosion and show why accurate quantification of its influence on the landscape remains so difficult.

1.2.4 Glacial Erosion – Mechanisms and Challenges

The mechanisms by which glaciers erode their beds can be categorised into four main groups: fluvial incision, chemical dissolution, abrasion, and quarrying. The transit of meltwater beneath a glacier can coalesce into efficient subglacial streams, which may form either tunnels in the ice as Rothlisberger channels (Röthlisberger, 1972), or Nye channels incised directly into the bed (Nye, 1972). Erosion from fluvial incision of Nye channels can be significant and lead to the formation of deep inner gorges and tunnel valleys over time (Montgomery & Korup, 2011; Beaud et al., 2018a), however these are very much spatially limited to meltwater pathways and thus not a process operating across the entire extent of the ice cover. Chemical weathering from the dissolution of bedrock by meltwater is an important component of the solute content in glacial runoff (Brown et al., 1996), though the efficacy of such a process will be largely dependent on the bedrock geology and the overall contribution to net glacial erosion is likely to be small (Louvat et al., 2008). Abrasion from the force of rock particles dragged along the ice-bed interface and quarrying of rock fragments and blocks detached by the force of the ice overburden pressure are considered the main mechanisms of glacial erosion, with quarrying deemed to be likely the most effective (Alley et al., 2019).

Effective abrasion is controlled by the rate of viscous drag induced by basal melt, as well as the concentration of debris particles in the basal ice which will act to enhance the sandpaper effect or, beyond a threshold thickness, act as a suppressant forming a protective deformable layer (Hallet, 1979, 1981).

Quarrying occurs from a concentration of forces from ice overburden and basal shear stress onto the edges of bedrock deformities, which drives fracturing. Quarrying will be

most effective on irregular bed lithologies with pre-existing planes of weakness and under ice conditions of low effective basal pressures and fast sliding which are conducive to extensive cavity formation and thus more focused concentration of shear stress (Hallet, 1996). The presence of subglacial water is also an important factor for several reasons: variable water pressures over diurnal and seasonal cycles are important for maintaining cavity networks and can enhance the sliding rate of a glacier (Iken & Bindschadler, 1986), but may also directly promote quarrying by increasing crack propagation (Cohen et al., 2006) or through stimulating basal freeze-on of clasts (Röthlisberger & Iken, 1981). Moreover, subglacial water is needed to flush the bed clear of the produced sediment and till, which may otherwise accumulate to dampen the effects of erosion (Alley et al., 2019). However, increasing surface debris cover has recently been suggested as a dynamic that may reduce overall meltwater input to the system and hence limit the potential for subglacial erosion (Delaney & Anderson, 2022).

Understanding these mechanisms of erosion and their controls has been achieved mainly through theoretical study, given that they operate in the inherently inaccessible subglacial environment which makes direct empirical measurement exceedingly difficult in all but a few very rare cases where tunnels beneath glaciers have been constructed, usually for commercial purposes like the development of hydropower systems (e.g. Boulton, 1982). Consequently, estimates of erosion rates have frequently been attained from mathematical scaling of the evacuated sediment yield of proglacial streams (e.g. Hallet et al., 1996). Often such estimates are from the suspended sediment flux, as accurate measurement of the bedload transport is traditionally very difficult. Whilst there have been recent advances in the use of seismic sensors to improve bedload monitoring, outputs have shown the proglacial forefield has a strong filtering effect on bedload fluxes over short distances, such that measurements any significant distance from the ice margin would prove very unreliable (Mancini et al., 2023a).

Deriving erosion rates from sediment yields is problematic in a number of ways. Firstly, significant quantities of the sediment flux may be sourced from supra or extra-glacial material that has been transported through the subglacial system, rather than freshly eroded bedrock. Cosmogenic nuclide measurements of evacuated sediment has shown the proportion of subglacially-derived material is highly variable, between 50-90% across sample sites at a single Mont Blanc glacier (Guillon et al., 2015). Sediment may also be held in storage at the bed for unknown periods of time before being accessed through changing hydraulic gradients (Swift et al., 2005). Whilst some have argued that long-term sediment

storage is likely negligible (Riihimaki et al., 2005; Egholm et al., 2012a), others have proposed that a bottlenecking of sediment transport near the terminus, or the influence of overdeepened topography complicating hydrological pathways, can disrupt regular scaling of sediment evacuation with discharge and lead to accumulation (Beaud et al., 2018b; Swift et al., 2021). Moreover, as ELAs rise with the warming climate, there will be greater regions of the bed at higher altitudes exposed to meltwater, potentially flushing out any previously undisturbed sediment (Delaney & Adhikari, 2020).

A comparison of erosion rates over a variety of timescales by Koppes & Montgomery (2009) has shown differences of over an order of magnitude between short-term (10^1-10^2 a) and long-term (>10^3 a) rates calculated from sediment yields and by two orders of magnitude when averaged over million year timescales using thermochronometry (Figure 1.7). This demonstrates the sensitivity limitations of the measurement technique to the timescale at which it is applicable. Low measures of erosion from the million-year timescale from thermochronometry or other dating techniques represent a time-averaged rate derived from a continuum of processes (e.g. glacial, fluvial, aeolian etc.) operating over a wide variety of climatic conditions (glacial and interglacial cycles), such that periods of high erosion are balanced out by periods of very little activity. In contrast, very high erosion rates measured more recently from proglacial sediment yields reflect a current period of highly dynamic glacial activity and climate, resulting in conditions that may favour more rapid erosion (Koppes & Hallet, 2002) and/or sediment evacuation.

Cosmogenic nuclide dating of sediment cores from the Mediterranean has revealed erosion output from the southern European Alps over the last glacial cycle and suggested that erosion was much higher during the LGM than today, with today's rates similar to moderately glaciated interstadials (e.g. ~75ka) (Mariotti et al., 2021). As such, erosion rates estimated from sediment yields of contemporary alpine streams should only be interpreted as contemporary rates that are likely inaccurate beyond the last few centuries. Even so, considerable inter-annual variations in sediment output from glaciers have been recorded and believed to be reflective of changes in subglacial hydrological regimes (Bogen, 1996). Consequently, rates obtained from temporally limited sediment data (e.g. single melt season) may contain significant margins of error and should be interpreted with caution.

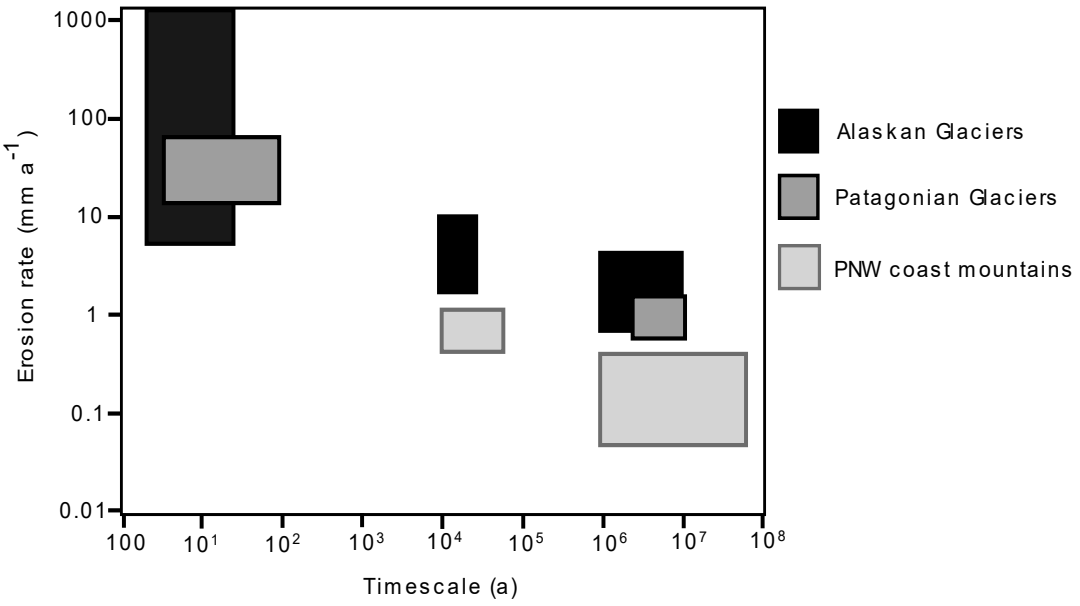

Figure 1.7: Compilation of erosion rate data from various regions including ranges in rate estimation (box height) and timescale (box width). Longer term erosion rates appear some two orders of magnitude lower than more modern rates, which appear to be especially rapid. Figure from Koppes & Montgomery (2009).

Deciphering patterns of environmental change becomes increasingly difficult the further back in time one wishes to target. This is for a number of reasons, most prominently, compounding uncertainties in climatic and environmental conditions (e.g. the exact timing and extent of glacial advances or retreats), resulting in ambiguous histories of sediment or rock samples – for example, glacial sediments or transported boulders may have been reworked several times by both glacial and non-glacial processes since their original deposition, muddying the overall interpretation (e.g. Lukas et al., 2007). Subsequently, a lot of work looking at the evolution of landscapes and the efficacy of glacial erosion frequently uses numerical modelling – representing real-world processes through mathematical equations and laws, which when combined and solved together can 'simulate' change over time. Naturally the limitation here becomes the choice of deterministic law to account for a process, and the constraints on its driving values. For some parameters, these values are well defined through easy empirical evidence (e.g. the density of glacial ice), but others are far more poorly constrained owing to either the sheer complexity of a process, a lack of sufficient empirical data, or a combination of both. Numerically representing glacial erosion

falls into the latter, given that it is a complex process driven by a multitude of different variables and operating in the hidden and inaccessible subglacial domain which makes empirical data collection exceptionally difficult. A common approach to overcome this is to use a simple law where glacial erosion E is the product of bedrock hardness or resistance to erosion K_G coupled with sliding velocity U_s raised to a dimensionless exponent l:

$$E = K_G \, U_S^l \tag{1.1}$$

This was used successfully by Harbor (1992) to show the transformation of valley cross-sections from fluvial V-shapes to glacial U-shapes. The same approach has also been used to demonstrate spatially focused erosion along the profile creating landforms like large steps and overdeepenings (MacGregor et al., 2000), which tended towards regions of high ice flux, such as the convergence of tributaries, where sliding velocities increased. Indeed, using ice flux as a proxy for sliding is also a common approach (e.g. Anderson et al., 2006) given that accurate determination of basal sliding remains a major challenge (Cuffey & Paterson, 2010). Whilst such models often agree with real-world observations (e.g. Jiskoot et al., 2017), they frequently fail to reproduce other elements, such as terminal overdeepenings or steps outside of confluences, which are only reliably created with higher order models incorporating more processes like subglacial hydrology (e.g. Herman et al., 2011; Egholm et al., 2012a; Liebl et al., 2021), which as discussed, plays a pivotal role in driving basal motion and quarrying.

Use of the simple erosion law is often still favoured even in these higher order models and aside from choice of sliding law, the value of K_G and l is critical and capable of producing markedly different outputs (Harbor, 1992; Prasicek et al., 2020; Seguinot & Delaney, 2021). In particular, the dimensionless exponent l has received considerable attention, being derived from a relationship between sliding velocity and erosion and whilst loosely constrained, is statistically justified given empirical data on the coupling of sliding and erosion rates (Cook et al., 2020). Frequently, a simplistic linear relationship is used in modelling where $l = 1$ (e.g. MacGregor et al., 2000, 2009; Tomkin, 2007; Egholm et al., 2009; Sternai et al., 2011). However, empirical data suggests non-linear trends to be more appropriate with lower $l \approx 0.65$ for broad landscape analysis and higher $l \approx 2$ for the individual catchment scale, the latter likely being required to more reliably capture variability in sliding and erosion mechanics along the profile (Herman et al., 2015; Cook et al., 2020). Variability in the l value has been explored at the scale of the entire Alps over the

last glacial cycle (Seguinot & Delaney, 2021), but an equivalent assessment at a higher resolution catchment scale is currently lacking and needed to progress the discussion.

Glacial erosion is a complex topic, though significant progress has been made in our understanding since the early days of discovery and postulation (e.g. Ramsay, 1862; Tyndall, 1864), to more advanced mathematical theoretical study in the 20th century (e.g. Hallet, 1979, 1996) and now the use of numerical models to test theories and simulate changes (e.g. MacGregor et al., 2009; Egholm et al., 2011; Prasicek et al., 2020) – the capability of which will only improve with time as computing infrastructure becomes more powerful and advanced. Improving our understanding of the spatial and temporal patterns of glacial erosion is scientifically beneficial in several ways: we can more rigorously evaluate theories of major landscape evolution, such as the glacier buzzsaw hypothesis discussed previously (Brozović et al., 1997); we can gain greater insights into the development of unique glacial landforms; we can improve understanding and constraints on numerical laws used to simulate erosion that will benefit future modelling studies – for example, palaeoglaciological reconstructions that permit improved hindcasting tests of global climate and ice models, which in turn enhances the accuracy of modelling glacier, ice sheet and landscape responses to current and future climate change (Stroeven & Swift, 2008). Beyond the purely scientific advances, there is an anthropogenic benefit to improving our understanding of glacial erosion as well, as the consequences can have far-reaching impacts on the infrastructure of glaciated regions. For example, long-term sedimentation rates affect the water-quality of downstream communities and are of critical concern for hydropower installations (Herman et al., 2021), whilst the need to store radioactive nuclear waste in deep geologic repositories requires certainty that they will not be exhumed by future glacial activity in the millennia to come (Fischer et al., 2014).

1.3 Aims and Objectives

The above overview of the current knowledge of the field demonstrates a broad understanding of how glaciation shapes whole mountain ranges over time but is lacking in detail and resolution of the processes and evolution operating in the high alpine catchments where ice occupation times are longest and today's glaciers are situated. The landscape should tend towards a dynamic equilibrium in which uplift is balanced by denudation, with theories like the glacial buzzsaw developed to explain the role of glaciation in this balance (Brozović et al., 1997). Yet the heterogeneity of high alpine catchments speaks to a highly spatially variable pattern of denudation that confounds such a simple balance.

Modern techniques permit improved monitoring of glacial sediment output to estimate contemporary erosion rates but carry high spatial and temporal uncertainties, whilst advanced geochronology methods can yield snapshot time-averaged erosion rates on the scale of hundreds to millions of years that can be difficult to interpret. Numerical modelling provides an avenue to explore possible pathways to glacial and landscape evolution but is only as reliable as the numerical laws driving it.

Consequently, there is a need for improved understanding of glacial erosion patterns at higher resolution scales within these individual high alpine catchments. This is important in order to improve constraints on non-linear erosion laws for numerical modelling, as well as greater understanding of how high alpine landscapes evolve over time. Consequently, the specific aim, research questions and objectives of this thesis are as follows:

Aim: To improve our understanding of the dynamism of glacial erosion operating at the sub-catchment scale under a range of glacier conditions.

Question 1: How do rates of exhumation vary along high alpine glacial profiles that include complex features and landforms unique to glacial erosional processes?

Question 2: How does glacial erosion vary spatially through time and is dynamic behaviour such as headward migration of features like icefalls or cirques plausible?

Question 3: Which erosion law is most applicable at the individual catchment scale and over a variety of timescales?

Question 4: What is the magnitude of potential bias in using contemporary sediment yields to estimate longer-term glacial cycle erosion rates?

These questions will be addressed through application of the following objectives which outline the work presented in the next four chapters:

Objective 1: Using a topographic GIS analysis, explore the spatial distribution and significance of icefalls as a major glacial landform and their influence on the evolution of alpine catchments.

Objective 2: Using the landscape evolution model iSOSIA, investigate the impact of using different erosion laws and climate conditions in the simulation of glacial erosion over time.

Objective 3: Using a novel approach of luminescence thermochronometry applied to field site samples, identify specific rates and pattern of exhumation across the glacier profile over the last glacial cycle.

Objective 4: Given the results from the previous objectives, assess the overall picture of how glacial erosion operates spatio-temporally at the sub-catchment scale and the influence this has on evolving the landscape and specific glacial landforms.

1.4 Thesis Structure

This thesis is comprised of five chapters, including this first chapter which has given a broad overview of the relevant literature and concepts, then outlined the main research questions and objectives. The subsequent chapters will address the objectives outlined above in turn, with a focus on the Swiss Alps as a study site to gather data and execute the methodology.

Chapter 2 looks at icefalls as a feature of importance in the glacial landscape that has so far received little scientific attention. It contains a first-order inventory of active contemporary icefalls in the Swiss Alps using a GIS approach and goes on to derive some foundational metrics to define the landform more reliably. Thereafter, the topographic distribution of icefalls in the landscape is explored with the finding of a remarkable spatial correlation to climatic gradients, leading to a discussion of the possible implications this has on patterns of glacial erosion and landscape evolution.

Chapter 3 focuses on the landscape evolution model iSOSIA (Egholm et al., 2011), which is used to test the impact of different erosion laws and climate conditions including LIA, interglacial, LGM and a glacial period. The simulations take place on two key field sites from the Swiss Alps – Glacier d'Otemma and Triftgletscher – which will be introduced with more detail.

In Chapter 4, the focus is on the application of a novel method of thermoluminescence thermochronometry to bedrock samples acquired from the two Swiss field sites. Acquisition and setting of the field samples is described, followed by preliminary sensitivity tests and then data from two different methodological approaches – Single Aliquot Regenerative protocol and Multiple Aliquot Additive Dose protocol. The latter approach produces a time series of exhumation data over the last glacial period for the catchments, which was previously unachievable using more traditional methods of geochronology.

The final section, Chapter 5, brings together all the elements from the previous chapters into an overall discussion around the aim of exploring the spatial and temporal patterns of glacial erosion at the sub-catchment scale, comparing the data, addressing each of the research questions, and finishing with a summary of the key findings and recommendations for future research directions.

Chapter 2

The Importance of Icefalls in Alpine Landscapes

2.1 Introduction

2.1.1 Chapter Overview

As a first step towards investigating the spatial dynamics of alpine glacier erosion and working towards the first two research questions, this chapter explores the widespread yet overlooked glacial landform of icefalls that have previously received little scientific attention. In this chapter I address this lack of prior research by investigating the prevalence of icefalls across contemporary glaciers in Switzerland and show how their scale and distribution demonstrates an apparently strong coupling to climate. I consider the important links to glacial erosion over time and the wider influence icefalls may have on mass balance and landscape evolution that had previously yet to be fully explored.

2.1.2 Dynamics of Glacier Long-profile Erosion

Glaciers exist in a state of dynamic equilibrium, adjusting constantly to changes in climate and tectonic uplift over time to balance the processes of accumulation and ablation. The strong coupling of glaciers to climate and the subsequent intrinsic differences in ice dynamics between the accumulation and ablation areas creates a uniquely variable driver of landscape modification as ice extent, thickness and thermal regime change not only over time, but spatially along the profile. This dynamism is captured in the highly heterogenous landscapes of glacially dominated catchments which indicate the existence of great spatial variability in the strength of glacial erosion (Figure 2.1a). The complexity of this pattern is in

part why a reliable model to explain and quantify glacial erosion has remained a significant challenge (Prasicek et al., 2018). Conversely, the reasonably simple and uniform longitudinal valley profiles of fluvial systems (Figure 2.1b) permit relatively straightforward quantification of fluvial erosion, with a strong empirical relationship between river channel length and drainage area captured in Hack's law (Hack, 1957) (Figure 2.2a) and the proportional scaling of incision rate to drainage area and slope quantified within the stream power incision model (Lague, 2014) (Figure 2.2b).

Topographic analysis and detailed study of glacial landforms has long been used as a method of investigating the impact of glacial erosion and a remarkable correlation exists between landscape hypsometry, equilibrium line altitude (ELA) and summit height, as per the glacier buzzsaw hypothesis (Brozović et al., 1997) (see Chapter 1, section 1.2.3). Particular attention has been brought to cirque landforms as drivers of the buzzsaw mechanism through headward erosion, due to the strong correlation between the altitudes of cirque floors and surrounding peaks (Mitchell & Montgomery, 2006; Barr & Spagnolo, 2015). As such, cirque floors have previously been interpreted to represent the location of a long-term average Quaternary ELA and hence region of erosion maxima (Foster et al. 2008).

The buzzsaw hypothesis is debated though, with contentions around its global applicability (Evans, 2021), or that the mechanism even exists at all (Hall & Kleman, 2014). Others have stressed the importance of basal thermal regime in dictating spatial patterns of erosion, regardless of climate and ELA (Godon et al., 2013; Lai & Anders, 2020, 2021). Further, theoretical considerations of glacial erosion would place higher effectiveness below the ELA where the presence of faster, thicker and warmer ice with the availability of meltwater and active sediment transport would all contribute to more dynamic erosional activity (Herman et al., 2011; Cook & Swift, 2012; Swift et al., 2015; Alley et al., 2019). Such power is evident from the high relief and major glacial landforms found further down-valley such as wide U-shaped trunk valleys, overdeepenings, tunnel valleys and inner gorges (Montgomery, 2002; Montgomery & Korup, 2011; Cook & Swift, 2012).

A major landform that is arguably missing from the debate and indeed lacking in major scientific attention is that of the icefall. These are large, obvious steps found frequently in glacier profiles (Figure 2.1), where the sudden steepening gradient presents a dramatic decline in base level, creating a zone of significant change in ice dynamics. Rapid extending

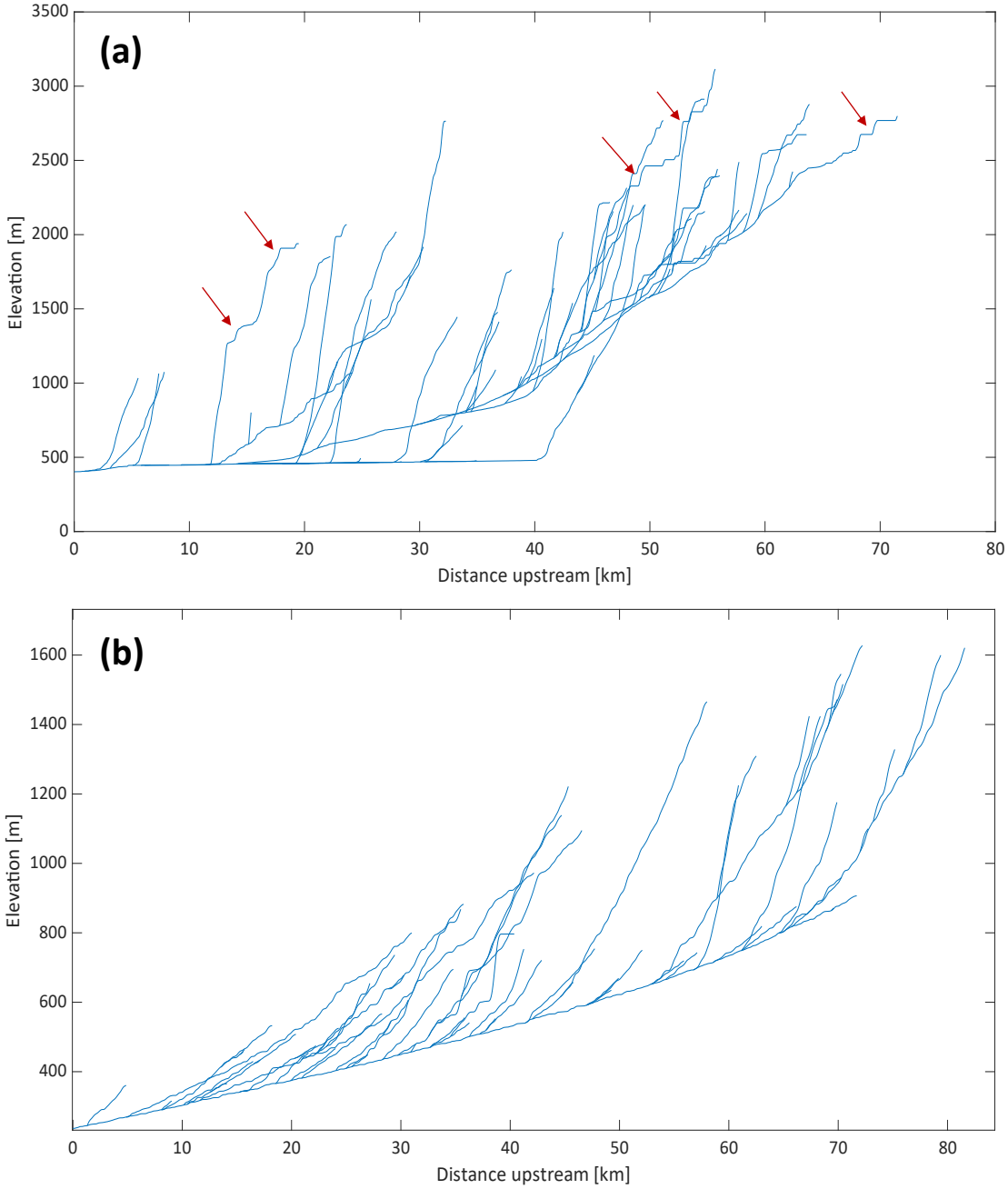

Figure 2.1: Contrasting longitudinal elevation profiles for a common glaciated catchment at Val de Bagnes, Switzerland (N 46.05°, E 7.27°) **(a)** and fluvially dominated catchment in the Sierra Nevada, Spain (N 37.17°, E -2.37°) **(b)**. Note the highly flattened lower reaches of the glacial profile from the deep excavation of trunk valleys, which then rapidly steepen going upstream, interrupted by substantial steps (red arrows), indicative of spatially focused erosion over changing climate and ice extents. In contrast, the fluvial profiles maintain a steady concave gradient, steepening gradually with distance upstream and containing occasional small knickpoints.

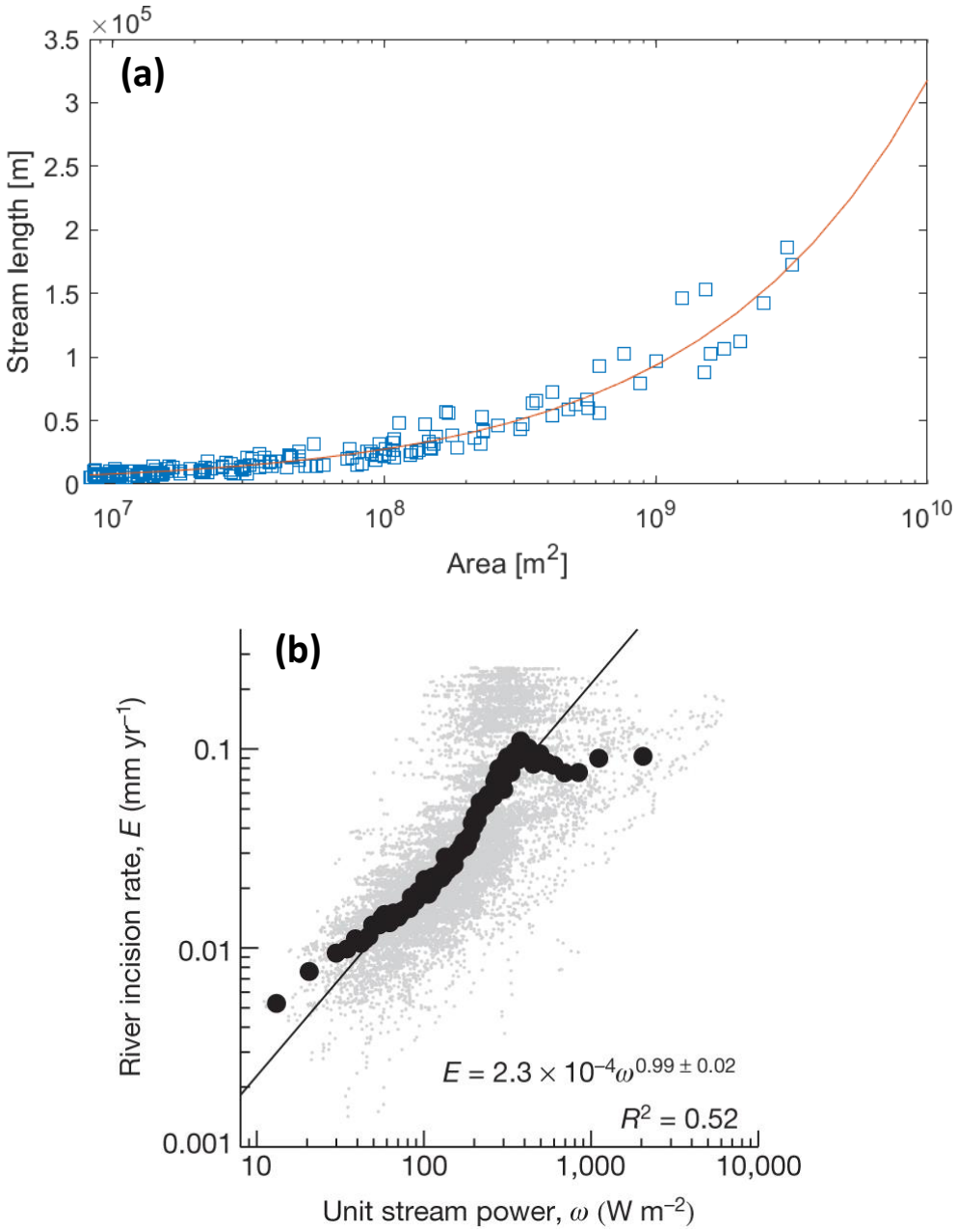

Figure 2.2: Examples of empirically constrained models of fluvial erosion. **(a)** Hack's Law demonstrating the scaling of basin area with channel length, figure from Schwanghart (2020). **(b)** The stream power incision model showing the scaling of river incision rate with stream power (derived from channel characteristics), figure from Ferrier et al. (2013).

flow occurs and ice thins under large tensile stresses, fracturing the surface into deep transverse crevasses and seracs (Benn & Evans, 2010). Observationally, icefalls appear frequently to be positioned near to present-day snowlines (Armstrong et al., 2017), an oft-used visual proxy for ELA (Rabatel et al., 2005). As such, a drastic declivity in the bedrock near the ELA – a region posited as a hot zone for glacial erosion (Herman et al., 2011) – evokes thoughts as to whether icefalls may in fact be important glacial landscape features, similar in perceived significance to that of cirques, in driving mountain landscape evolution.

This poses the question: As ELAs migrate throughout glacial cycles, and tectonic uplift on such timescales continues steadily, could a signal of strong erosion travel through a valley in the form of an icefall, analogous to fluvial waterfalls and their tendency to migrate up-stream in response to changes in base-level (Crosby & Whipple, 2006)? In other words: are they the manifestation of more effective erosion in the ablation area being communicated up-slope to the catchment's upper reaches? Alternatively, might icefalls instead simply be a feature of *in-situ* erosion near the long-term average ELA? The latter may at first appear rather more obvious, yet this would imply that they represent a critical *disconnection* in the landscape, where erosion at high elevation is outpaced by faster, melt-driven erosion at lower elevations, which could not possibly be a stable situation over the long timescales of mountain range evolution (i.e. 1 Ma +).

Such questions have not been asked or explored in previously published material. Fundamental literature quantifying icefalls as a landform in itself is largely absent and thus needed to progress these ideas further. Therefore, this Chapter sets out to mainly establish just how prevalent icefalls are in the glaciated landscape, their fundamental characteristics, and whether this indicates a predominantly climate (excavation in-situ) or dynamic (headward eroding) development of such features.

2.1.3 Icefall Etymology

Icefalls are chaotic and dangerous places on a glacier, as any mountaineer will know. Perhaps the most famous, the large Khumbu Icefall on Mount Everest presents a formidable initial hurdle to any alpinist hoping to scale the world's tallest mountain. An ever changing maze of gaping crevasses and towering serac blocs, it has reportedly claimed 22% of deaths on the Nepalese side of Everest since 1953 (The Himalayan Database, 2023).

It is perhaps no surprise then, that data on published use of the word 'icefall' sees a large spike around the 1950s period (Figure 2.3), coinciding with mountaineering attempts on Everest changing from the northern Tibetan side, to the western Nepalese side where the Khumbu glacier is located, culminating in the first documented successful summit in 1953 (Unsworth, 1982). According to the Google Books Ngram Corpus (Michel et al., 2011), which contains frequency data on words used in a corpus of published material from 1800 onwards, first use of 'icefall' appeared in 1810 (Figure 2.3). A few of these early uses appear in relation to weather (e.g. snow or hail), avalanches, or the literal fall/collapse of glacial ice – such as in relation to the Giétro Glacier lake outburst flood disaster of 1818 in Switzerland (Simond, 1823). Some of the earliest easily accessible published uses of the term icefall as a descriptor for the glacial landform comes from pioneering glaciologist Professor James D. Forbes and his series of 'Letters on Glaciers' first starting in 1841 (Forbes, 1859). In these, the term icefall is used frequently as he documented notable features of glaciers on his travels around the Alps, particularly in relation to the light and dark striped surface features of the Mer de Glace that emerge conspicuously beneath the large icefall and would come to be known as 'Forbes Bands', or later, 'ogives'.

The term 'icefall' (or the translated equivalent) is notably absent in the French language, whilst in German the term 'Eisbruch' (icebreak) is used. Maps of the French and Swiss alpine regions simply show glacier icefalls as steeper, crevassed regions, though sometimes recognition is given in the form of a specific name assigned to the area (e.g. Seracs du Geant, Seracs du Brenay), or other times the glacier name itself may be split into an upper (obere) and lower (undre) region that appears to recognise the presence of an icefall without specifically referring to it. It appears likely then, that the term 'icefall' stemmed from the writings of early British mountaineers and scholars and has since stayed in the vocabulary of English mountaineering and academic literature.

While simple online searches of published material does not yield an account of how first use of the term came about to describe the glacial landform, it would not be a far reach to assume its inception occurred as a simple analogy to a fluvial waterfall given that early texts on alpine glaciers often conjured descriptions of them being equivalent to large frozen rivers – e.g. "The regulated progression of the glacier… has a much more precise analogy to that of a river…" (Forbes, 1859, pp. 44).

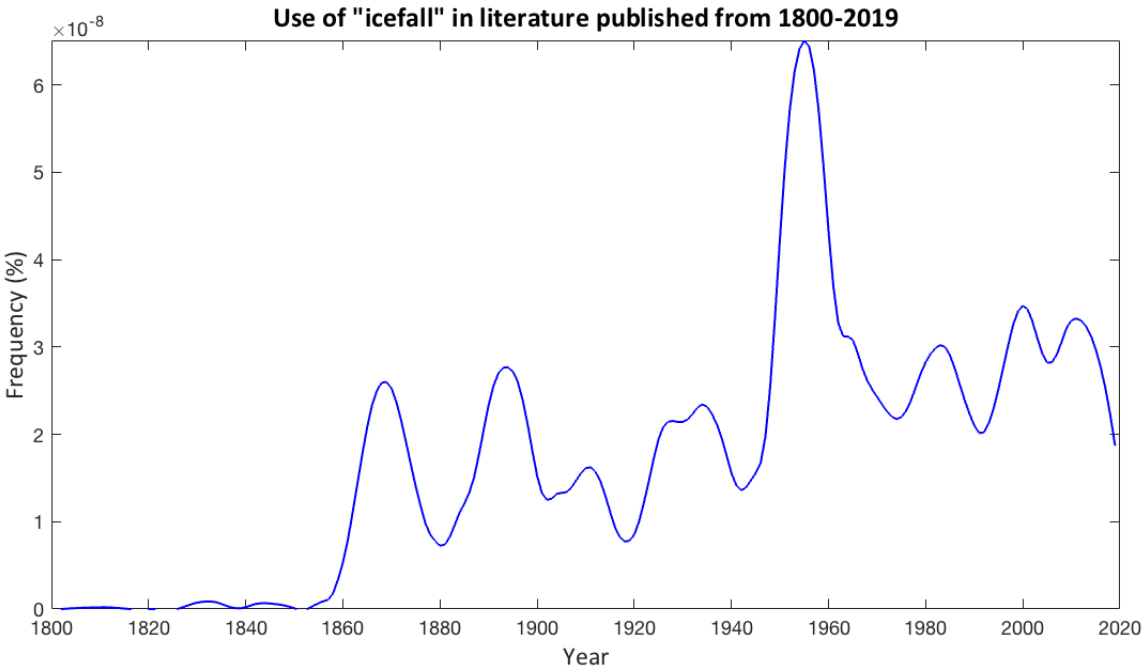

Figure 2.3: Frequency of appearance of the word 'icefall' in the Google Books Ngram corpus of scanned literature in the English language between 1800 and 2019 (Michel et al., 2011). Initial uptick in the latter half of the 19th century as academic discourse on glaciology increased. Peaking in mid 1950s with media attention around successful summits of Mount Everest.

2.1.4 Previous Research Regarding Icefalls

Any continued academic focus on icefalls has been confined largely to the further study of ogives after Forbes' initial findings, notably by: Nye (1958, 1959), King & Lewis (1961), Posamentier (1978), Waddington (1986), and Goodsell et al. (2002). These studies sought to understand what specific combination of processes – unique to some icefalls – were responsible for producing ogives below them. The importance of gradient and enhanced velocity in the icefall for influencing seasonal differences in mass balance and ice density were considered (Nye, 1958; King & Lewis, 1961), as well as the potential for subglacial thrusting and rotation of ice columns from high compression at the base of icefalls (Goodsell et al., 2002). However, each of these studies were conducted at a limited scale, often at a single glacier site, with no wider data on the prevalence or characteristics of icefalls generally.

A detailed study of Griesgletscher, Switzerland by Hambrey et al. (1980) recognised the great influence that the icefall had on ice dynamics, with significant localised changes in ice velocity, thickness, deformation and strain rates. Installation of instrumentation in the field was limited to either side of the icefall, however, likely due to the aforementioned dangerous nature of these features.

Outside of this, icefalls are afforded only cursory attention within studies focused largely on other matters. Early work on modelling glacial erosion by MacGregor et al. (2000) frequently mentions 'steps' in glacial valley long-profiles at trunk glacier and trunk-tributary confluences (notably forming 'hanging valleys'), as was initially observed long ago by Penck (1905) (Note: neither Penck nor Macgregor et al. specifically used the term icefall in this scenario). The 1D model from MacGregor et al. (2000) produced these steps just down-valley from confluences as the increase in ice discharge resulted in a step-change in sliding velocity and thus erosion rate (via a simple sliding-dependent erosion rule). Further, step size was found to grow as the ratio of tributary to trunk discharge increased, because this similarly increased the step-change in sliding rate. In the absence of a tributary valley, any smaller steps formed by the model were subsequently smeared out and overwritten under different climate scenarios that generated different glacier lengths and thus variable regions of peak discharge and sliding velocity that migrated up- and down-profile.

Thorough empirical analysis of Shackleton Glacier, Canada by Jiskoot et al. (2017) corroborated the modelling work of Macgregor et al. (2000), finding the size of steps to be related to the ratio of tributary and trunk discharge at confluences, but also suggesting an

enhancement of quarrying processes following icefall formation likely due to the propagation of crevassing (Hooke, 1991).

Similarly, Anderson et al. (2006) discussed the formation of glacial valleys over time and showed major step formation at the coalescence of headwater valleys (or convergence of cirques) as well as tributary junctions once more, using an even simpler linear coupling of ice discharge, rather than velocity, to attribute effective erosion. It was suggested erosion may be focused around the long-term mean ELA, though when accounting for different mathematical variability in ELA over time and particularly in cases where the mean ELA lies above the topography, a more reliable measure may be that maximum erosion occurs at approximately a third of the distance from the valley head to the limit of the largest glacier.

More recently, limited attention has been brought to icefalls as a potential catalyst for rapid mass loss of contemporary glaciers (Rowan et al., 2015, 2021; Rippin et al., 2020; Davies et al., 2022). Given that ice is generally believed to be thinner in the icefall due to extensional flow over the steep gradient, this presents a vulnerable point in the glacier mass profile. Continuously rising ELAs will expose icefalls to more sustained ablation and negative mass balance, which can eventually lead to exposure of bedrock, followed by full disconnection of the glacier. Such disconnection at the icefall region can then result in stagnation and mass wastage of the lower tongue as it is no longer sufficiently supplied by the accumulation area above. These situations have been described so far for regions in the Himalaya (Rowan et al., 2015, 2021), Columbia Icefield of Canada (Rippin et al., 2020), and at the Juneau Icefield of Alaska (Davies et al., 2022).

2.1.5 Chapter Aims and Objectives

Given such limited detailed study, icefalls remain rather enigmatic. What exactly constitutes an icefall and how can we define it beyond a commonly vague descriptive term? Like many glacial landforms, they are difficult to define in absolute quantitative terms but are visually obvious features found frequently in glaciated landscapes. While they have sometimes been delineated in past studies using gradient – such as 18° (Jiskoot et al. 2017) or 22° (Budd et al. 1979) – such instances are rare and with little-to-no reasoning for the choice of threshold value. Rather, icefalls tend to be noted purely as observational features in the majority of studies, seldom providing any further detail than acknowledging their

localised impact on ice dynamics – for example, a study on crevasses by Colgan et al. (2016, pp.155) uses a crevasse-focused description of icefalls as "a series of crevasses resulting from the breakdown of laminar flow as a glacier flows over a convex bed".

In order to progress hypotheses surrounding the variability and impact of glacial erosion on landscape evolution and dynamics of theories like the glacier buzzsaw, a more thorough understanding and quantification of icefalls is needed. As such, the overall aim of this chapter is to explore the prevalence of icefalls in a contemporary glacial landscape and analyse what their characteristics and topographic distribution may suggest for patterns of glacial erosion and catchment evolution. The key objectives of this chapter are therefore:

1. Create a regional inventory of icefalls across contemporary glaciers in Switzerland to note their prevalence and specific locations within the landscape.
2. Measure the physical characteristics of identified icefalls – such as size, ice thickness and velocity, gradient, geological context, and elevations – to establish more rigorous quantitative definitions for the future.
3. Examine what this collated data may indicate in terms of icefall genesis, evolution and overall impact on high alpine landscape dynamics and evolution.

The following methods section will detail how icefalls were identified and categorised, as well as the type of data extracted from each feature. The inventory and data are then presented in the results section, which raise some questions and hypotheses around icefall evolution and their importance that are then critically considered in the discussion section.

2.2 Methods

2.2.1 Icefall Identification

Icefalls come in many shapes and sizes, making it difficult to quantitatively define them. As such, automated mapping of icefalls is an exceedingly difficult task due to the high likelihood of false positives for other areas of the glacier profile – initial experiments to find icefalls using a simple gradient threshold was carried out, but this frequently resulted in erroneous delineation of regions like the headwall or a hanging glacier due to similarly steep slopes. Thus, the need for visual interpretation is difficult to overcome outside the development of complex machine learning approaches with rigorous training datasets. Indeed, this is an issue that is frequently encountered when mapping other glacial landforms, such as drumlins (e.g. Dowling et al., 2015; Jorge & Brennand, 2017; Putkinen et al., 2017).

Davies et al. (2022) have presented likely the most comprehensive regional mapping of icefalls published so far, as part of a wider study on the Juneau Icefield, Alaska. To achieve this, they used a series of visual criteria to identify icefalls as: a region of extensional arcuate transverse crevassing at the top, descending down a steep slope of intense, dense crevassing and seracs, with the frequent presence of ogives emanating at the base (Davies et al., 2022, pp. 77).

Here, I take a conservative approach to compiling an inventory of currently glaciated icefalls across the Swiss Alps using three main observational criteria in unison:

1) A distinct zone of increased gradient along the centre flow-line of active ice (distinct meaning a separate, isolated region that acts to 'punctuate' adjacent zones of lower-gradient ice).
2) A similarly distinct region (as per 1) showing enhanced ice surface velocity.
3) Presence of extensive transverse crevassing.

The occurrence of ogives are an obvious feature confirming the presence of an icefall, since all ogives require an icefall to form; however, this was not an essential criteria, as not all icefalls produce ogives (King & Lewis, 1961; Waddington, 1986).

It should be emphasised that the term 'icefall' is used here only to describe landforms fulfilling the above criteria; they are distinguished as being distinct zonal features contained along the central flowline where a steep reach is isolated between two shallower reaches. Steep accumulation areas, headwalls and hanging glaciers, whilst often visually similar to icefalls, are separate features that do not have the same impact of separating a glacier into distinctly different zones of ice dynamics (Armstrong et al., 2017). Moreover, the term icefall has also been previously used to describe mass movement events of glacial debris (Pralong & Funk, 2006), I suggest the term ice avalanche ought to instead be used in such situations to avoid misinterpretation.

2.2.2 Mapping and Classification

Icefalls were initially mapped using Google Earth Pro (version 7.3) as it provides a quick and easy environment in which to view high resolution aerial imagery and gradient in 3D. This was further aided by the use of a regional surface velocity dataset from Millan et al. (2022) at 50 m spatial resolution to examine changes in surface velocity. Up-to-date high-resolution (3-5 m) satellite imagery from Planet Labs (Planet Team, 2017) was also used in situations where Google Earth imagery was of poor quality or more than a few years old. Finally, publicly available field photos via web searches or Google Earth's 'photos' layer were also sometimes consulted for a high-quality ground view when satellite imagery proved insufficiently clear.

Upon identification, a centre flowline was drawn from the top of the icefall at the point the gradient begins to suddenly steepen down to the base where it begins to flatten out once more. A second central flow line was then drawn for the rest of the glacier, excluding the icefall region, in order to compare ice characteristics.

Each icefall was categorised into a geomorphological type according to its context within the landscape (Figure 2.4), these being:

1. **Cirque** – Icefall that flows off the exit lip of a cirque at the head of a glacier.
2. **Plateau** – A steep descent off a plateau accumulation area.
3. **Tributary** – The step from a glaciated hanging valley at the point it joins the main trunk glacier.
4. **Confluence** – Icefall downstream of the confluence of two glaciers.
5. **Mid-Profile** – An isolated step further down the glacier profile, not associated with the above geomorphology.
6. **Other** – Other icefalls that do not fit into the above types.

Furthermore, the connectivity status of the icefall with regard to the whole glacier profile was also noted as follows (Figure 2.5):

i. **Fully connected** – icefalls homogeneously connected with ice above and below it.
ii. **Partially disconnected** – thinning has begun to expose significant regions of bedrock within the icefall, but there is still largely continuously connected and flowing ice.
iii. **Fully disconnected** – the icefall is now a region of fully exposed bedrock, with serac collapse off the new dynamic terminus at the top feeding an isolated tongue below.

Figure 2.4: Icefalls were categorised into geomorphic types according to their context. Examples of each type are shown here. See text body for descriptions of each type. Glaciers shown here are – 1: Bisgletscher. 2: Glacier de Ferpècle. 3: Ewigschneefäld. 4: Fiescherglетscher. 5: Glacier de Corbassière. 6: Vadret de Morteratsch.

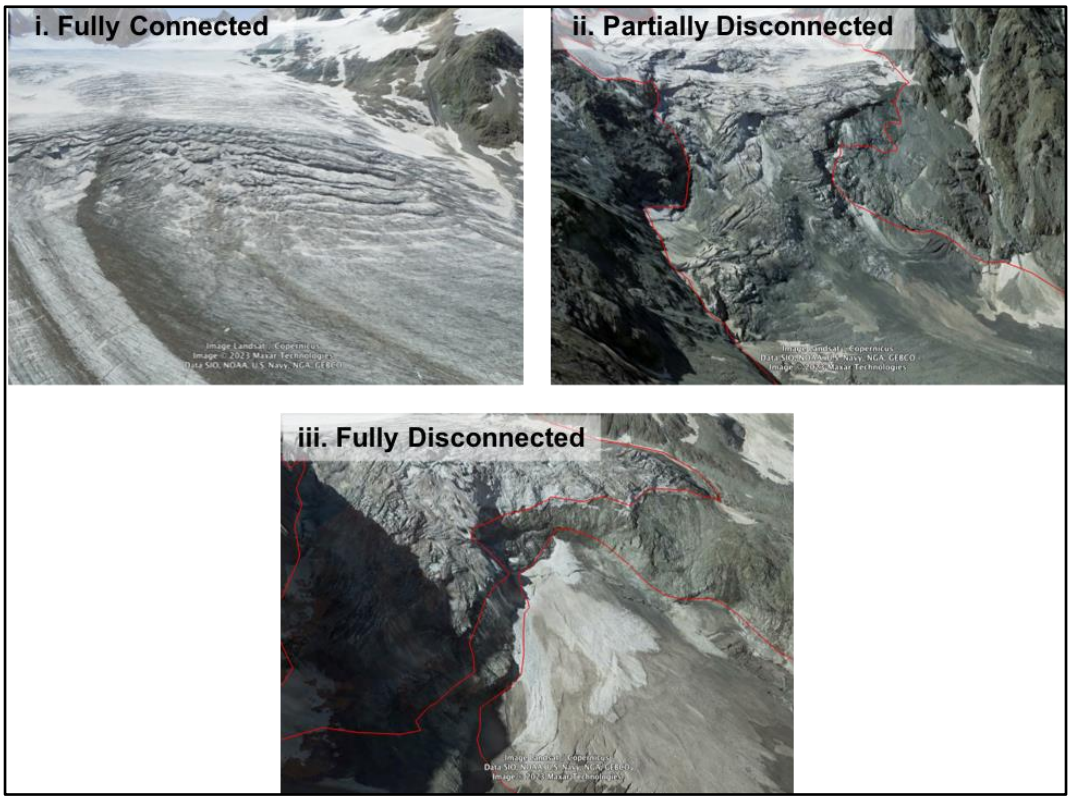

Figure 2.5: Examples of icefall connectivity categories with Swiss Glacier Inventory 2016 outlines in red for visibility. See text body for full descriptions. Glaciers shown here are – i: Glacier de Corbassière. ii: Glacier de Tsijiore Nouve. iii: Glacier du Mont Miné.

2.2.3 Data Extraction

The icefall and glacier profile flowlines were subsequently imported into QGIS where they were used to extract minimum, maximum and median values for a variety of data at each glacier. An overview of all datasets used in the inventory and analysis can be found in Table 2.1. Median values were used rather than mean as the high degree of variance found within icefalls and from the manual delineation of start and end points of the flowline had the potential to significantly skew mean outputs.

Further datasets used for the analysis included an updated surface elevation model and ice thickness estimations at 10 m resolutions from Grab et al. (2021), and modelled regional LGM ELA estimates from Višnjević et al. (2020). An approximation of modern day ELA was established through digitisation of end of summer snowlines at each icefall site using the Planet Labs September monthly basemap for the year 2020 (Planet Team, 2017), which was a year of approximately average levels of mass balance over the past decade according to the Swiss GLAMOS network (SCNAT, 2020). This is a quick and easy method that has been shown to provide an effective estimate for the ELA (Rabatel et al., 2005). Finally, a digital vectorised geological map of Switzerland from the Federal Office of Topography swisstopo (2022) was consulted to ascertain the potential influence of lithology on icefall locations.

Table 2.1: Overview of datasets used to compile and analyse the icefall inventory.

Dataset	Source	Use
Planet Monthly Basemaps (Sept. 2020 & Summer 2021, 3-5 m res.)	Planet Team (2017)	Icefall identification and snowline mapping.
Glacier Surface Velocity (2017/18, 50m res.)	Millan et al. (2022)	Icefall identification and data analysis of velocity variability.
Digital Surface Elevation Model (2019, 10m res.)	Grab et al. (2021)	Data analysis of icefall and snowline elevation and gradient.
Ice Thickness (2020, 10m res.)	Grab et al. (2021)	Data analysis of icefall and glacier ice thickness variability.
GeoCover - Geological Map of Switzerland	Federal Office of Topography swisstopo (2022)	Interpretation of lithology surrounding icefalls.
Modelled Last Glacial Maximum ELA	Višnjević et al. (2020)	Interpretation of glacier and ELA variability.
Swiss Glacier Inventory (2016)	Linsbauer et al. (2021)	General glacier outlines and statistics

2.3 Results

2.3.1 Overview

A total of 66 icefalls across 56 individual glaciers in Switzerland were identified using the criteria (Figure 2.6). Given the method and intrinsic subjectivity of manual mapping, this should be thought of as a conservative minimum – there are arguably more features that may be considered icefalls but were not identified in this first-order approach. In several instances, icefalls were identified in Google Earth imagery that was many years old and upon consultation of the present-day situation from Planet Labs imagery, it was found the ice had subsequently fully retreated such that the icefall and tongue no longer exist. In this respect, it is worth reiterating that only icefalls constituting of *active ice* (as of date of mapping i.e. 2022) were added to this particular inventory.

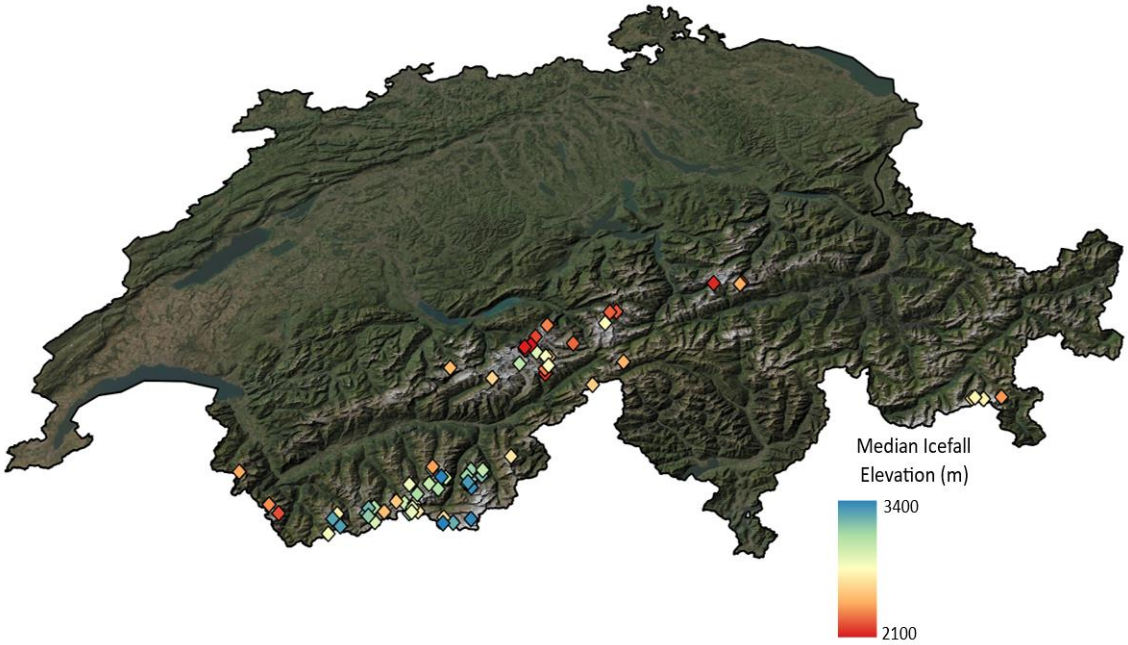

Figure 2.6: Overview map of the 66 contemporary icefalls identified across Switzerland, coloured according to median elevation. A strong correlation to latitude appears to be present, with icefalls further south found at higher elevations. This climate link to icefall position is a key finding that is explored further throughout this chapter.

Some descriptive summary statistics for the dataset are provided in Table 2.2. Individual median gradient was found to be as low as 13° and as high as 45°, with an overall dataset mean of 29.6°, which is consistent with values reported by Davies et al. (2022) for the Juneau Icefield. Icefall gradients are approximately 150% steeper than the rest of the glacier profile. Overall median surface velocities were on average 181% greater in the icefall than the rest of the glacier profile, though there was substantial variance in this with multiple smaller, slower, and shallower sloped glaciers and/or disconnecting icefalls not displaying a significant change in velocity. In the most 'active' glaciers, it was common to see velocities significantly greater in the icefall than the surrounding tongue or accumulation area, with the highest measured increase being 427%. Overall median ice thickness was on average 46% less in icefalls compared with the rest of the profile, quantitatively demonstrating the plastic deformation impact of extensional flow over these large steps in the bed.

Geomorphological categorisation of the icefalls revealed 30 (45%) classified as cirque lips, 14 (21%) as plateau lips, 6 (9%) as tributary steps, 3 (5%) as confluences, 10 (15%) as mid-profile steps and finally 3 (5%) as 'other'. The only particularly notable point of interest amongst the categorised data of Table 2.2 is the considerably lower average altitude of the mid-profile icefalls (2465 m) compared to the rest of the dataset (2656 m – 2975 m). This is entirely expected, given that by definition these icefalls were designated as such for being isolated further down the profile.

Of the 66 icefalls, 39 (59%) were categorised as still fully connected, 16 (24%) were partially disconnected and 11 (17%) were fully disconnected. It was perceptible during the mapping process that in recent years there had been a rapid deterioration of icefall connectivity, with several cases of connections changing status between older Google Earth imagery and more recent basemaps from Planet Labs or GIS (Figure 2.7). It is clear that an increasing number of icefalls will begin to disconnect in the coming decades as the climate continues to warm and ELAs rise further up the profile.

Table 2.2: Descriptive summary statistics for the inventory. Median values are taken for each icefall/glacier and then an overall mean of these for each sub-category is displayed here.

	No.	Elevation (m)	σ	Surface Velocity (m a^{-1})	σ	Gradient (°)	σ	Ice Thickness (m)	σ
Icefall	66	2856	317	54.6	46.8	29.6	6.5	56	25.5
Rest of Profile	56	2937	342	19.4	15.7	12.2	4.1	103.7	62.7
Type:									
Cirque	30	2975	237	41.8	33	30.7	5.5	51.3	20.8
Plateau	14	2912	313	46	25.1	28.6	5.6	52	16.2
Tributary	6	2856	384	103.1	56	25.8	7.7	68.7	27.8
Confluence	3	2656	71	62.2	60.3	27.8	9.5	66.2	49.8
Mid-Profile	10	2465	236	43.3	34.7	30	8.3	66.1	33.6
Other	3	2902	52	156.2	44.3	30	2.7	52.8	9.1
Connectivity:									
Connected	39	2927	267	64.4	51.1	27.1	5.8	60.3	25.8
Partially Disconnected	16	2817	291	30.2	30.6	32.1	5.3	54.1	29.1
Disconnected	11	2562	279	51.6	32.4	34.2	6.8	45.5	12.5

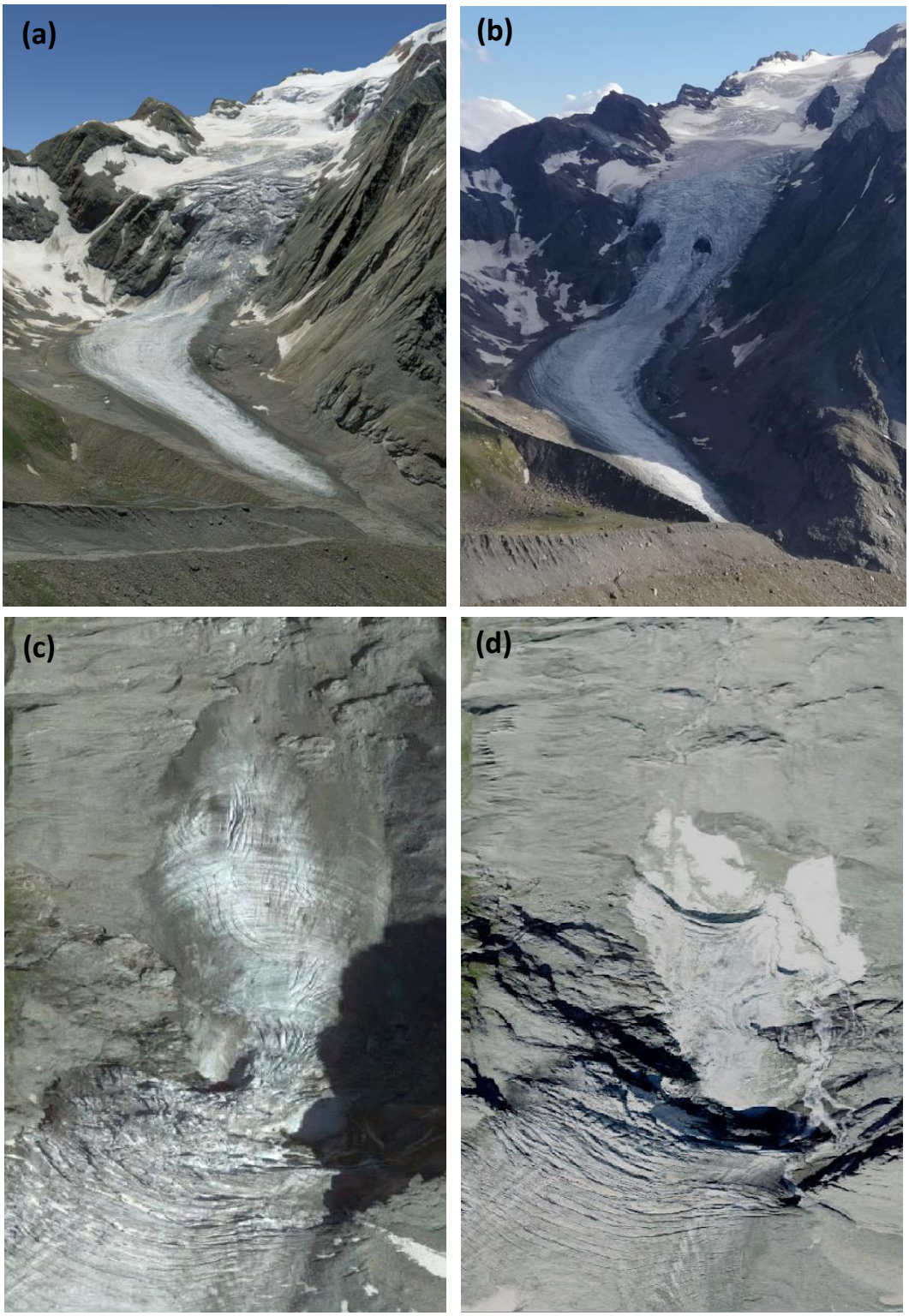

Figure 2.7: Observed icefall thinning during mapping: Glacier de Valsorey (top) fully connected in 2016 Google Earth image **(a)** and then a large central hole of bedrock appearing sometime since 2017, which has since persisted and grown in size **(b)** (image from Cabane de Valsorey – valsorey.ch). Turtmanngletscher (bottom) still partially connected in 2016 Google Earth imagery **(c)**, followed by full disconnection in 2020 Esri basemap imagery **(d)**.

2.3.2 Links with Climate

The initial map of icefall distribution across the region presented in Figure 2.6 indicates a strong coupling of icefall elevation with latitude. To investigate this trend further, the median elevation distribution of the inventory was plotted against the respective 2020 snowline altitudes as a proxy for current ELA (Figure 2.8). The strong and statistically significant trend present (R^2 = 0.53, p = <0.001) with icefall elevations rising linearly in line with ELA, suggests there exists a significant climatic impact on the positioning of icefalls in the landscape.

Given the dominant control of climate on glaciation, it may be reasonably expected that this trend with icefall elevation is simply the manifestation of a wider coupling of the overall glacier elevation to regional climate. In order to test this, median icefall and glacier elevations were plotted according to latitude (Figure 2.9). The result shows a far stronger relationship for the icefall elevations (R^2 = 0.41) than that of the overall glacier (R^2 = 0.18) suggesting the positioning of icefalls to be a significant climate-controlled component given the north-south climate gradient present across the Alps (Seguinot et al., 2018).

The cirque lip and plateau type icefalls have the strongest correlation to ELA, lying closest to the 1:1 line in Figure 2.8, while the confluence, tributary, mid-profile and 'other' types are distributed more sporadically and away from the ELA, potentially indicating different dominant controls, which will be explored in the next section and later in the discussion.

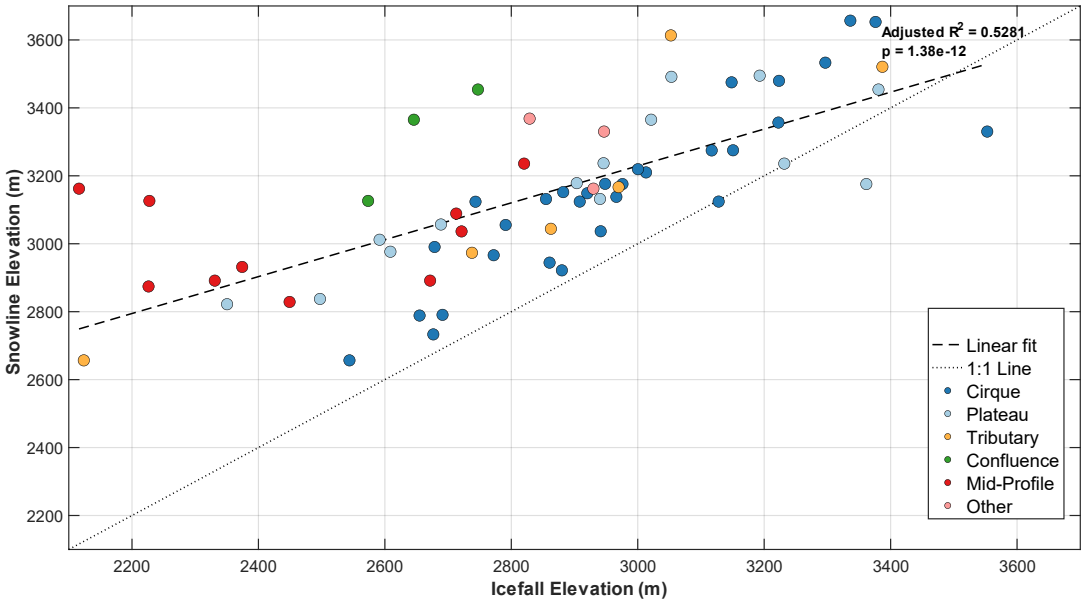

Figure 2.8: The distribution of median icefall elevations according to category, with their respective snowline elevation from the year 2020 as a proxy for ELA reveals a remarkably strong correlation that suggests the formation and evolution of icefalls are heavily influenced by climate. Overall mean icefall altitude is 2847 m, overall mean snowline altitude 3151 m.

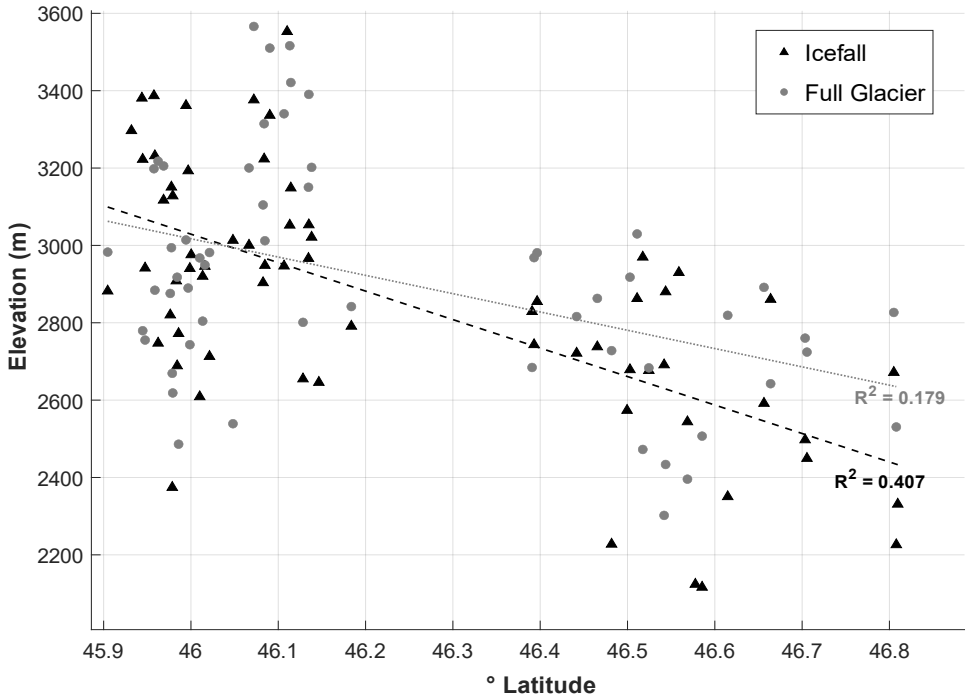

Figure 2.9: Median elevation of icefalls and the full glacier according to latitude. A stronger correlation is present for icefalls than the glacier itself, which can be interpreted as an indication of a strong climatic control on the positioning of icefalls.

2.3.3 Other Possible Influences

Given only 66 icefalls were mapped here out of a total of 1400 documented individual glaciers in the Swiss Glacier Inventory (SGI) 2016 (Linsbauer et al., 2021), an obvious question that surfaces is: why do only some glaciers create icefalls and not others, or indeed, not all glaciers?

A simple analysis of whether glacier size enacts any influence on icefall presence or size was considered by comparing the distribution of glacier area/length across all recorded SGI units along with those that contain icefalls (Figure 2.10a), as well as glacier area alongside specific icefall relief (Figure 2.10b). The data reveals that mapped icefalls are found exclusively from the top 15% largest glaciers in Switzerland in terms of both area and length (Figure 2.10a). This finding should be treated with caution, however, as the criteria of only including actively glaciated icefalls at the time of mapping (2022) will have led to many instances where previously active icefalls are now deglaciated and therefore not included in the analysis, which is likely to have disproportionately affected smaller glaciers.

Conversely, no significant trend is found for icefall relief according to glacier area (Figure 2.10b), so whilst larger glaciers are exclusively responsible for the presence of icefalls in this inventory, the size of the glacier appears to bear no impact on the size of the icefall. An interesting observation from this plot though, is the tendency of mid-profile and confluence type icefalls to be consistently smaller in terms of relief.

To account for the importance of lithology and tectonic structure in driving local erosion (Hallet et al., 1996; Dühnforth et al., 2010; Cook et al., 2020) the geologic map was consulted at each icefall site, where notable changes in lithology or the presence of faults around the icefall were recorded. Of the 66 icefalls, 26 were located at regions of lithological heterogeneity (Table 2.3). There is no particular dominant pattern according to icefall type, with the exception of the mid-profile types, where 9 of the 10 categorised icefalls were situated at an area of lithological variability or fault line presence. This suggests a potentially important mechanism for these specific features, differing from other icefall types, which is in line with their unique situation further down the profile. Theories and implications of this are discussed in the following section.

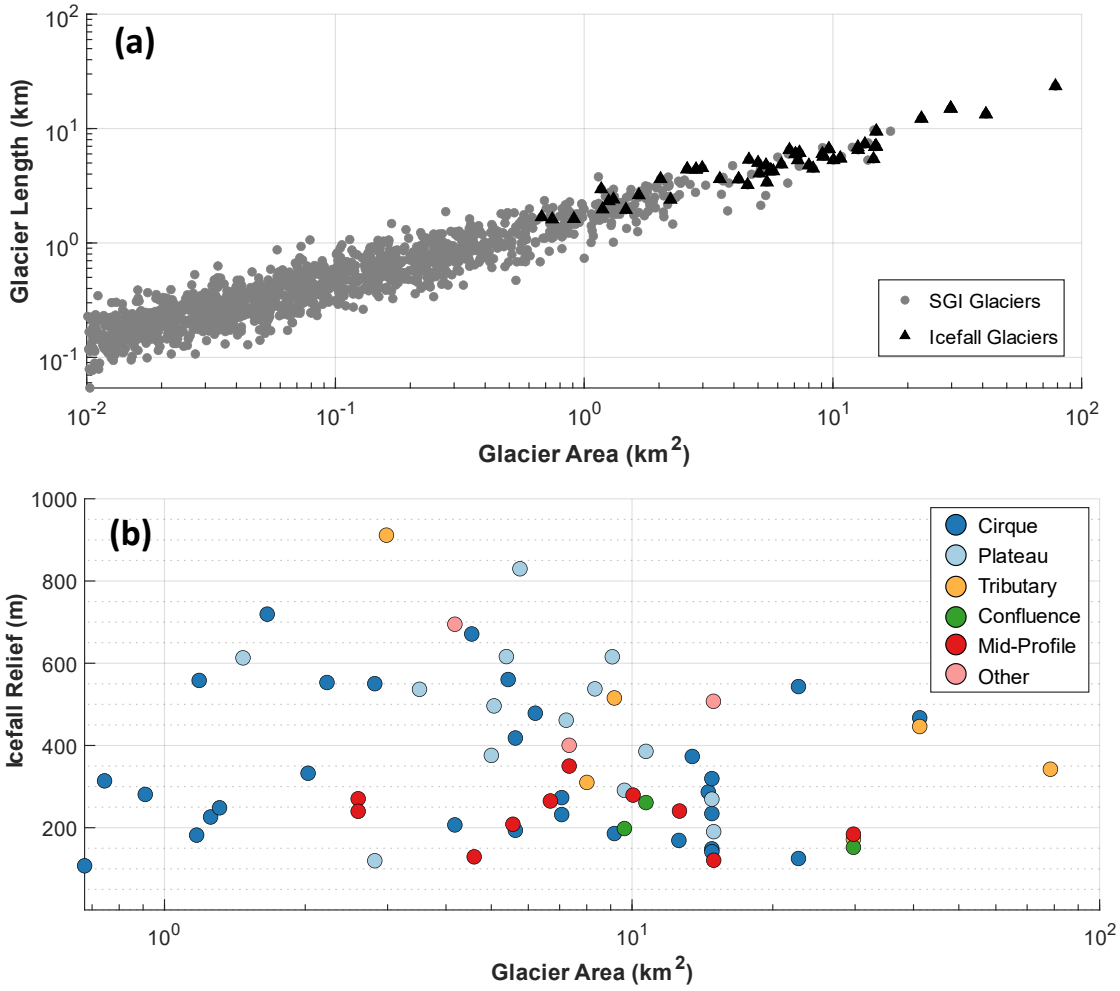

Figure 2.10: (a) Data on the area and length of icefall glaciers show them to be exclusively amongst the largest glaciers in the entire 2016 Swiss Glacier Inventory. **(b)** The size of icefalls (in terms of relief) does not scale in accordance with overall glacier area. This does also show some clustering of relief according to icefall type, with confluence and mid-profile icefalls consistently at the lower range of relief.

Table 2.3: Number of icefalls per category with lithological variation and/or fault lines present in the vicinity, according to the Swisstopo (2022) GeoCover map.

Category	Total	No. with lithological variation
Cirque	30	9
Plateau	14	4
Tributary	6	1
Confluence	3	1
Mid-Profile	10	9
Other	3	2

2.4 Discussion

2.4.1 Initial Findings

The overall aim of this chapter was to firstly bring about more quantitative data on the glacial feature of icefalls to facilitate more reliable definition and secondly, to explore what the topographic distribution of icefalls may indicate about their role in glacial landscape evolution. The initial data presented in the Results section (2.3.1) has achieved the former, as we can now see icefalls are approximately 50% thinner, 180% faster flowing and 150% steeper than the rest of the glacier profile, with an average gradient of 30°. An important caveat though is the high amount of variance in some of these metrics, particularly surface velocity with a standard deviation of 47 m a^{-1}, as they will depend on other localised factors governing ice dynamics, such as current glacier extent. As such, it remains a challenge to devise absolute threshold values or a one-size-fits-all approach to delineating icefalls as the multiple factors of gradient, velocity and crevassing need to be collectively taken into consideration within the specific local context, often requiring a degree of human inference. Regardless, this is a good step towards instigating further discussion and research on these landforms.

The mapping and data extraction have revealed a wealth of information on where contemporary icefalls are situated within the actively glaciated landscape. This permits the conception of some hypotheses on their possible means of formation and contribution to overall landscape evolution, which will be explored in the following sections, progressing some of the overall research questions of the thesis surrounding the spatial variability of glacial erosion and dynamism of catchments over time.

The fact that icefalls documented here are only found on the largest contingents of Swiss glaciers could be interpreted as large ice flux being a necessary condition for icefall formation (Figure 2.10a). With approximately 90% of glaciers in the SGI less than 1 km^2 in area and 80% less than 1 km in length, such small bodies of ice may lack the erosive power necessary to construct an icefall, or alternatively they may simply contain large steps further down the profile that are subsequently not highlighted in this study given their present limited ice extent.

If larger glaciers are indeed necessary to create bedrock steps, it might naturally be expected that icefall size would increase proportionately with glacier size, particularly given prior work that couples rate of erosion with ice flux, and step size with discharge

(MacGregor et al., 2000; Anderson et al., 2006; Jiskoot et al., 2017). However, the lack of any significant correlation between glacier area and respective icefall relief in Figure 2.10b would seem to refute such a concept. In fact, the largest icefalls are conversely situated on some of the smaller glaciers from the inventory between 1 km^2 and 10 km^2 in area. The high dispersion in this data comparison, as well as the clustering of mid-profile and confluence type icefalls at lower reliefs point towards a more complex interplay of processes over time and the possibility for multiple mechanisms of formation, theories of which will be discussed in the next section.

2.4.2 Different Mechanisms of formation

Previous work put forward the notion that large step formation occurs primarily at tributary junctions and confluences, as the glacial cross sectional area must expand in order to accommodate the sudden increase in ice flux (Penck, 1905; MacGregor et al., 2000; Anderson et al., 2006). Whilst this may reasonably explain such features, 'tributary' and 'confluence' type icefalls account for less than 15% of the total inventory presented here. Moreover, there are many cases of glacier confluences in the Swiss Alps with no such step present, primary examples being at Aletschgletscher and Unteraargletscher, the largest and fourth largest glaciers in Switzerland respectively (Linsbauer et al., 2021). Here instead, a large overdeepening of the bed has occurred (Haeberli et al., 2016), seemingly as an alternative reaction to the sudden change in ice flux. Exactly why a glacier in such cases would act to form an overdeepening rather than an icefall or vice versa is unclear and speaks to our current lack of understanding of both features. Like the icefalls presented here, overdeepenings have been found to occur in a variety of topological settings and take many different shapes and forms – a likely consequence of the complex interplay of topography, sediment, hydrology and ice dynamics at different regions of the glacier profile and under different climate conditions (Cook & Swift, 2012; Haeberli et al., 2016; Magrani et al., 2020; Swift et al., 2021).

The 'mid-profile' type of icefalls presents perhaps the most intriguing case given their isolation along the glacier profile, which is evident from the predominant clustering away from the snowline in Figure 2.8, suggesting an absent or diminished climatic influence. Further, they are all at the lower range of icefall sizes, not exceeding 400 m in relief (Figure

2.10b). With all but one of these icefalls situated at a fault line or change in geology (Table 3), the influence of lithology may well be a key factor and is worth examining.

Consider the case of Bifertenfiren, which contains two mid-profile icefalls in rapid succession, followed by a further two large topographic steps down-profile that are now deglaciated (Appendix 2.6.1). Consultation of the geological map reveals each step to be located near perfectly at the transition between major geological units (e.g. changes between igneous, metamorphic and sedimentary rocks) (Figure 2.11). Such a remarkable coincidence is difficult to assign purely to chance, instead indicating that lithological heterogeneity could be a potential catalyst for the formation of some icefalls due to contrasting bedrock erodibility, as is frequently the case in the setting of fluvial waterfalls (Raming & Whipple, 2019).

The single outlying mid-profile icefall with no local changes in lithology is at Fieschergletscher. Here, the presence of a retreated hanging cirque glacier immediately adjacent to the icefall may be a sufficient explanation for a localised enhancement of erosion from increased ice flux when they were still connected, degrading the lower reach and leaving the step behind up-valley (Appendix 2.6.2). If such a coalescence of these two glaciers were still present today, the icefall would likely have instead been classified as a 'confluence' type. The presence of the deglaciated tributary and likely ice flow during larger extents was not taken into consideration during mapping and as such the isolated icefall here was categorised as 'mid-profile'.

Lithological heterogeneity is also present at other types of icefall, though less frequently (Table 2.3). In these instances, the lithology may serve to enhance erosion and icefall formation in place (see section 2.4.4), or the specific change in geology may not be conducive to any significant impact (e.g. from one hard metamorphic rock to another slightly different type). The specific detailed changes in geology at each icefall site were not examined here as it was beyond the scope of this work but is certainly worthy of future investigation.

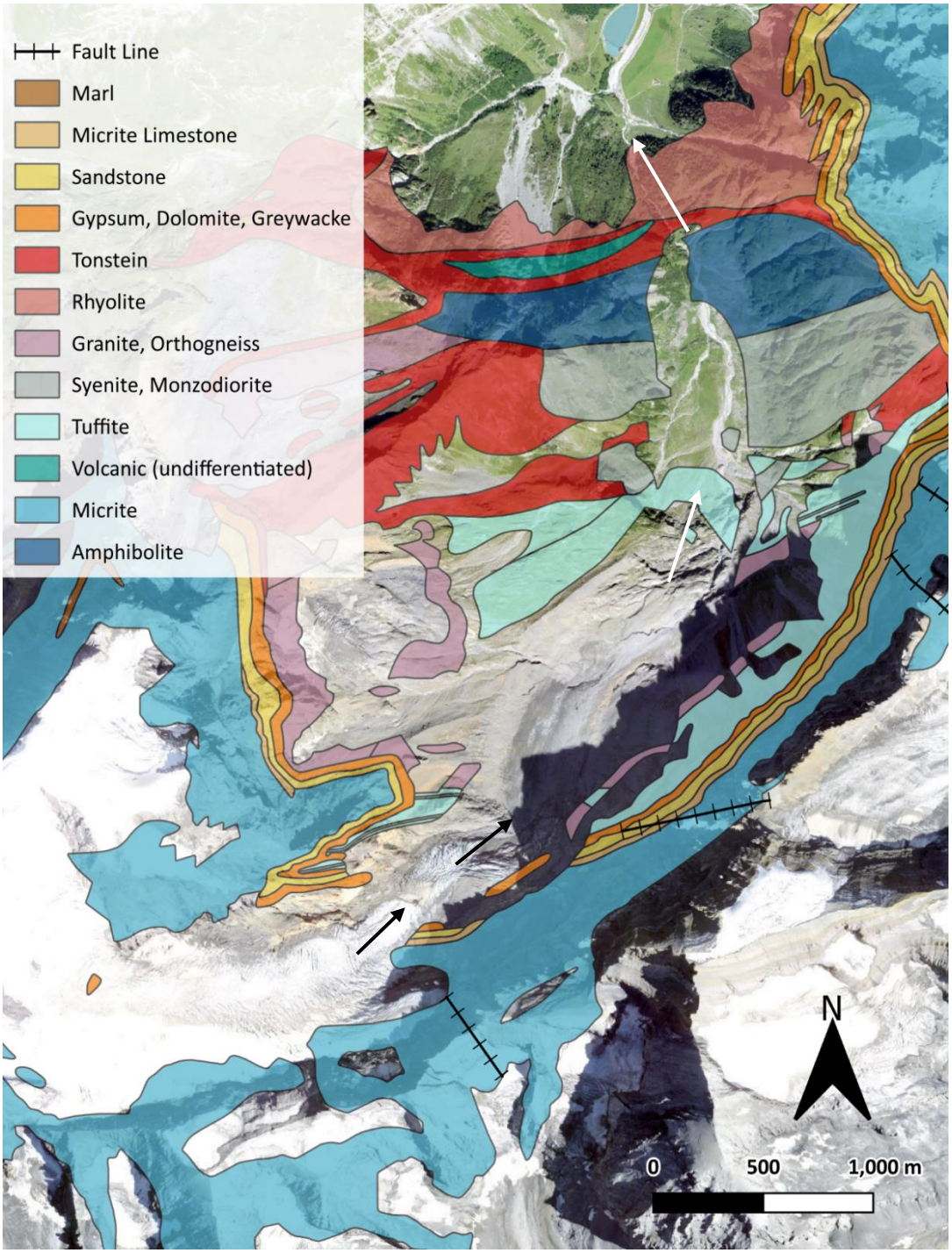

Figure 2.11: Geological map of Bifertenfiren, Switzerland. Black arrows show the position of the two current icefalls, whilst white arrows show the two relic deglaciated steps further down. Note the strong coincidence of icefall/step positions with major changes in lithology and presence of fault lines. Sudden changes in bed resistance to erosion may be a catalyst for the formation of these mid-profile icefalls. See Appendix 2.6.1 for oblique Google Earth view of this catchment.

The above discussion presents plausible theories of why three of the icefall types – tributary, confluence and mid-profile – are more decoupled from a spatial climate forcing and instead focused in regions of specific erosional efficacy due to topography. Removing these three types from the icefall/snowline elevation plot of Figure 2.8 results in an increase to the R^2 value from 0.53 to 0.66 (Appendix 2.6.3), demonstrating the remaining 'cirque lip' or 'plateau' icefalls are strongly coupled to climate. The mechanisms of this climate forcing are discussed in the next section.

Note that there is no specific discussion provided for the 'other' icefall category, as the complex topographic situation and limited data (3 icefalls total) make them enigmatic and difficult to speculate on, though certainly worthy of possible future study.

2.4.3 A Theory of Formation over Quaternary-Averaged Conditions

For a large bedrock step to develop and become an icefall it seems necessary for a substantial contrast in erosion rates to be present during the initial occupation period of glaciation as fluvial valleys are re-shaped, such that the lower portion of the profile deepens and builds relief away from the upper reach, which has been seen in synthetic numerical models (Liebl et al., 2021). Whilst changes in lithology may aid such a process, seeing as 61% of mapped icefalls are in geologically homogenous areas (Table 2.3), a more dominant climatic driver is required. In this respect, icefalls may be features formed about the long term average ELA (Porter, 1989; Foster et al., 2008), as a disconnection between time-averaged regions of effective and ineffective erosion over Quaternary time-scales.

During interglacial periods or very early stages of glaciation, minimal ice extent confines glaciers to cirques or higher peaks, excavating small basins in-place and not extending further. Equally, during full glacial extents such as that experienced during the LGM (c. 25 ka), the extremely low temperatures mean that ice in the upper reaches may be cold-based and therefore contributing very little to erosion (Seguinot et al., 2018; Seguinot & Delaney, 2021). However, over Quaternary timescales of multiple glacial and inter-glacial cycles, such states occupy only a very brief minority of the whole period, with the majority of time existing in a far more intermediary state. This point was made by Porter (1989) who, upon examining three major deep sea oxygen isotope records used as a proxy for global climate over the entire Quaternary, found that only 6% of the total interval is occupied by

conditions similar to today and only 1% equal to LGM conditions. Overall mean isotope values approximate to conditions similar to that of the Lateglacial period around 12 ka. Consequently, a time-averaged pattern of erosion should emphasise glacial extents equivalent to the Lateglacial.

Glacial erosion has often been suggested to be most effective around and above the ELA (Brozović et al., 1997; Whipple et al., 1999) as this is the point of greatest ice flux and likely therefore, basal shear stress and effective normal stress leading to high sliding velocities. This has been reproduced using numerical models (MacGregor et al., 2000; Anderson et al., 2006; Egholm et al., 2009), though the evidence is circular in nature given that such models used simplified rules for erosion that scales according to ice discharge. As outlined earlier in Chapter 1 (1.2.4), multiple other factors such as sediment and meltwater supply will collectively impact the efficacy of glacial erosion, such that it may be reasonable to expect higher rates below the ELA where these inputs are more abundant (Herman et al., 2011; Cook & Swift, 2012; Alley et al., 2019).

Consequently, a scenario can be envisaged in which higher rates of erosion occur about and below the average Quaternary ELA (hereafter referred to as QELA), smoothing the valley into the typical U-shape form which is then gradually deepened over time (Harbor, 1992). Erosion higher up in the accumulation zone is limited during these average glacial extents due to colder basal conditions (Godon et al., 2013; Lai & Anders, 2021), lack of meltwater and likely large amounts of sediment storage (Delaney & Adhikari, 2020), which collectively inhibit effective abrasion and quarrying processes (Alley et al. 2019). Subsequently, a step and icefall may develop at the inflection point between these zones of erosion (Figure 2.12).

Does the icefall data collated in this study support such a theory? By plotting the icefall elevations against the maximum glacier altitude (i.e. upper limit of glaciation) and modelled LGM ELAs (i.e. lower limit of glaciation) (Višnjević et al., 2020), it is revealed that the mapped icefalls lie in a central elevation window between the two states, which could be interpreted as the QELA region (Figure 2.13).

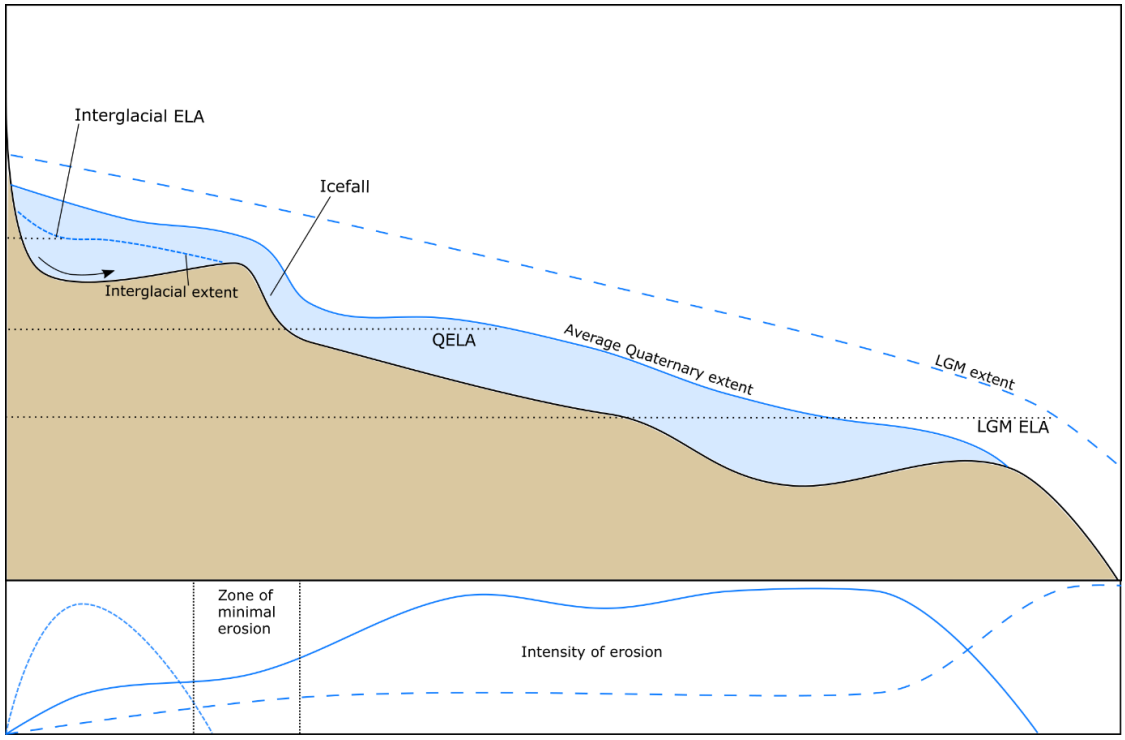

Figure 2.12: Illustrative diagram demonstrating the potential for icefall formation as a result of a disconnect in erosional efficacy of the upper and lower profiles over average quaternary conditions. Minimal glacier extents during interglacial periods confine ice to cirques where basins are deepened through rotational flow (black arrow) as well as sediment inputs and freeze-thaw processes from the bergschrund. Under maximum glacier states (e.g. LGM), little erosion occurs in these upper reaches due to cold-based conditions and lack of meltwater. Main trunk valleys are excavated into deep troughs. In between these extents, which represents the longest time-averaged state, erosion is focused about and below the average Quaternary ELA, deepening the valley profile. The upper accumulation and cirque regions may erode slowly from rotational flow but are limited from sediment storage, lack of meltwater and potential cold-based conditions. A disconnect in erosional efficacy between these two regions presents a zone of minimal erosion where the large bedrock step will form.

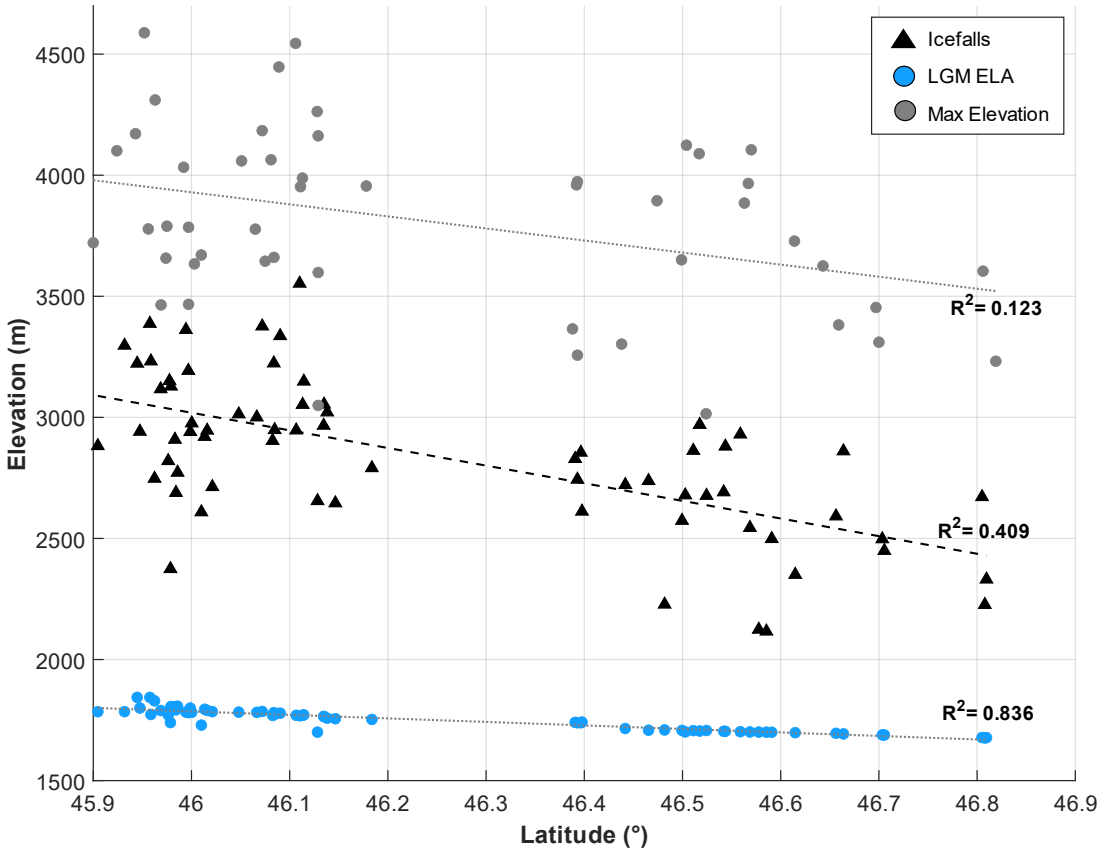

Figure 2.13: Elevations of icefalls, LGM ELA (from Višnjević et al., 2020) and glacier maximums across latitude show that icefalls are positioned in a window approximately midway between these lower and upper limits of glaciation, potentially indicative of a long-term average Quaternary ELA region.

In the Swiss Alps, ELAs during the Younger Dryas period (i.e. Lateglacial) derived from Egesen stadial moraines (c. 12 ka) are estimated to be 250-350 m lower than during the LIA (Ivy-Ochs, 2015). Late 20th century ELAs are estimated to be approximately 100 m higher than during the LIA (Greene et al., 1999; Joerin et al., 2008) and have since risen a further 100-200 m (Huss et al., 2015; Žebre et al., 2021), therefore giving a total Lateglacial ELA depression of approximately 450-650 m relative to today. In other words, we would expect the average icefall elevation from the inventory to be approximately this distance lower than the average mapped snowline elevations, if they are indeed artefacts of a time-averaged QELA position. Comparing total mean snowline elevation (3151 m) to total mean icefall elevation (2847 m) (Figure 2.8) gives a difference of 304 m, placing the mapped icefalls on average 100 m above this estimated QELA.

A couple of key factors will influence this result, though. Firstly, given the icefall inventory presented here is for currently glaciated icefalls only, there are many cases of recently deglaciated bedrock steps that would have served to significantly lower the overall dataset mean and thus bring it further towards the QELA – notable examples of such glaciers being Rhonegletscher or Kanderfirn (Appendix 2.6.4).

Secondly, palaeo-ELA estimations are commonly achieved by applying an accumulation area ratio of ~0.67 to reconstructed former glacier extents and surface elevations (e.g. Greene et al., 1999; Joerin et al., 2008; Ivy-Ochs, 2015), but in reality ELAs are significantly affected by local factors such as aspect, topographic shading, avalanching, local weather patterns and debris cover, which will influence mass balance (Žebre et al., 2021). Empirical and modelled data shows significant (100's m) regional and inter-annual variability between ELAs measured across the Alps in the last several decades due to such factors (Rabatel et al., 2013; Huss et al., 2015; Žebre et al., 2021). Consequently, the estimate for a QELA in this scenario is somewhat crude and requires some flexibility in its interpretation given the uncertainties involved.

If the majority of icefalls form in concordance with the QELA region, a couple of crucial considerations must be accounted for. First, how are they prevented from growing exponentially over time? Second, how is rapid erosion communicated up-catchment to the accumulation area and cirque regions, such that they are kept in balance with uplift rates to maintain overall landscape equilibrium? The current offset between average icefall elevation and rough QELA elevation calculated above could be interpreted as evidence of the features being dynamic, eroding headward up through the profile over time, which could potentially be a mechanism to account for these problems.

These questions are discussed in the following two sections which develop hypotheses for icefalls forming in-situ and maintaining a static position or being more dynamic with up-valley migration of a large step.

2.4.4 The Case for Static In-Situ Formation

Continual lowering of the trunk valley could lead to an increase in bedrock step relief over time, as too could strong erosion at the base of the icefall where a combination of rapid sliding velocity from the steep gradient and high shear stress from compression could lead to rotational flow, enhancing abrasion (Clark & Lewis, 1951). Moreover, the steep relief of icefalls can sever the glacier into two distinct zones of ice dynamics, such that observations of seasonal changes in velocity can cover the entire tongue region up until the base of the icefall, beyond which no changes are felt, which has been suggested as a mechanism by which icefall relief may grow over time (Armstrong et al., 2017).

If icefalls are merely a passive feature formed in-situ, it may then be reasonable to expect their size to be a function of overall ice flux, as larger glaciers would excavate deeper steps over time. Yet the results here have shown no such clear correlation (Figure 2.10b). Whilst there is the potential for differences in lithology to have contributed to the variance present, generally the mapped icefalls are located in regions of broadly-defined high bedrock erosional resistivity where, unsurprisingly, the highest and presently glaciated topography is situated (Kühni & Pfiffner, 2001), so such significant differences seem unlikely. Further, if rotational flow and greater potential for erosion exists at the base of the icefall, a rational assumption may be the excavation of an overdeepened basin, which has been previously suggested (Leighton, 1951), analogous to the plunge pools found at the base of fluvial waterfalls. However, previous detailed mapping and analysis of overdeepenings bears no mention or relation to icefalls, instead finding them predominantly within cirques, confluences and at terminus positions (Haeberli et al., 2016; Magrani et al., 2020).

It is possible for icefall relief not to grow over time if erosion of the accumulation area and cirque basins above are able to keep pace with the overall rate of uplift, as implied by the buzzsaw hypothesis (Brozović et al., 1997), as well as with the lower valley following initial glacial carving. Numerical modelling from MacGregor et al. (2009) demonstrated enhanced rates of quarrying at the valley head capable of overdeepening the bed. Bergschrunds commonly found at the interface of cirque glaciers and headwalls can provide a conduit for meltwater, debris supply and diurnal air temperatures to reach the bed and contribute towards cirque basin erosion (Hooke, 1991). Moreover, the base of headwalls have been found to be ideally situated within an altitudinal window conducive to effective frost cracking processes, further wearing down valley heads over time (Scherler, 2014).

In this scenario, icefalls could persist in-situ as the more rapid excavation of cirque basins during more limited glacial extents (Crest et al., 2017; Liebl et al., 2021) via the processes outlined above, allows the upper portion of the catchment to maintain equilibrium with both the lower portion and uplift rate. Due to the hypsometry of the landscape in this upper region of the catchment, just a small lowering of the ELA would serve to significantly extend the ice margin, such that it would flow over and beyond the icefall in a short period of time. This rapid switching in states, combined with extended flow over the icefall thinning the ice and likely decoupling from the bed, means there is little potential for erosion on the steep gradient portion itself, thus maintaining the functional discontinuity of erosion above and below the feature. Additionally, however, speed up in ice velocity from extensional flow going into the icefall and potentially enhanced by sediment trapping and suppression of efficient hydrological routing by the cirque overdeepening (Cook & Swift, 2012; Swift et al., 2021b) could result in enhanced rates of abrasion on the top lip of the step. If such a process was to keep pace with rates of valley lowering, the icefall may feasibly maintain a steady relief over time in a fixed position as shown in Figure 2.14.

Evidence against such a process comes from analysis of cirques with modelled ice occupation times across Britain and Ireland, which has presented the view that cirque growth may slow over time after initial formation in early glaciations, as they develop into a form that impedes effective erosion due to feedbacks like subglacial sediment trapping (Barr et al., 2019). The form and processes of glaciation across the British Isles is somewhat different though to the Alpine setting, as the high topography of the latter allows glaciers to persist for much longer periods of time into warmer climate intervals and thus may permit sediment flushing and more effective rates of erosion during interglacial periods (Crest et al., 2017).

Ultimately the potential for in-situ dynamic equilibrium of icefalls is dependent on both the timescales of glacial and interglacial conditions conducive to effective erosion in the upper and lower regions of the profile, as well as the overall efficacy of erosion in these regions, both of which will be explored in the following two chapters. If static in-situ evolution is implausible, another mechanism must be responsible for communicating high denudation of the lower catchment up-valley into the cirques and headwalls, lest they otherwise continuously grow with uplift. A theory of icefalls as dynamic, headward migrating features similar to that of fluvial knickpoints is discussed in the next section as a means of addressing this.

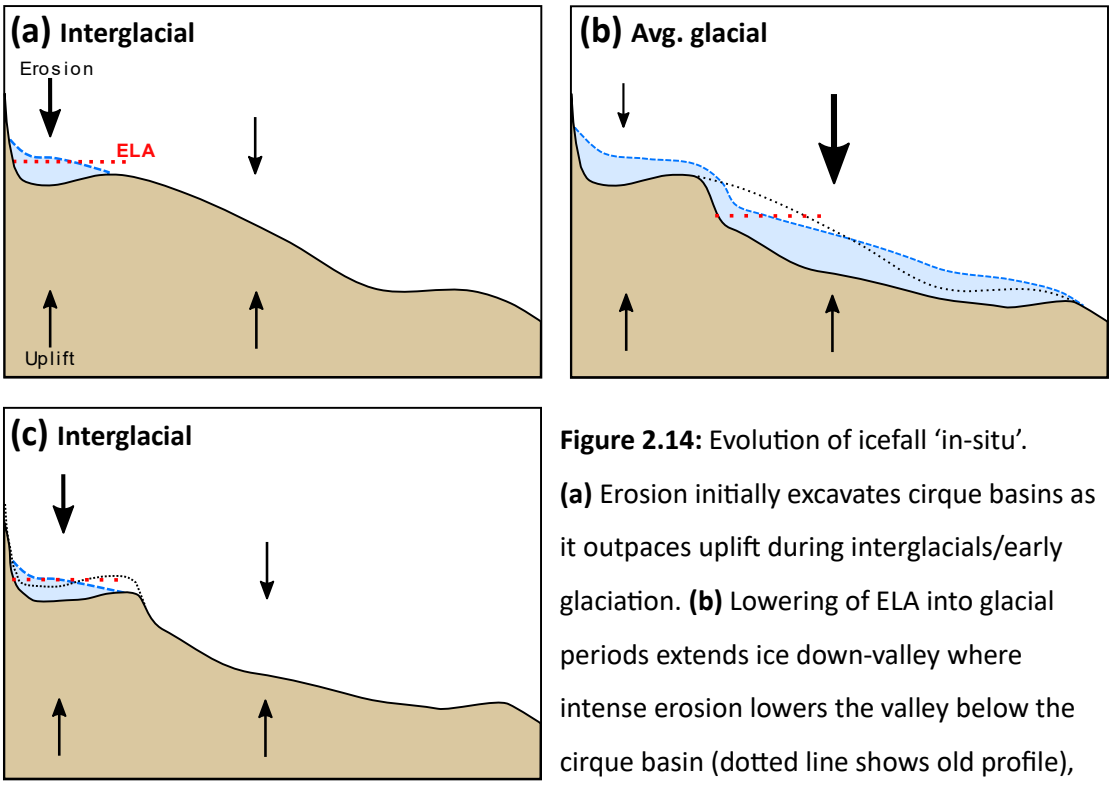

Figure 2.14: Evolution of icefall 'in-situ'. **(a)** Erosion initially excavates cirque basins as it outpaces uplift during interglacials/early glaciation. **(b)** Lowering of ELA into glacial periods extends ice down-valley where intense erosion lowers the valley below the cirque basin (dotted line shows old profile), cirque region experiences little erosion that matches or is lower than uplift. Icefall step develops between the two regions. **(c)** Return to interglacial conditions focuses erosion in cirque regions once more, denuding the top lip of the icefall step, whilst the main valley maintains or lags behind uplift rate. This switching in states and regions of erosion allows icefall relief to be maintained in dynamic equilibrium.

2.4.5 The Case for Dynamic Headward Migration

An alternative hypothesis is that icefalls represent a dynamic feature that erodes headwards over time through detachment-driven retreat from intense abrasion and quarrying processes on the feature itself, as a means of maintaining overall landscape equilibrium with uplift rate (Figure 2.15). This process is well recognised in fluvial geomorphology, with knickpoints (waterfalls) initiating under a variety of conditions and perturbations and subsequently retreating headwards to enable the profile to adjust to changes in base level (e.g. Crosby & Whipple, 2006; Castillo et al., 2013; Ye et al., 2013). This ultimately serves to dynamically reorganise the catchment, migrating drainage divides to maintain equilibrium (Willett et al., 2014).

Divide migration in glacial settings has been evidenced from topographic analysis of multiple landscapes. In the Bitterroot Range, USA, Naylor & Gabet (2007) show northern glaciated valleys to be 50% longer than southern unglaciated basins, suggesting divide migration from dominant glacial lateral erosion. Similarly, more than 2 km of lateral retreat over the Quaternary has been proposed in the Sierra Nevada, USA (Brocklehurst & Whipple, 2002). Further evidence across several studies is reviewed by Evans (2021, pp. 33). The core focus of such studies tends to be rapid lateral incision of cirques and headwalls. For example, topographic analysis of the central Asian Kyrgyz Range led Oskin & Burbank (2005) to suggest cirque retreat dominated initial glacial landscape evolution, pushing back the drainage divide at two to three times the rate of valley incision. Such a process forms the crux of the argument for the much debated buzzsaw hypothesis (Mitchell & Montgomery, 2006; Barr & Spagnolo, 2015). But these ideas are incompatible with current principles of glacial erosion being more effective around regions of high ice flux and meltwater availability, neither of which is concentrated in the upper cirque regions during intermediary or full glacial conditions.

Instead, an alternative scenario is not a simple buzzsaw effect operating solely at the valley head, but erosion focused initially in the lower reaches which then propagates up-valley over time as the landscape evolves from a fluvial to glacial state (Sternai et al., 2013). Numerical modelling from Herman et al. (2011) produced a strong signal of headward eroding bedrock steps with the inclusion of non-linear erosion laws and seasonal

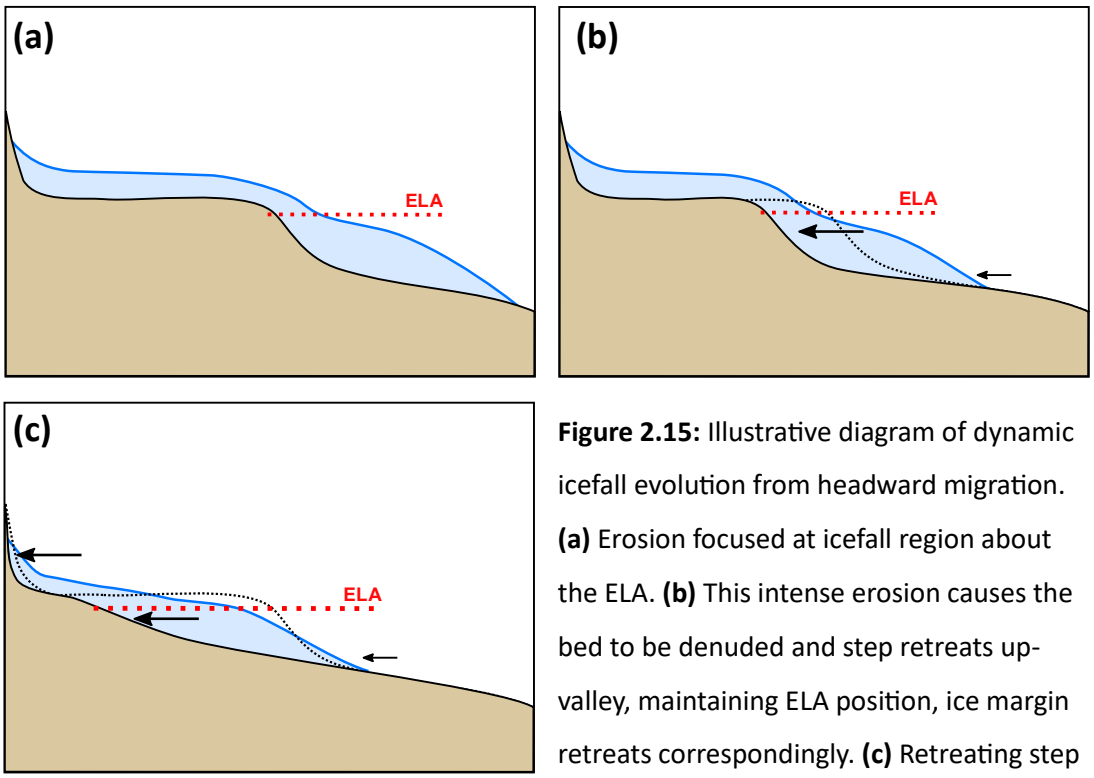

Figure 2.15: Illustrative diagram of dynamic icefall evolution from headward migration. **(a)** Erosion focused at icefall region about the ELA. **(b)** This intense erosion causes the bed to be denuded and step retreats up-valley, maintaining ELA position, ice margin retreats correspondingly. **(c)** Retreating step eventually diffuses into the head of the valley, steepening cirque profiles and contributing to divide back wearing.

hydrological inputs. Under a steady climate scenario, headward erosion maintains the position of the ELA around the step as it migrates up-valley. Of course, climate is not steady over glacial timescales, so the feasibility of such a process under a variable Quaternary climate must be questioned.

Quantification of exhumation patterns over ~2 Ma in Fiordland, New Zealand, using (U-Th)/He thermochronometry fitted to a thermokinematic landscape evolution model found that the observed field data could only be reproduced in model runs where erosion was transmitted headwards in the form of large, kilometre-scale migrating steps (Figure 2.16a) (Shuster et al., 2011). Correspondingly, modelling of the Rhône Valley, Switzerland, over glacial-interglacial cycles shows the propagation of intense erosion from the lower reaches up towards presently occupied catchments, which was said to be enhanced by the presence of steep slopes at the head of initially carved deep troughs (Figure 2.16b) (Sternai et al., 2013). Both of these cases certainly look to be exhibiting migrating icefalls over Quaternary timescales, potentially in relation to a QELA region which could perhaps reproduce the behaviour of Herman et al's (2011) modelling of a steady climate.

Theoretically, the waterfall analogy of icefalls as dynamic features of erosion retreating over time seems plausible and indeed, the use of modern advanced thermochronometry techniques appears to provide empirical field evidence to support it (Shuster et al., 2011; Brown, 2017). A new question then emerges: what happens to the migrating step once it reaches the headwaters? There are two possible scenarios: first, the rate of erosion slows to the point headward migration ceases to be the dominant process of adjustment to the profile and the step maintains a steady position near the valley head, degrading slowly through time, as per the 'in-situ' scenario proposed in the previous section. Second, it continues right up to the valley head, steepening cirque profiles before reaching the headwall and contributing to back-wearing and divide migration (Figure 2.15c).

The first scenario considers a similar process found to occur with fluvial knickpoints, where rate of retreat slows with progression up-valley as the contributing drainage area decreases (Bishop et al., 2005; Berlin & Anderson, 2007). Naturally, ice flux (and erosion) does not scale linearly along the profile due to the intrinsic link with climate among other variables previously discussed. However, despite cirques being the region of longest ice residency, it seems unlikely that much erosion would be taking place outside periods of marginal glaciation when ice is warmer and meltwater is available (Barr & Spagnolo, 2015; Barr et al., 2019). The likely inefficacy of glacial erosion in the upper cirque regions when the majority of time is spent at far greater ice extents (Porter, 1989) may then feasibly result in the rate of headward retreat for a step slowing or even halting entirely as it gains a position towards the cirques. Here, the functional discontinuity in erosion rates over time is present and the step instead degrades gradually in place to maintain equilibrium, as discussed in the theory of 'in-situ' formation (Figure 2.14).

In the alternate second scenario, climate variability is sufficient to allow enough time where the step is exposed to intense erosion that it continues to retreat upwards to the headwall. Despite likely decoupling of the ice-bed interface in an icefall, the thinning of the ice and extensive crevassing provide a means for penetration of meltwater and seasonal and diurnal temperature cycles to the bed to contribute to frost shattering processes, predisposing the bedrock to more efficient quarrying (Hooke, 1991). Additionally, over-steepened steps will become susceptible to failure and collapse during periods of deglaciation (see next section). Step migration through the cirque would result in a steep profile, enhancing sliding speeds and erosion rates until it diffuses laterally into the headwall and contributes to divide migration (Figure 2.15c).

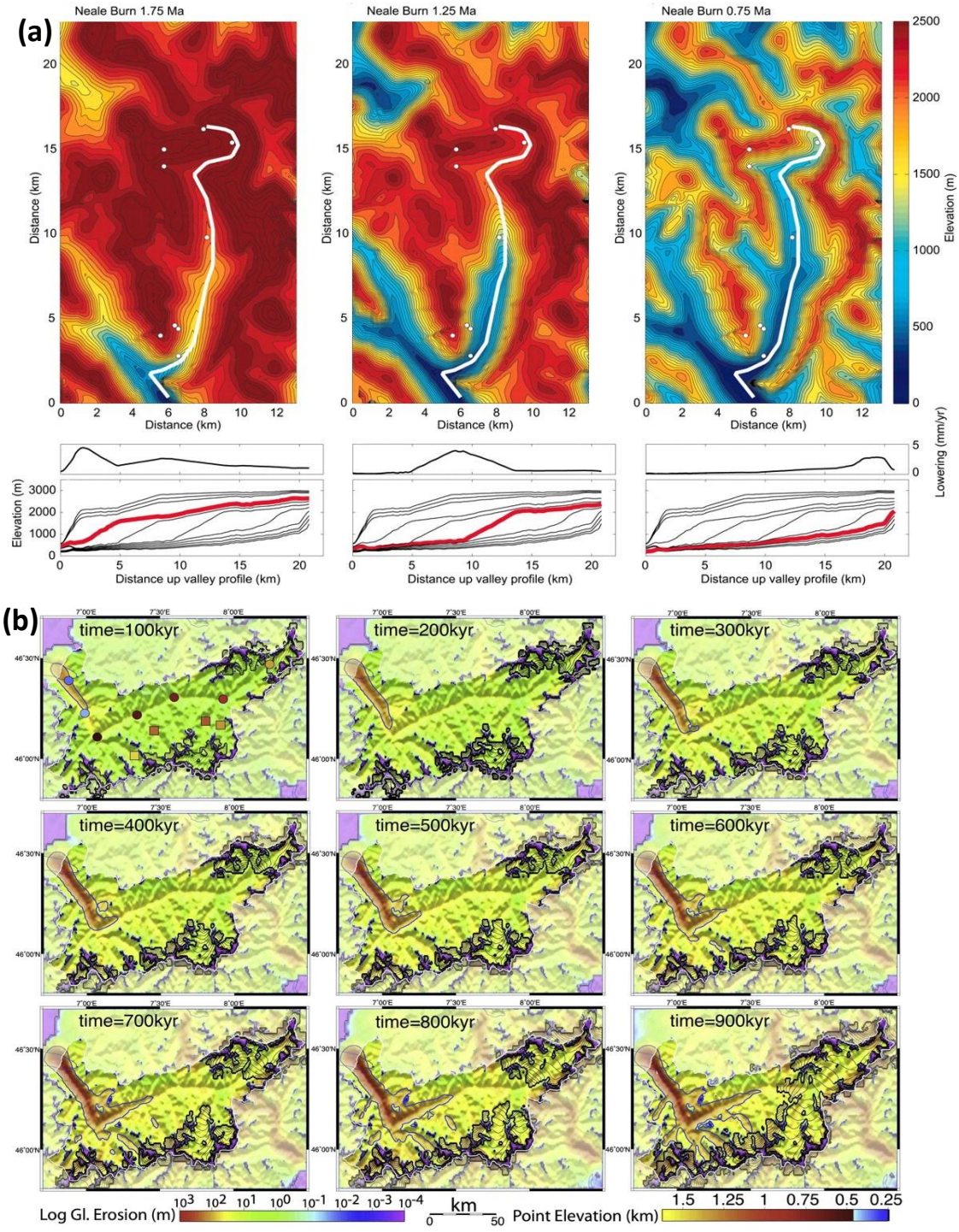

Figure 2.16: Results from two separate studies which demonstrate the likelihood of glacial landscape evolution dominated by a headward signal of large steps. **(a)** The best fit topographic evolution model to match field observations from thermochronometry in Neale Burn, New Zealand, involving up-catchment migration of a large step, from Shuster et al. (2011). **(b)** Numerical modelling of glacial cyclicity over 900 ka in the preglacial topography of the Rhône Valley, Switzerland, demonstrating a signal of 100m deep erosion denoted by the blue isoline, moving up-catchment over time, from Sternai et al. (2013).

In this latter scenario we would expect to see instances where cirques have been steepened to the point they no longer have the characteristic bowl shape and icefall lip down to the main trunk, instead prograding almost uniformly. Indeed such cases do exist in the Swiss Alps, a strong example being present at Oberaletschgletscher (Figure 2.17), which constitutes the fifth largest glacier in Switzerland in terms of area (Linsbauer et al., 2021) and is one of the largest outliers in the plot of glacier sizes (Figure 2.10a) for not containing an icefall. The size of such a glacier may suggest that dynamic step erosion has been sufficiently quick here for it to have eaten backwards through the cirque basins, leaving steepened slopes in the present state.

The modelling work of Sternai et al. (2013) simulated both the pre-glacial and present-day topography for the Rhône catchment and found that whilst initial glaciation focuses erosion strongly at the lower reaches and moves up valley, subsequent occupation of present-day topography results in a bimodal distribution of erosion at both the lower and upper reaches. The intensity of such erosion in the upper reaches over time could dictate which of the above two scenarios is most plausible.

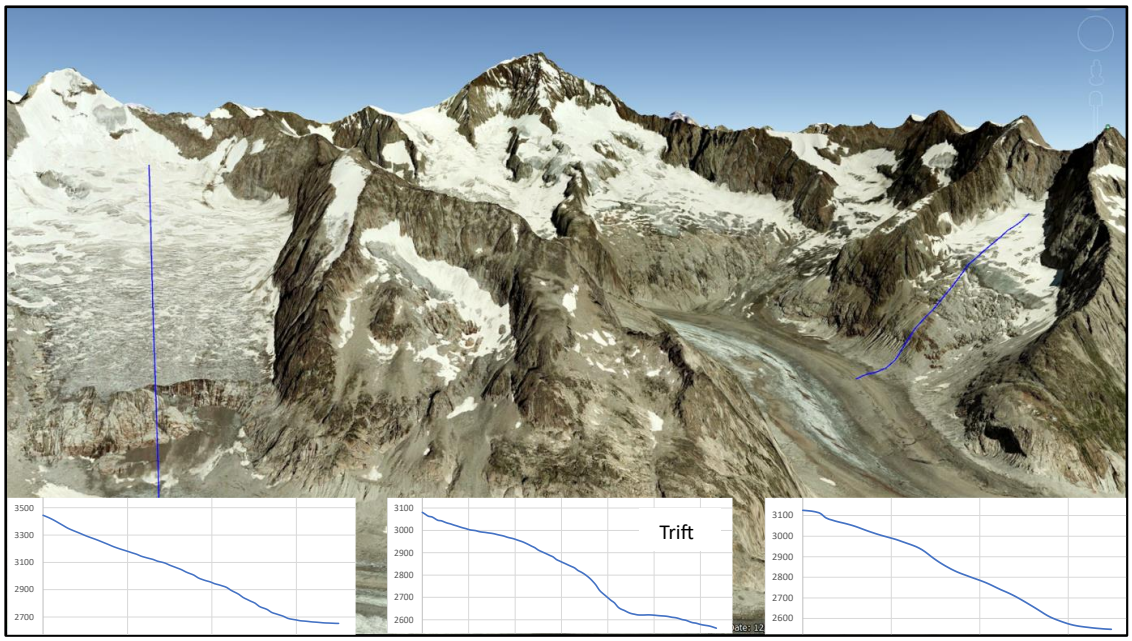

Figure 2.17: Oblique Google Earth view of the upper catchment of Oberaletschgletscher, Switzerland (N 46.424°, E 7.959°). Cirques at the head of this large glacier do not contain regular basins with steep icefall lips, but rather prograde smoothly and steeply down to the main trunk valley, which may be indicative of the icefall step having eroded headward through the basin. Two cirques are highlighted here with blue lines running from their top to bottom on the left and right of the image, with respective elevation profiles beneath. For comparison, the elevation profile for a regular cirque icefall at nearby Triftgletscher is shown in the bottom centre – note the major convex step between the upper cirque and lower glacier which is not present in the profiles from Oberaletschgletscher.

2.4.6 A Note on the Contemporary Perspective

Away from icefalls in the context of their role in long-term landscape evolution, it is worthy to note their importance in impacting contemporary glaciers through important mass balance feedbacks. Certainly, the processes occurring today will likewise operate during the changing of glacier states in previous and future glaciations and thus impact the scenarios of erosion and evolution discussed in the previous sections.

Today, as ELAs have risen, greater areas of glacier profiles have been exposed to higher temperatures and increased ablation rates. Thicker ice in tongues are able to sustain mass loss for longer compared to icefalls, where the steep gradient and highly dynamic nature (e.g. high velocities, crevassing, avalanching) prevents the build-up of debris cover, which combined with thinner ice can result in a zone that is highly vulnerable to greater rates of ablation and down wasting. Reduction in mass flux through the icefall due to this down wasting can result in a dynamic detachment between accumulation areas and stagnant glacier tongues, with the icefall effectively becoming the new dynamic terminus (Rowan et al., 2015, 2021).

Ongoing negative mass balance in the icefall can then ultimately lead to full exposure of bedrock, which will in turn enhance ablation further through preferential absorption and emittance of shortwave and longwave radiation. Such cases were documented in this study under the category of partial disconnection (Figure 2.5). Continued mass loss and bedrock exposure in the icefall will eventually result in full physical disconnection between the accumulation areas above and the lower tongue below (Rippin et al., 2020; Rowan et al., 2021; Davies et al., 2022). Such processes have the potential to enact rapid, vast changes in glacier mass balance and extent as lower tongues cease to be nourished with regular ice flow from the accumulation area.

A fully disconnected icefall will comprise of a steep, exposed portion of bedrock that is periodically transited by ice avalanches from serac collapses on the new dynamic terminus above. Full exposure to the open air also enables periglacial processes to attack this region of the bedrock, which may already have been weakened by quarrying from the former ice coverage. Subsequently, disconnected icefalls are vulnerable to dramatic rock slope failure events (Figure 2.18)(Hählen & Keusen, 2022), which pose a serious risk to nearby human infrastructure or activities. Material eroded from these regions – either through gradual frost shattering, or sudden collapse events – can serve to form a protective debris layer on the surface of the former ice tongue, reducing ablation rates and potentially negating the

rate of mass loss otherwise incurred following severance from the accumulation zone. The rates and efficacy of these feedbacks are currently largely unknown, however, as the significance of icefall vulnerability to disconnection is only recently being realised (Rowan et al., 2021; Davies et al., 2022).

Recent melt seasons have resulted in average thinning rates of approximately 3 m a^{-1} across Switzerland (Huss, 2022). Given the median ice thickness value of 56 m for icefalls mapped in this study, it can be expected that a significant number of Switzerland's major glaciers will experience disconnection in the coming decades, the impact of which is not fully known and therefore possibly unaccounted for in projections of future glacier retreat and certainly worthy of future investigation.

Figure 2.18: Recent rock slope failure at the rapidly deglaciating icefall of Steingletscher, Switzerland. Three separate events between November 2019 and April 2020 resulted in the breakaway of 300,000-400,000 m^3 of debris which fell 1.5 km down-glacier (Hählen & Keusen, 2022). The runout area is a popular ski touring and mountaineering route to access the Tierbergli mountain hut in the upper valley, which was subsequently closed for a brief period as a consequence of this event to deter people from making the journey. Such dangers will likely become increasingly common across the Alps as more steep cliffs and steps lose their ice cover.

2.5 Summary

In this chapter I have produced a novel inventory of contemporary icefalls across Switzerland, permitting a more systematic approach to defining icefalls as a glacial landform. Extracting a variety of data from icefall regions and comparing across the rest of the glacier profile has provided empirical evidence on the significant impact that icefalls have on ice dynamics – representing a zone of greatly enhanced gradient, surface velocity and reduced ice thickness.

Analysis of the topographic distribution of icefalls in respect to elevation has revealed a strong and statistically significant correlation to ELAs, which indicates the features are strongly driven by climate during initial formation and/or development over time. This coupling of climate with a major landform has potentially substantial implications for the processes and influence of glacial erosion on long-term alpine landscape evolution. Using these inferences from the data I set out some theories on possible mechanisms by which icefalls initially form and subsequently evolve through time over fluctuating glacier extents.

The presence of icefalls only on the larger contingents of glaciers could suggest the necessity of greater ice extents to set up sufficient bimodal variation in erosional efficacy for the features to form. Though an important caveat to this evidence is the conservative mapping approach taken here precluded inclusion of deglaciated steps further down the profile, such that it may be possible that small glaciers at present-day extent do indeed contain icefalls during more extensive glaciation. The lack of correlation between glacier and icefall size confounds matters somewhat, but likely speaks to the complex nature of spatially variable erosional efficacy over long timescales.

The dominating presence of icefalls towards the head of the catchment near cirques or plateaus could be interpreted as evidence for either formation in-situ, or dynamic behaviour whereby large bedrock steps erode headward up the catchment through glacial-interglacial cycles. The persistence of some mid-profile icefalls around regions of heterogeneous lithology is suggestive of in-situ formation that consequently remains in place. However, this theory is contingent on the ability of cirques and upper accumulation areas to erode at a sufficient rate to keep pace with valley lowering and uplift rate.

The alternative theory of dynamic headward erosion has credence in past studies using topographic analysis, thermochronometry samples and modelling, which have advocated for such a process to occur in the context of cirques and valley excavation over glacial and Quaternary timescales. It seems feasible then that a large bedrock step, formed initially

either lower down during maximum glacier extents, or in the mid-profile region about the average Quaternary extent ELA, could subsequently propagate up-valley through time as a mechanism of maintaining landscape steady-state with uplift rate.

A question arises as to what occurs to a migrating step once it arrives in the upper reaches. Here, the case has been made for either a slowing of the rate of erosion such that the icefall becomes fixed in place, or a continued retreat up through the cirque basin to meet the headwall. The topography of the Swiss Alps provides specific cases in which either scenario can be envisaged.

Ultimately, topographic analysis alone cannot provide hard evidence for the prevalence of one theory or another, as it lacks the vital temporal component of landform evolution over glacial cycles. The use of numeric computer models is needed to explore such processes further, as it permits the simulation of ice dynamics and erosion through a time-varying climate. The next chapter will use a numerical model to investigate the efficacy of glacial erosion in two contrasting catchments under different climate and glacier states, as well as exploring the impact of using different numeric representations for erosion that are commonly used by others. Subsequently, data from the field is needed to constrain such model outputs and this is provided later, in Chapter 4. Together, these following two chapters will provide further data and evidence that can be used to explore the theories outlined here, as well as the overall research aim of how glacial erosion operates within individual catchments over a range of glacier conditions.

2.6 Appendices

2.6.1 Bifertenfiren oblique view

Appendix 2.6.1: Oblique Google Earth view of Bifertenfiren, which contains two current icefalls in rapid succession (green lines), as well as two large deglaciated steps further down the valley (red lines). Each step is located within a region of significant change in lithology. See page 71 for full discussion.

2.6.2 Fieschergletscher icefall situation

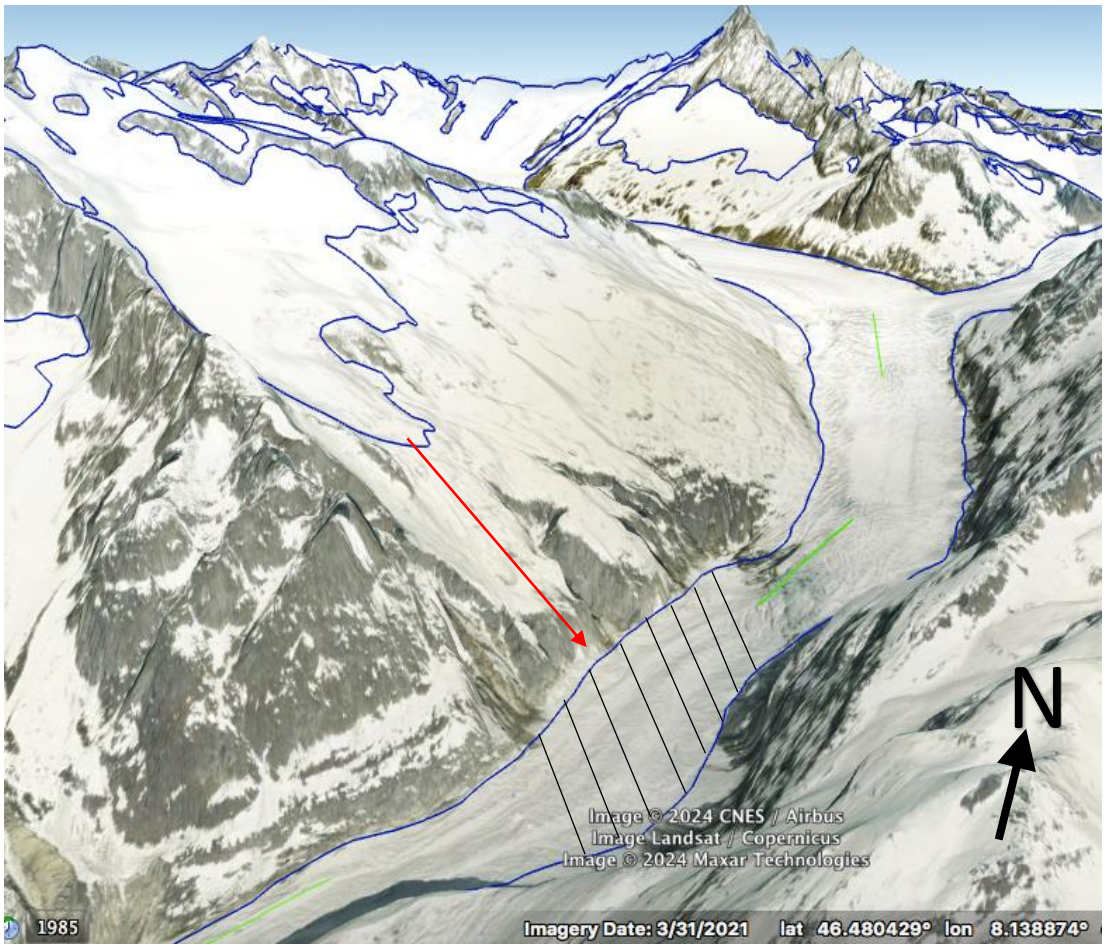

Appendix 2.6.2: Oblique Google Earth view of Fieschergletscher and surrounding glaciers outlined in blue. The mid-profile icefall here (green line, centre right) represents the sole outlier of mid-profile icefalls in the inventory with no nearby variation in bedrock lithology. Bedrock in this area is comprised homogeneously of granite.

An alternative explanation for major step formation here is the presence of the hanging glacier above to the left. During greater ice extents, this would have connected to the main glacier via the red arrow, locally raising ice flux, which may have sufficiently increased erosion rate to preferentially deepen this portion of the valley profile (black hatched region).

This demonstrates a limitation of the current classification regime of icefalls from the inventory, in that under different ice extents they could well be considered under an entirely different topology. In this case, connection of the two ice masses would more likely classify this icefall as a confluence type rather than mid-profile.

2.6.3 Icefall and snowline elevation with outliers removed

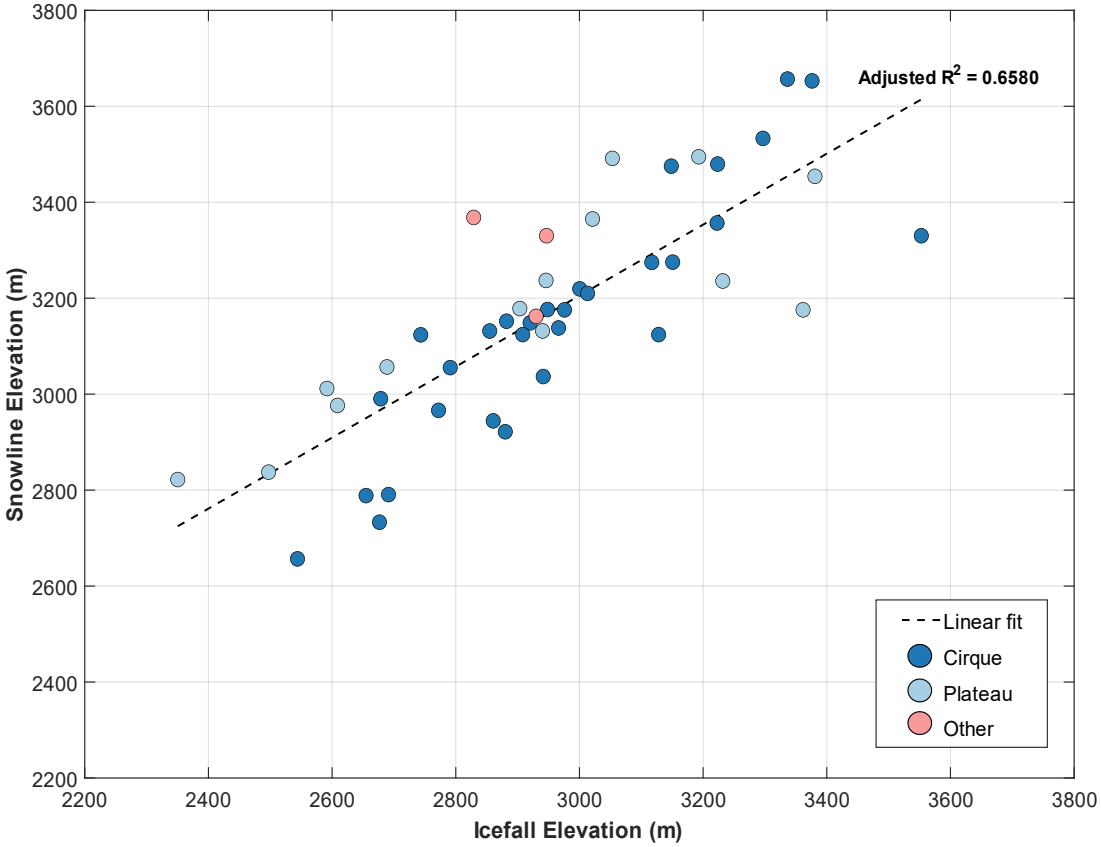

Appendix: 2.6.3: Icefall and snowline elevations with tributary, confluence and mid-profile types removed, which strongly improves the correlation, showing how these remaining types are more climate controlled. See page 73 for details.

2.6.4 Deglaciated icefall steps at Rhonegletscher & Kanderfirn

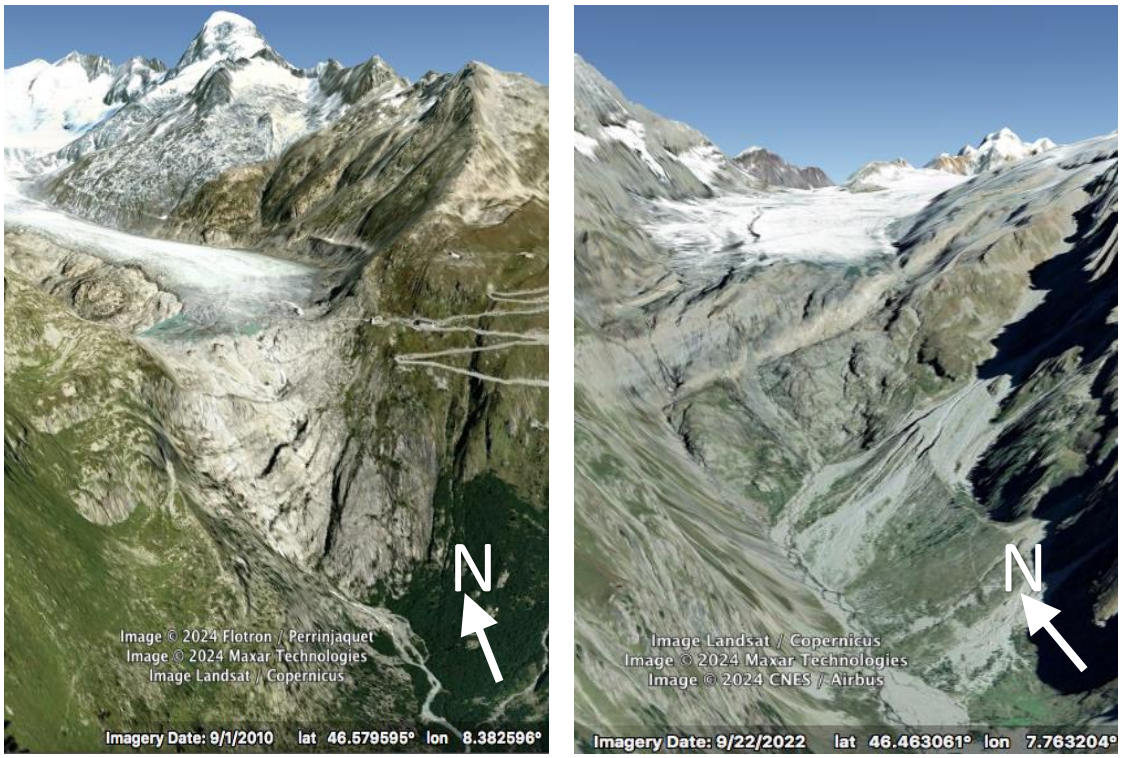

Appendix 2.6.4: Oblique Google Earth imagery of Rhonegletscher **(left)** and Kanderfirn **(right)**, both containing large bedrock steps at lower elevations (~2100 m) just beyond their current terminus, which were previously very large icefalls during the Little Ice Age (c. 1850). As these steps are now deglaciated, they were not included in the icefall inventory. Hence, they appear as anomalously large glaciers without icefalls – a problematic interpretation given the large 'relic icefalls' just beyond present ice extent. Note also the impressive fault line and variation in lithology running diagonally across the cliff at Kanderfirn, a possible catalyst to the step formation?

Chapter 3

Numerically Modelling Glacial Erosion Under Different Climate Conditions

3.1 Introduction

3.1.1 Chapter Overview

In the previous chapter I used a topographic analyses of the present-day Swiss Alps to demonstrate that, despite great variation in climate and glacier extents in the past, the glacial landforms of icefalls are situated within an elevation window that is strongly coupled to climate. The implications for this are the strong focusing of glacial erosion over time-averaged conditions and the importance this has on driving long-term landscape evolution beyond the presently postulated 'buzzsaw mechanism' (Brozović et al., 1997; Mitchell & Montgomery, 2006).

In this chapter I use the numerical landscape evolution model 'iSOSIA' to simulate spatial patterns of glacial erosion over a variety of timeframes and climate conditions, permitting a more thorough exploration of some of the insights gained from the previous chapter. Two contrasting catchments from the Swiss Alps are used to demonstrate the impact of basin topography on ice dynamics and erosion, and a range of erosion law parameters are considered to more thoroughly test their impact on the outcomes of modelling work.

3.1.2 Numerically Modelling Glaciers

Acquiring quantitative data beyond the qualitative descriptions of glacier characteristics has been integral to the development of knowledge in the field since some of the earliest glaciology studies by the likes of Forbes (1859). However, data collected from the field represents a highly limited view of the overall situation. It is often spatially limited to individual point measurements, physically limited by the accessibility of that which is being measured (e.g. englacial or subglacial processes) and temporally limited to the time at which measurements are taken. Consequently, numerical models can be used to circumvent such constraints and allow analysis of glacier behaviour over a broad range of spatial and temporal scales.

By the mid-20th century, numerical representations of glacier flow through mathematical expressions permitted a deeper exploration of glacial processes (e.g. Nye, 1952, 1958) and paved the way for more detailed finite element models over time. Early one-dimensional models have been used to explore the dynamics of ice flow in surging glaciers (Bindschadler, 1982), propagation of wave ogives (Waddington, 1986) and ice-bed responses to glacial erosion under changing climate conditions (Oerlemans, 1984; MacGregor et al., 2000). Improvements in computation power over time have facilitated the use of more complex 2-D (e.g. Schmidt & Joshi, 1982; Harbor, 1992) and 3-D models (e.g. Herman & Braun, 2008; Jouvet et al., 2008; Egholm et al., 2011). Today, numerical modelling is an essential component driving research on the response of the cryosphere to anthropogenic climate change (IPCC, 2019) and has expanded to the point of becoming a substantial sub-discipline within the field of glaciology itself. There are now many different glacial models that have been developed over time and are ready to be used by researchers – such as PISM (Bueler & Brown, 2009), Elmer/Ice (Gagliardini et al., 2013) or OGGM (Maussion et al., 2019), to name a few.

A primary consideration for choice of model is the level of detail for how ice flow is simulated through time. Solving the full-Stokes equations for the most complete accountability of fluid dynamics (as in Elmer/Ice) should give the most accurate representations, but is considerably more computationally expensive, often limiting the application to smaller domains or coarse resolutions. Alternatively, a far simpler approach is often used in the form of the shallow ice approximation (SIA) (Hutter, 1983), which calculates ice flow according to basal shear stress and gravitational driving stress driven by the local gradient and ice thickness, assuming small aspect ratios of vertical to horizontal

extents. The SIA approach significantly improves the efficiency of numerical models, permitting more detailed studies at greater scales and/or resolutions, whilst still maintaining similar levels of accuracy to full-Stokes alternatives when applied to ice sheet interiors away from ice streams or ice shelves (Pattyn et al., 2008; Seddik et al., 2017). In more dynamic scenarios, however, where there are large changes in gradient and ice dynamics over short distances (such as at ice sheet margins or smaller alpine glaciers), the SIA will fail to create realistic outputs (Le Meur et al., 2004). To remedy this, higher order models such as the second order SIA (SOSIA) include more terms, like longitudinal deviatoric stresses, to improve performance in more complex terrain without resorting to full-Stokes solutions in order to maintain efficiency (Baral et al., 2001; Kirchner et al., 2016).

Another significant consideration are the values used to drive the numeric representations of processes. Here, valid empirical data often underpins the treatment of these calculations with the intention of achieving more accurate outputs. However, reliable empirical constraints are lacking for many key processes, which is highlighted as a major challenge for ongoing modelling of the cryosphere (Derksen et al., 2022).

Some of the main values and assumptions used in this study are outlined later along with the model description (Section 3.3.1). The following section will provide more detail on the treatment of glacial erosion in numeric modelling, as this is the primary focus of the thesis.

3.1.3 Numerically Modelling Glacial Erosion

Glacial erosion is a complex process, not least due to the inherent inaccessibility of the subglacial domain preventing acquisition of reliable empirical data on the rates and mechanisms at play. Aside from a few limited situations in which man-made tunnels have provided direct access and observations of the ice-bed interface (e.g. Haefeli, 1951; Boulton, 1982), the evidence and impact of glacial erosion is only readily apparent once the ice has retreated from the landscape, leaving behind signature signs of abrasion and quarrying processes, or larger landforms like overdeepened basins (Cook & Swift, 2012). As a result, much of the understanding and treatment of glacial erosion comes from theoretical considerations of abrasion and quarrying, supported by small scale lab experiments (Hallet, 1979; Röthlisberger & Iken, 1981; Boulton, 1982). The importance of basal stresses and sliding velocity in determining the effectiveness of abrasion was recognised early on by

Gilbert (1910) and would come to form the cornerstone of foundational theories of glacial abrasion from Hallet (1979, 1981).

As outlined in Chapter 1 (section 1.2.4), a streamlined expression of these theories can be used where erosion is the product of a dimensionless constant K_g – a general term for bedrock lithology and resistance to erosion – alongside basal sliding velocity U_s, raised to a dimensionless exponent l, which defines the linearity of the scaling relationship between sliding and erosion:

$$E = K_G \, U_S^l \tag{3.1}$$

This simplified approach has been widely adopted in numerical models and used to successfully reproduce common aspects of glacial geomorphology such as U-shaped valleys, large profile steps and overdeepened basins (e.g. Harbor, 1992; MacGregor et al., 2000; Herman et al., 2011; Liebl et al., 2021).

Whilst separate models for quarrying have been developed (Hallet, 1996; Iverson, 2012; Ugelvig et al., 2016), the more complex mechanical theory involved is dependent on aspects like bed topography that may not be reliably captured in the model resolution, as well as cavitation and hydrological pressure variability which are difficult to measure accurately in the field. Moreover, current methods of estimating erosion in the field (e.g. proglacial sediment flux) cannot distinguish between the relative outputs from the two processes of abrasion and quarrying. As such, treating erosion in a uniform manner as in Equation 3.1 provides an easier means for empirical constraint using measurements of sliding (or surface) velocity compared to estimates of erosion rates. Despite this, the terms K_g and l are still loosely constrained as measurements of sliding velocity that coincide with respective estimates of erosion are rare. A compilation of globally reported velocities and erosion rates by Cook et al. (2020) yielded a statistically significant relationship in which l is 0.65 and K_g is 1.6×10^{-4} (Figure 3.1). Variance and uncertainty in this relationship are derived from the numerous different sources of data acquired from the literature where different methods were used. Erosion rates were calculated from a variety of sampling techniques (proglacial sediment discharge, lacustrine or marine sediment accumulation etc.) and velocity data was from direct sliding measurements or converted surface velocities from an array of positions along the glacier profile and over a range of temporal scales

(Cook et al., 2020). Moreover, in many instances of past literature, erosion estimates are reported for glaciers without accompanying measurements of velocity and so could not be used. Any attempts to remediate such cases with more recent velocity data (e.g. using remote sensing) could prove highly inaccurate due to significant changes in ice dynamics between the two measured periods. For example, one of the data points used by Cook et al. (2020) is Muir Glacier in Alaska, with a reported erosion rate of approximately 25.1 mm a^{-1} (Hallet et al., 1996) and surface velocity of 1700 m a^{-1} (Hunter et al., 1996). Since these measurements, Muir Glacier has undergone extensive retreat such that it is no longer a marine-terminating tidewater glacier and now terminates terrestrially (Hansen, 2020). Consequently, modern remote sensing measurements show a dramatic reduction to Muir's surface velocity to approximately 80 m a^{-1} (Millan et al., 2022).

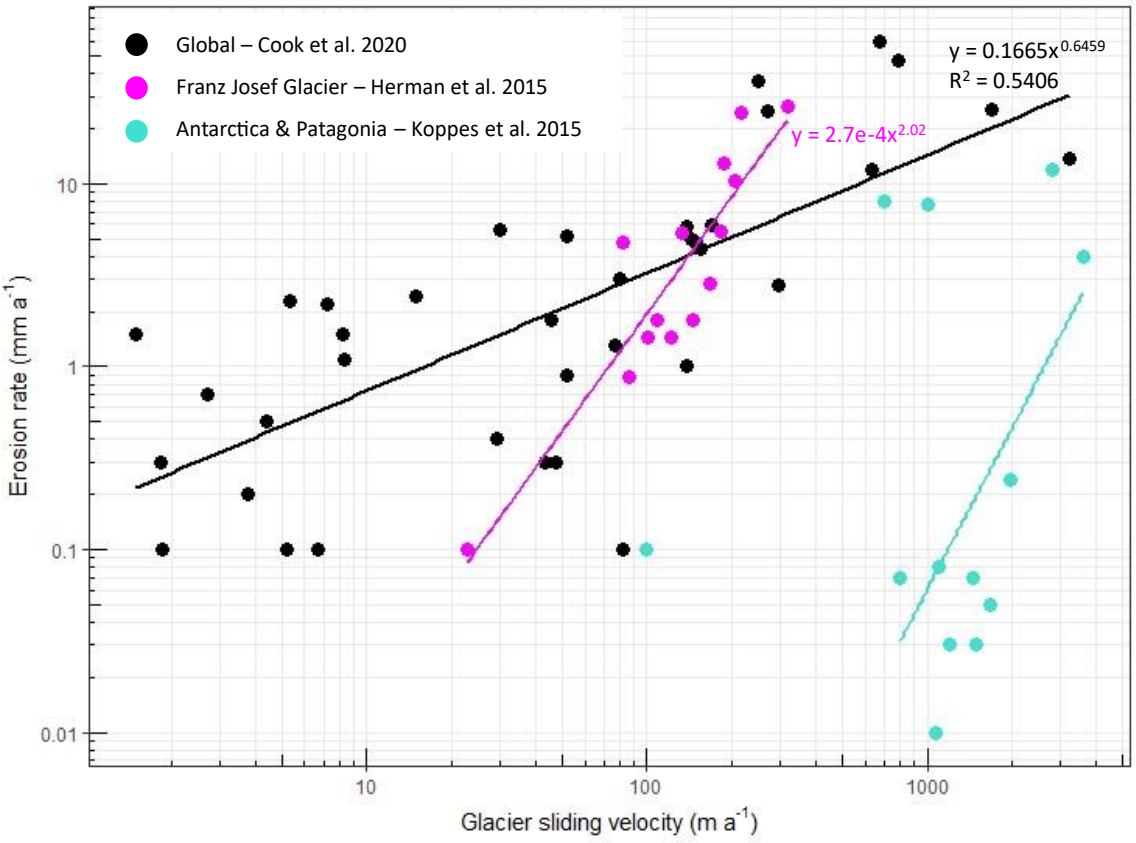

Figure 3.1: Compilation of glacial erosion and sliding velocity data used to constrain values of l and K_G. Global data from Cook et al. (2020) yields a non-linear relationship where l = 0.65 and K_G is 1.6×10^{-4} when erosion is expressed as m a^{-1}. A stronger non-linear law is found by Herman et al. (2015) from multiple data points within the single Franz Josef glacier, New Zealand, where l = 2 and K_G is 2.7×10^{-7}, whilst a similar degree of non-linearity is reported by Koppes et al. (2015) across spatially integrated rates of erosion and sliding for tidewater glaciers in Antarctica and Patagonia. Figure adapted from Cook et al. (2020).

Whilst the broad data compilation of Cook et al. (2020) produces an l value of 0.65, suggesting the rate of change in erosion is lower than the coupled change in sliding velocity, a simple linear relationship of l = 1 has been used extensively in numerical models (e.g. MacGregor et al., 2000, 2009; Tomkin, 2007; Herman & Braun, 2008; Sternai et al., 2013; Dürst Stucki & Schlunegger, 2013), based off observations from a single surging glacier (Humphrey & Raymond, 1994), which is not particularly representative of smaller alpine glaciers. More recently, quantification of sliding and erosion rates across a single alpine glacier in New Zealand led to a non-linear relationship where l was approximately 2 (Herman et al., 2015), with similar non-linearity found in a compilation of tidewater glaciers across Patagonia and Antarctica from Koppes et al. (2015) (Figure 3.1).

Few studies have tested the impact of different values for l. In the modelling of valley cross sections Harbor (1992) found that narrower and deeper channels were formed with higher l values. Others have shown that choice of l had relatively little impact on the modelling of hydrology (Herman et al., 2011) or basal shear stress (Brædstrup et al., 2016). The main impact of applying non-linear laws appears to be an increase in the heterogeneity of erosion patterns, which can influence valley evolution (Liebl et al., 2023) and re-equilibration time after changes in climate (Herman et al., 2018). All of these studies were conducted on synthetic landscapes with characteristic glacial valley features (U-shape, overdeepenings, steps etc.) and therefore lacking in any direct comparison to real world data for model validation.

The constant K_G directly controls the magnitude of erosion produced by a model and as such is frequently described as a term for bedrock resistivity to erosion (e.g. Harbor, 1992). Values for this are not well constrained but need to vary in line with the choice of l. In some cases, K_G is tuned until the erosion output is at an acceptable level given the scenario (e.g. Herman et al., 2011), but lack of reliable field data on erosion rates makes this difficult and uncertain. Consequently, the choice of K_G value is often overlooked and a wide range have been used across modelling studies (Table 3.1), often without justification as to whether the chosen value is necessarily appropriate for the given application. The compilation of data from Cook et al. (2020) (Figure 3.1) provides a good resource to calibrate an appropriate value of K_G based off rates of sliding velocity where no erosion data is available but calls for the need to improve data availability on glacier erosion rates across a range of topographic, climate and time scales to improve the accuracy of such determinations. It is worth noting that application of a single value for K_G across large model domains is itself a gross simplification given the impact of changes in lithology on glacial erosion and development

of major landforms like overdeepenings (Swift et al., 2008; Preusser et al., 2010; Magrani et al., 2020). As such, spatially varying K_G to reflect these changes could have significant effects on model outputs (Harbor, 1992; Prasicek et al., 2018), though this is not commonly implemented on many models at present and would further increase the complexity of how to appropriately calibrate such variance.

Currently, there is a lack of evaluation on the impact of different erosion laws through systematic variation in l and K_G coupling on real alpine landscapes. Seguinot & Delaney (2021) explored the effect of four different pairings on erosion rates over the last glacial cycle for the entire Alps at a relatively coarse resolution of 1-2 km, thus analytically restricted to the larger trunk valleys and alpine forelands. Higher-resolution assessments are therefore needed to capture smaller scale changes in the high-mountain catchments occupied by today's glaciers where ice residency time is longest and important processes like the glacier buzzsaw mechanism are said to enact strong influences on landscape evolution (Brozović et al., 1997; Mitchell & Montgomery, 2006).

Table 3.1: Examples of the wide range of different values used for K_G across modelling studies over the last couple of decades. Units are in m a^{-1} unless otherwise stated.

Authors	**Model**	l	K_G
MacGregor et al. (2000)	Bespoke	1	1×10^{-4}
Egholm et al. (2011)	iSOSIA	1	1×10^{-3}
Herman et al. (2011)	Bespoke	1 2	2×10^{-4} 3×10^{-6}
Egholm et al. (2012a)	iSOSIA	2	1×10^{-5}
Pedersen & Egholm (2013)	iSOSIA	2	2×10^{-5} 3×10^{-5}
Brædstrup et al. (2016)	iSOSIA & Elmer	1 2	8×10^{-5} 2.5×10^{-6}
Egholm et al. (2017)	iSOSIA	2	5×10^{-8}
Herman et al. (2018)	Bespoke	1 2	1×10^{-4} 7×10^{-6}
Ugelvig & Egholm (2018)	iSOSIA	N/A	2.8×10^{-9} Pa^{-1} 5.6×10^{-9} Pa^{-1}
Ugelvig et al. (2018)	iSOSIA	2	1×10^{-7}
Deal & Prasicek (2021)	SIIM	1 2	1×10^{-4} 5×10^{-6}
Liebl et al. (2021)	iSOSIA	N/A	1×10^{-4} Pa^{-1}
Magrani et al. (2021)	iSOSIA	2	5×10^{-3} Pa $s^{1/3}$
Liebl et al. (2023)	iSOSIA & OpenLEM	1 2	2×10^{-4} 1×10^{-5}

3.1.4 Chapter Aims and Objectives

This chapter directly addresses Objective 2 of the thesis and provides insight towards all four of the research questions.

The specific overarching aim of this chapter is to use the landscape evolution model iSOSIA to explore the spatial and temporal variation of glacial erosion at a high resolution in upper alpine catchments under steady and variable climate scenarios. Tests are also conducted to investigate the impact of using different erosion laws. Together, this provides insight on how glaciers in the high-mountain basins act to shape the landscape over time.

The key objectives of this chapter are as follows:

1. Explore plausible pairings of l and K_G parameters to use in different erosion law scenarios.
2. Examine the impact of different erosion laws under steady state Little Ice Age (LIA) and Last Glacial Maximum (LGM) conditions.
3. Examine patterns and rates of glacial erosion over idealised glacial period (GP) and interglacial (IG) scenarios mimicking that of the last glacial cycle and Holocene and explore the impact this has on landform and landscape evolution.

3.2 Study Sites

Two study sites in the Swiss Alps, Glacier d'Otemma and Triftgletscher, were chosen for this work as they have contrasting catchment hypsometry and features – the former being relatively flat with few major landforms and the latter being much steeper with the presence of large landforms like an icefall, overdeepening and riegel ridge. This permits an interesting comparative analysis in the operation of glacial erosion in different terrain. As well as differences in character, the two sites are relatively easy to access, which facilitated the acquisition of field samples used later in Chapter 4. An overview of each site is given below.

3.2.1 Glacier d'Otemma

The Glacier d'Otemma is situated on the south-western border of Switzerland in the Val de Bagnes catchment area of the Valais canton (Figure 3.2). The present glacier is approximately 6 km in length and covers an area of 12.6 km^2, making it the 14th largest glacier in Switzerland by area, according to the Swiss Glacier Inventory (SGI) 2016 (Linsbauer et al., 2021). It has an approximate mean ice thickness of 62 m (Grab et al., 2021) and mean surface velocity of 6 m a^{-1} (Millan et al., 2022) and is believed to be comprised of temperate ice (Langhammer et al., 2017).

The Otemma basin consists of a flat-topped accumulation area at an elevation of approximately 3015 m at the Col de Charmotane, which is shared with the Glacier du Mont Collon that flows down to the north-east into the neighbouring Val d'Arolla. The highest point is the nearby summit of the Pigne d'Arolla at 3796 m, though the ice of this upper summit region is currently disconnected from the main glacier at the plateau below. The main trunk of Otemma flows in a south-westerly direction with a gentle gradient averaging approximately 5°. The shallowness of this valley profile exposes Otemma to significant changes in ablation area from any increases in temperature and ELA, though the length of the glacier helps to slightly offset this sensitivity by increasing the response time (Mancini & Lane, 2020). As a result, it has undergone a steady retreat from its LIA extent, now terminating about 4 km back from the LIA margin. Late melt season snowlines from 2020

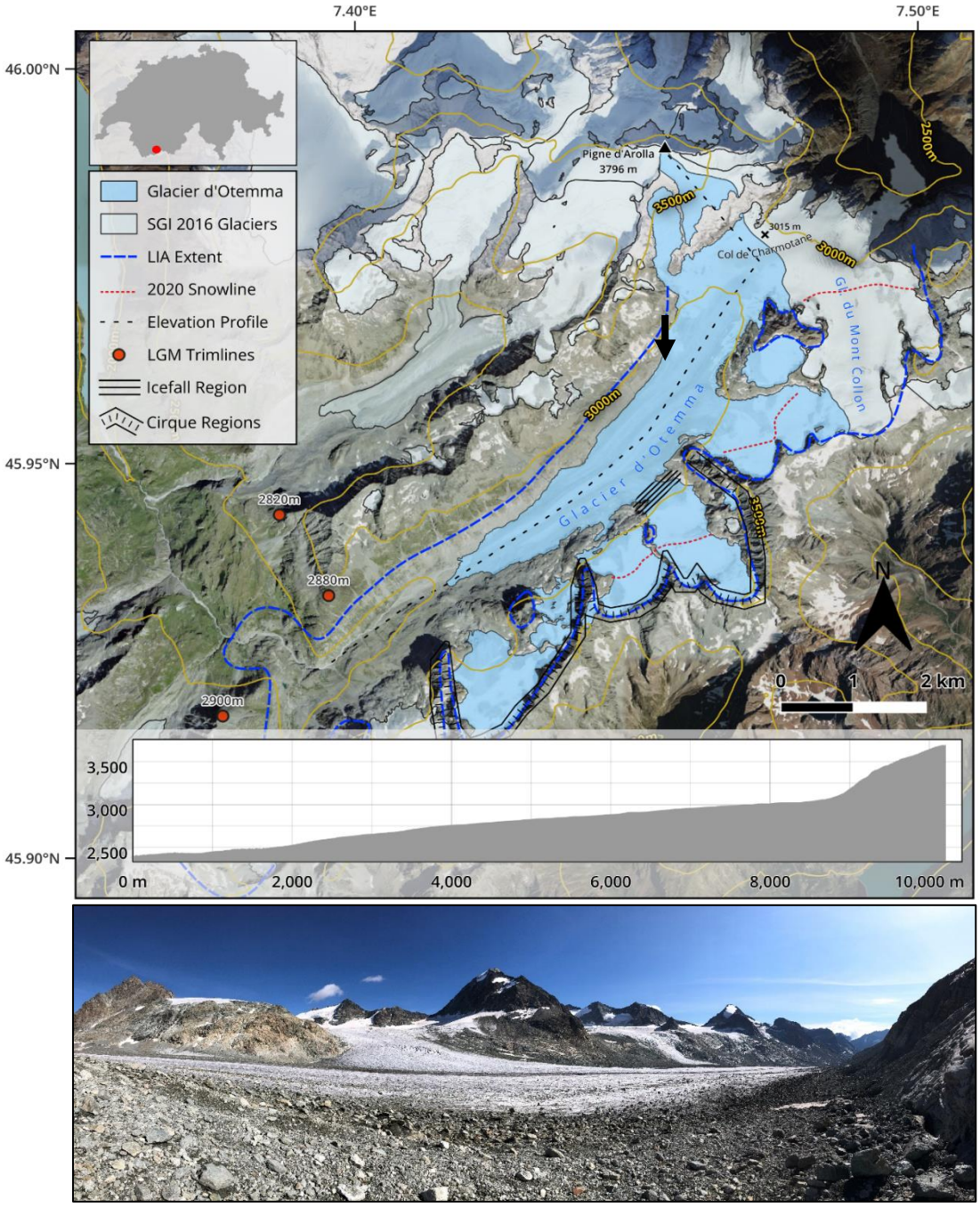

Figure 3.2: Map of Glacier d'Otemma, Valais, Switzerland, as of SGI 2016 extents. LIA extent based off the historical Dufour map of 1864 (Federal Office of Topography swisstopo, 2024). LGM trimline data from Kelly et al. (2004). Approximate snowlines outlined from satellite imagery of the late 2020 melt season. Black arrow indicates position of panoramic field photo looking down glacier towards the cirques on the southern side of the catchment.

satellite imagery imply the modern ELA lies above ~3100 m (Wetterauer et al., 2022).

A series of cirques are cut into the southern drainage divide and have small icefall lips down onto the main glacier below, whilst the northern margin contains steeper, deglaciated south facing slopes. The valley ends at a constriction with a narrow gorge at an elevation of approximately 2350 m, occupied by the proglacial river Dranse de Bagnes.

During the LGM the Glacier d'Otemma was the valley source of a substantial tributary feeding into the main Rhone Glacier trunk that flowed northwards to present-day Lac Léman (Kelly et al., 2004).

3.2.2 Triftgletscher

Triftgletscher is a temperate glacier (Dalban Canassy et al., 2012) situated in the central Swiss Alps in the canton of Bern. As of the SGI 2016 it was 5.4 km long and covered 14.5 km^2, ranking tenth largest by area in Switzerland (Linsbauer et al., 2021). It has a mean ice thickness of 55 m (Grab et al., 2021) and a mean surface velocity of 13 m a^{-1} (Millan et al., 2022).

In stark contrast to Otemma, the Triftgletscher basin is highly heterogenous with many steep gradients and significant landforms (Figure 3.3). It flows in a north-westerly direction from a wide, multifaceted accumulation area with a maximum elevation of approximately 3380 m, which includes a large cirque approximately 1 km in diameter. The present-day terminus is at around 2300 m elevation resting on the top lip of a ~600 m long, >35° steep bedrock step, which is approximately 4 km back from the LIA margin at an elevation of ~1350 m.

Between the LIA and present-day terminus is a large, >100 m high bedrock riegel wall whose local relief suggests resistance to significant erosion that has lowered the landscape either side of it, despite being largely ice covered during the LIA up until a period between 1948 and 1960 (Steinemann et al., 2021). Retreat back from the riegel from 1998 onwards revealed an overdeepened basin that began to accumulate meltwater into a proglacial lake. Lake formation and record summer temperatures in the early 2000's facilitated substantial mass wastage of the tongue, resulting in an extremely rapid retreat of almost 2 km between

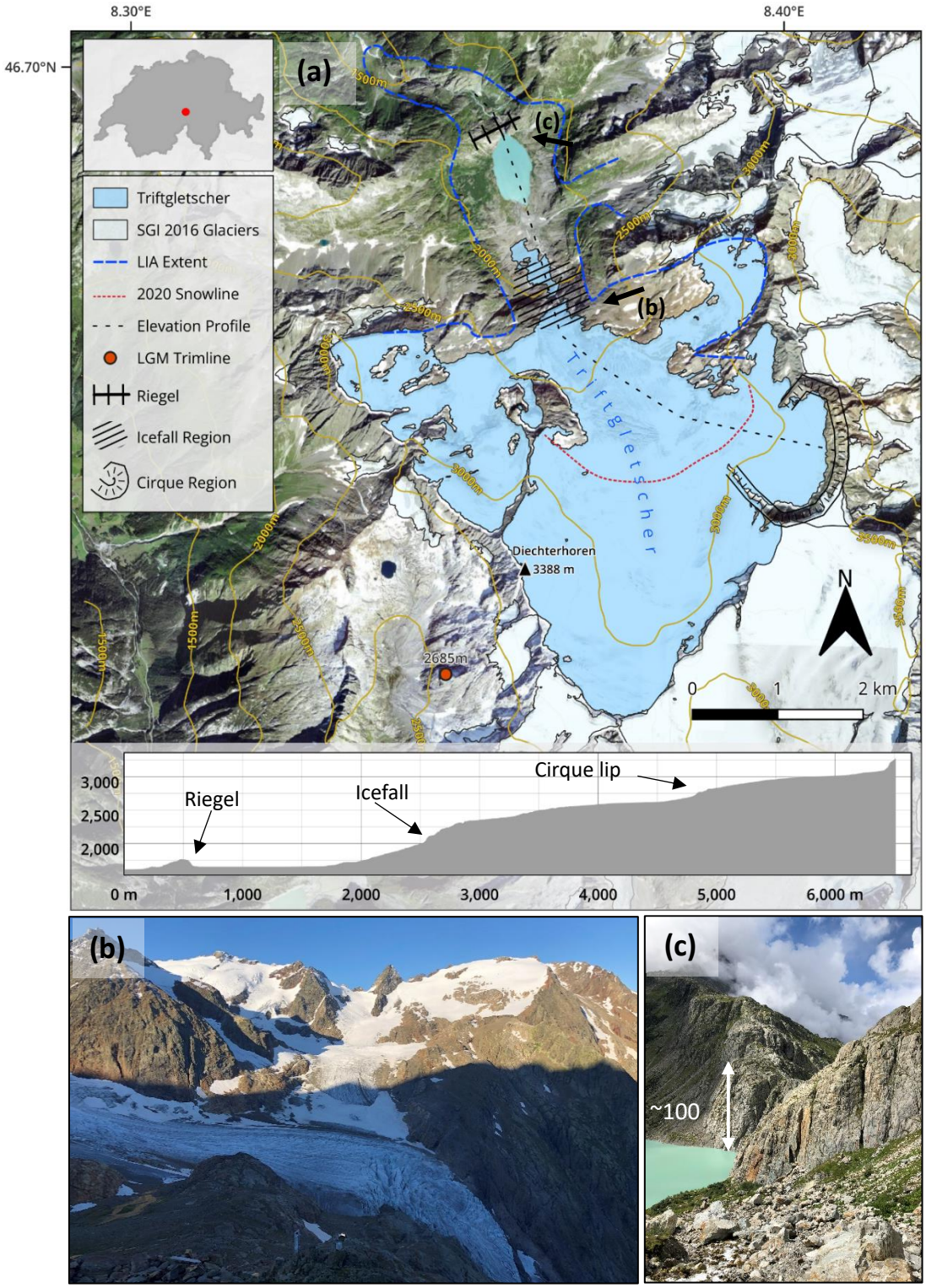

Figure 3.3: Map of Triftgletscher, Bern, Switzerland, as of SGI 2016 extents **(a)**. LIA extents based off historical Dufour map of 1864 (Federal Office of Topography swisstopo, 2024). LGM trimline from Wirsig et al. (2016). Approximate snowline outlined from satellite imagery of the late 2020 melt season. Black arrows indicate position of respective field photos showing the present-day terminus and steep icefall region **(b)** and the large riegel wall **(c)**.

2000 and 2013 (GLAMOS, 2018), reaching a maximum rate of 175 m a^{-1} and earning the glacier an unfortunate Guiness World Record for fastest recorded terrestrial glacier retreat (Guinness World Records, 2024). In 2013 the icefall became fully disconnected, leaving stagnant dead ice below and the new dynamic terminus at the top present location. The average gradient of the current glacier long-profile is ~14°, whilst including the old icefall would raise this towards 19°. Late melt season snowlines from satellite imagery in 2020 suggest the present ELA is at approximately 2800 m.

During the LGM, ice from small side valleys to the east and west of the main basin coalesced with Trift to form a tributary of the main Aare glacier in the Gadmertal Valley below, which flowed north-west onto the foreland towards present-day Bern (Wirsig et al., 2016).

3.3 Methods

3.3.1 Glacial Landscape Evolution Model iSOSIA

This study uses the integrated second order shallow ice approximation model (iSOSIA, version spm-3.4.8). It is a higher-order finite volume solver that maintains many of the computational efficiencies gained from the SIA, but includes the effects of longitudinal and transverse stress gradients which vastly improve the accuracy of depth-integrated flow velocities in steeper and variable topography (Egholm et al., 2011). This makes the model far more suitable to simulating the basal shear stress, sliding velocity and subsequent erosion in alpine valley settings compared to the traditional SIA (Egholm et al., 2012b). These higher-order effects mean the model produces more accurate outputs that are comparable to full-Stokes alternatives, whilst maintaining the efficiency of the SIA to permit higher resolution and/or longer simulations (Egholm et al., 2011; Brædstrup et al., 2016). Full in-depth details of the model can be found in Egholm et al. (2011, 2012b), a simple overview of the key components will be outlined here, with main values available in Table 3.2.

In iSOSIA, ice thickness H responds to changes in flow over time t and is computed with the following continuity equation:

$$\frac{\partial H}{\partial t} = -\nabla \cdot (H\bar{u}) + M \tag{3.2}$$

where $\bar{u}$ is the vector of depth-averaged ice velocity and M is a mass source term for the local rate of accumulation or ablation.

Mass balance is modelled with a simple positive-degree-day (PDD) approach, using a melt degree factor of $4.5e^{-3}$ m w.e. $°C^{-1}$ day^{-1}, which strikes a balance between values determined for snow ($3e^{-3}$) and ice ($6.1e^{-3}$) on glaciers in the Alps (Six & Vincent, 2014). The climatic influence is modelled according to a set sea level temperature (see Table 3.3) which varies according to altitude at a lapse rate of $6e^{-3}$ °C m^{-1} and with an annual temperature amplitude of 10 °C.

Precipitation is spatially uniform across the domain and set to a rate of 1 m a^{-1}

Table 3.2: Main model parameters used in iSOSIA. See Egholm et al. (2011, 2012b) and Ugelvig et al. (2018) for full details on parameters and

Term	Description	Value
Climate		
lrate	Lapse rate	6×10^{-3} °C m^{-1}
mPDD	Degree-day melt factor	4.5×10^{-3} m w.e. $°C^{-1}$ day^{-1}
dTa	Annual temperature amplitude	10 °C
T	Sea level temperature	Variable (see Table 3.3)
P	Precipitation rate	1 m a^{-1}
Ice		
ρi	Ice density	910 kg m^{-3}
B	Ice viscosity constant	73.3×10^{-6} Pa $s^{1/3}$
n	Ice creep constant	3
C_s	Sliding coefficient	5×10^{-3} Pa $s^{1/3}$
ava_{slope}	Critical avalanche slope	0.5 m/m
Hydrology		
k_{min}	Minimum hydraulic conductivity	0.01 $kg^{-1/2}$ $m^{3/2}$
β	Cavity shape parameter	0.7
L_s	Cavity spacing	4 m
L_c	Channel spacing	200 m
S	Cavity size	Equation 3.3
C	Channel size	Equation 3.4
L_i	Latent heat of fusion	3.4×10^5 J kg^{-1}
Erosion		
K_G	Erosion constant	Varied (see Table 3.3)
l	Sliding exponent	Varied (see Table 3.3)

across all model runs. Whilst it is recognised that maintaining a constant precipitation across all scenarios is unrealistic, it is done for the sake of model simplicity and stability, striking a balance between modern rates of precipitation > 1 m a^{-1} (MeteoSwiss, 2024) and reconstructed drier rates < 1 m a^{-1} over the Holocene and LGM (Ivy-Ochs et al., 2009; Višnjević et al., 2020; Jouvet et al., 2023). Whilst different rates of precipitation will affect the magnitude of simulated erosion, it should not drastically alter the spatial patterns (Magrani et al., 2021). Avalanching of snow on cells exceeding a critical slope threshold (0.5 m/m) is also included in the model to prevent snow and ice accumulation on steep slopes, feeding it instead onto shallower cells below (Scherler & Egholm, 2020).

Hydrology in the model is treated using a channel and cavity approach described in detail by Ugelvig et al (2018). Supra or englacial flow is not considered, with all surface melt assumed to be immediately transmitted into the subglacial system. The subglacial domain is a spatially distributed system of channels and cavities that can evolve through time according to changes in effective pressure (ice overburden pressure subtracted by subglacial water pressure). As detailed in Magrani et al. (2021), implementation of the system in iSOSIA does not account for seasonal or diurnal variability in water pressure, but computes steady-state effective pressures to classify a grid cell as either cavity or channel dominated. The size evolution of cavities S and channels C is calculated as:

$$S = \frac{1}{\beta\, h_s}\left(\frac{L_s q_w}{k_{min}\sqrt{\nabla\Psi}}\right)^{0.8} \tag{3.3}$$

$$C = \left(\frac{L_c q_w}{k_{min}\sqrt{\nabla\Psi}}\right)^{0.8} \tag{3.4}$$

Here β is a cavity shape parameter set to 0.7 (Anderson, 2014), h_s the height of a step in the bed, L_s and L_c are the mean spacing for cavities and channels, set to 4 and 200 m respectively (Ugelvig & Egholm, 2018; Bernard et al., 2020; Magrani et al., 2021). Subglacial water flux is q_w, whilst k_{min} is the minimum hydraulic conductivity set to 0.01 $kg^{-1/2}\, m^{3/2}$ (Magrani et al., 2021) and $\nabla\Psi$ is the hydrological gradient calculated according to water flux and ice thickness.

The modelled hydrology influences the determination of sliding speed through a basal sliding law simplified from Ugelvig et al. (2018), which accounts for the impact of changes in water pressure from cavity systems (Iken, 1981). This provides a more realistic simulation of basal sliding U_b for the rough bed topography of Alpine glaciers compared to more simplistic Weertman or Budd laws commonly used in numeric models (Weertman, 1957; Budd et al., 1979), thus ensuring a more accurate determination of erosion (3.6). The cavity sliding law in iSOSIA takes the form:

$$U_b = \frac{C_s {\tau_b}^3}{(1 - SLf)} \tag{3.5}$$

where C_s is a sliding coefficient set to 5e^{-3} Pa s$^{1/3}$ (Magrani et al., 2021), τ_b the locally determined basal shear stress and SLf the ice-bed contact fraction accounting for the amount of cavitation as a simple function of the calculated cavity size S divided by mean cell cavity spacing L_s.

Whilst a separate law has been developed to simulate erosion by quarrying in iSOSIA (Ugelvig et al., 2016), this study maintains the use of a simple uniform law for erosion that scales with sliding velocity as this is more readily constrained with empirical data (e.g. Cook et al. 2020) and is the most commonly used method across numeric models. The simple law simulates erosion E in a similar fashion to Equation 3.1 from the introduction, using the dimensionless constant ${K_G}^*$ and basal sliding velocity with exponent l, but also integrates the basal shear stress and local bed slope b_s which impose limits to avoid unrealistic runaway scenarios of erosion:

$$E = K_G \, \tau_b \, U_b^l \sqrt{1 + {b_s}^2} \tag{3.6}$$

A range of values for K_G and l are considered in this study, both as part of initial model calibration and for the investigation of influence on erosion rates and patterns (see next section).

* Note: In iSOSIA this parameter is actually listed as K_a but will be referred to here as K_G for the sake of continuity from the previously discussed literature.

Given the simplifications and assumptions made in the model, only temperate, warm-based ice is considered, as in similar work using iSOSIA (Liebl et al., 2021; Magrani et al., 2021). Due to the difficulties in accurately constraining the temperature and heat flux of basal ice (Cuffey & Paterson, 2010) along with the idealised climatic forcings, attempts to include cold-based ice in the model would have led to highly uncertain and inaccurate outcomes (see section 3.5.3 for further discussion).

3.3.2 Model Setup and Scenarios

An overview of the model scenarios and runs along with key parameters can be found in Table 3.3. In essence, there are four main model scenarios: steady-state LIA, steady-state LGM, interglacial (IG), and glacial period (GP).

Model domains for Otemma and Trift were prepared by first removing the present-day ice coverage through subtracting the latest calculated ice thickness dataset from an up to date surface DEM of the same year (2019); both of these datasets were acquired from Grab et al. (2021). Further editing of the proglacial area of both domains was required to remove large lakes that would otherwise manifest as extensive and unrealistically flat regions, affecting simulated ice flow and dynamics. In the case of Otemma, the ~5 km long Lac de Mauvoisin and associated hydroelectric dam were removed by digitising contours on a historic national map of Switzerland from 1955 before the dam was built (*Service topographique fédéral*, 1955). At Trift, the ~500x800 m proglacial lake occupying the overdeepened basin was removed based on bathymetric data reported in Steinemann et al. (2021).

Smaller domains at 50 m resolution were used for smaller ice extent scenarios (LIA, IG), whilst domains for larger ice extents over the LGM and GP scenarios necessitated a coarser resolution of 200 m in order to maintain model efficiency and stability. Whilst the coarser resolution somewhat diminishes the prominence of some features in the catchments, it still maintains the overall spatial heterogeneity of key landforms and is at least five times greater resolution than previous studies modelling last glacial cycle conditions in the Alps (Seguinot et al., 2018; Jouvet et al., 2023). For LGM and GP conditions at Otemma, only the Val de Bagnes was modelled to ensure model efficiency and stability, since tests showed the Otemma catchment to be sufficiently isolated from the Rhone trunk valley that it was not necessary to simulate much wider ice coverage across the landscape (see Appendix 3.7.1).

Table 3.3: Setup overview of the model runs.

	LIA	**LGM**	**Interglacial**	**Glacial Period**
Resolution (m)	50	200	50	200
Time (ka)	2	2	10	90
Sea Level Temperature (°C)	10.7 (Otemma) 8.5 (Trift)	3 (Otemma) 1 (Trift)	Variable (see fig. 3.4)	Variable (see fig. 3.4)
Erosion Law				
Steady-State	None	None	None	None
Er1	l = 0.65 K_G = 1x10^{-5}	l = 0.65 K_G = 1x10^{-5}	l = 1 K_G = 1x10^{-5}	l = 1 K_G = 1x10^{-5}
Er2	l = 1 K_G = 1x10^{-5}	l = 1 K_G = 1x10^{-5}	l = 2 K_G = 1x10^{-8}	l = 2 K_G = 1x10^{-8}
Er3	l = 2 K_G = 1x10^{-8}	l = 2 K_G = 1x10^{-8}		

Reference steady-state LIA and LGM models were achieved by adjusting the sea level temperature and running for 2 ka until the ice extent stabilised in a position that matched that of the historic Dufour map from 1864 (Federal Office of Topography swisstopo, 2024) for the LIA, or consistent with trimline elevations reported for the valley near Otemma (Kelly et al., 2004) and Trift (Wirsig et al., 2016) in the case of the LGM (see section 3.4.1). Steady-state occurred when ice extent stabilised with minimal changes in thickness and velocity under a fixed temperature without erosion enabled.

Following calibration of the K_G parameter (see section 3.4.1), these steady-state LIA and LGM models were then run for a further 1 ka using three different erosion laws where l = 0.65 (Cook et al., 2020), 1 (e.g. MacGregor et al., 2000) and 2 (Herman et al., 2015), in order to examine the impacts of using the different laws.

Models for both catchments were also run for 10 ka at 50 m resolution to simulate glacial evolution through an interglacial period akin to the Holocene. Reconstructed climate data for the Holocene from Erb et al. (2022) was used to calculate a magnitude of temperature change over time, which was then applied to the equivalent model

temperature field at 500 year intervals, ensuring a credible magnitude of temperature variability (Figure 3.4a). These models were started and spun-up in a LIA steady-state for the first 500 years to ensure stability before having the variable temperatures applied.

Glacial period models were run for 90 ka at 200 m resolution to simulate a scenario akin to the last glacial cycle (from 115 ka BP to the LGM at 25 ka BP). Reconstructed climate data from Jouvet et al. (2023) was used in the same way as the Holocene data and IG models to apply a reasonable magnitude of change over the period at 10 ka intervals (Figure 3.4b). These models were run from a steady-state at the starting temperature for 500 years before the variable temperature forcing was applied.

Detailed analyses are only performed within the catchment bounds of LIA extents, regardless of the model scenario, as these upper catchments are the region of interest in this study and the models are not appropriately set up to simulate realistic conditions further down the valley.

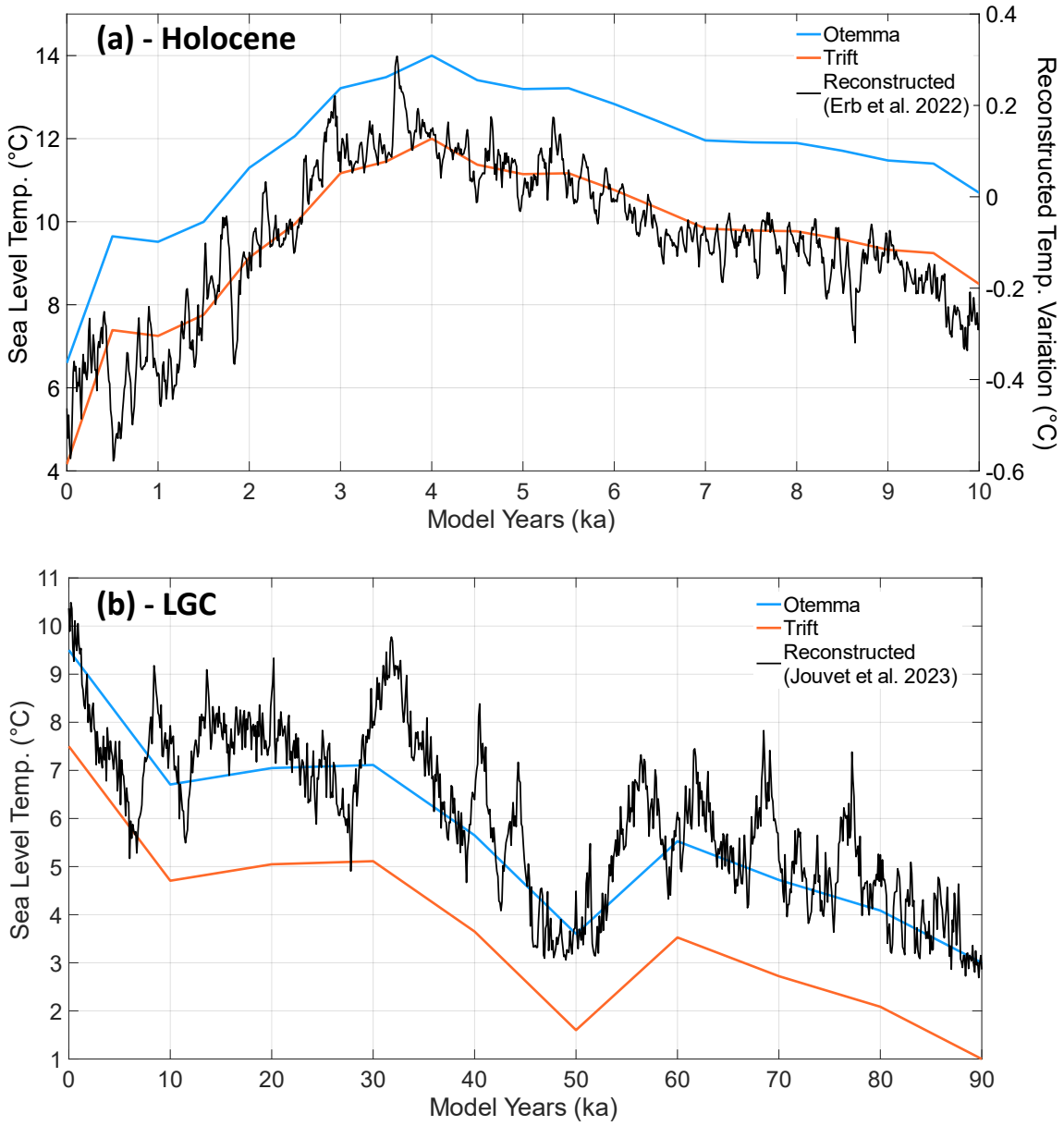

Figure 3.4: Temperature inputs used for iSOSIA models of idealised Holocene **(a)** and last glacial cycle **(b)** scenarios alongside reconstructed temperature data used to force a sensible magnitude of change. Reconstructed Holocene climate from Erb et al. (2022) **(a)** is available only as a variation from a 0 °C reference period (between 3-5 ka). Reconstructed LGC climate from Jouvet et al. (2023) **(b)** was adjusted to sea level temperature using a lapse rate of 6e-3 °C m^{-1}. Data is presented in chronology of the model runs – i.e. model start at year 0 is the oldest time in the reconstructed climate, running forward to the finishing state (25 ka BP for LGM, or the LIA for Holocene).

3.4 Results

3.4.1 Steady State Models

Following sensitivity tests to find the appropriate fixed temperature, in which sea level temperature was systematically varied across multiple model runs of 2 ka in length to examine ice extent responses, steady state LIA and LGM models for both catchments were achieved. For LIA models, a fixed sea level temperature of 10.7 °C for Otemma and 8.5 °C for Trift produced ice extents that closely matched that of the historical Dufour map of 1864 (Federal Office of Topography swisstopo, 2024) (Figure 3.5). At Otemma, an elevation point at the Col de Charmotane on the Dufour map reads 3084 m, whilst the modelled elevation is 3066 m for the same position, suggesting an appropriate ice thickness has been achieved. Similarly, at Trift an elevation point on the Dufour map near the riegel is 1956 m and another at the base of the icefall is 2058 m, whilst in the model it is 1925 m and 2045 m respectively. Modelled ELAs for the LIA were 2997 m for Otemma and 2631 m for Trift, which is consistent with previously reported estimates for LIA ELAs in the Swiss Alps (Greene et al., 1999; Joerin et al., 2008; Žebre et al., 2021).

To check that the model was producing sensible rates of ice velocity despite other assumptions and simplicities (e.g. precipitation and temperature), the modelled surface velocity was compared to remotely-sensed measurements of present-day surface velocity from Millan et al. (2022). At Otemma, the mean present-day velocity is 6.5 m a^{-1}, whilst the mean modelled surface velocity is 4.1 m a^{-1} in a steady state at present-day extent and 8.6 m a^{-1} at LIA extent. At Trift, measured present-day mean velocity is 11.3 m a^{-1} and modelled at 6.5 m a^{-1} in steady-state present-day and 15.4 m a^{-1} at LIA. Overall, this suggests the model and sliding law is producing appropriate ice velocity, given that the present-day glaciers are not in a steady state.

For LGM extents, steady sea level temperatures of 3 °C for Otemma and 1 °C for Trift were used to build up sufficient ice thicknesses, with an ice surface elevation that correlates well to observed trimline elevations for each valley (Figure 3.6). The LGM ELA was 1714 m at Otemma and 1381 m at Trift, consistent with a depression of 1000-1500 m relative to the LIA (Ivy-Ochs, 2015).

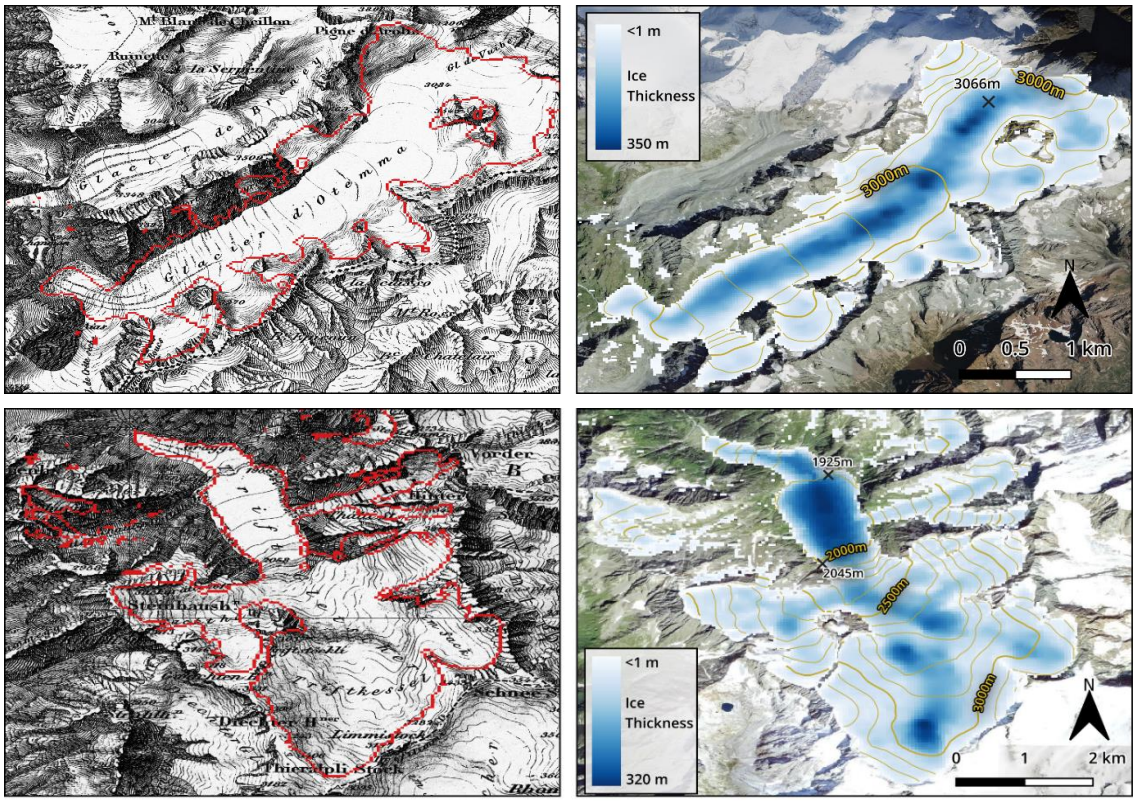

Figure 3.5: Steady state LIA models for Otemma **(top)** and Trift **(bottom)** with contours at 100 m intervals **(right)**, compared with the Dufour map of 1864 **(left)**, which records the approximate LIA extents of glaciers for the Swiss Alps (Federal Office of Topography swisstopo, 2024). Modelled ice margin is overlaid as red on the historical map for reference. Elevation points on the historic map agree well with modelled elevations, suggesting appropriate ice thicknesses have been achieved – see text for details.

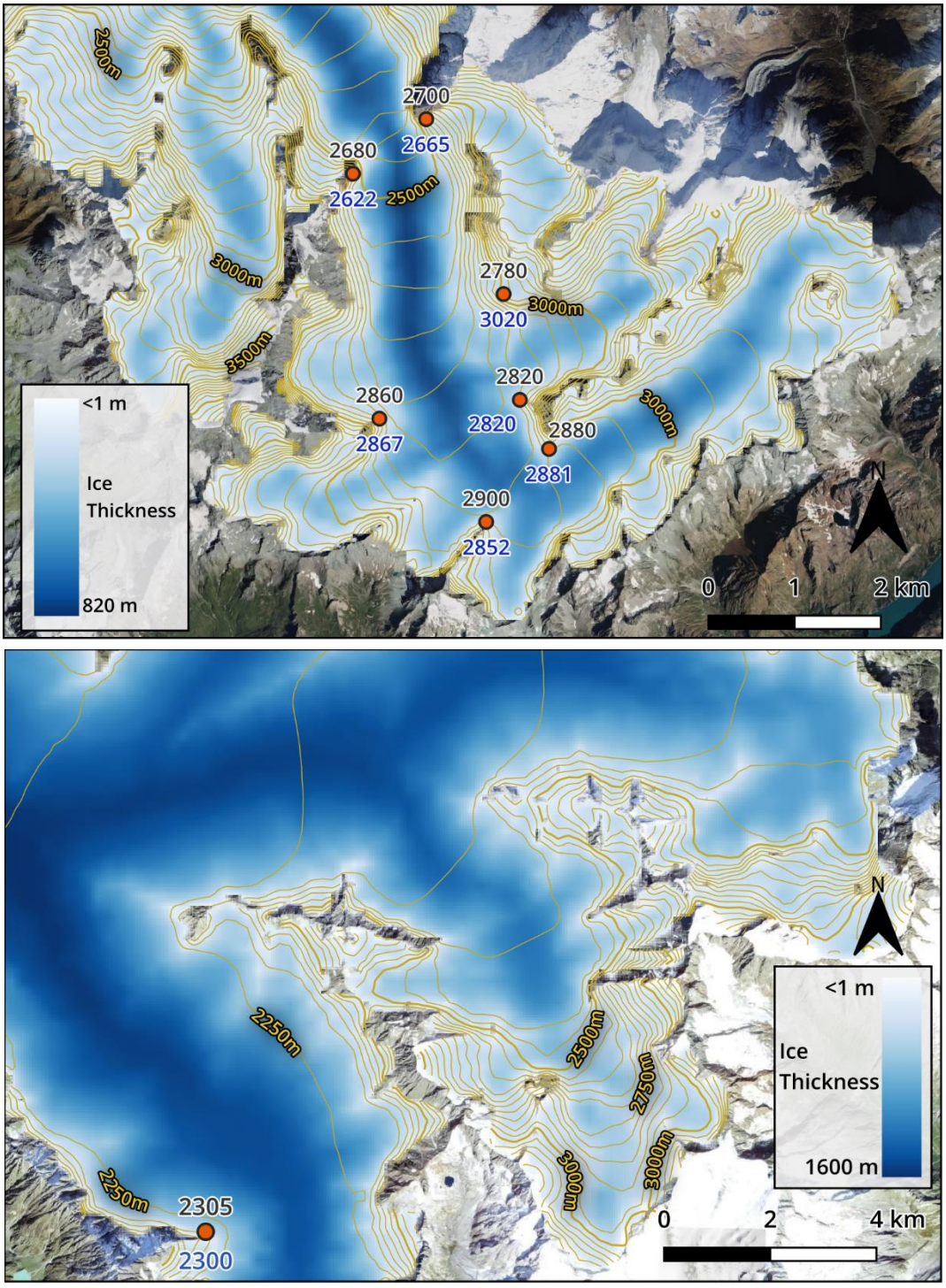

Figure 3.6: Steady state LGM models for Otemma **(top)** and Trift **(bottom)**, with contours at 50 m intervals. Elevations of observed trimlines are displayed above each orange point, with the modelled ice surface elevation shown below the point in blue. The multiple trimline elevations for the Val de Bagnes (Otemma) are from Kelly et al. (2004). At Trift only a single trimline reported by Wirsig et al. (2016) is within the model domain, as the rest of the Aare valley where more positions are recorded was not modelled for the sake of computational efficiency.

Water flux through the subglacial hydrological system in the models show a clear formation of channel networks in the ablation zone (Figure 3.7a, c). Minimal hydrological activity is present above the ELA in the accumulation zone due to lack of meltwater input, this being particularly prevalent in the LGM models where the entire upper catchment region is > 1 km higher than the ELA and thus experiencing very cold surface temperatures year-round (Figure 3.7b).

As expected, the hydrology has an important influence on sliding velocities, particularly on the flatter profile of Otemma, with higher sliding rates found in the ablation zone of the LIA extent (Figure 3.8a). Topography clearly enacts a strong control, however, with the steeper steps coming off cirques locally enhancing sliding rates, as well as the constriction of the narrow gorge at the end of the Otemma valley. Under LGM extents the sliding at Otemma is uniformly low across the upper catchment due to the homogenous gradient imposed by very thick ice (Figure 3.8b). Actual sliding rates at LGM are not dissimilar to that of LIA conditions though, despite the lack of hydrological input, suggesting the driving stresses of the thicker ice are sufficient to maintain such velocity.

At Trift, topography appears to be the primary control on velocity patterns, with the steep gradient of the icefall locally doubling or tripling sliding rates, whilst flow is greatly reduced in the basin below as it becomes impeded by the riegel wall (Figure 3.8c). Under LGM at Trift, the highest sliding rates are found in the higher reaches of the catchment, shifting up from the icefall region (Figure 3.8d), likely as this area maintains a steep gradient whilst the rest of the catchment and wider Aare valley become filled with vast ice thicknesses that smooth and reduce the surface gradient, as can be seen in the contours of Figure 3.6.

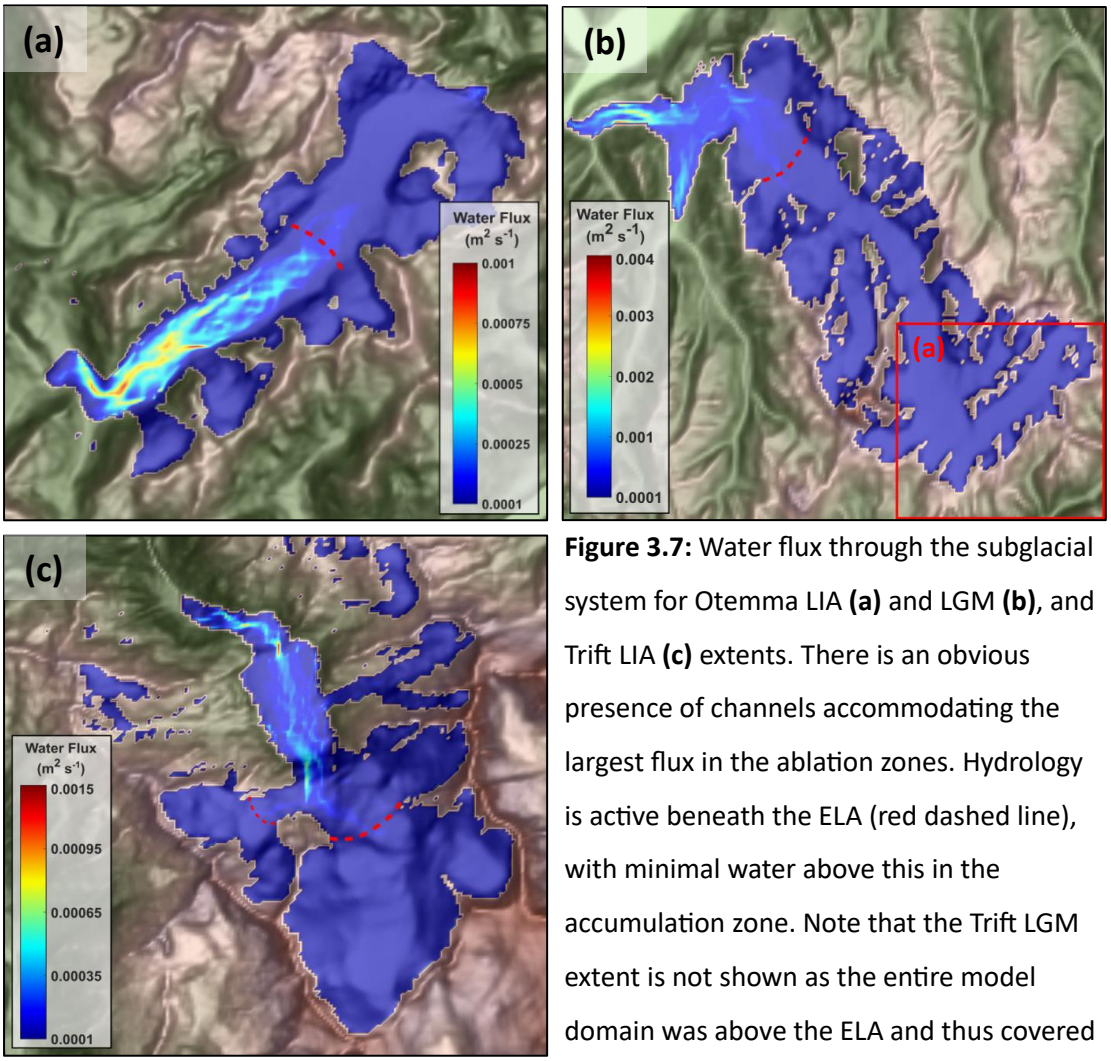

Figure 3.7: Water flux through the subglacial system for Otemma LIA **(a)** and LGM **(b)**, and Trift LIA **(c)** extents. There is an obvious presence of channels accommodating the largest flux in the ablation zones. Hydrology is active beneath the ELA (red dashed line), with minimal water above this in the accumulation zone. Note that the Trift LGM extent is not shown as the entire model domain was above the ELA and thus covered by minimal water flux.

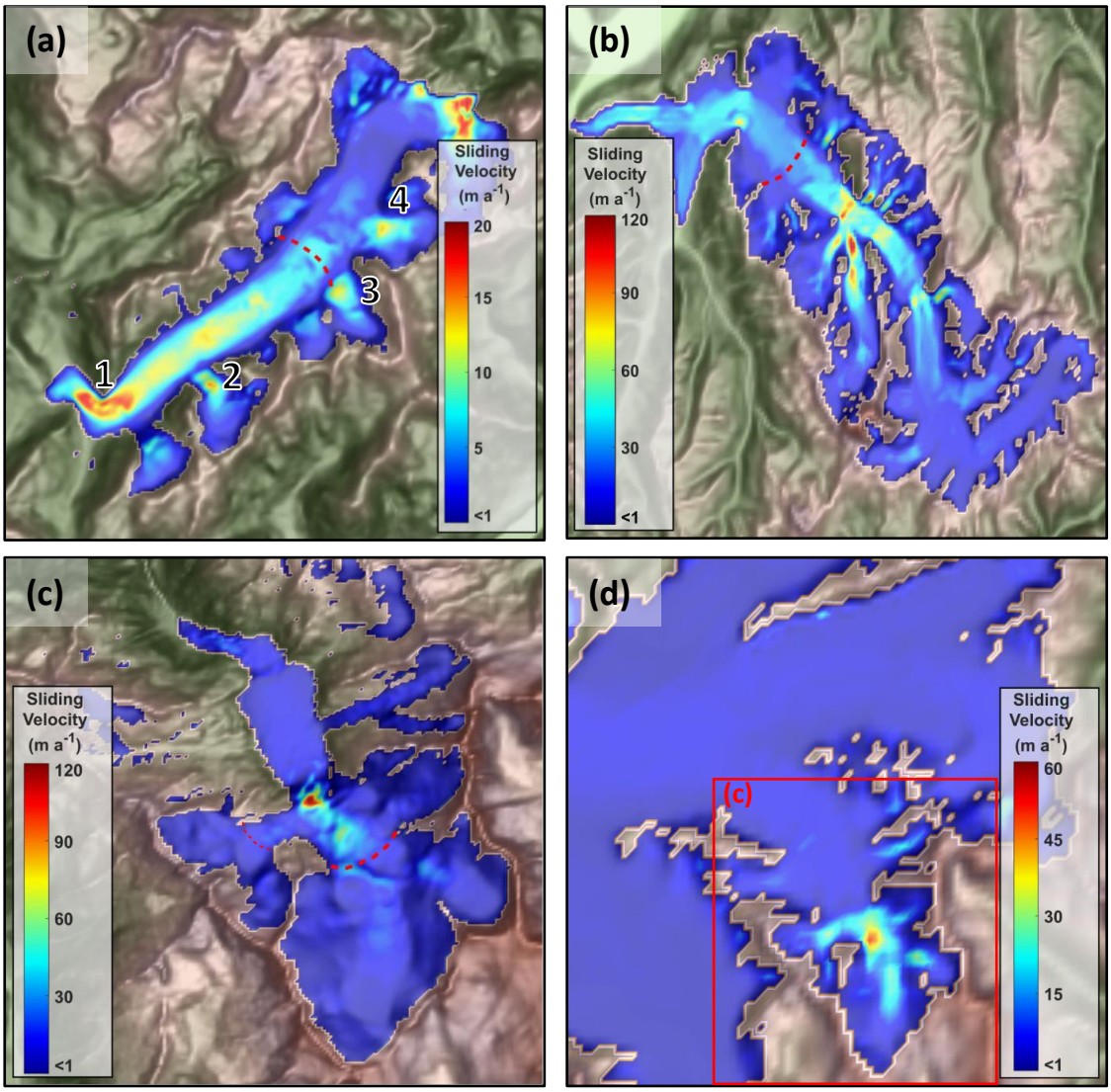

Figure 3.8: Sliding velocities for LIA and LGM extents at both catchments, with ELA shown by red dashed line. Sliding is enhanced in the ablation region of Otemma LIA **(a)** likely due to the influence of hydrology, with some localised hotspots due to topography such as the constriction at the valley mouth (1) and small icefalls (2-4). Note the high velocity at the top right is anomalous due to the proximity of a large topographic step and the edge of the catchment mask where ice is set to rapidly ablate, this region is excluded from the analyses. At LGM extent velocities are low across the Otemma catchment **(b)**, rates lower down the valley (centre to top left of figure) are ignored as LGM ice is not modelled appropriately here. At Trift the topography imposes more control than hydrology with the presence of the icefall dominating velocity, reaching a maximum of 120 m a^{-1} at LIA extent **(c)**. Under LGM conditions the highest velocity at Trift is shifted further uphill from the icefall region **(d)**.

In an effort to find an appropriate value of K_G mean modelled sliding velocities (x) were used to determine the average erosion rate (y) that would be expected according to the statistical relationships from Cook et al. (2020) for l = 0.65 ($y = 0.1665x^{0.65}$) and l = 1 ($y = 0.1x^{1}$) and Herman et al. (2015) for l = 2 ($y = 2.7 \times 10^{-7}x^{2}$). Multiple model runs at steady state were then conducted over a range of K_G values to find the one that produced erosion rates closest to the statistically derived amount (Figure 3.9). These best matching values of K_G under each instance of l were then taken to be used for all future model runs. It was noteworthy that the best fitting K_G values were an order of magnitude lower than reported for the statistical fit by Cook et al. (2020) (1e-4) and Herman et al. (2015) (2.7e-7).

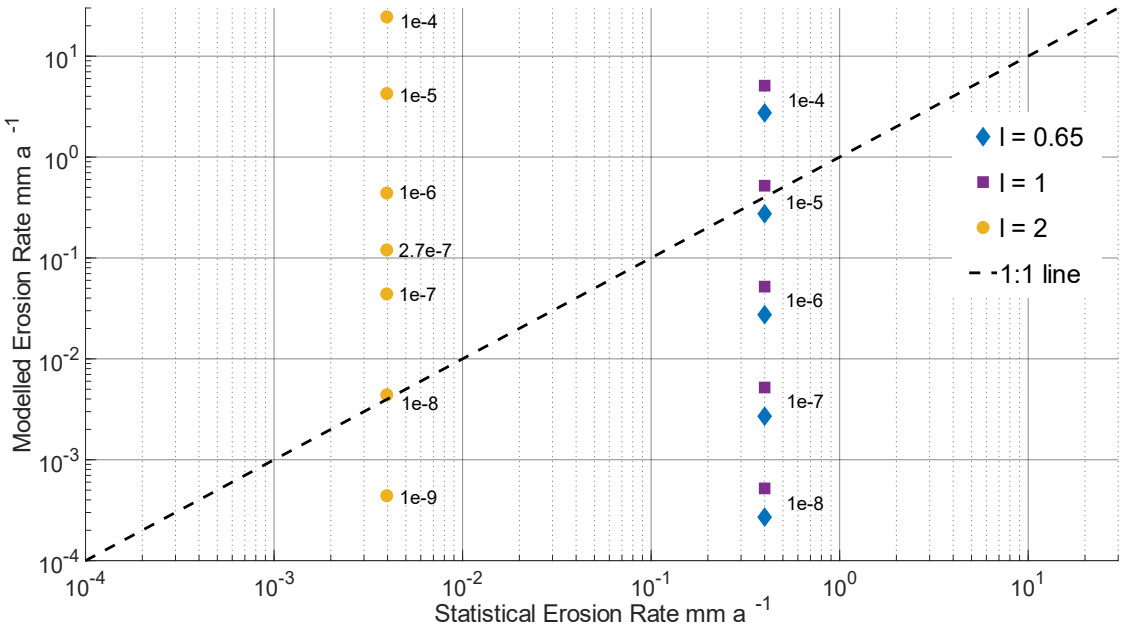

Figure 3.9: Calibration of the K_G parameter by comparing modelled erosion rates with statistically derived rates from Cook et al. (2020) for l = 0.65 and 1, and Herman et al. (2015) for l = 2. Values closest to the 1:1 line where statistical and modelled rates are equal were then taken forward for all future model runs. Note K_G values expressed here as erosion in m a^{-1} as is standard in the literature.

3.4.2 Comparing Erosion Law Outputs Under Steady State

In the first tests, the three different erosion laws were applied under steady state LIA and LGM conditions to assess their impact. The differences in magnitude and spatial distribution of erosion across both catchments are examined here in turn, where a notable influence of the underlying bed topography and key landforms can be seen.

At Otemma LIA, the influence of the chosen erosion law in the scaling of erosion rates with sliding velocities is immediately apparent (Figure 3.10a). The simple law where l = 1 scales linearly with increasing rates of erosion at higher sliding velocities, yielding an overall mean catchment erosion rate of 0.52 mm a^{-1}, whilst the global law from Cook et al. (2020) where l = 0.65 shows a much slower, sub-linear increase in erosion according to sliding, giving a mean erosion rate of 0.27 mm a^{-1}. The highly non-linear law where l = 2 scales very slowly at low sliding rates and rapidly increases erosion as sliding increases. Erosion rates from this latter law are two orders of magnitude lower than the other laws, a consequence of the necessarily smaller K_G value when l = 2 is used but also due to the effect of this non-linearity, in that Otemma overall is experiencing relatively low sliding rates and hence results in very low erosion, with an overall mean rate of 0.004 mm a^{-1}.

Plotting erosion according to the surface elevation of the ice allows the spatial distribution to be examined in a linear up-catchment manner. Under LIA conditions at Otemma, a multi-modal pattern is present as a result of the impact of local topographic features (Figure 3.10b). Major landforms such as the narrow gorge at the valley mouth and small icefalls flowing out of cirques cause local enhancement in sliding and thus erosion (Figure 3.10e). Similarly, a small hotspot of erosion occurs at ~3300 m elevation due to the steep slopes descending off the Pigne d'Arolla summit. Smaller peaks in erosion such as between 2600 and 2800 m correlate with regions of increased velocity in the valley centre profile likely due to hydrological forcings (see Figure 3.7, Figure 3.8a). It is noteworthy that there is no significant increase in erosion at the position of the ELA, outside of heightened rates from nearby landforms. Moreover, a general trend of decreasing erosion rate with elevation is present, with a clear difference in frequency distribution of rates between accumulation and ablation zones (see Appendix 3.7.2). Spatially, the different erosion laws are not dissimilar in where the erosion is being focused, rather they serve to alter the intensity of that erosion.

Under LGM conditions at Otemma, sliding and erosion maintain similar rates to that of the LIA extent (Figure 3.10c), giving a mean erosion rate of 0.2, 0.44 and 0.004 mm a^{-1} for

l = 0.65, 1 and 2, respectively. The distribution of erosion across elevation is changed greatly under LGM conditions though, with the multi-modal influence of smaller topographic features now largely quashed by large ice thicknesses which reduce the surface slope (Figure 3.10d, e). The main peak persists at the valley constriction where the ice takes an almost 90° turn to flow northwards down the Val de Bagnes (see Figure 3.6) and smaller hotspots of erosion occur still in the upper catchment around steeper terrain.

At Trift, the same scaling relationship of erosion rates with sliding across the three laws is of course present, though the much higher sliding rates from the icefall result in a small number of cells experiencing very high rates of erosion up to 50 mm a^{-1} for the linear law under LIA (Figure 3.11a). The impact of higher velocities on the non-linear l = 2 law is also apparent, with erosion rates now only one order of magnitude lower than the other laws, as opposed to the two orders of magnitude at Otemma. Overall, mean erosion rates for Trift at LIA state are 1.15, 1.55 and 0.09 mm a^{-1} for l = 0.65, 1 & 2, respectively.

The highest erosion rates at Trift are situated on the upper half of the large icefall, with a few other peaks in erosion occurring at smaller topographic steps in the upper basin slightly below and above the ELA (Figure 3.11b, e). The ELA yet again does not enact any significant effect on erosion rates beyond the influences of local topography. In the lower half of the catchment, an interesting point is a small uptick in erosion on the top of the riegel, diminishing again as the ice moves over it, before increasing once more in the lower tongue region where a narrow gorge causes valley and ice constriction.

The response of Trift to LGM state differs to Otemma in that the range of sliding and erosion rates more than halves from that of the LIA (Figure 3.11c), with overall mean erosion rates of 0.24, 0.59 and 0.01 mm a^{-1} for l = 0.65, 1 & 2, respectively. The distribution across the catchment shows the suppression of erosion across all elevations (Figure 3.11d), with sporadic areas of higher rates corresponding to regions above the icefall (now situated at ~2400 m) where ice thickness is similar to LIA state and hence steeper gradients are maintained, permitting faster sliding (Figure 3.11e). There is another small peak in rates beyond the riegel, as with the LIA extent, at the valley constriction/gorge.

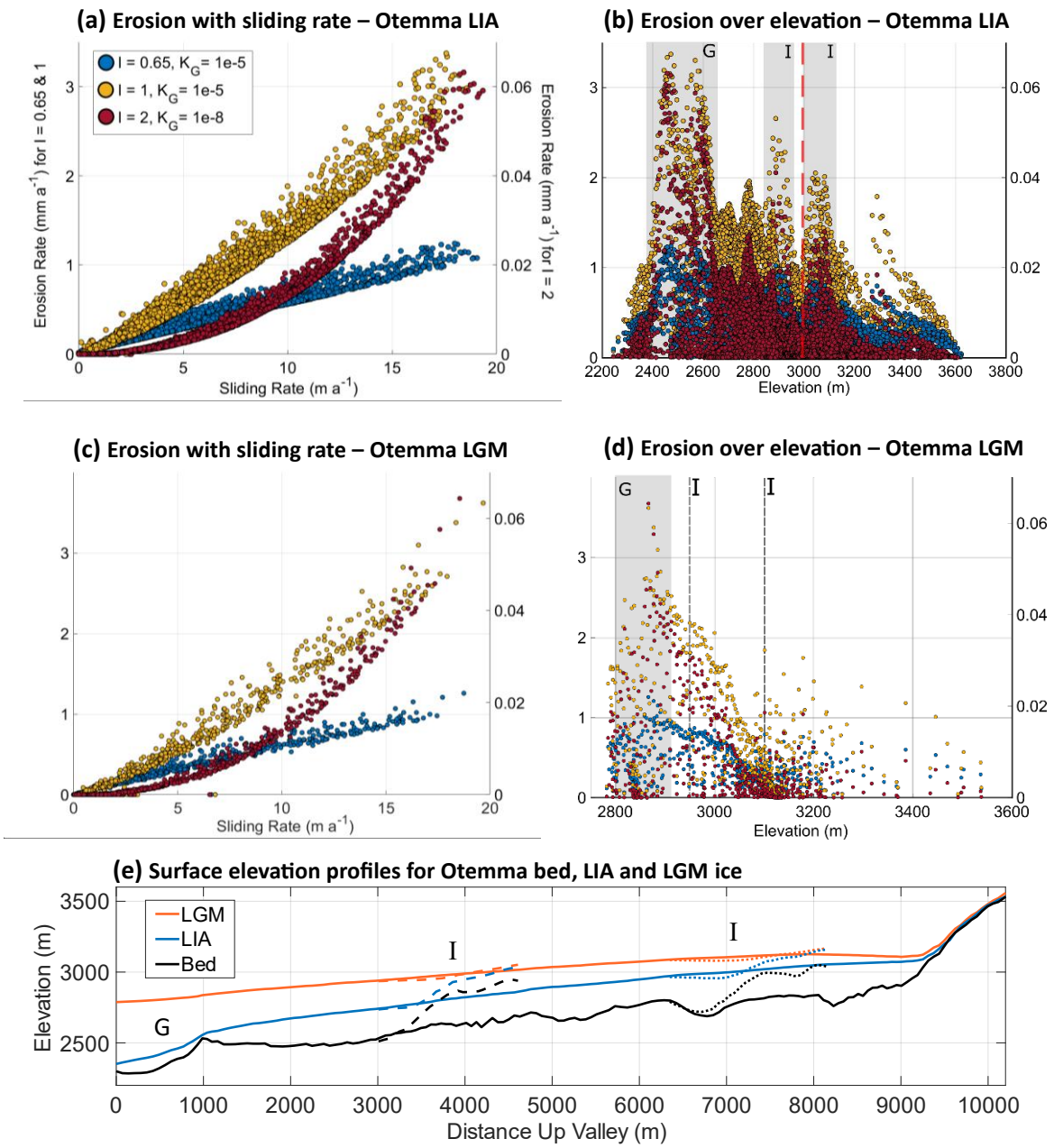

Figure 3.10: Erosion rates for Otemma from the three tested erosion laws according to sliding rate and ice surface elevation for LIA (**a, b**) and LGM (**c, d**) conditions along with surface topographic long-profile of the main valley (solid lines) and two tributary cirques (dashed lines) at bed, LIA and LGM ice elevations **(e)**. Each point corresponds to one model cell (50x50 m for LIA, 200x200 m for LGM). Note that rates for l = 2 (red dots) correspond to the right-hand y axis across all plots. Rates of sliding and erosion are similar across both scenarios, but erosion distribution according to elevation differs significantly, with multi-modal peaks in erosion under LIA conditions corresponding to topographic forcing from the gorge constriction (G) and small icefalls (I). Position of the ELA for the LIA is shown by the red dashed line.

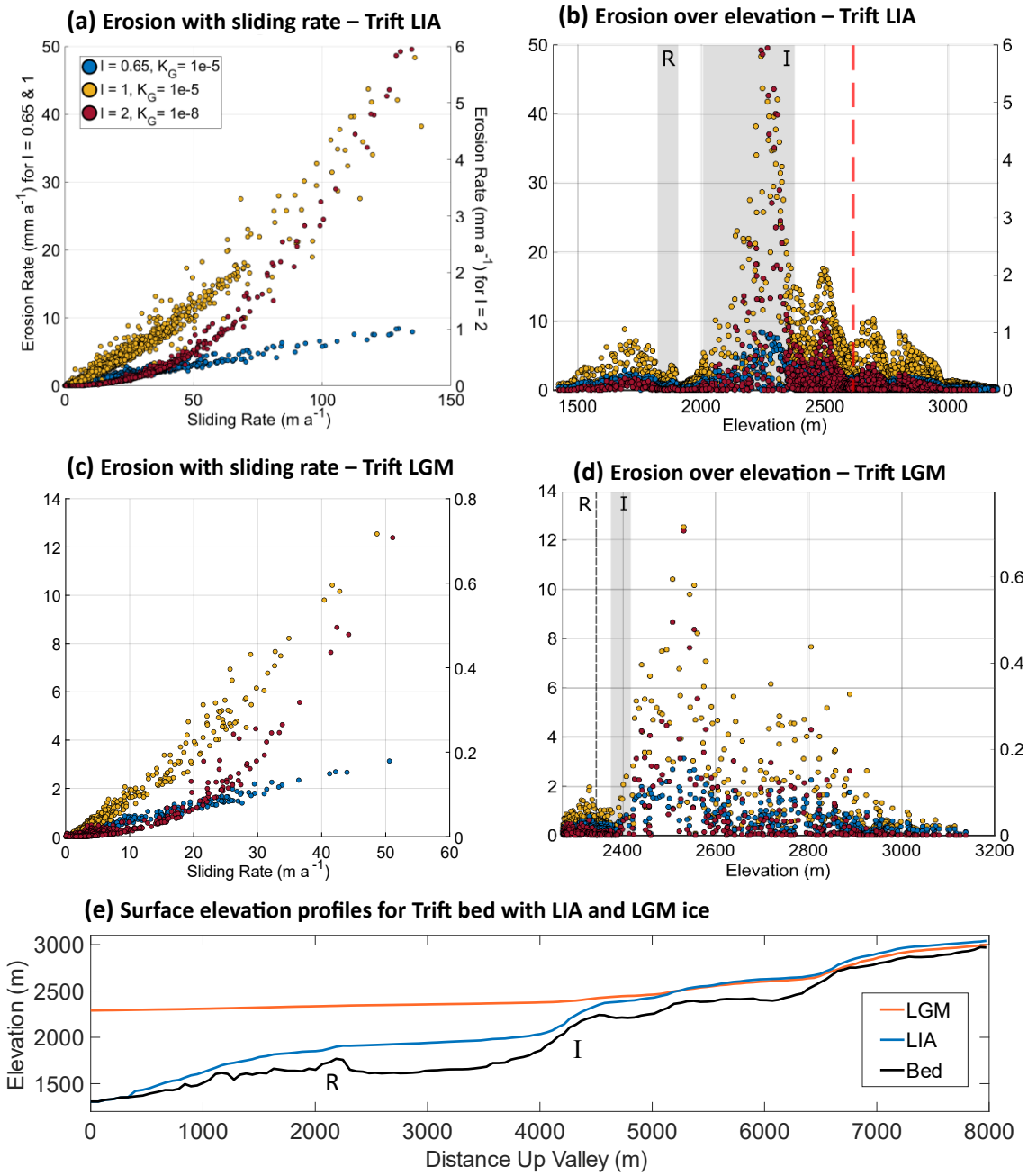

Figure 3.11: Erosion rates for Trift across the three different erosion laws according to sliding rate and ice surface elevation for LIA (**a, b**) and LGM (**c, d**) conditions along with topographic long-profile for the bed, LIA and LGM surfaces **(e)**. Both sliding and erosion rates see a significant decrease under LGM conditions. Erosion at LIA is focused on the large icefall (I) and a small uptick is present on the upstream side of the riegel (R). Position of the ELA is shown by the red dashed line.

3.4.3 Erosion Under Variable Climates

The previous section showed how the use of different erosion laws impacts the magnitude and spatial distribution of erosion across the catchment. It also showed marked differences in these two aspects according to the glacier size under a steady state LIA or LGM condition. Steady-state conditions are not realistic in the long-term though, so this section will explore how time-varying climates impact patterns of erosion.

Runs were conducted for both the linear (l = 1) and non-linear (l = 2) laws over variable interglacial (IG) and glacial period (GP) scenarios. However, model instabilities experienced during the GP scenarios for the linear law caused these runs to fail approximately half-way through, limiting the available data presented for this particular scenario. The non-linear law was unaffected, running to completion, as were both modelled erosion law formulations under IG conditions.

Changes in ice volume under the IG scenarios closely follow changes in temperature forcing, though Trift both loses ice volume at a slower rate than Otemma and gains it back faster due to its larger, steeper accumulation area (Figure 3.12a). Both catchments reach a minimum of little-to-no ice volume at 3.5 ka into the run when temperatures reach maximum (analogous to the Holocene Climate Optimum – e.g. Bohleber et al., 2020).

In GP conditions, both catchments begin to steadily increase in ice volume as temperatures fall over the first 10 ka before stabilising. From here, Otemma maintains a stable volume despite further changes in temperature, whilst Trift sees a dramatic and rapid increase of ice between 35 and 40 ka as temperature drops, before stabilising and maintaining a steady volume through later temperature changes towards LGM (Figure 3.12b). The stark contrast between the two glaciers can be explained by the different topographic situation of the catchments. Since Otemma is a narrow, shallow-graded glacier at the head of a long valley fed by multiple other ice masses, it reaches maximum ice thickness and equilibrium state quite quickly. Further, its position approximately 40 km away from the main Rhone trunk valley isolates it from fluctuations in ice volume that are driven by outputs from adjacent catchments over this time period (e.g. Appendix 3.7.1). In contrast, the wider and steeper Trift catchment accommodates more ice volume and is located just 3 km from the tributary Gadmertal valley and 10 km from the main Aare trunk valley, both of which were major ice arteries fed by very active adjacent catchments. Consequently, sudden increases in ice volume from climate cooling is able to rapidly

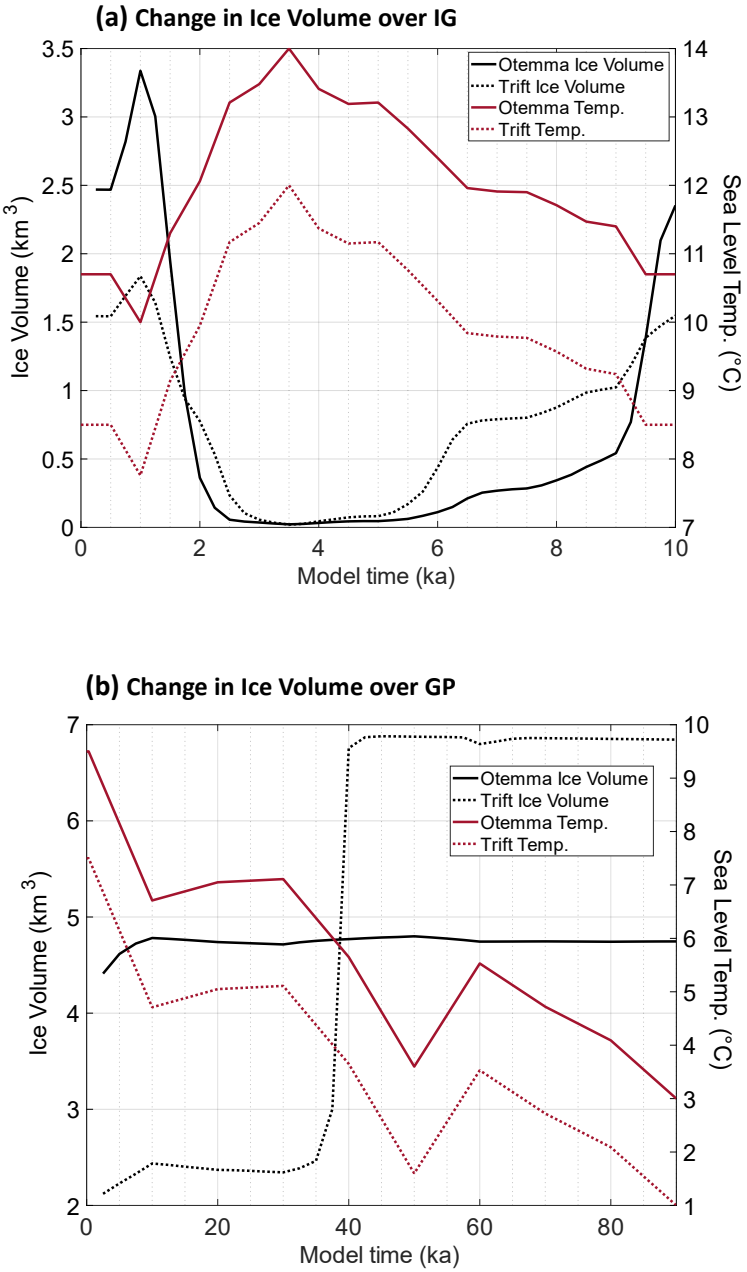

Figure 3.12: Time series evolution of modelled ice volume according to changes in temperature for both Otemma and Trift under interglacial (IG) **(a)** and glacial period (GP) **(b)** scenarios. Ice volume changes in concordance with temperature in IG conditions, but GP conditions show a significantly different behaviour between the catchments with Otemma remaining relatively steady and Trift undergoing a dramatic change during the first major cooling event.

inundate Trift as it links with the Gadmertal tributary and main Aare glacier (e.g. Jouvet et al., 2023) (see Figure 3.6 to contrast ice volume/extent of Otemma and Trift at LGM state).

Examining the distribution of total cumulative erosion over the same LIA and LGM ice surface elevations as previously plotted in the steady state runs (i.e. Figure 3.10, Figure 3.11) allows direct comparisons of changes in the erosion pattern brought about by variable climate and ice dynamics.

Under IG conditions at Otemma, high erosion is still present at the site of the gorge as per the steady-state LIA scenario, but this is now matched, or even exceeded in the case of the linear law, by erosion occurring at the higher elevation icefall and summit regions (Figure 3.13a). This is a direct consequence of the changing climate conditions altering the distribution of erosion across the catchment due to time-varying ice extent and erosional efficacy, which can be seen in changes of catchment-averaged erosion rate and terminus elevation through time in Figure 3.13b. Tracking the terminus elevation shows the gorge region is only covered by ice for the first ~1.5 and final 0.5 ka when erosion rates are highest, whilst features further up the profile experience much longer ice residency, enabling similar total erosion despite otherwise diminished erosion rates under reduced ice volumes (Figure 3.13b).

Over GP conditions at Otemma, the main locus of erosion is at the gorge region in the narrow valley mouth and decreases at higher elevations beside some localised increases around steeper terrain (Figure 3.13c). This response is very similar to the LGM steady-state, as Otemma very quickly establishes LGM-equivalent ice flux early on in the run (Figure 3.12b), resulting in marginal changes to both ice volume and erosion rates thereafter (Figure 3.13d).

At Trift, distribution of total erosion over the IG scenario closely mimics that of the steady state LIA scenario, with highest rates at the icefall region, though as with Otemma there has been an increase in magnitudes of the higher elevation features due to longer ice residency (Figure 3.14a). The redistribution of erosion over elevation is not as pronounced at Trift, however, as the steeper catchment results in a slower rate of ice loss with elevation under a warming climate and thus a slower decline in erosion rates, allowing the lower elevation regions to receive longer and more substantial erosion than the comparative situation at Otemma (Figure 3.14b). Moreover, Trift experiences greater ice loss and thinning at the high elevations during the warm interval, including a 500-year period of complete deglaciation, resulting in a 3 ka hiatus in erosion when the terminus elevation is above 2800 m.

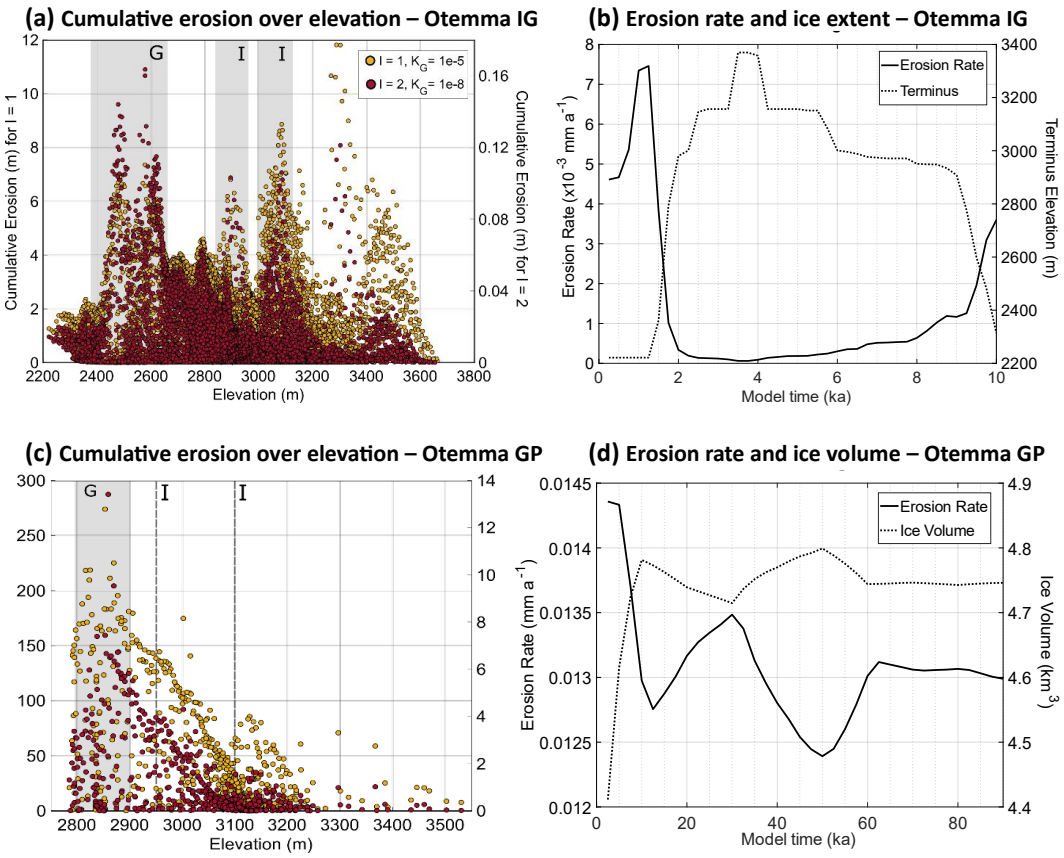

Figure 3.13: Total cumulative erosion over ice surface elevation for Otemma interglacial with key catchment features of the gorge (G) and icefalls (I) in shaded regions **(a)**, with timeseries changes in mean erosion rate (for l = 2) that correlates with elevation of glacier terminus **(b)**. Equivalent cumulative erosion for the glacial period **(c)** (note total erosion for l = 1 is only as of final model output at 40 ka). Mean catchment erosion rate under the glacial period has an inverse relationship with ice volume **(d)**.

The distribution of erosion over the GP scenario for Trift differs greatly from the steady-state LGM and Otemma responses. In contrast to the steady-state LGM, total erosion at the icefall and lowermost portion of the profile beyond the riegel equals the depth of material removed from the upper region of the catchment above the icefall (Figure 3.14c). This is due to the initial lower ice volumes and high erosion rates in the first 35 ka of the period enabling rapid sliding and excavation of these lower elevations at the icefall and valley constriction, as ice can flow freely and unrestricted into the main Gadmertal valley below. The sudden change of states towards 40 ka when large temperature decreases result in a rapid three-fold increase in ice volume causes an equally drastic reduction in mean erosion rates (Figure 3.14d). This occurs as ice pools in the lower valley, joining with the LGM trunk glaciers and consequently sliding velocity is greatly diminished as the influence of underlying topography is muted by very thick ice. A switch in erosion distribution then occurs as higher velocities can still be maintained on the thinner and steeper slopes of the upper catchment above the icefall (e.g. Figure 3.6, Figure 3.11e). In essence, the locus and magnitude of erosion switches between the lower and upper regions of the catchment for the first and second half of the simulation respectively at Trift, which is a substantially different response to that of Otemma and demonstrates the significance of both catchment hypsometry and position within the wider drainage basin.

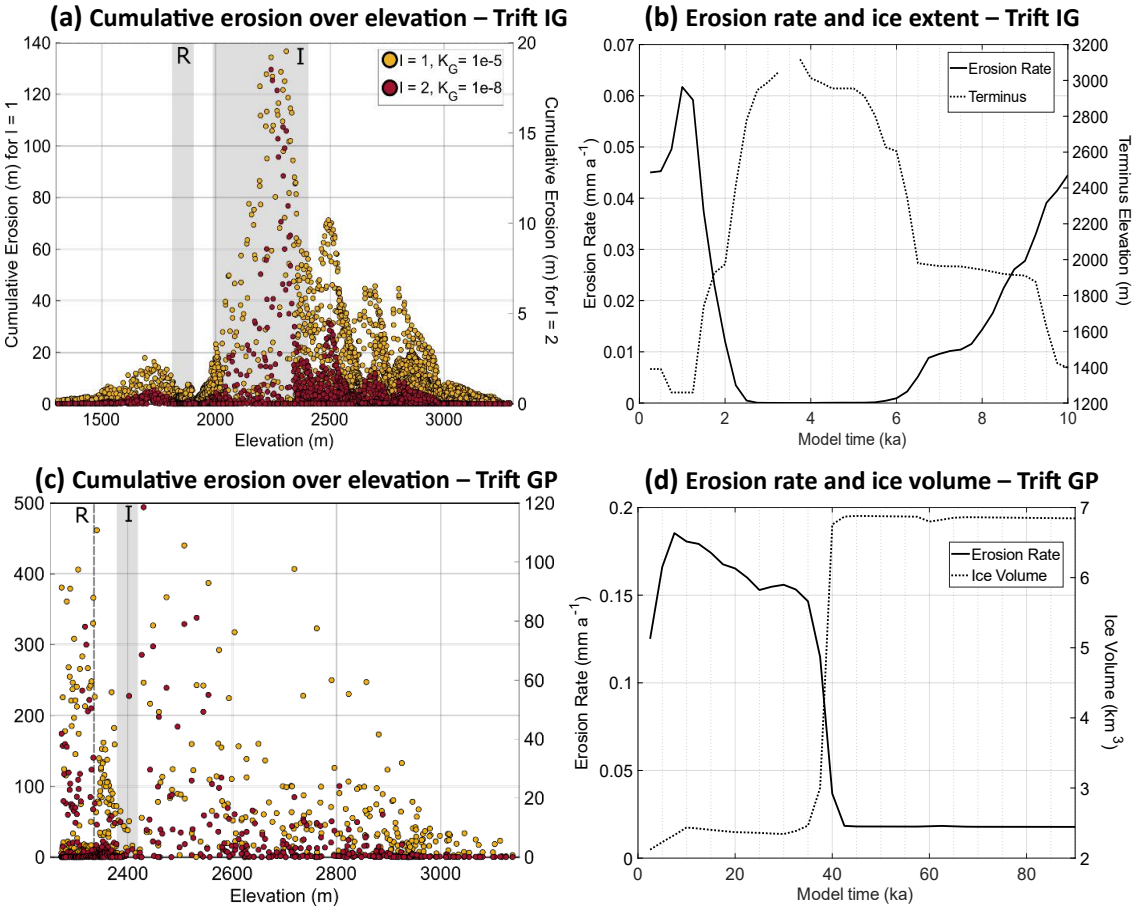

Figure 3.14: Total cumulative erosion over ice surface elevation for Trift interglacial with key catchment features of the riegel (R) and icefall (I) in shaded regions **(a)**. Timeseries evolution of mean erosion rate (for l = 2) along with change in glacier terminus elevation showing a long period of very little ice and erosion **(b)**. Equivalent outputs of cumulative erosion under glacial period scenario **(c)** along with substantial changes in erosion rate and ice volume **(d)**.

3.4.4 Erosion at Key Landforms

In the previous section (3.4.3) there was a clear trend of decreasing mean erosion rates in line with reduced ice extent under IG conditions and relatively stable or decreasing rates with larger ice volumes under GP conditions. The cumulative erosion over elevation also gave an indication of a strong spatial component to this variable behaviour, particularly at Trift. In order to explore these themes further, erosion rates and bed profile evolution were extracted from three key landforms at low, mid and high elevations at each catchment (Figure 3.15).

At Otemma these key features are the valley constriction and gorge at the valley mouth (Figure 3.15a), a small icefall step from one of the raised branch cirques (Figure 3.15b) and the steep sidewall leading up to the Pigne d'Arolla summit region at the top of the catchment (Figure 3.15c).

At Trift the key features are the riegel and valley constriction with a gorge at the end of the catchment (Figure 3.15d), the large icefall at the mid-central region (Figure 3.15e) and the large cirque at the catchment head (Figure 3.15f).

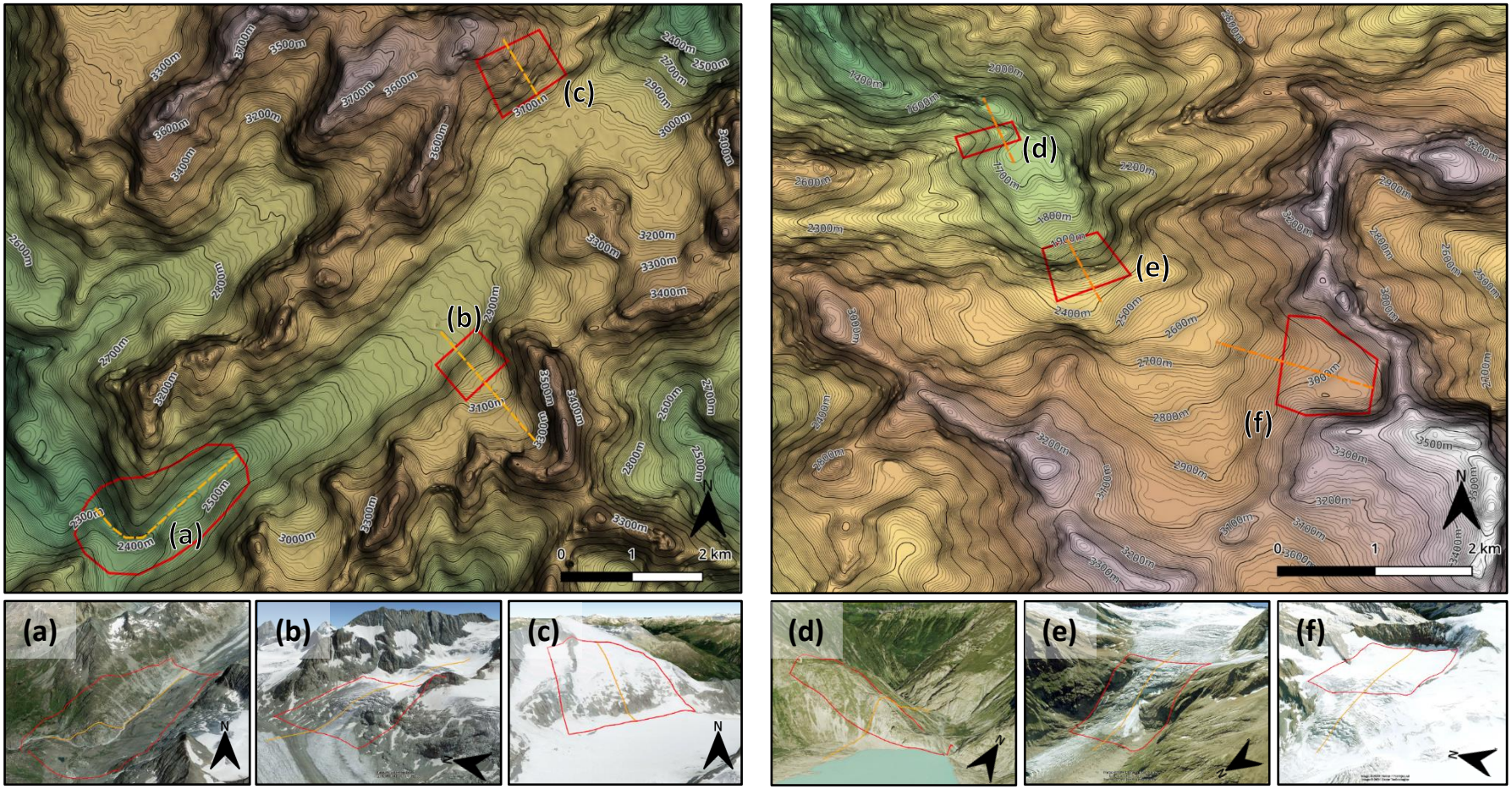

Figure 3.15: Overview of key landforms at each catchment for erosion rate (red box) and profile (orange line) analyses. At Otemma: the valley constriction and gorge **(a)**, small tributary icefall **(b)** and steep summit slope **(c)**. At Trift: riegel and valley constriction **(d)**, large icefall **(e)** and cirque **(f)**. Overview maps show bed elevation with 10 m contour intervals.

3.4.4.1 Changes in Erosion Rates

The change in mean erosion rates for the non-linear law (l = 2) from these specific regions under IG and GP scenarios are presented in Figure 3.16.

At Otemma the effects of deglaciation under warming conditions during the IG are immediately apparent with the gorge losing all glacial erosion approximately 1 ka before the icefall, whilst the summit region persists throughout the run, albeit at much diminished rates (Figure 3.16a). The higher elevation of the icefall allowed erosion to occur here for approximately 67% of the simulation, compared to just 20% for the gorge, enabling the near equal cumulative denudation seen earlier in Figure 3.13a, despite nearly an order of magnitude lower erosion rates. Across the GP run changes are negligible with generally stable erosion rates due to the minimal adjustments in ice flux over the whole period (Figure 3.16b).

At Trift, the IG scenario once again shows the impact of cyclical ice extent, this time with the mid-elevation icefall receiving both far greater erosion rates *and* ice residency than the lower riegel region (Figure 3.16c), enabling the dominant erosion patterns present in the earlier elevation plot (Figure 3.14a). The cirque region at Trift experiences its highest rates of erosion during periods of greater ice extent at the start and end of the run but drops down to effectively nothing ($< 10^{-5}$ mm a^{-1}) during the warmest times of almost total deglaciation.

During the GP cycle the cirque at Trift mimics features at Otemma in that it maintains a steady, low rate throughout the entire run, as it is isolated from the significant changes in ice dynamics further down the catchment (Figure 3.16d). The riegel and icefall begin the GP cycle with high rates of erosion, though the icefall drops significantly through time as ice begins to build up and pool in the overdeepened basin below, continuously lowering the surface slope over the icefall and suppressing sliding velocity. Towards 40 ka when the ice volume increases dramatically, a similarly dramatic decrease in erosion occurs for both features, with rates that fall below that of the cirque for the remainder of the run as ice volume stabilises.

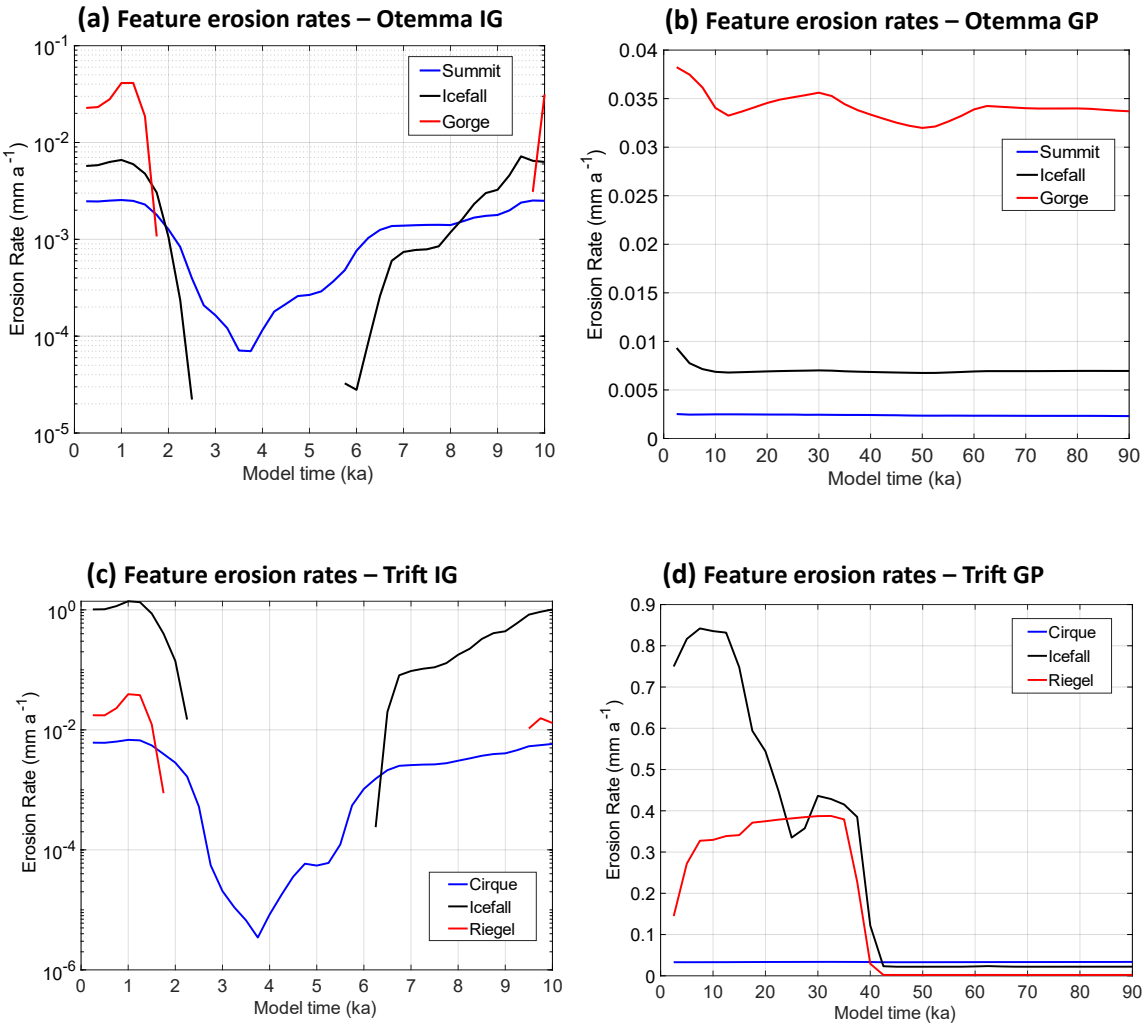

Figure 3.16: Timeseries evolution of erosion rates of the non-linear law (l = 2) for key landform features at Otemma over IG **(a)** and GP scenarios **(b)** and similarly for Trift during IG **(c)** and GP **(d)**. The effects of deglaciation in disrupting erosion of lower elevation features are clear in the IG scenarios, while under GP changes in ice volume are very prevalent.

3.4.4.2 Spatio-temporal Evolution of Topographic Profiles

The effect of these time-varying changes in erosion over different climate conditions on the evolution of the landscape itself can be seen by examining changes in the bed topography of the example features, starting with Otemma (Figure 3.17).

Across Otemma, generally the form of each feature is maintained over the IG simulations, as total erosion is limited under the linear law and indistinguishably small for the non-linear law for such a limited 10 ka time period (Figure 3.17). Longer interglacial periods may well result in sufficient cumulative erosion to significantly denude the features as occurs under GP conditions, though this would be dependent on the specific climate variability of such a period.

Under GP conditions at Otemma, feature form is preserved with the non-linear law, again due to its limited erosion potential (from low sliding velocities and small value of K_G), but some large changes take place with the linear forcing despite only having run for the first 40 ka (Figure 3.17). This is particularly noticeable at the gorge and icefall, where the focusing of erosion in the higher velocity regions under the linear law causes a substantial lowering of the profile both upstream and downstream of the features. At the gorge, the riegel ridgeline through which the gorge is cut is accentuated, forming a sharp adverse slope upstream. At the icefall, high denudation occurs on the top step before the lip, where ice is drawn more rapidly downwards, as well as below the icefall from the large ice flux of the main glacier. The centre region of the icefall receives comparatively little erosion, resulting in an overall situation where the feature as a whole is eroded in place and maintains its form.

The summit region of Otemma presents an interesting situation. Under IG conditions, a small lowering of the profile occurs on the upper-most portion, which remains ice covered throughout the simulation. However, under GP conditions the whole profile is able to erode slightly under the non-linear law, whilst erosion rates under the linear law are insufficient to offset an isostatic response from very intense denudation occurring further down-valley and hence the profile at 40 ka is raised slightly above the original starting elevation.

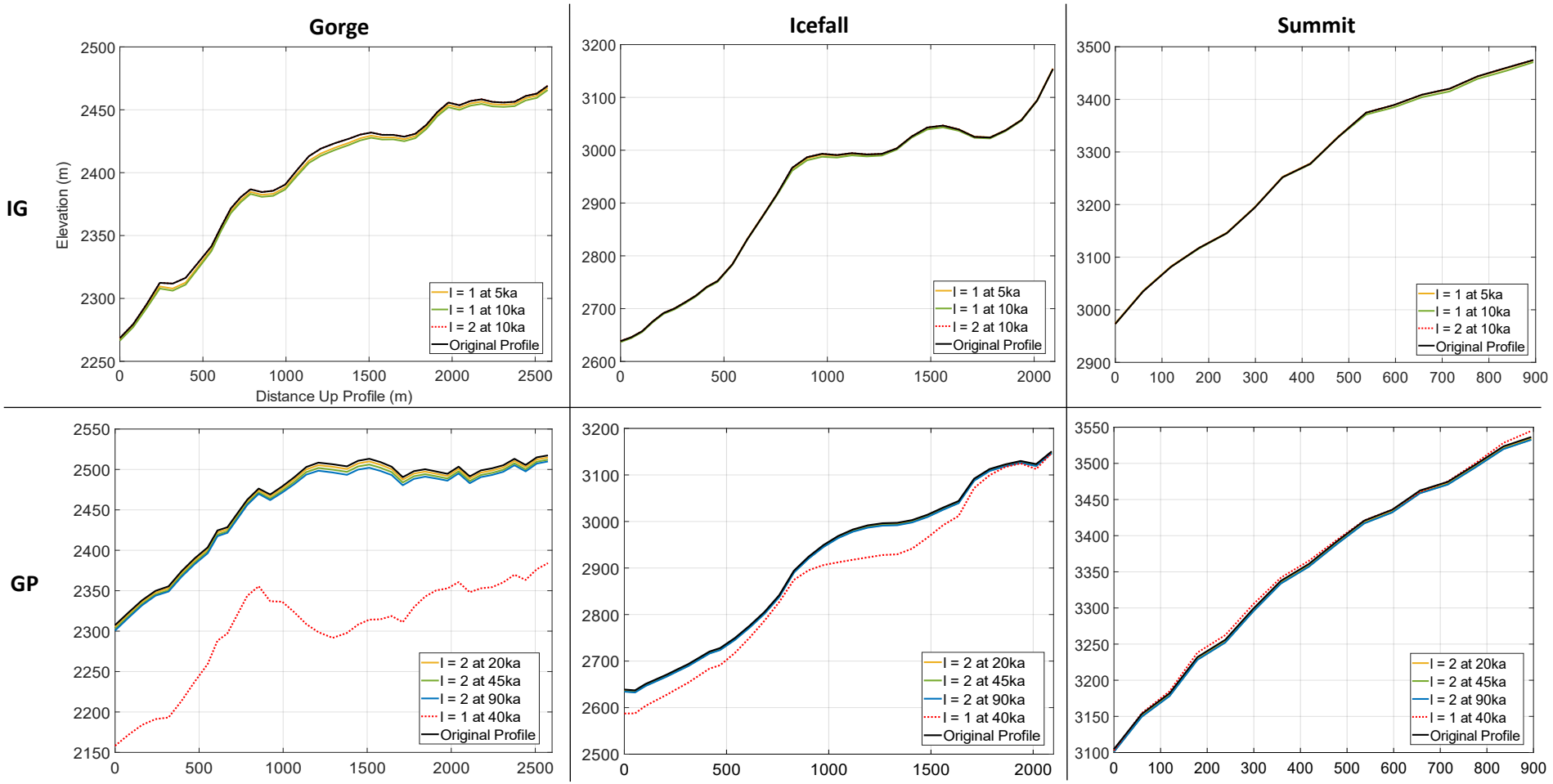

Figure 3.17: Bed profile evolution for the gorge, icefall and summit regions of Otemma over IG **(top)** and GP **(bottom)** scenarios. Note that the non-linear law in the IG profiles (red-dashed line) produces such little erosion that it is indistinguishable from the original bed at this scale. For the GP profiles, the red-dashed line is the output of the linear law for the first 40 ka of the simulations before instability occurred.

At Trift, higher erosion rates make the response to IG conditions more obvious and whilst the profiles of the riegel and cirque remain largely unchanged, there is a clearer spatial focusing of erosion that has slightly reduced the slope angles in the most intense regions (Figure 3.18). The very high rates of denudation at the icefall result in an interesting evolution of the profile, whereby the most intensely focused erosion on the lip has acted to lower the inflection point of this large topographic step and smooth the profile out to a lower gradient over time.

The situation under GP conditions at Trift is quite different particularly at the icefall where, similar to Otemma, the overall form of the feature is preserved and the inflection lip is instead protected from rapid erosion due to thick ice reducing the surface slope (cf. Figure 3.11e), causing erosion to be focused instead on regions further up and downstream (Figure 3.18). A large overdeepening is excavated by the linear law in the first kilometre up-profile from the icefall where higher sliding velocities are maintained. Similarly, an extensive 300 m excavation occurs just beyond the riegel under the linear law where velocities increase due to the valley constriction, whilst the riegel itself is preserved through time due to lower rates of erosion on the feature itself (Figure 3.18).

The cirque region of Trift under GP conditions generally maintains its overall form, though with a slight reduction in the convex lip under the linear forcing. The large change in profile between 20 and 45 ka under the non-linear law is likely the result of a significant isostatic depression in response to the sudden increase in ice volume over the whole domain from 40 ka, since the actual rate of erosion at this feature remained largely unchanged throughout the whole period as seen earlier in Figure 3.16d.

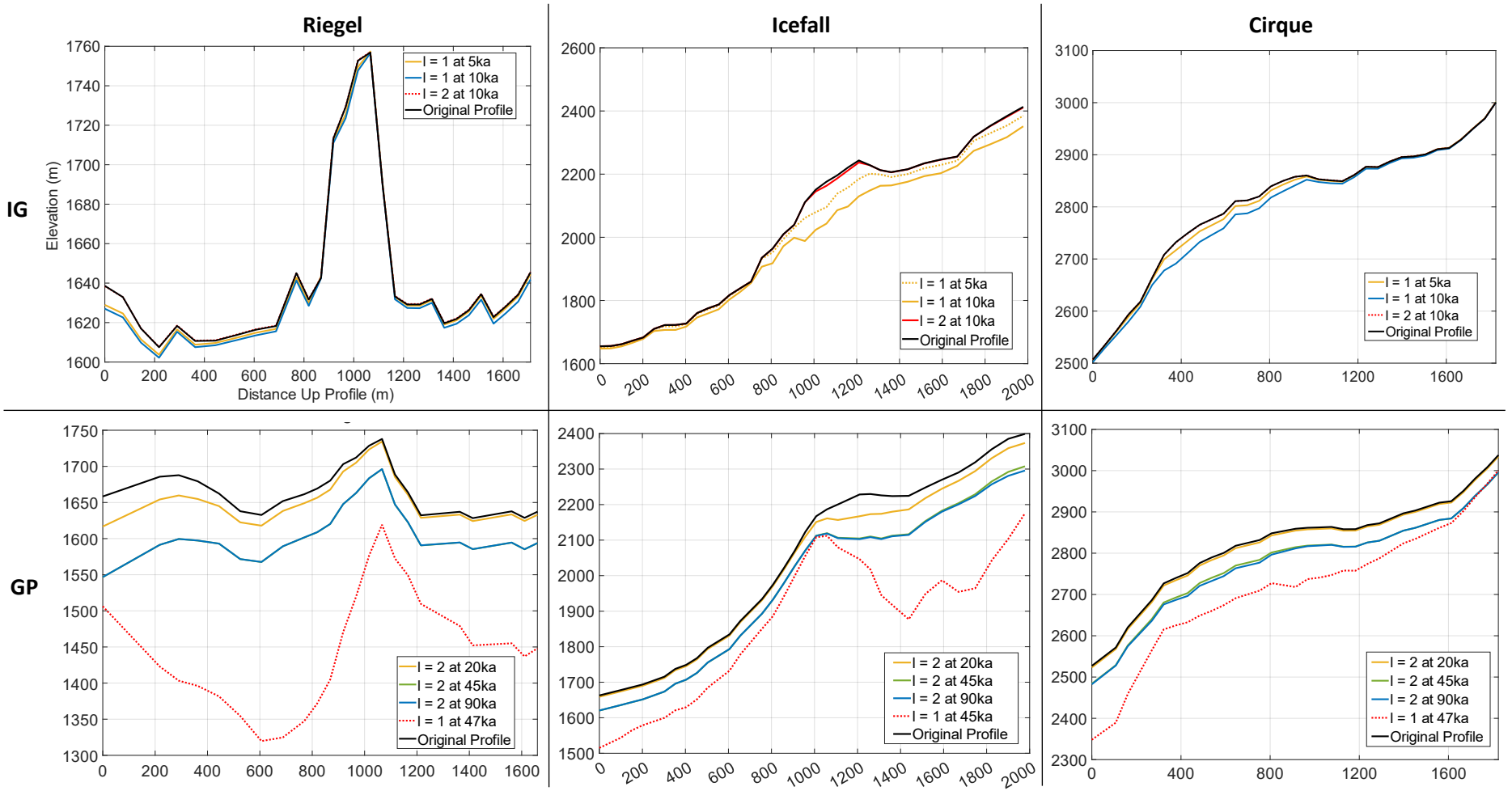

Figure 3.18: Bed profile evolution for the riegel, icefall and cirque regions of Trift over IG **(top)** and GP **(bottom)** scenarios. Note that linear law data for GP scenarios (red-dashed line) is only up to 47 ka before model instability occurred.

3.5 Discussion

3.5.1 Choice of Erosion Law

One of the key objectives of this chapter was to examine the impacts of using different erosion law exponents that have been invariably used in past modelling studies and recently debated as to which is most appropriate given our current understanding of glacial erosional processes and limited empirical data (e.g. Cook et al., 2020).

The model results here have shown that the choice of sliding exponent l does not necessarily impact *where* strong erosion occurs, since this is dictated by the rate of sliding and hence the influence of local topography and hydrology which does not change significantly between tested laws. Rather, the strength of that relationship to sliding is altered such that the low non-linear exponent 0.65 acts to more evenly distribute denudation across the catchment (Figure 3.19a), smoothing the landscape. The linear law, on the other hand, results in far greater rates of erosion in the hotspots and similar or lower amounts to the sub-linear in the low sliding regions, accentuating changes in the landscape and the impact of key landforms (Figure 3.19b), as does the higher non-linear value of 2, which further increases the disparity between regions of high and low erosion (Figure 3.19c). These findings are consistent with previous testing across these laws at the much larger and coarser scope of the entire Alpine range by Seguinot & Delaney (2021).

There has been much debate on which value of the exponent l is most suitable for modelling purposes (Cook et al., 2020; Herman et al., 2021), which given the impacts outlined above, is of great significance. Using mean or median values for erosion and sliding across whole glaciers tends towards the more linear scenarios of l = 1 (Humphrey & Raymond, 1994), or 0.65 (Cook et al., 2020). Such determinations are problematic, however, given the high spatial ranges in both sliding and erosion throughout the catchment, as is evident from the outputs of this study, as well as the potential shortfalls of previous estimations of these crucial parameters in past studies, as discussed earlier in section 3.1.3.

Taking into consideration the internal variability of sliding and erosion rates at the individual glacier scale points towards the use of non-linear values (i.e. l = 2 or more) (Herman et al., 2015, 2021). But this too is somewhat problematic, as it implies rapidly increasing erosion with higher sliding velocities which goes against conventional theories of

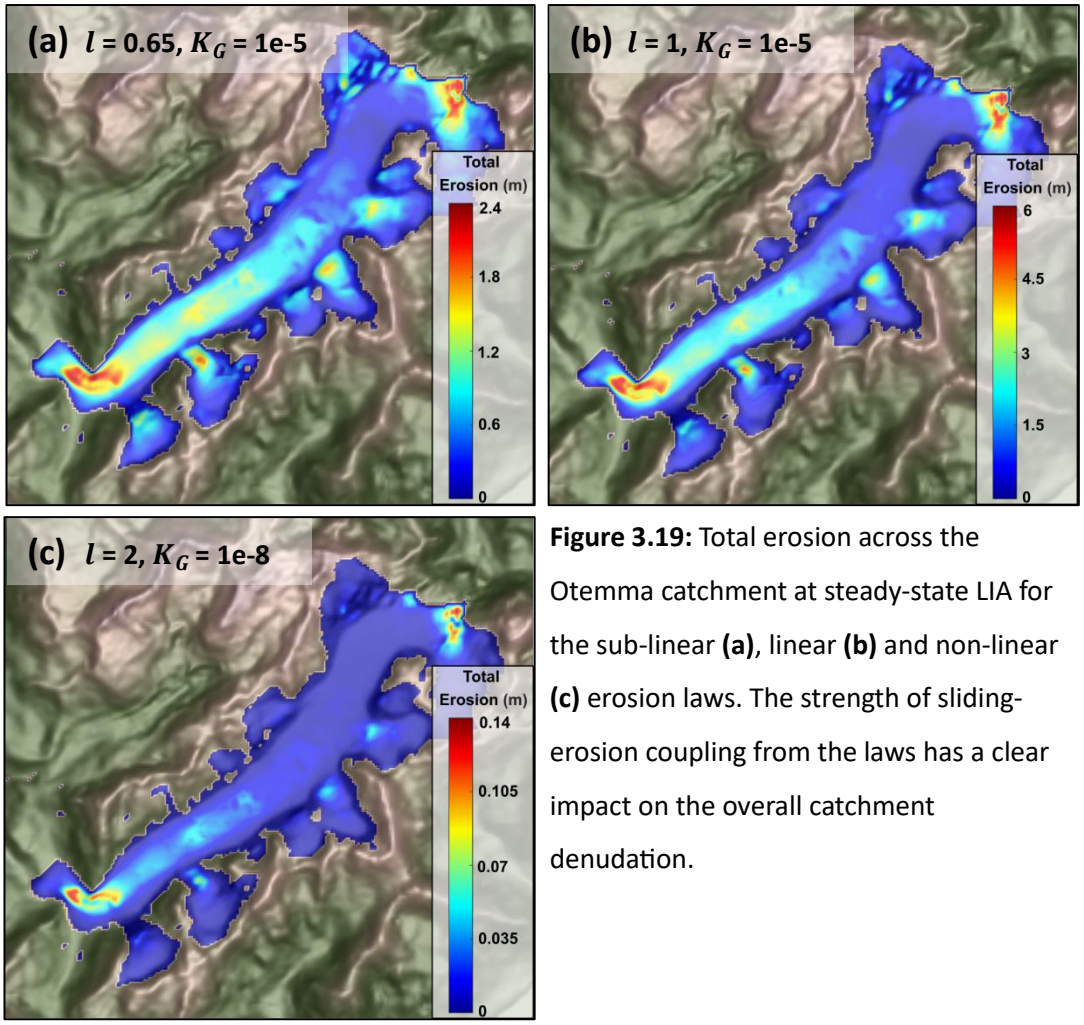

Figure 3.19: Total erosion across the Otemma catchment at steady-state LIA for the sub-linear **(a)**, linear **(b)** and non-linear **(c)** erosion laws. The strength of sliding-erosion coupling from the laws has a clear impact on the overall catchment denudation.

basal shear stress decreasing at higher velocities due to greater ice-bed separation from increased cavitation (Lliboutry, 1968), in turn lowering the viscous drag necessary for affective abrasion to occur (Zoet & Iverson, 2015; Iverson et al., 2019). Such a process is not accurately modelled here, as the derivation for cavity size and ice-bed contact (SLf) in iSOSIA are reliant on some assumed constants and changes in hydrology (Equation 3.3) and does not take sliding velocity into account.

The non-linear l = 2 also intrinsically implies much diminished erosion under slower sliding rates due to the power relationship (see for example Figure 3.10a), as well as the coupled low value of K_G. This results in a situation which yields mean catchment erosion up to two orders of magnitude lower than the linear or sub-linear laws, which may or may not

be appropriate considering wide ranges of < 0.1 to 1.5 mm a^{-1} for velocities < 1 to 10 m a^{-1} reported in the global compilation dataset of Cook et al. (2020).

The value of K_G clearly has a significant impact on the model outcomes, particularly at the two studied catchments where velocities are far below the point at which erosion rates from the non-linear law would match that produced by the linear law. As a result, the overall denudation of the bed is very minimal under non-linear l = 2 forcing and far outpaced by the linear law. In studies where the goal is to determine accurate rates of glacial erosion, the choice of K_G should therefore be a critical consideration. In some cases tuning of the parameter using ensemble models until the simulated erosion rates match that of independent empirical data, as done in this study and by Herman et al. (2011, 2015), may improve the accuracy of the overall outcomes. However, this is still flawed for the reasons previously outlined for the use of observations in constraining l (i.e. spatio-temporal disparity of point or catchment-averaged observations compared to modelled scenarios), as well as the complex reality of real catchments, whose substratum may vary considerably between different lithologies and deformable beds. A singular K_G forcing is therefore a large simplification that requires further study on the quantification of abrasion on different materials (e.g. Boulton, 1979).

3.5.2 Spatio-temporal Erosion Patterns

Past work has emphasised the importance of the ELA position as the region of greatest erosion, since this is where maximum ice flux is achieved (MacGregor et al., 2000; Anderson et al., 2006). The results here show no such impact of the ELA, with erosion under steady-state LIA conditions clearly greater in the ablation zone (see Appendix 3.7.2). Here, particularly for the gentle profile at Otemma, increased erosion is caused by meltwater flux leading to enhanced sliding rates (Figure 3.7a, Figure 3.8a), echoing the work of others that highlight the importance of hydrology (Herman et al., 2011). However, simulations by Magrani et al. (2021) over synthetic catchments with fixed ice extents have suggested the possibility of total erosion in the accumulation area outpacing that of the ablation area in higher precipitation scenarios (> 2 m a^{-1}), likely due to greater meltwater flux forcing more efficient drainage systems that reduce sliding velocity in the ablation area. Since precipitation is kept constant at 1 m a^{-1} in this study, such a process was not observed.

Under variable interglacial conditions, ice residency time is a dominant control on denudation across the catchment, with regions of enhanced erosion at higher elevations able to match or exceed the total erosion of features lower down the profile (e.g. Figure 3.13a) despite otherwise lower annual rates of incision (Figure 3.16a). In spite of the highest ice residency time, features at the valley head such as the summit slope at Otemma and the cirque at Trift experience consistently very low rates of erosion during both GP and IG scenarios, dropping even further according to climate-induced changes in ice dynamics during the cycle (Figure 3.16). While this is in line with theories of valley deepening further down the profile outpacing that of cirque/summit regions (Cook & Swift, 2012), it is not consistent with theories and field evidence that cirque denudation is significantly lower during full glacial periods and undergoes most erosion during more temperate interglacial periods (Barr & Spagnolo, 2015; Crest et al., 2017). The inconsistency here is likely due to simplifications of the model (see next section for further details), notably the absence of cold-based ice conditions that may have occurred at these high elevations during full glacial periods, which would further reduce the erosion rates during GP runs, and the overall simple nature of the erosion law which does not account for the enhancement of abrasion from sediment particles that are believed to be strongly influential in driving cirque abrasion during IG periods (Barr & Spagnolo, 2015). Such particles would be derived from glacially eroded material itself, as well as extra-glacial erosion on exposed ridges and headwalls, which are not accounted for in the model, yet have been measured to increase markedly during deglaciation (Wetterauer et al., 2022).

Cirque erosion, particularly of the headwalls, is said to be a crucial process for the ‘buzzsaw hypothesis’ of glaciation limiting mountain elevations (Evans, 2021). However, previous modelling work using iSOSIA which includes such periglacial processes have shown that although periglacial erosion is enhanced during interglacial periods, the total contribution to catchment erosion is negligible compared with the overall impact of glacial valley incision that amplifies relief (Liebl et al., 2021). As such, while there is no evidence of the buzzsaw mechanism in operation under the simplified model outcomes presented here, it is not necessarily clear that a more complex model setup including more peri-glacial processes would find a significantly different outcome.

A key finding from the results has been the dominant influence of pre-existing glacial topography and landforms in dictating patterns of erosion in a continuous form-process feedback. Previous modelling studies emphasising the importance of mass balance, ice flux and hydrological controls on patterns of erosion have used simple smooth profiles which

accentuate the impact of these inputs as the only major controlling variables (e.g. Harbor, 1992; MacGregor et al., 2000, 2009; Anderson et al., 2006; Herman et al., 2011; Prasicek et al., 2018). However, real glacial basins have complex heterogeneous topography which impact the longitudinal and transverse stresses of ice flowing through them and subsequently the basal shear stress and sliding velocity that drive erosion. These feedbacks between topography and ice stress are only reliably captured in higher order models like iSOSIA (Egholm et al., 2012b) and have been shown to significantly affect erosion patterns in synthetic landscapes (Pedersen et al., 2014; Liebl et al., 2021).

Modelling of the entire Alps range across the last glacial cycle by Seguinot & Delaney (2021) shows clear focusing of erosion in the main alpine valleys, but spatial resolution is too poor to identify the smaller-scale changes occurring in the high alpine head catchments. The higher-resolution models in this chapter demonstrate that the spatial distribution of erosion in these upper catchments is dominated by local topographic features and landforms across all climate scenarios (e.g. Figure 3.10, Figure 3.11, Figure 3.13, Figure 3.14).

Detailed analysis of a few of these key features enables a better understanding of how these high alpine valleys likely evolve through time. Erosion of the riegel at Trift occurs similarly across both limited and large ice extents, with limited erosion on the upstream wall of the feature, as ice flow halted by the large obstacle increases the longitudinal stress component, reducing basal shear stress and sliding velocity. A rapid increase in shear stress and velocity then occurs as ice overtops the riegel, creating a localised increase in erosion consistent with field evidence derived from cosmogenic nuclide measurements by Steinemann et al. (2021). This is outpaced by erosion either side of the riegel in the overdeepened basin upstream and the valley constriction/gorge downstream, thus maintaining the prominence of the riegel through time.

The gorge region at Otemma is also responsible for locally increasing erosion rates, but the process occurs in different ways depending on ice extent. Under reduced ice extents (e.g. LIA), erosion is focused in the gorge itself as the ice flow is constricted, however, under greater ice extents (e.g. LGM), the region of highest erosion is shifted uphill outside of the LIA margin, where higher shear stress occurs on an adverse slope and ice velocity increases as a local step in bed and surface gradient is created from flow over and down a truncated spur of the nearby Pointe d'Otemma (Figure 3.20). This demonstrates the dynamism of spatio-temporal patterns of glacial erosion, as larger ice extents not only 'switch-off' regions of previously high erosion in the valley, but also access and more rapidly denude terrain that

is otherwise usually undisturbed by glacial activity. In this respect, the gorge at Otemma is consistent with theories that inner gorges are resistant to erasure during intense glaciation (Montgomery & Korup, 2011), though the model data here suggests that more limited glaciation (i.e. IG & LIA scenarios) certainly concentrates erosion in these regions. It is likely that the channel itself within the gorge would continue to incise fluvially even under glacial cover though, as this is a natural conduit for subglacial meltwater.

Steep topographic steps that form icefalls are key drivers of erosion in both catchments, particularly under thinner LIA and IG glacier extents where they dominate local rates of denudation on the lip of the step as ice is drawn down rapidly into the steep gradient below. This can be largely neutralised, however, during colder full glacial conditions if ice thickness is sufficient to cause a significant reduction in surface slope, which lowers the basal shear stress and sliding velocity (Pedersen et al., 2014). This is particularly clear at Trift, where the volume of ice from 40 ka onwards fills the entire lower basin and brings the surface effectively level with the upper reaches (Figure 3.6). In this case, the region of strongest erosion is shifted up-glacier where ice thickness is at a similar level to that of LIA conditions and hence steep slopes are maintained (Figure 3.11e). This has significant consequences for the evolution of the main topographic step/icefall itself, as can be seen in the long-profiles of Figure 3.18, where erosion focused largely on the lip during thinner ice conditions acts to reduce the relief of the feature and return the profile to a more uniform gradient, whilst thicker ice conditions maintain the prominence of the inflection point at the lip and instead focus erosion above and below the feature, effectively maintaining overall relief. This switching of erosion patterns between glacier states is potentially a mechanism by which an icefall may maintain some form of steady state, eroding gradually in place. The relatively simple models here show no particular propensity for headward erosion, though this may be due to a need for much longer run times with multiple glacial-interglacial cycles coupled with tectonic uplift to create such behaviour (e.g. Shuster et al., 2011; Sternai et al., 2013; Liebl et al., 2021).

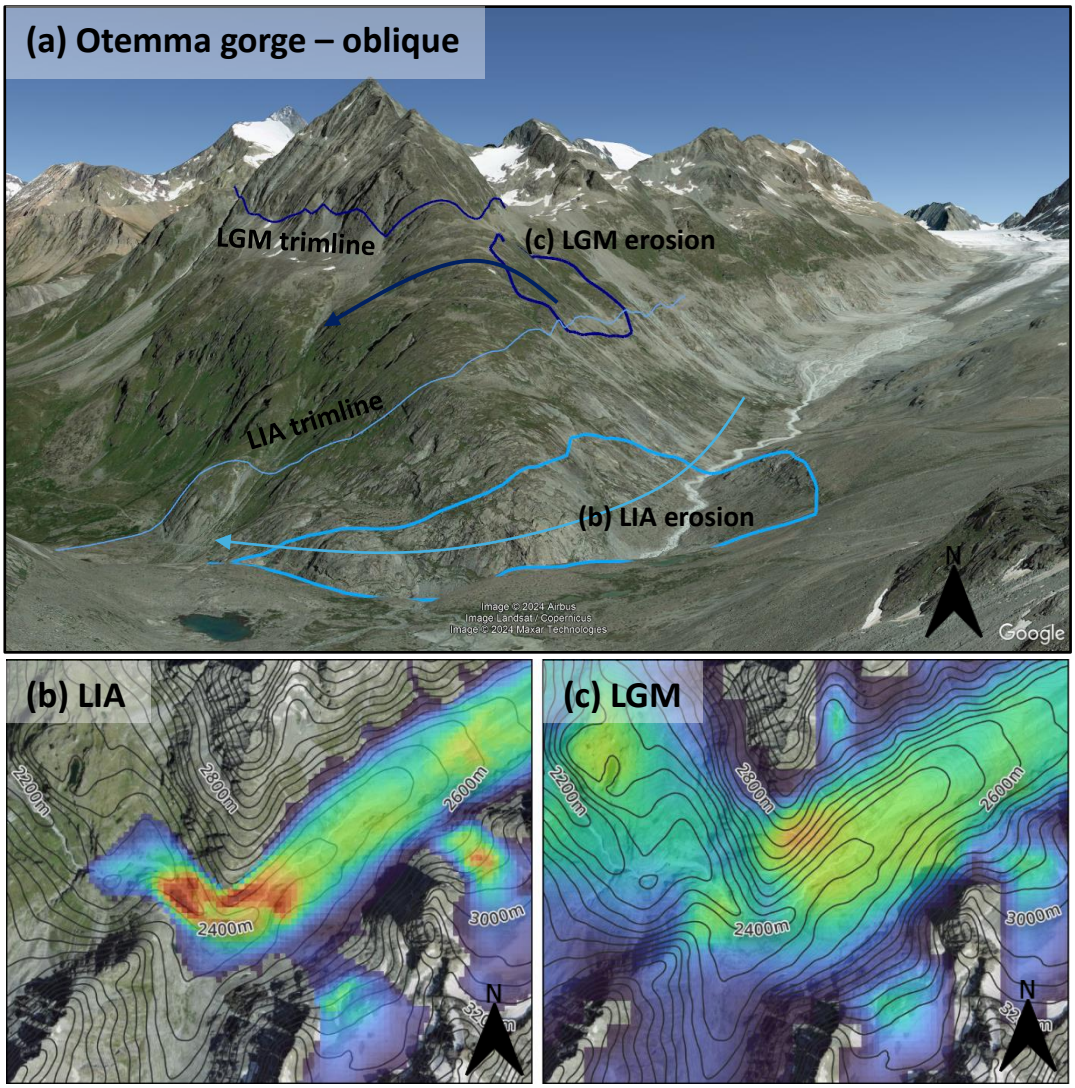

Figure 3.20: Oblique Google Earth view of the gorge region at Otemma, with marked trimline extents and fastest flowline arrows for the LIA and LGM along with circled outlines of areas of highest erosion **(a)**. Under LIA, erosion is focused directly in the gorge itself, with warmer colours indicating higher erosion **(b)**, whilst thick LGM ice shifts the focus of erosion uphill as ice is drawn over the ridge and down the truncated spur **(c)**.

3.5.3 Model Limitations and Simplifications

Improving model accuracy often comes at the cost of increased complexity and reduced computational efficiency, whilst in other cases it is limited by the present boundaries of theoretical treatment for certain processes. In this model a number of limitations and simplifications were present for both these reasons.

Firstly, as mentioned previously in the model setup (section 3.3.2), a number of simplifications were made in the climatic forcing, such as fixed values for positive degree day factor, annual temperature amplitude and precipitation rate across all run scenarios. Whilst it is recognised that significant variation in these parameters occur in reality and impact overall mass balance and subsequent subglacial erosion (e.g. Magrani et al., 2021; Jouvet et al., 2023), they were fixed for the sake of maintaining model simplicity and thus stability, which was necessary given the high spatial resolution of the models. Likewise, the climate variability for interglacial and glacial period scenarios was achieved through the simplification of high temporal resolution temperature reconstruction data for the Holocene and last glacial period (see Figure 3.4), likely resulting in periods of over or under estimation of mass balance across these runs. The scope of this study, however, was not to accurately simulate the Holocene and Würmian periods themselves, but to explore erosion response to idealised interglacial and glacial conditions, with the Holocene and Würm data from Erb et al. (2022) and Jouvet et al. (2023) providing reasonable magnitudes of change that can be easily applied to such scenarios. Moreover, under full glacial conditions the positioning of the high-alpine catchments make them largely isolated from smaller-scale climate variations which are more important in affecting the position and dynamics of the terminus regions some hundreds of kilometres away (Seguinot et al., 2018; Jouvet et al., 2023).

Only temperate ice was simulated in this study, ignoring any potential for cold-based conditions. Models of the Würm glaciation over the Alps have suggested the presence of cold-based ice for long periods of time in the upper mountain domain (Seguinot et al., 2018; Jouvet et al., 2023), with simulated ice surfaces well above field-observed trimline elevations (Kelly et al., 2004). There is some debate over whether trimlines correspond to the LGM ice surface as commonly interpreted in the past, or if they in fact represent the thermal boundary between warm and cold ice conditions (Rootes & Clark, 2020). Evidence for the latter has been presented for the last British and Irish Ice Sheet using cosmogenic nuclide exposure dating (Fabel et al., 2012). However, no geomorphic evidence is currently available to suggest widespread cold-based conditions in the Alps outside limited regions at

present on the highest summits (Godon et al., 2013; Bohleber et al., 2018) and LGM reconstructions supported by cosmogenic nuclide dating in some Swiss valleys support an ice surface origin for trimlines here (Wirsig et al., 2016). The current integration of cold-based ice in iSOSIA is a simple process law that prohibits any sliding or erosion in regions below the pressure melting point (Egholm et al., 2017), which is potentially overly restrictive given some evidence of limited erosion under cold-based conditions (Boulton, 1979; Atkins et al., 2002) and unsuitable for this study since climate parameters have been simplified.

The treatment of subglacial hydrology in the models follow the cavity and channel approach of Ugelvig et al. (2018) but under a steady-state solution in balance with water flux as in Magrani et al. (2021), thus neglecting diurnal or seasonal fluctuations in meltwater that can act to temporarily enhance rates of sliding and potentially erosion (Iken & Bindschadler, 1986; Swift et al., 2002). Furthermore, sediment produced by erosion is treated as immediately evacuated in the model, whilst in reality it can provide clasts to further enhance erosion (Hallet, 1981), or if left to accumulate without sufficient evacuation, may act as a layer of protection over bedrock to suppress erosion and create feedback mechanisms to inhibit further excavation of features like overdeepenings (Cook & Swift, 2012; Alley et al., 2019). As such, the great depth of erosion in some regions of the profiles modelled here, such as the large overdeepening at the top of the Trift icefall under GP conditions (Figure 3.18), is possibly unrealistic. Inclusion of these feedback mechanisms would necessitate a more advanced erosion law that accounts for basal ice debris concentration, which has been shown to increase the variability in erosion (Ugelvig & Egholm, 2018), but would be difficult to empirically constrain.

The model also neglects the contributions of fluvial and peri-glacial processes to erosion of the landscape, which would be particularly applicable during the warmer IG and LIA scenarios. Freeze-thaw and frost-cracking processes in particular are believed to be important for driving cirque and headwall erosion as mentioned previously (Barr & Spagnolo, 2015; Alley et al., 2019). Whilst proglacial fluvial activity is important for maintaining catchment evolution and key features like gorges during periods of deglaciation (Montgomery & Korup, 2011), this was not within the scope of this study.

Finally, although the model accounts for isostatic response to loading from thick ice and unloading from significant erosion, a constant background uplift is not implemented. Over the short timescales simulated here this is not particularly significant, though it could certainly cause changes from height/mass balance feedbacks over much longer situations

across multiple glacial/interglacial cycles and would thus need to be accounted for in any future work on longer timeframes.

3.6 Summary

This chapter used the ice and landscape evolution model iSOSIA to simulate changes in glacial erosion in two upper alpine catchments according to different laws where erosion is coupled to basal sliding velocity in linear or non-linear fashions, as well as over a variety of climate conditions. The model outcomes here provide vital spatial and temporal context for erosion patterns and implications for catchment evolution that will be discussed later in Chapter 5 which links together all of the results.

The key findings of this chapter are:

- Pre-existing glacial topography dominantly controls the spatial focusing of erosion.
- Erosion rates and patterns under different glacier extents have the potential to differ significantly or very little depending on the specific catchment hypsometry and position in the wider basin structure.
- Choice of both l and K_G parameters in simple erosion laws substantially alter the outcome of simulated erosional responses and require further empirical data to improve constraints for appropriate values on a case-by-case basis.

Pre-existing topography was found to be the dominant influence in dictating spatial patterns of erosion, with the highest rates found at features that are conducive to rapid sliding velocity and raised basal shear stress such as large topographic steps (icefalls) or valley constrictions. Steady-state LIA conditions also demonstrate a clear bias towards higher erosion in the ablation zone with regions of enhanced sliding and erosion due to meltwater inputs and a subsequent steady decrease in erosion with increased elevation. Sliding and erosion rates under steady-state LGM conditions were not dissimilar to LIA at Otemma where there is little change in valley gradient, whilst the steeper basin of Trift showed a marked decrease in rates under thicker ice conditions which act to smooth out the heterogenous landscape below. Therefore, catchment hypsometry plays a crucial role in how much erosion differs between these two states of glaciation.

Variable climate introduces significant changes to both erosion rates and patterns, which are influenced heavily by changes in ice volume and extent over time. Under IG scenarios erosion rates decreased as glaciers retreat, but the longer ice residency time at higher elevations enabled the total erosion here to be greater than under steady-state LIA conditions and in some places able to match or exceed that of rapidly incising regions further down the profile. The two catchments responded very differently to GP climate forcing as a consequence of their position in the wider valley structures, with Otemma quickly attaining and stabilising near-LGM ice thickness whilst Trift underwent more limited glaciation during the first half of the cycle conducive to rapid erosion, before a rapid switch into LGM thickness and diminished erosion. Consequently, erosion rates and patterns at Otemma during GP forcing is similar to steady-state LGM, whilst Trift differed markedly between the two scenarios.

The different laws tested here have produced quite substantially different outcomes, both in patterns and magnitude of erosion over time and variable climate. The highest rates of erosion are achieved using the simple linear law (l = 1), whilst the sub-linear law (l = 0.65) gives a reduced response for more homogeneous denudation across the landscape. The low sliding velocities at both catchments mean the non-linear law (l = 2) yields very small amounts of erosion, though the difference between high and low regions is accentuated, acting to amplify landscape heterogeneity.

The scaling factor K_G has been shown to be highly influential on the magnitude of erosion produced and necessitates careful consideration for studies where the aim is to simulate realistic amounts of denudation, particularly if no feedback mechanisms are in place to limit continuously high excavation of key areas in the profile (e.g. overdeepenings).

Lack of reliable empirical data makes accurate determination of appropriate values for K_G and l difficult. The next chapter will use a novel method of luminescence thermochronometry to acquire exhumation rates across the two catchments modelled here in a new approach to providing such needed field data that will be useful not only for assessing the results of this modelling work, but to improve constraints on numerical representations of glacial erosion processes overall.

3.7 Appendices

3.7.1 Otemma Isolation Tests

To reduce the computation cost of modelling upper alpine catchments at high resolution under large ice extents it is necessary to forego modelling all of the surrounding ice from neighbouring catchments. Naturally, a concern then arises that this could lead to inaccuracies in the modelled ice for the target catchment if it is not coupled with the numerous other large glaciers that made up the entire Alpine Ice Sheet over the last glacial period.

To test this the model domain was artificially adjusted to create a large wall at the mouth of the Val de Bagnes valley where ice would buttress and thicken as a proxy simulation of the Otemma LGM glacier joining the large Rhone trunk glacier (Figure A3.7.1a). The affects of allowing ice flow off the back of the Otemma plateau down into the neighbouring Arolla valley was also tested (Figure A3.7.1b). Ice thickness and sliding velocities for Otemma were then compared across these tests and showed the catchment is generally isolated and unaffected by changes at the mouth of the Val de Bagnes, or by flow off the back into Arolla (Figure A3.7.1.2). This brought confidence that Otemma could be simulated at LGM extent without also having to include neighbouring valleys or large trunk glaciers.

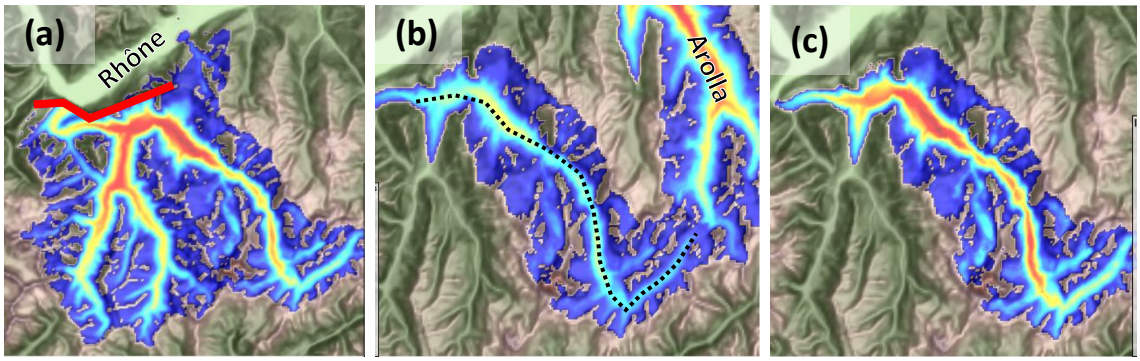

Appendix 3.7.1: Overview of different test models used to assess the isolation of Otemma from down valley perturbations. **(a)** Buttressing ice with an artificial wall (red line) in the landscape to simulate presence of Rhone glacier in the trunk valley. **(b)** Allowing flow down to the neighbouring Arolla valley on the right side (dashed line indicates profiles in Figure A3.2). **(c)** The standard model allowing ice only in the Val de Bagnes.

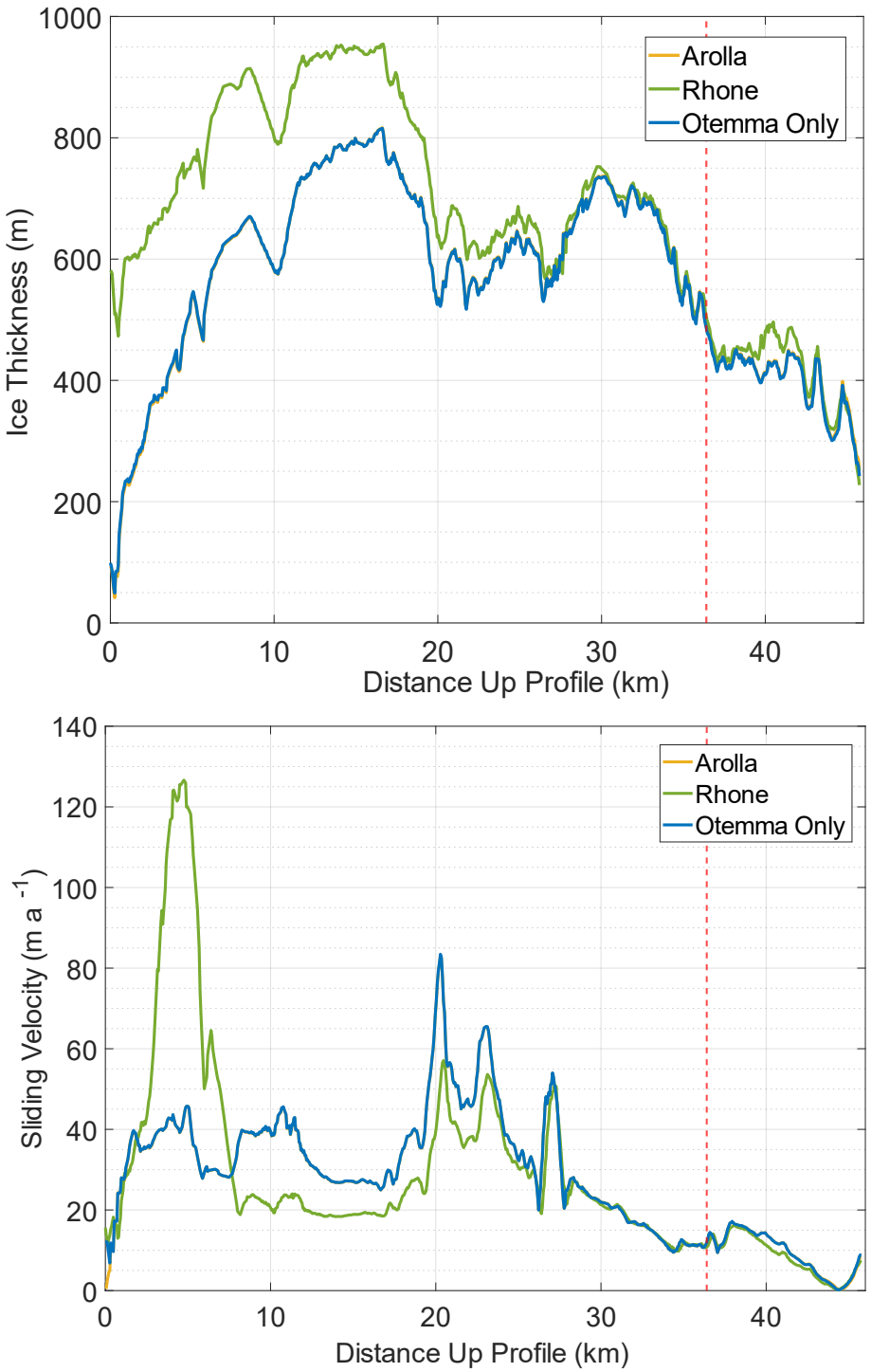

Appendix 3.7.1.2: Modelled ice thickness (top) and sliding velocity (bottom) across the three test scenarios moving from the Val de Bagnes valley mouth to the top of Otemma (see Figure A3.1b for profile line), with the start of the Otemma catchment shown by the red dashed line. Ice thickness is generally consistent within Otemma except for a slight difference of about 50 m in the central region, which is thicker under the Rhone scenario. This has minimal impact on sliding velocity though, with a variation of about 3 m a^{-1}.

3.7.2 Frequency plots of erosion under LIA steady-state

Otemma

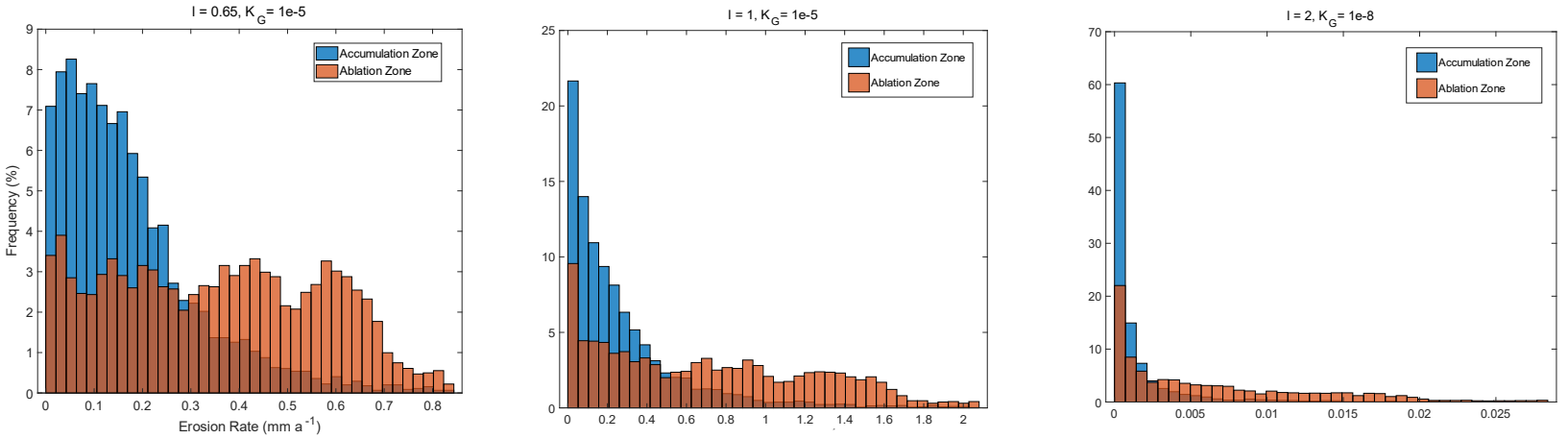

Trift

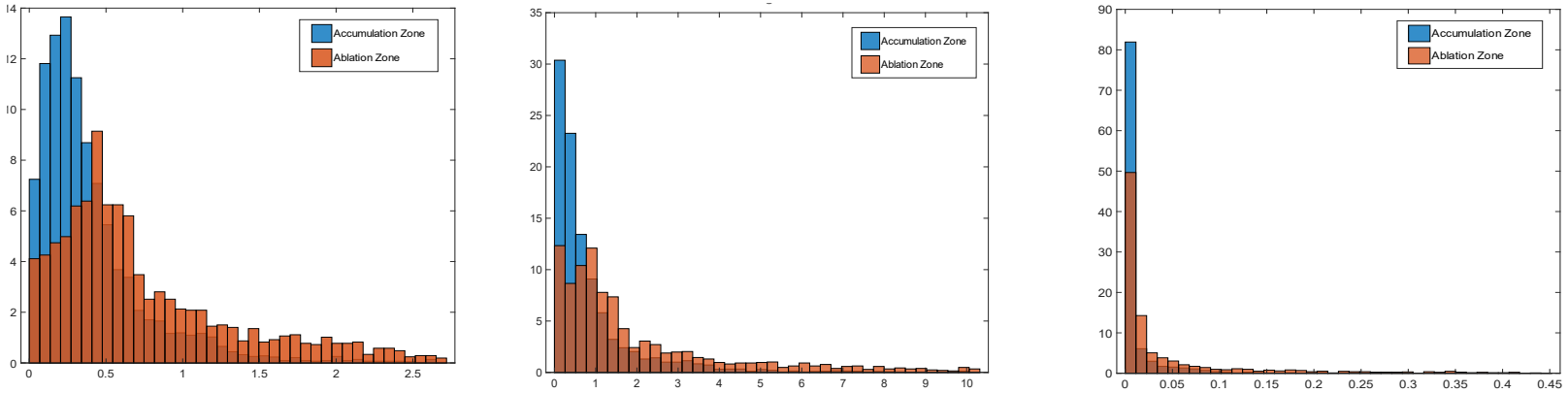

Appendix 3.7.2: Frequency plots of erosion rates for each erosion law at Otemma (top) and Trift (bottom) at steady-state LIA conditions, split according to ablation and accumulation zones. There is a clear tendency for the higher rates of erosion to occur in the ablation zone, whilst the accumulation zone sees the greater proportion of lowest erosion rates.

Chapter 4

Determining Exhumation Rates from the Field with Thermoluminescence Thermochronometry

4.1 Introduction

4.1.1 Chapter Overview

In the previous chapter I showed how numerical modelling can be used to simulate various states of glaciation under different climate conditions and how this subsequently impacts rates and patterns of subglacial erosion over time. These models, whilst very useful for exploring a wide range of scenarios across whole landscapes, are driven by numerical representations of physical processes and as such are limited by uncertainties brought on by such a simplification of the complex reality of nature. Empirical data is a necessary component to creating and constraining these numeric laws, as well as for testing the accuracy of model outputs.

In this chapter I delve into the use of a novel method of thermochronometry initially developed by Brown & Rhodes (2022) which, when applied to bedrock samples acquired from the two study catchments, unlocks a continuum of exhumation rate history over the last glacial period (~100 ka). This promising new technique is demonstrated to provide a wealth of unique data that can be used to better constrain numeric models, as well as directly explore the broader questions of spatial patterns of glacial erosion and landscape evolution over timeframes relevant to glacial cycles.

4.1.2 Use of Geochronology in Geomorphology

In the study of surface processes, geochronology is an essential tool to aid understanding of how landscapes change over geologic timeframes of the order 10^2 to 10^6 years. Radiometric dating is a commonly employed method of finding the age of samples by exploiting the natural radioactive decay of target elements like radiocarbon or uranium. For example, radiocarbon dating has been used extensively to find the ages of a variety of sample materials – from primitive skis (e.g. Finstad et al., 2018), ice cores (e.g. Bohleber et al., 2020) and the infamous 'Otzi' mummified corpse found melting out from the ice on the Italian-Austrian border (e.g. Bonani et al., 1994) – all of which provided evidence to help constrain changes in glacier extents during the Holocene.

Terrestrial cosmogenic nuclide (TCN) and luminescence techniques permit the dating of non-organic samples by measuring the relative accumulation and depletion of natural ionising radiation. This has proved particularly useful for sediment and rock from glacial landforms (e.g. moraines) to retrieve the timing of processes of deposition, burial and/or exposure, providing critical constraints on the chronology of major ice sheet fluctuations over past glacial cycles (e.g. Clark et al., 2018).

Beyond the derivation of single ages, acquiring information on the surface erosion rate of bedrock requires some ingenuity outside the standard application of these techniques. The exponential decrease in production of cosmogenic nuclides with depth below the surface of a rock enables a unique opportunity to calculate an erosion rate according to the prior inheritance of nuclide concentrations from previous exposure and erosion events (Briner & Swanson, 1998; Fabel & Harbor, 1999). However, such a determination requires accurate constraints on the timing of glacial cover and subsequent surface exposure, which must often be acquired through other cosmogenic or luminescence measurements.

The field of thermochronometry avoids the need for accurate knowledge of these surface process events by measuring the temperature-time (T - t) history of rocks as they cool through the geothermal gradient moving up towards the surface. This provides a mechanism to independently date samples using their closure temperature – the point at which they begin to accumulate radiation and thus the starting point of their determinable age – and to estimate the rate at which they were exhumed to the surface. Once again, various minerals and elements can be targeted, each uniquely sensitive to different closure temperatures (Figure 4.1). Fission track methods, for example, are sensitive to closure temperatures upwards of 200°C in the case of zircon, whilst apatite annealing occurs around

approximately 100°C (Gallagher et al., 1998). Lower temperature thermochronometers (e.g. apatite (U-Th)/He) offer the ability to determine changes in exhumation increasingly closer to the surface – i.e. geomorphological change from landscape evolution. Comparing the ages of samples distributed across a study site can give insight into the *relative* patterns and magnitudes of erosion and uplift in that, in a broad sense, younger ages indicate areas more rapidly brought to the surface, whilst older ages signify a slower journey to the surface since passing their closure isotherm (e.g. Swift et al., 2008).

Obtaining *absolute* estimates of exhumation or erosion has been approached in a couple of different ways. Firstly, inversion methods that employ thermokinematic models have been applied to thermochronometric data to derive an exhumation rate for each sample in the landscape by relating the age and closure temperature data to a specific isotherm depth and geothermal gradient calculated by the model (Fox et al., 2014, 2016; King et al., 2016c). Elsewhere, thermochronometry has been used as a tracing tool to locate the source of detrital sediment which, when aggregated using traditional methods of upscaling sediment flux to erosion rate, yields spatially distributed rates of erosion (Herman et al., 2015; Ehlers et al., 2015; Falkowski et al., 2021). Both methods carry important limitations that will affect the uncertainty of the final data, such as the accuracy of thermokinematic parameters used to drive the model in the first case, or the inherent inaccuracies of deriving erosion rates from sediment flux data due to the influence of sediment storage or channel pathways (Mancini et al., 2023a) and the variable contribution of sub-glacial and peri-glacial processes (Guillon et al., 2015).

So far, investigating geomorphology and landscape evolution using erosion rates calculated through radiometric methods are ultimately hindered by the same limitation: they can only resolve a single value that represents an average rate of exhumation or erosion over a timeframe determined by the local situation and method employed. In the case of TCN dating, this may be as little as 1-3 ka (Sarr et al., 2019), whilst ages from apatite (U-Th)/He dating may infer relative exhumation over the past >100 Ma (Swift et al., 2008). Such outputs are of limited use when looking at the impact and variability of glacial erosion over periods governed by climatic forcing (10-100 ka). Herein lies the opportunity afforded by thermoluminescence thermochronometry, using the unique attributes of luminescence to unlock a continuum of radiation history that can be converted into a variable exhumation rate through time on the order of 10^3 to 10^5 years (Brown, 2017; Brown & Rhodes, 2022).

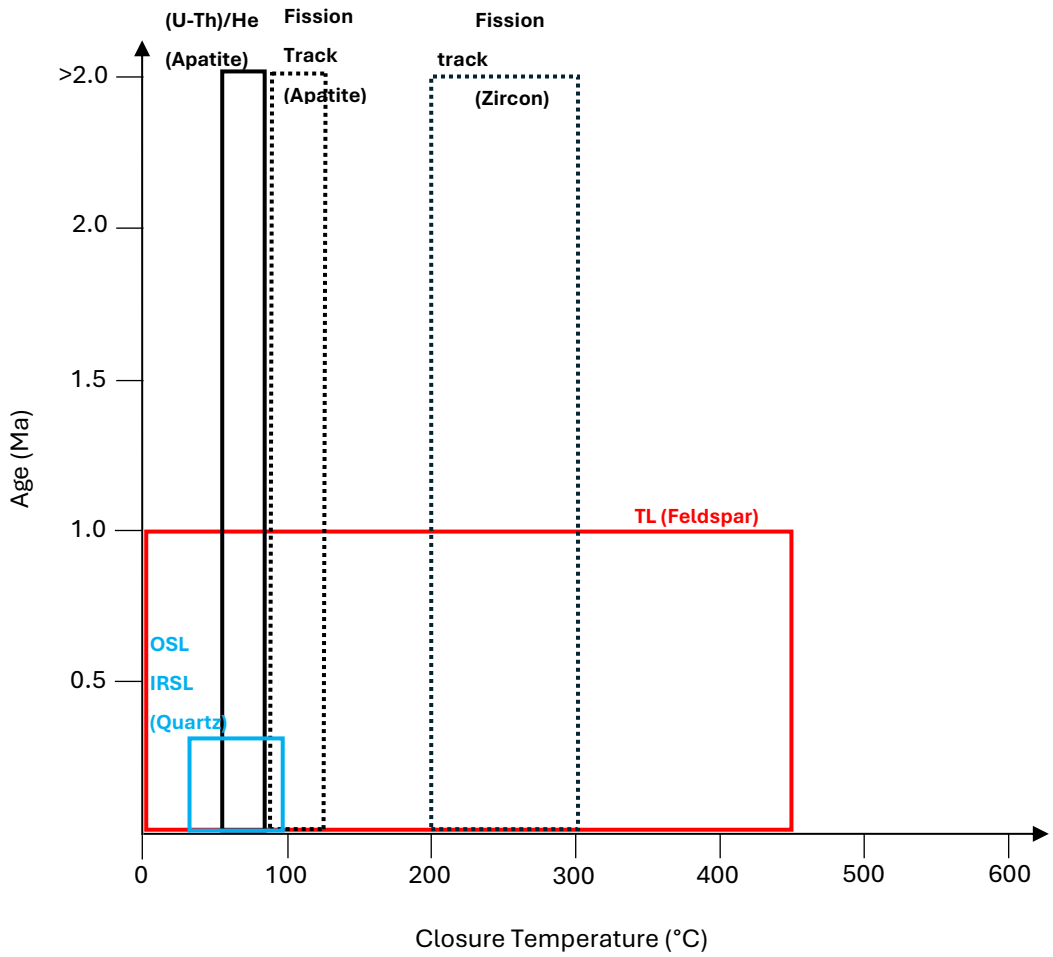

Figure 4.1: Applicable closure temperatures and determinable ages of some commonly used thermochronometers. Thermoluminescence of feldspar is unique in its ability to provide data on a continuum of thermal stabilities from a single sample. Ranges provided here are approximate, exact limits are dependent on sample, local situation and continued technical development.

In the following sections I will provide a brief overview of the concepts of luminescence dating and thermochronometry to show why thermoluminescence is the method chosen to be employed in this study.

4.1.3 Basic Overview of Luminescence Dating

In nature, low level environmental radiation is constantly emitted in the form of alpha, beta and gamma rays from the decay of uranium, thorium, potassium and rubidium elements, as well as from cosmic rays at the surface (the latter being particularly relevant for TCN). When minerals within a sediment or rock are subjected to this ionising radiation, the atoms structured in a crystalline lattice of positive and negative ions are excited (Aitken, 1985). As this occurs, some electrons are able to break free from their ground state in the valence band (*g*) and diffuse around the crystal via the conduction band in an excited state (*e*) (Figure 4.2a-b). During this process they may become trapped at a metastable level within impurities in the crystal lattice (*m*) (electron traps), where they will stay trapped until given enough energy (*E*) to be shaken free and return to their *e* state. From here they may either become re-trapped or will recombine at a luminescence centre (*L*) where the energy is released in the form of light, i.e. luminescence (Figure 4.2c) (Aitken, 1985). The required energy *E* to free the electrons is often referred to as the trap depth (*m* – *e*) (McKeever, 1985).

The number of trapped electrons therefore increases over time with prolonged exposure to radiation, analogous to a battery charging up (Duller, 2008), until either all traps become filled and the material is said to have reached saturation, or traps are progressively emptied by the input of energy in the form of light (optical) or heat (thermal) sources (Figure 4.2c). A material that is held in continued exposure to light or heat can result in the release of all of its trapped charge, whereby it is said to have been 'zeroed' or 'bleached', with the rate at which this occurs dependent on the minerals, trap depths and intensity of stimuli involved (Brown, 2020). If exposure was only transitory, then signals may instead be 'partially-bleached', for example during the transport, deposition and burial of fluvial sediments (Smedley & Skirrow, 2020).

The trapped charge population can be determined in a lab by artificially stimulating a sample either optically or thermally and measuring the emission of luminescence, which consequently reflects the amount of charge accumulated since the last bleaching event. By systematically re-measuring the sample after applying known doses of radiation in the lab, a dose response curve can be constructed to find the relationship of dose to luminescence

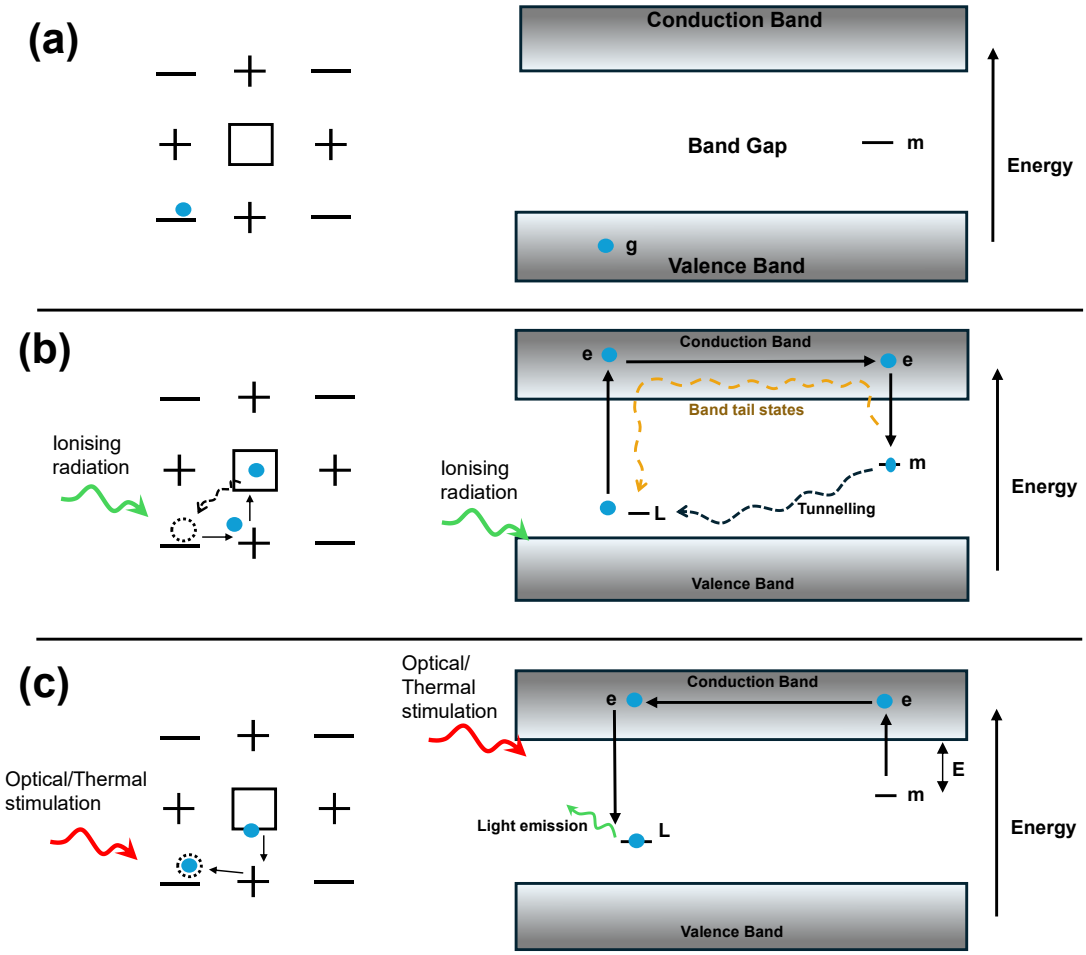

Figure 4.2: Illustrative overview of the luminescence process with the crystal lattice structure, left, and energy band states, right. **(a)** Crystal lattice structure of positive and negative ions contains occasional defects (box, left; m, right), under normal conditions electrons (blue dot) are held in the valence band in ground state, *g*. **(b)** Ionising radiation causes electron diffusion in an excited state *e,* up into the conduction band where it is attracted towards the nearest defect trap, *m*. The loss of this electron from its parent nuclei leaves behind a hole that may later act as a luminescence centre, *L*. In feldspars, loss of electrons from traps to recombination centres can occur athermally through processes of quantum mechanical tunnelling or via the conduction band through lower-energy band tail states. **(c)** Stimulation from optical or thermal sources cause vibrations in the lattice which will shake electrons free from their traps and some will travel to the nearest radiative recombination centre where energy is released in the form of light emission. The energy required for trap escape back to the conduction band, *E* is often termed 'trap depth'. Figure created after: Aitken (1985), Smedley & Wintle (2018), Mahan & DeWitt (2019).

intensity (Wallinga et al., 2000). Interpolation of the natural luminescence signal with the dose response curve will yield the equivalent dose (D_e) in Gy, which can subsequently be divided by the environmental dose rate (Gy/ka) to obtain the sample age (Figure 4.3c) (Mahan & DeWitt, 2019). These procedures in the form of thermoluminescence (TL) (i.e. heating the sample for measurement) were initially predominantly used in the field of archaeology as a method to date the age of artefacts such as pottery – where the intense heat during the firing process in its creation is sufficient to fully reset the signal (Aitken, 1985). The addition of optically stimulated luminescence (OSL) and infra-red stimulated luminescence (IRSL) methods opened the way for a wide variety of applications across the field of geomorphology (see Brown, 2020).

4.1.4 Luminescence Thermochronometry and Kinetic Considerations

Given the significance of heat as a de-trapping energy, it was recognised that the determined apparent age of an unbleached sample (i.e. surface bedrock that has not been exposed to significant heat) must be associated with a specific temperature within the crust at which a mineral changed from being empty in a continuously excited state, to increasing stability, instigating electron trapping and accumulation of charge. Determination of this 'closure temperature' (Dodson, 1973), along with information on local geothermal gradients thus permitted the application of thermochronometry in luminescence (Figure 4.3a).

The very low closure temperatures of luminescence methods (e.g. Guralnik et al., 2013, 2015) enables a higher resolution determination of near-surface exhumation compared to other thermochronometers (Figure 4.1). For example, OSL thermochronometry using quartz has previously been applied to decipher rates of exhumation and landscape evolution on the scale of 10's ka with closure temperatures down to 30°C (e.g. Herman et al., 2010). However, such a method is limited by the low sensitivity nature of quartz, saturating much more rapidly at lower doses than feldspar, which is typically 10-15 times brighter and applicable to much higher dose rates, as well as being the most ubiquitous mineral on Earth (Aitken, 1985). As such, targeting feldspar minerals for OSL thermochronometry has successfully obtained ages and exhumation rates on the longer scale of 100's ka (King et al., 2016b). One of the shortcomings of OSL, however, is that the stimulation and release of luminescence using a laser source is instantaneous, providing only a single measure of the

total trap charge. Recently, the use of a Multi-OSL approach was developed in an attempt to overcome this by combining IRSL measurements over a range of temperatures to extract data from different closure temperatures, giving improved, multiple constraints on recent cooling history (King et al., 2016c).

An alternative and arguably more suitable approach is the use of TL for thermochronometry (TLT). Using heat rather than light allows the stimulating energy to be increased gradually, sequentially releasing traps that are associated with different closure temperatures and thus measuring the full range of luminescence emissions as a function of temperature across the continuum of thermal stabilities within a sample (Figure 4.3a-b). This has the potential to provide far more detailed data on the exhumation journey of a single sample up through the crust, which is itself a lightless but thermally varying system, enabling analysis to much lower cooling histories (e.g. <0°C) for evidence of rapid exhumation and surface changes on the scale of 10^2 to 10^6 years (Brown et al., 2017). In this way, TL has been described as a multi-thermochronometer (Biswas et al., 2018).

Whilst calculation of age can be relatively straightforward using only the equivalent dose and dose rate (Figure 4.3c), extracting the full cooling history of a sample is rather more complex, requiring robust constraints on the kinetic parameters that govern trapping and detrapping behaviour as a function of temperature (*T*) and luminescence over time (*t*). Luminescence of quartz follows general first-order kinetics that can be constrained from measurements and represented mathematically (Table 4.1) – a thorough review is available from King et al. (2016a). Following Brown (2020), a simple electron trapping rate can be expressed as a saturating exponential:

$$\frac{d}{dt}\left(\frac{n}{N}\right) = \frac{\dot{\mathrm{D}}}{D_0}\left(1 - \frac{n}{N}\right) \tag{4.1}$$

Here, the number of filled traps (n) grows over time according to dose rate ($\dot{\mathrm{D}}$) and degree of saturation (filled traps n, divided by total traps, N) governed by the saturation dose (D_0).

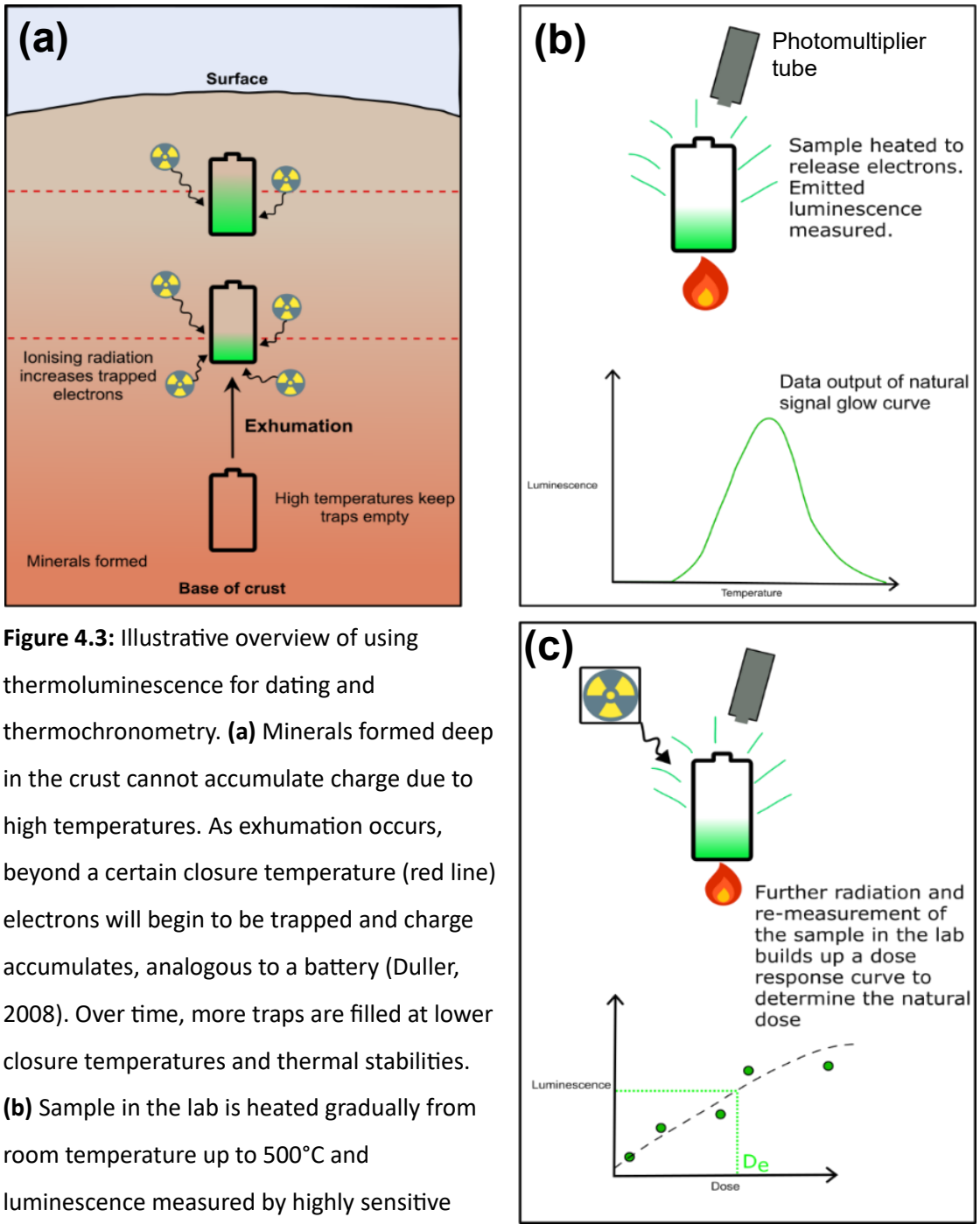

Figure 4.3: Illustrative overview of using thermoluminescence for dating and thermochronometry. **(a)** Minerals formed deep in the crust cannot accumulate charge due to high temperatures. As exhumation occurs, beyond a certain closure temperature (red line) electrons will begin to be trapped and charge accumulates, analogous to a battery (Duller, 2008). Over time, more traps are filled at lower closure temperatures and thermal stabilities. **(b)** Sample in the lab is heated gradually from room temperature up to 500°C and luminescence measured by highly sensitive photomultiplier tube. Resulting glow curve records the amount of trapped charge that has been released over the continuum of thermal trap depths, a function of luminescence intensity. **(c)** Re-measuring the sample after a series of known control radiation doses builds up a dose response curve of luminescence intensity with dose rate. From this, the equivalent dose (D_e) of the natural sample can be interpolated from its luminescence

Table 4.1: Some standard kinetic parameters used to describe luminescence behaviour.

Term	Description
E	Activation energy/Trap depth (eV)
s	Escape frequency factor (s^{-1})
N	Total number of traps in crystal lattice
n	Number of filled traps
N - n	Number of available traps
n/N	Saturation ratio
ρ	Recombination centre density (m^{-3})
D_0	Characteristic dose of saturation (Gy)
$\dot{D}$	Dose rate (Gy/ka)

The rate of thermal detrapping can then be expressed according to trap depth (*E*), escape frequency (*s*), temperature through time (*T*) and the Boltzmann constant (k_B):

$$\frac{d}{dt}\left(\frac{n}{N}\right) = -\frac{n}{\mathrm{N}} \cdot s\, exp(-E/k_B T) \qquad (4.2)$$

As well as the first order behaviour outlined above in equations 4.1 and 4.2, thermoluminescence of feldspars is controlled by more complex athermal kinetics that need to be accounted for. Anomalous fading of feldspar signals following laboratory irradiation was found to occur beyond an expected amount from small proportions of thermally unstable traps close to the conduction band by Wintle (1973). This is believed to arise due to non-first-order kinetics, whereby electron detrapping and recombination can occur without significant thermal or optical stimulation through the processes of quantum mechanical tunnelling and/or diffusion through lower energy band-tails at the edges of the conduction and valence bands (Figure 4.2b) (Poolton et al., 2009).

Furthermore, it is important to recognise the potential impact of sensitivity changes in a sample between measurement of natural doses acquired over long geologic timescales, to measurements of shorter but stronger doses administered in the lab. Such a difference has the potential to yield inconsistent saturation (n / N) values and so must be constrained and accounted for during the measurement process (Brown et al., 2017; Brown, 2020).

4.1.5 Chapter Aims and Objectives

Despite the added challenges of non-first-order behaviour in feldspar TL as outlined above, it remains a better choice of target mineral for thermochronometry applications as it provides a brighter signal that saturates less readily than quartz over geologic timescales. Consequently, in this chapter, Thermoluminescence Thermochronometry (TLT) is applied to potassium feldspars extracted from samples of bedrock from two glacial catchments in the Swiss Alps, following the methodology of Brown et al. (2017) and Brown & Rhodes (2022), to determine the spatial and temporal patterns of exhumation likely governed by glacial activity. The overall objectives of this chapter are to:

1. Demonstrate the sensitivity and suitability of acquired samples to TL measurements.
2. Using the most appropriate method, constrain the necessary kinetic parameters to enable determination of cooling histories and exhumation rate.
3. Examine the exhumation rate from a spatial distribution of samples at each catchment to explore the patterns through time and discuss possible influences of glacial erosion.

In the following section I will describe the sample collection process, their location in the field sites and the subsequent preparation back at the lab before measurement. Following from this, in the methods section I will outline the main Multiple Aliquot Additive Dose (MAAD) method that was employed to get the final results, as well as the numerical model used to constrain the kinetic parameters. Several preliminary tests that were carried out to investigate sample sensitivity and TL characteristics will also be outlined briefly. Afterwards, the main results from each catchment will be presented followed by a discussion on what these results suggest for patterns of glacial erosion over the last glacial cycle.

4.2 Sample Collection, Context and Preparation

4.2.1 Sample Collection and Context

Samples were collected from the two study catchments outlined earlier in Chapter 3 (section 3.2) – Glacier d'Otemma and Triftgletscher. A total of 41 samples were extracted from the bedrock across the two catchments with a hammer and chisel. Time constraints meant that only 11 samples were ultimately measured to completion: 5 at Otemma and 6 at Triftgletscher. The remaining samples are semi-prepared but unmeasured and remain available for future study. Samples were approximately hand-sized and ranged in weight from ~0.5-1.5 kg.

At Glacier d'Otemma, a total of 21 samples were collected, 15 from the main glacier basin during an initial visit in 2021 and a further 6 samples in 2022 from the top of the catchment and ridges around the locally highest summit of the Pigne d'Arolla (3796 m). Samples were extracted along a broad profile distribution at a range of elevations from deglaciated bedrock that would have been covered by ice during the LIA, if not more recently (Figure 4.4). Of these, 5 broadly distributed samples were measured to completion for the final results. The lowest measured sample, beyond the present-day floodplain over 1km from the current terminus, was at an elevation of 2462 m, whilst the highest sample was acquired from a ridge just below the Pigne d'Arolla summit at an elevation of 3688 m. The lower sample was taken from a smooth bedrock bump with significant striations indicating glacial abrasion, whilst the others were taken from rough blocks indicative of quarrying and extra-glacial processes. The valley geology is comprised of similarly hard bedrock, with mostly orthogneiss on the southern side and granodiorite to the north (Figure 4.5), which is reflected in the samples, containing a mixture of quartz and feldspar.

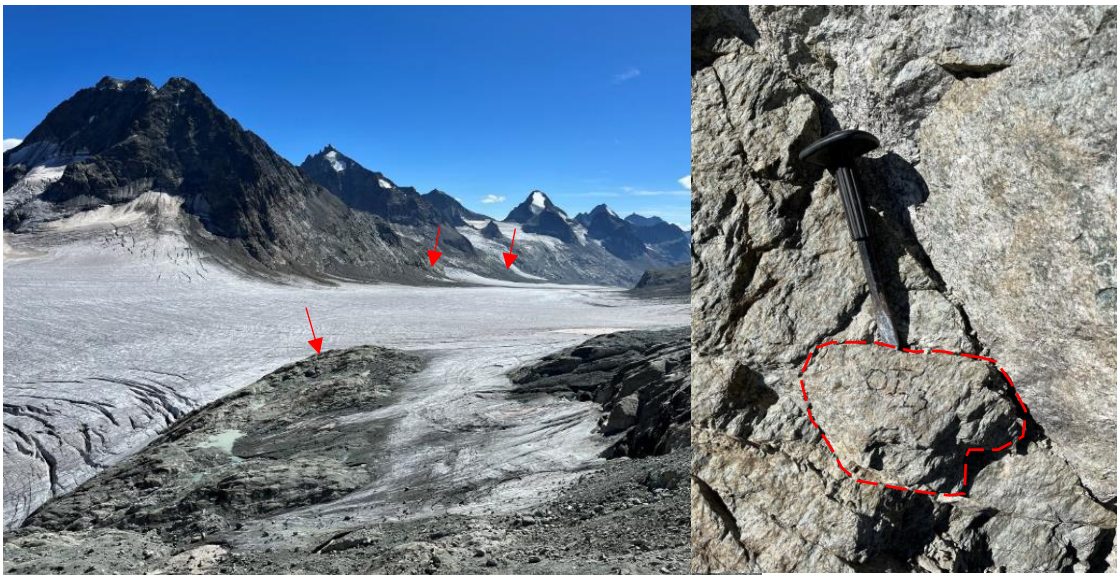

Figure 4.4: Field photos from Glacier d'Otemma. **Left**: view looking back down valley from the top plateau of the glacier. Approximate locations of samples indicated by red arrows (see Figure 4.5 for map overview), from bedrock that was only recently deglaciated in the past few years. **Right**: example of one of the granodiorite samples extracted from the bedrock by hammer and chisel, outlined in red for visibility. Chisel is approximately 25 cm in length.

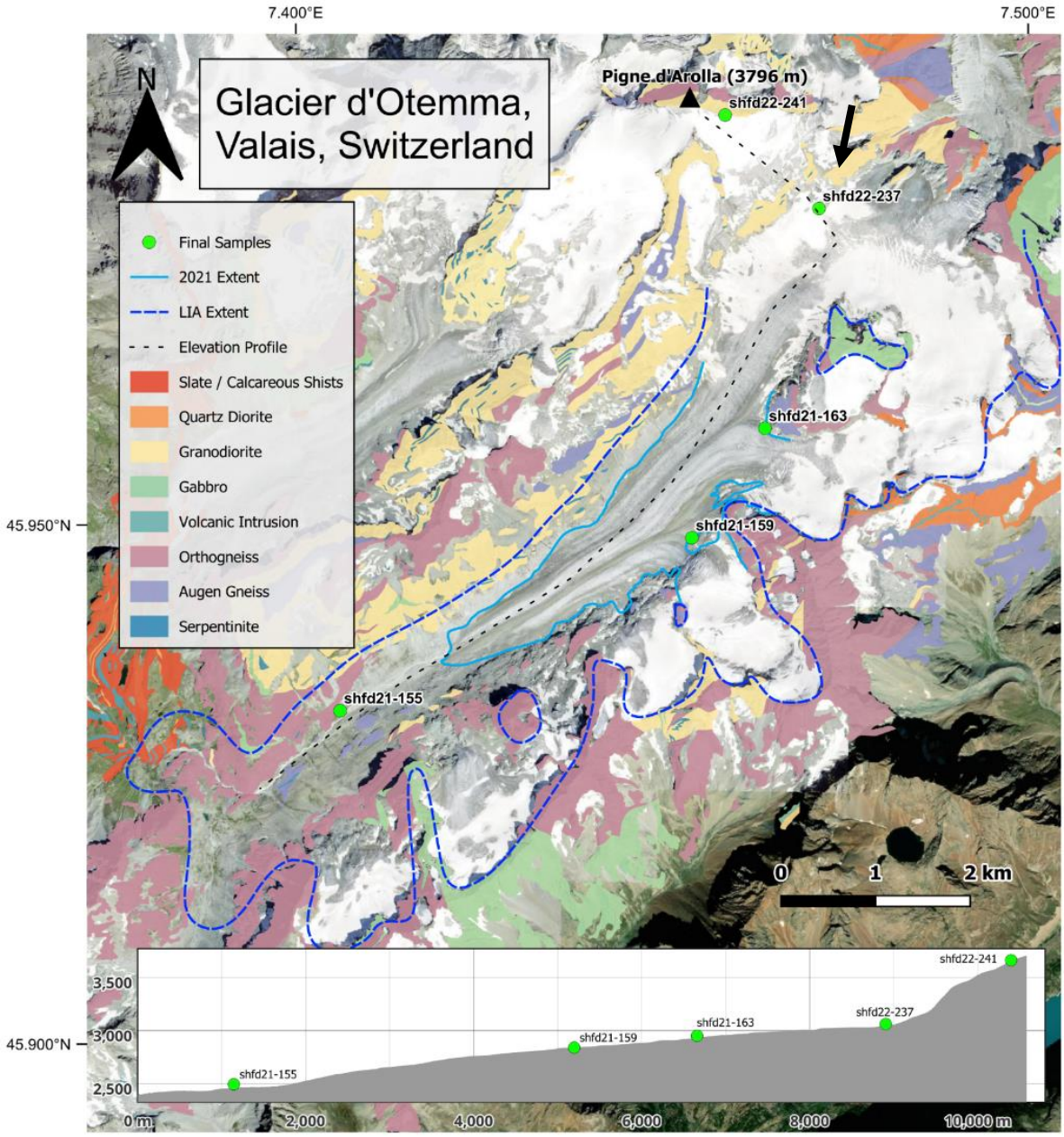

Figure 4.5: Map overview of the final samples used in the analysis from the Galcier d'Otemma site. The lower three samples are from gneiss bedrock, whilst the upper two are comprised of granodiorite. The elevation profile shows the gentle gradient of this glacier, until the steep side heading up to the Pigne d'Arolla summit, which is no longer connected to the main glacier. Sample 155 is located approximately 1km from the current terminus, but well within the LIA extent. Black arrow indicates position of photo from Figure 4.4. (Geology data simplified from Swisstopo, 2022).

At Triftgletscher a total of 20 samples were collected across the catchment in 2021. Several samples were acquired along the long axis of the large bedrock riegel wall (Figure 4.6a) and specifically next to sites previously used for TCN analysis by (Steinemann et al., 2021). A couple of samples were taken from within the deep U-shaped basin portion of the profile, beneath the large bedrock step and proximal to the Triftsee lake currently occupying the overdeepened region. The rest of the samples were acquired in the upper portion of the catchment where the current terminus sits, including a couple on the lip edge of the large step (previous icefall).

Ultimately, 6 samples were measured to completion for the final results at this catchment, the lowest of which was at an elevation of 1647 m and the highest at 2443 m (Figure 4.7). All of these samples would have been covered by ice during the LIA with the exception of shfd21-146 which was situated outside of the large LIA moraine (Figure 4.6b). The catchment is comprised largely of orthogneiss, though there is some complexity in the lithology around the large step with the presence of metamorphic rocks like shist and some slate, often in the form of large bedrock intrusions (Figure 4.6c) (Figure 4.7).

There was an intention to return to this field site to collect further samples from the uppermost portion of the catchment around the cirque headwall; however, temporary closure of the mountain refuge and trail leading to this upper region in the following year (2022) prevented this from being undertaken.

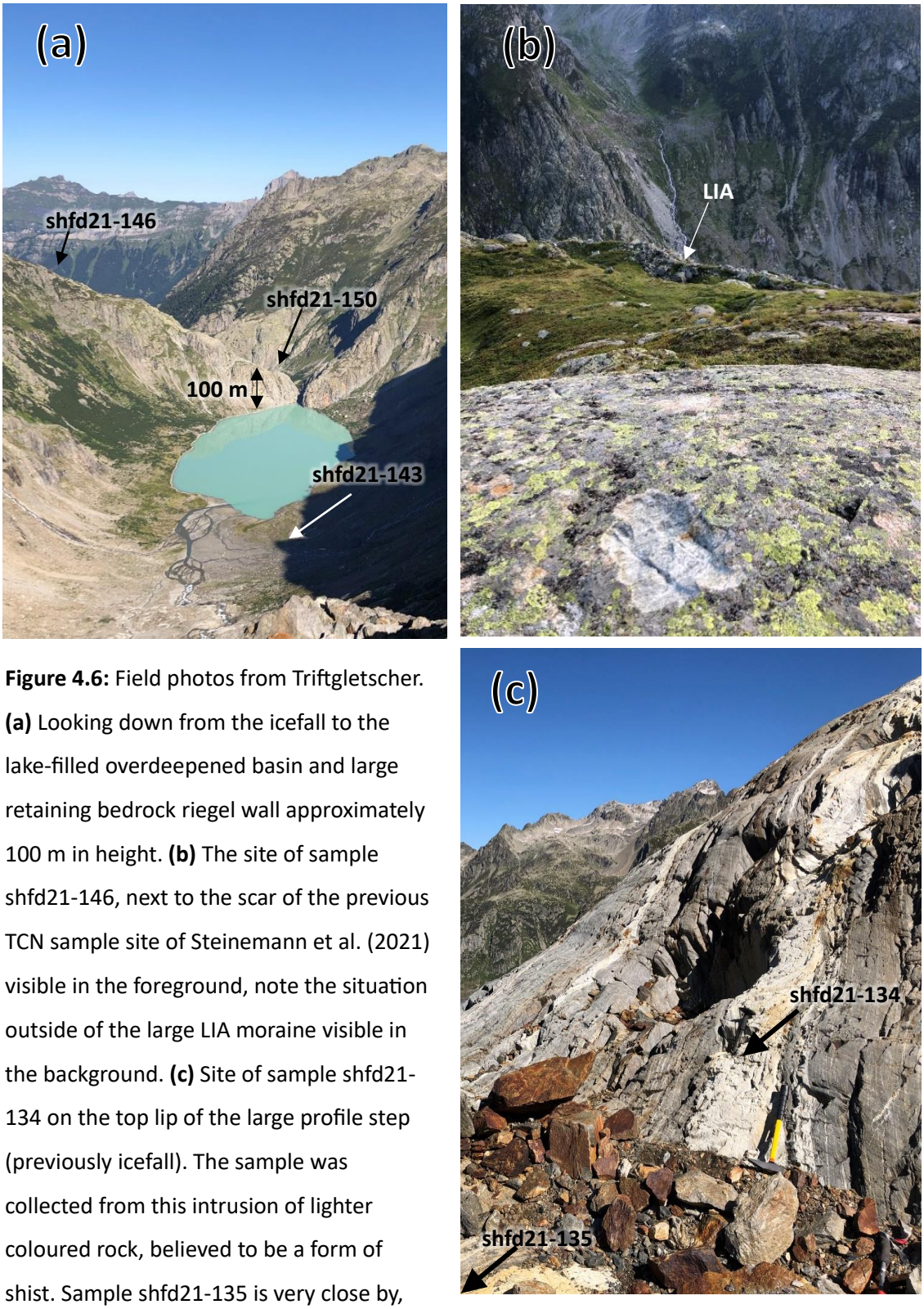

Figure 4.6: Field photos from Triftgletscher. **(a)** Looking down from the icefall to the lake-filled overdeepened basin and large retaining bedrock riegel wall approximately 100 m in height. **(b)** The site of sample shfd21-146, next to the scar of the previous TCN sample site of Steinemann et al. (2021) visible in the foreground, note the situation outside of the large LIA moraine visible in the background. **(c)** Site of sample shfd21-134 on the top lip of the large profile step (previously icefall). The sample was collected from this intrusion of lighter coloured rock, believed to be a form of shist. Sample shfd21-135 is very close by, less than a metre behind the camera position, taken from different orthogneiss bedrock.

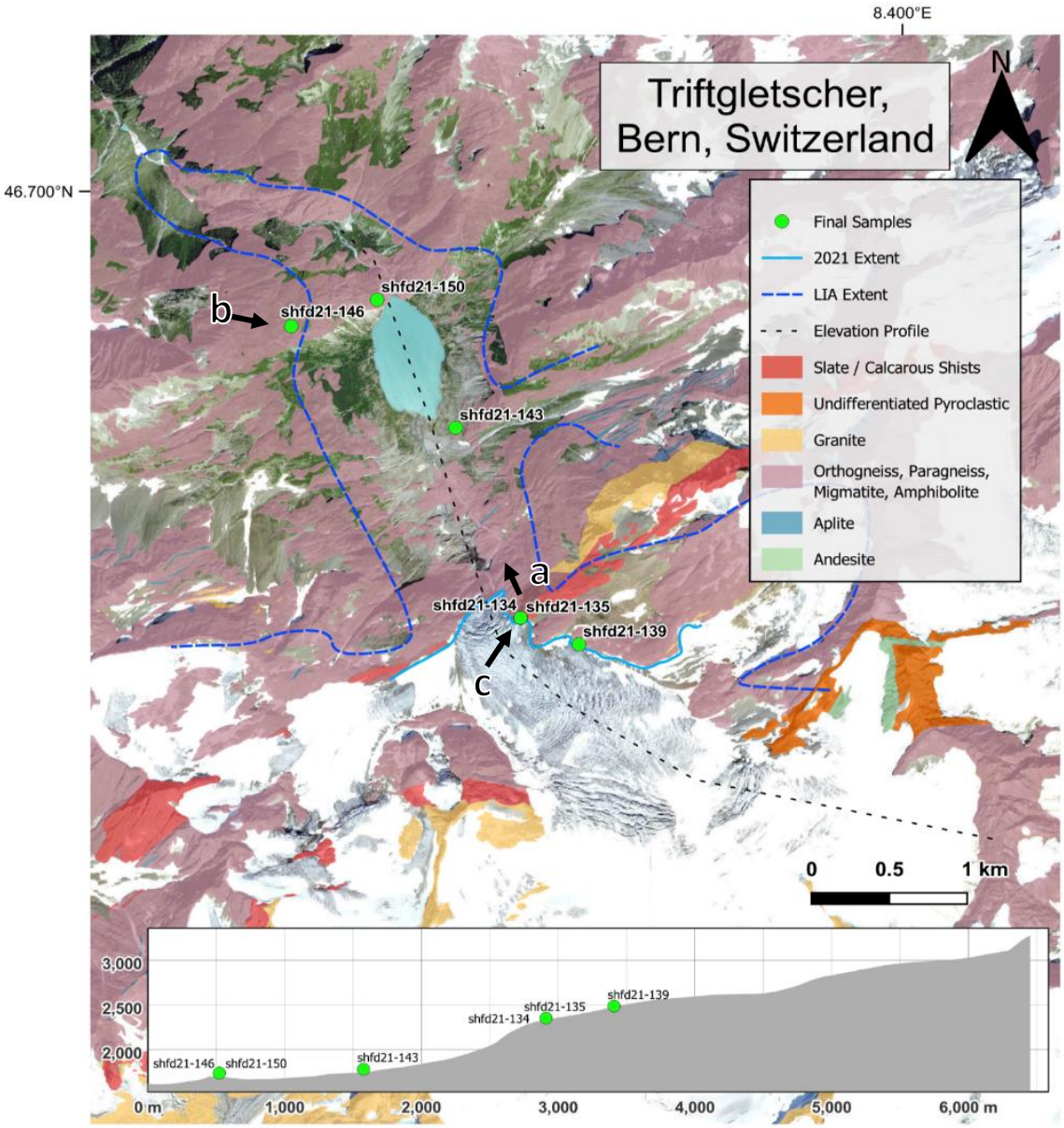

Figure 4.7: Map overview of final samples used in the analysis from Triftgletscher. Samples predominantly come from orthogneiss bedrock, with the exception of shfd21-134 from a shist intrusion (Fig. 4.6c). The elevation profile shows the great variability in catchment gradient and features here, in stark contrast to Otemma. The lower two samples are taken from the large riegel ridge, with shfd21-146 outside of the LIA margins, shfd21-143 is from the deeply scoured basin close to the overdeepening occupied by the lake. Samples shfd21-134 and 135 are just at the top of the large icefall lip, whilst shfd21-139 is a few hundred metres further up on some quarried bedrock. Black arrows indicate positions of photos from Figure 4.6. (Geology data simplified from SwissTopo, 2022).

4.2.2 Sample Preparation

A benefit of the TLT technique is that initial rock samples extracted in the field do not need to be protected from light exposure, as is the case in OSL or TL dating of sediments (Bateman, 2019). Moreover, the TL signal is stable at ambient air and room temperatures, as these only affect the shallow, least thermally stable traps which are removed during measurement with pre-heat protocols. Consequently, bedrock clasts extracted from the field were simply transported in individually labelled bags back to the luminescence lab at the Department of Geography, University of Sheffield.

In order to extract unexposed material for measurement (which does need to be free from light exposure), each clast was spray painted black to make the outside edge easily distinguishable. Thereafter, the edges were broken off under dim red-light conditions in the lab to extract the inner material beyond 1cm depth. Some of the waste edge material was put through a rock mill, crushing it to a fine powder to be sent off to Geochem Client Services, SGS Canada Inc. for analysis with inductively-coupled plasma (ICP) mass spectrometry to determine the U, Th and K contents of each sample, which is required to determine the environmental dose rate (Gy/ka) following conversion factors from Adamiec & Aitken (1998) (Table 4.2).

Upon extraction of the inner portion of each sample, the inner material was split into smaller pieces, gently crushed further in a small hand mill, and then sieved to isolate the 125-180 µm size fraction. This fraction was then separated further using sodium polytungstate heavy liquid ($\rho < 2.58$ g/cm^3) to isolate the potassium feldspar grains, as these provide the best sensitivity and avoid any interference in the measured signal from quartz crystals (Rhodes, 2015).

Table 4.2: Data from ICP analysis and the converted geologic dose rate per sample used for final measurements. Note sample shfd21-139 did not undergo ICP analysis so the dose rate from the nearest sample (135) was used instead.

Sample	K (%)	Th (ppm)	U (ppm)	Dose Rate (Gy/ka)
Triftgletscher				
Shfd21-134	3.9 ±0.2	11.6 ±0.58	4.5 ±0.23	6.32 ±0.36
Shfd21-135	3.5 ±0.18	2.6 ±0.13	4.48 ±0.22	5.36 ±0.32
Shfd21-139	*N/A*	*N/A*	*N/A*	*N/A*
Shfd21-143	1.9 ±0.1	15.3 ±0.77	3.34 ±0.17	4.44 ±0.24
Shfd21-146	2.0 ±0.1	11.2 ±0.56	5.92 ±0.3	4.86 ±0.26
Shfd21-150	3.1 ±0.16	17.6 ±0.88	3.34 ±0.17	5.69 ±0.31
Otemma				
Shfd21-155	1.5 ±0.08	10.5 ±0.53	3.25 ±0.16	3.78 ±0.23
Shfd21-159	3.4 ±0.17	7.8 ±0.39	3.55 ±0.18	5.43 ±0.33
Shfd21-163	3.9 ±0.2	17.4 ±0.87	5.03 ±0.23	6.85 ±0.38
Shfd22-237	3.4 ±0.17	12.4 ±0.62	6.78 ±0.34	6.52 ±0.37
Shfd22-241	2.5 ±0.13	12.3 ±0.62	4.51 ±0.23	5.19 ±0.31

4.3 Methods

A number of different tests and methods were conducted over the course of this project, both to explore the sensitivity and reproducibility of sample responses to TL, as well as the final goal of constraining the kinetic parameters to decipher cooling history and exhumation rate.

I will begin by describing the main successful method used to produce the final results (MAAD), then briefly outline a couple of other minor tests (bleaching profiles; SAR) that were undertaken preliminarily in the initial stages of the project to examine the sensitivity of the samples to TL and to gain some initial insight from SAR-determined sample ages.

4.3.1 Multiple Aliquot Additive Dose (MAAD)

Whilst multiple aliquot procedures were considered the standard approach to luminescence dating in the late 20th century, they have since fallen out of favour, being replaced largely with single aliquot regenerative (SAR) approaches (section 4.3.3). The development of SAR came with the advantage that D_e could be estimated from just a single aliquot of a sample by measuring the natural signal before repeatedly irradiating and re-measuring the same aliquot, reducing the labour intensity and amount of sample material required (Duller, 1994; Wallinga et al., 2000). Such an approach requires accountability for changes in sensitivity between measurements, which often takes the form of a test dose at the end of each measurement sequence. However, since TL measurements fundamentally alter the shape of subsequent regenerative glow curves after heating (Figure 4.8a), this approach is insufficient (Brown & Rhodes, 2022). The multiple aliquot additive dose (MAAD) procedure avoids these issues through the use of several aliquots for each sample, whereby the laboratory irradiation is applied first in addition to the natural dose before subsequent measurement of the entire signal. This provides a means to accurately determine the fraction of saturation from the field that will be essential for obtaining the thermochronometry data (Figure 4.8b) (Section 4.3.1.2).

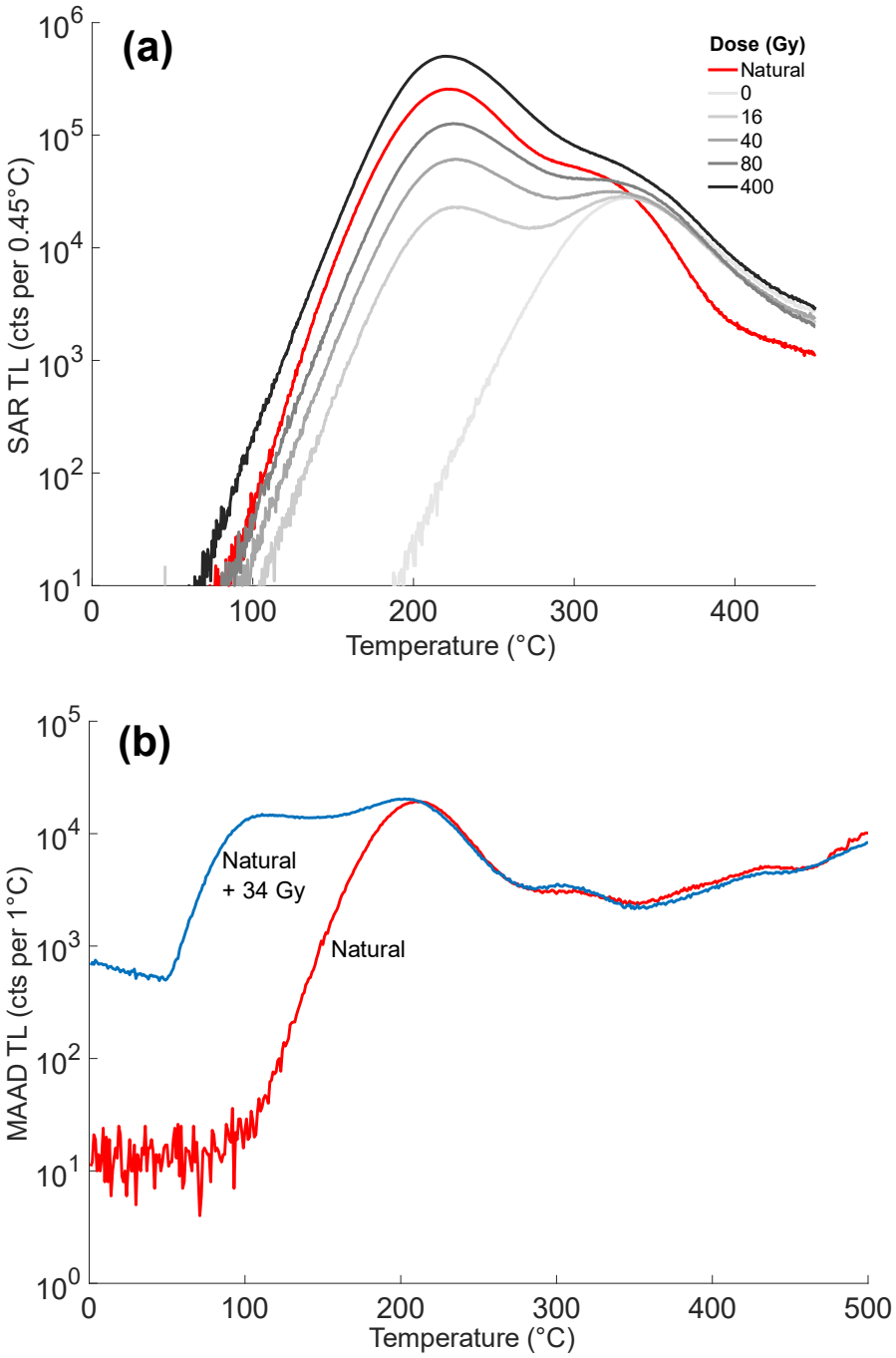

Figure 4.8: Comparing outputs between SAR and MAAD measurements. **(a)** Different SAR doses produce differing amounts of TL intensity at the low and mid temperature ranges, but then converge in the higher temperature region in systematically different behaviour to the natural signal. **(b)** In the MAAD sequence, the additional dose maintains the behaviour of the natural TL from the peak and up into the higher temperature region, permitting more reliable constraints on sample saturation.

4.3.1.1 Measurement Sequence

The MAAD procedure of Brown & Rhodes (2022) was followed (Table 4.3): a total of 23 aliquots per sample were prepared, with 10 individual grains of feldspar applied to each disc using silicon adhesive. The first 15 of these aliquots were used for the additive dose-response measurements at different levels of irradiation (Table 4.3**,** step 1), followed by a pre-heat, before measurement by heating each aliquot from 0 to 500 °C at a rate of 0.5 °C/s with TL emission recorded at every 1 °C.

To quantify rates of athermal fading the remaining 8 aliquots per sample were given the same pre-heat, but the natural signal was measured to a maximum temperature of 310 °C rather than 500 °C, as this covers the main region of interest in the glow curve (150-300 °C) but minimises any changes to the TL recombination kinetics induced by the heating (Brown & Rhodes, 2022). Afterwards, these aliquots were given a dose of 50 Gy and subjected to the same pre-heat once more. Two aliquots were then measured immediately following the previous additive dose procedure outlined in steps 3 – 8 of Table 4.3, whilst the remainder were stored at room temperature as pairs of two before subsequent measurement after a set time had elapsed: 3 ks, 10 ks and several weeks.

Table 4.3: MAAD TL measurement sequence for the 15 additive dose aliquots and 8 fading quantification aliquots. Adapted from Brown & Rhodes (2022).

Step	Treatment	Purpose
Additive aliquots (n = 15)		
1	Additive Dose (Gy): 0 (n = 6), 34 (n = 1), 67 (n = 1), 340 (n = 1), 670 (n = 3), 3375 (n = 3)	Populate luminescence traps
2	Pre-heat (T = 100 °C, t = 10 s)	Removal of unstable traps
3	TL (T = 0-500 °C, t = 0.5 °C/s)	TL signal measurement
4	TL (T = 0-500 °C, t = 0.5 °C/s)	Background measurement
5	Test dose (D_t = 10 Gy)	Uniform dose for normalisation
6	Pre-heat (T = 100 °C, t = 10 s)	Removal of unstable traps
7	TL (T = 0-500 °C, t = 0.5 °C/s)	Test dose signal measurement
8	TL (T = 0-500 °C, t = 0.5 °C/s)	Background measurement
Fading aliquots (n = 8)		
i	Pre-heat (T = 100 °C, t = 10 s)	Removal of unstable traps
ii	TL (T = 0-310 °C, t = 0.5 °C/s)	TL signal measurement
iii	Dose (50 Gy)	Populate luminescence traps
iv	Pre-heat (T = 100 °C, t = 10 s)	Removal of unstable traps
v	Pause for t = 0 s (n = 2), 3 ks (n = 2), 10 ks (n = 2), ~3-7 wk (n = 2).	Time for anomalous fading
vi	Measurement as of steps 3-8 of additive aliquots	Measurement of anomalous fading

4.3.1.2 Determination of Kinetic Parameters and Cooling History

A reliable determination of the kinetic parameters that govern trapping and detrapping behaviour is required for each sample in order to unlock the full cooling history and respective rate of exhumation. To achieve this, the localised transition model of Brown et al. (2017) is used, which assumes trapping and detrapping probability by localised excited state tunnelling to the nearest luminescence centre. An overview of the fundamental terms are provided here, but the reader is directed to Brown et al. (2017), from which the following equations are taken, for a complete breakdown and description of the model.

The net change in trapped electron concentration is expressed as:

$$\frac{dn(r')}{dt} = \frac{\dot{\mathrm{D}}}{D_0}\big(N(r') - n(r')\big) - n(r')\exp\left(-\Delta E/k_B T\right)\frac{P(r')s}{P(r') + s} \tag{4.3}$$

Here, accumulation is dependent on the proportion of unoccupied traps $N - n$ as a function of the dimensionless recombination centre distance r', dose rate $\dot{\mathrm{D}}$ (Gy/s) and limited by the characteristic dose of saturation D_0 (Gy). Loss is expressed through multiplication of the concentration of trapped electrons at some distance $n(r')$ by their probability of recombination from activation energy, or trap depth ΔE (eV), temperature T (K), Boltzmann constant k_B (eV/K), escape frequency factor s (s^{-1}) and excited-state tunnelling probability $P(r')$ (s^{-1}). The tunnelling probability $P(r')$ is itself governed by a tunnelling frequency factor P_0 (s^{-1}) and dimensionless recombination centre density ρ' (see Brown et al. 2017).

Equation 4.3 is solved numerically within MATLAB code written by Nathan Brown (Brown, pers. comm.), where the resulting $n(r')$ array is converted back to TL intensity (Brown et al., 2017). This permits the artificial simulation of TL measurements across many different combinations of kinetic parameters which can subsequently be compared to the TL data from the original samples measured in the lab to find the best fitting kinetic values where the TL data matches. Following Brown & Rhodes (2022), the MATLAB code uses a Monte Carlo approach to run 5000 iterations of randomly selected values of kinetic parameters from within the ranges listed in Table 4.4. An outline of the model process is given in Figure 4.9.

Table 4.4: Known, assumed and modelled kinetic parameters used in the model to derive cooling and exhumation rate from MAAD TL thermochronometry.

Term	Description	Value	
Constants			
$\dot{D}$	Dose rate	**Geologic** (Gy/ka): sample specific (Table 4.2) **Laboratory** (Gy/s): 0.081	
$\hbar$	Dirac constant	1.054571817 x 10^{-34} (J·s)	
k_B	Boltzmann constant	8.617 x 10^{-5} (eV/K)	
m_e	Electron mass	9.109383 x 10^{-31} (kg)	
Assumptions			
			Source
m_e^*	Effective electron mass in alkali feldspars	0.79 x m_e	(Poolton et al., 2001)
G_g	Geothermal gradient	30 (°C/km)	(Spooner et al., 2020)
s, P_0	Escape and tunnelling frequency factors	3 x 10^{15} (s^{-1})	(Brown et al., 2017; Brown & Rhodes, 2017)
E_g	Ground-state trap depth	2.1 (eV)	(Brown & Rhodes, 2019)
Modelled			
ΔE	Activation energy	0.8 to 1.2 (eV)	
ρ	Recombination centre density	10^{24} to 10^{28} (m^{-3})	
D_0	Characteristic dose of saturation	Sample specific (kGy)	
N	Trap concentration	Sample specific (m^{-3})	

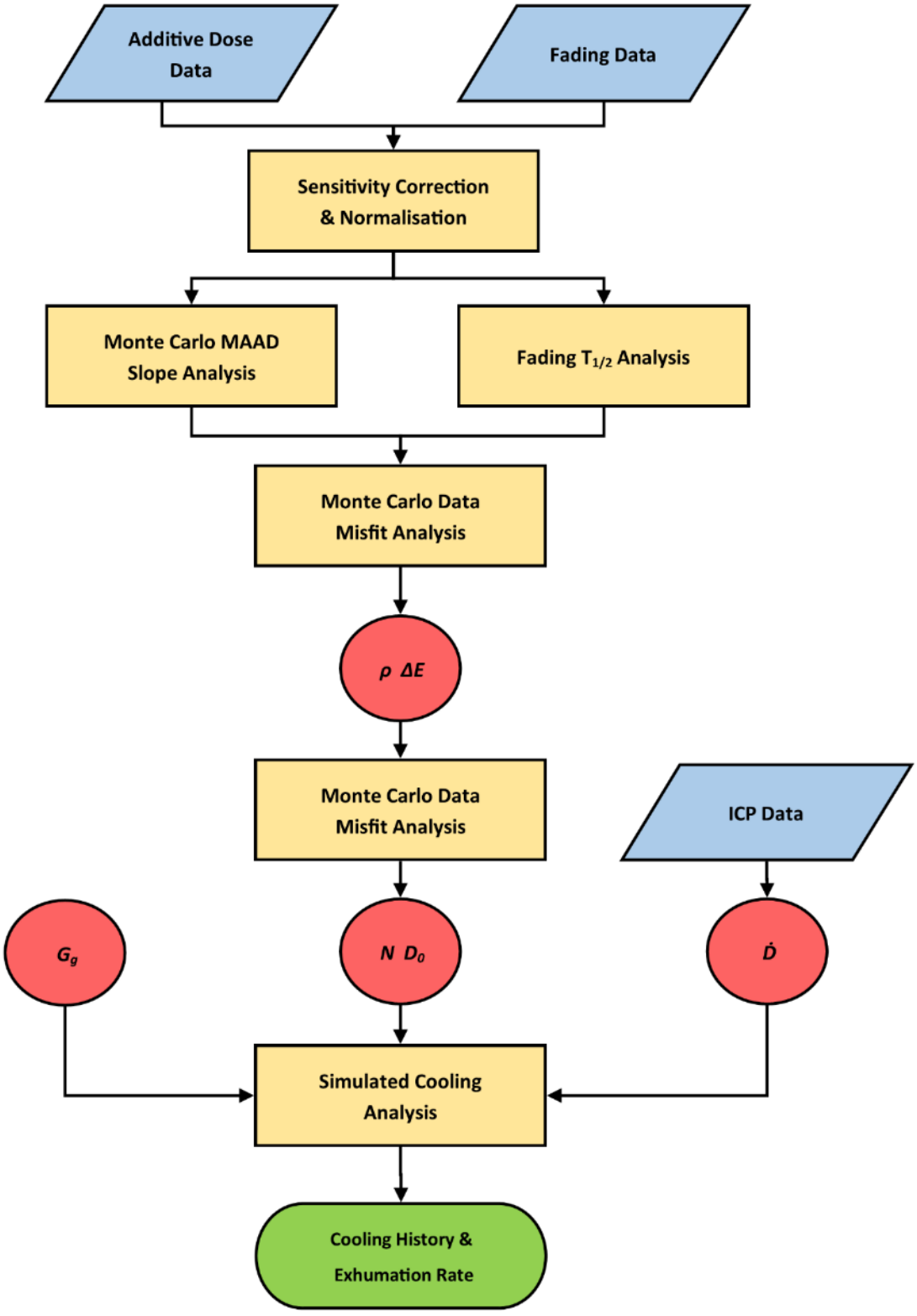

Figure 4.9: Flowchart illustrating the processes of the kinetic model in MATLAB. Datasets represented by the blue parallelograms, model process by yellow squares, kinetic parameters by red circles and the final output as the green oval. Modified from Brown & Rhodes (2022).

The approach is similar to that of King et al. (2016c), in that forward modelling is first used to determine kinetic parameters and test the sensitivity of signals to possible cooling histories, followed by inverse modelling to extract the actual cooling history based on the naturally measured TL data (Brown, 2017).

Firstly, on a per sample basis, data from the MAAD measurements are fed into the MATLAB code and sensitivity corrections are performed by subtracting the background measurements from the main TL data and normalising data according to test doses (Table 4.3, steps 4-8). Secondly, quantification of anomalous fading is performed by extracting the $T_{1/2}$ (temperature at half the maximum luminescence intensity) across the curves at each time-delayed measurement (Figure 4.10a). The $T_{1/2}$ value should progressively increase with storage time as lower temperature, less thermally stable traps are emptied through athermal fading processes.

Monte Carlo simulations are then run across a range of ΔE and ρ values and the data misfit between these simulated and laboratory curves are plotted with an error-weighted sum of squares at the best fit fifth and tenth percentiles (Figure 4.10b). Using values from the best fit tenth percentiles, further simulated MAAD curves are produced and compared once more to the real data, this time to compare the *N* and D_0 misfits (Figure 4.10c). Finally, having determined the best fitting ΔE, ρ, *N* and D_0 values, they are collectively used along with the geologic dose rate to calculate a *n/N* matrix, which combined with assumed local geothermal values (Table 4.4) are used to simulate a geologic cooling history to derive the closure temperature along with cooling and exhumation rates. A 95% confidence interval is applied to the final cooling/exhumation data through application of statistical bootstrapping.

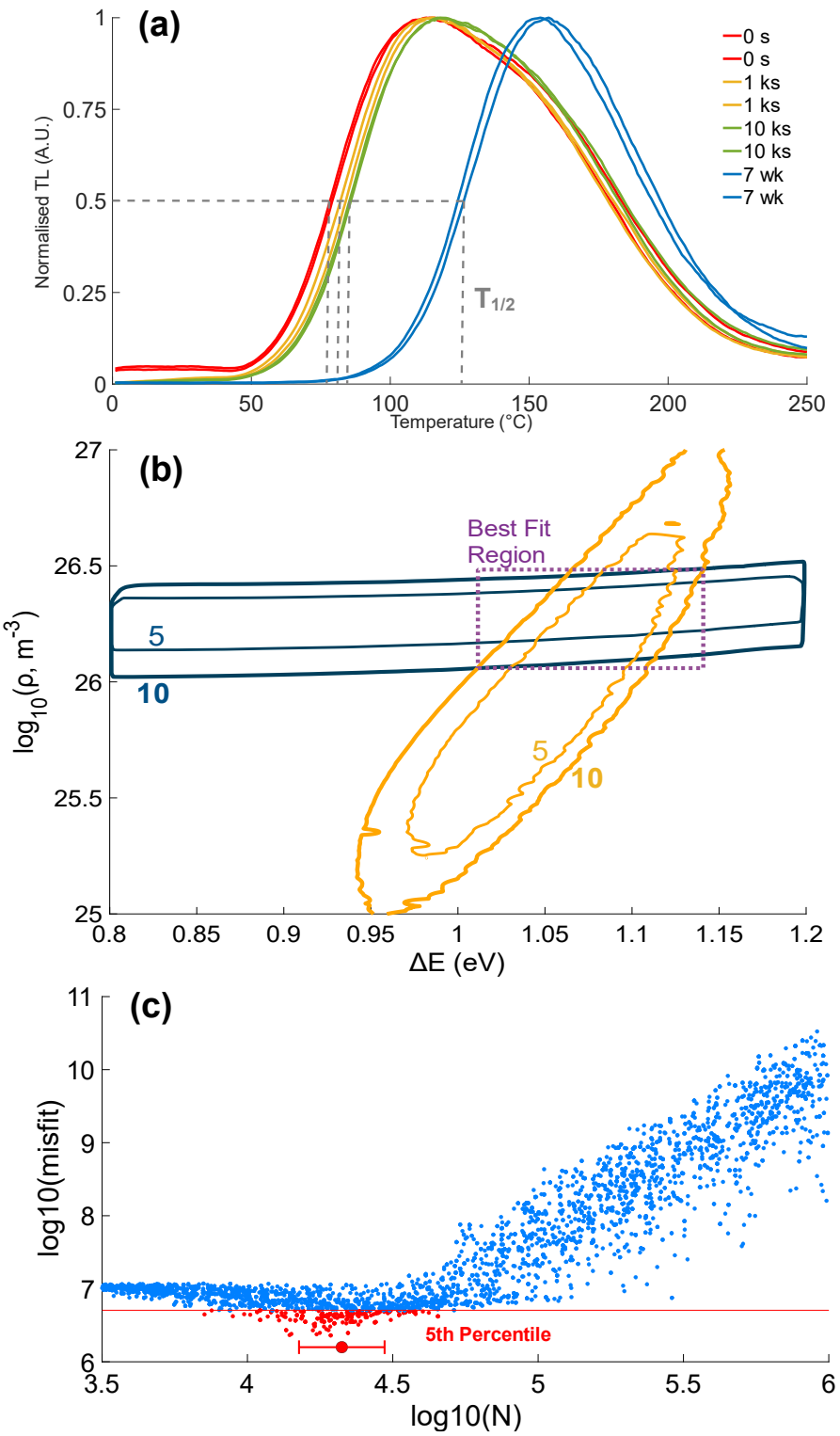

Figure 4.10: Determination of kinetic parameters during the MAAD procedure, here for sample shfd21-135. **(a)** Quantification of athermal fading through analysis of the $T_{1/2}$ shifting to progressively higher temperatures with longer storage time. **(b)** Determination of ΔE and ρ values with best fit 5th and 10th percentiles across Monte Carlo simulations. **(c)** Calculation of best fit mean N value (red circle with 5% error bars) from the best fit 5th percentile (red points) of Monte Carlo runs. A similar plot is produced to determine D_0 values.

4.3.2 Determination of Bleaching Susceptibility

As mentioned prior (section 4.2.2), an advantage of applying luminescence to bedrock samples rather than sediments is that they do not need to be obscured from light sources during field acquisition, as material can simply be extracted from the interior under controlled lighting conditions in the lab. However, this approach requires careful consideration of the amount of the external edge to be removed from the clast to ensure sample material is sufficiently free from any bleaching of the signal caused by penetration of the external sunlight. Bleaching signals from OSL and IRSL methods have been found to occur at depths of ~5 mm in samples of gneiss (Lehmann et al., 2018) and up to 12 mm in granite (Jenkins et al., 2018).

To determine the surface bleaching susceptibility of the samples in this study, a 33 mm core was extracted using a specialised drill from sample shfd21-153, which was comprised of orthogneiss and characteristic of the rest of the samples used in the final analysis. The core was then sequentially cut into a series of 1 mm thin slices which were then measured for TL up to 450 °C at a rate of 0.5 °C/s.

The outcome of this test showed no significant systematic bleaching profile present through the core (Figure 4.11). Significant but unsystematic variation in the natural TL response between slices was an indication of influence from differing proportions of mineralogy (i.e. some slices likely contained more quartz than others). Given such mineralogical irregularity within sliced discs is difficult to control for and that no significant systematic trend with depth was found, there was a decision not to pursue this testing further and to simply take a conservative approach to sample extraction by ensuring well over 1 cm of external edge was removed from sample clasts.

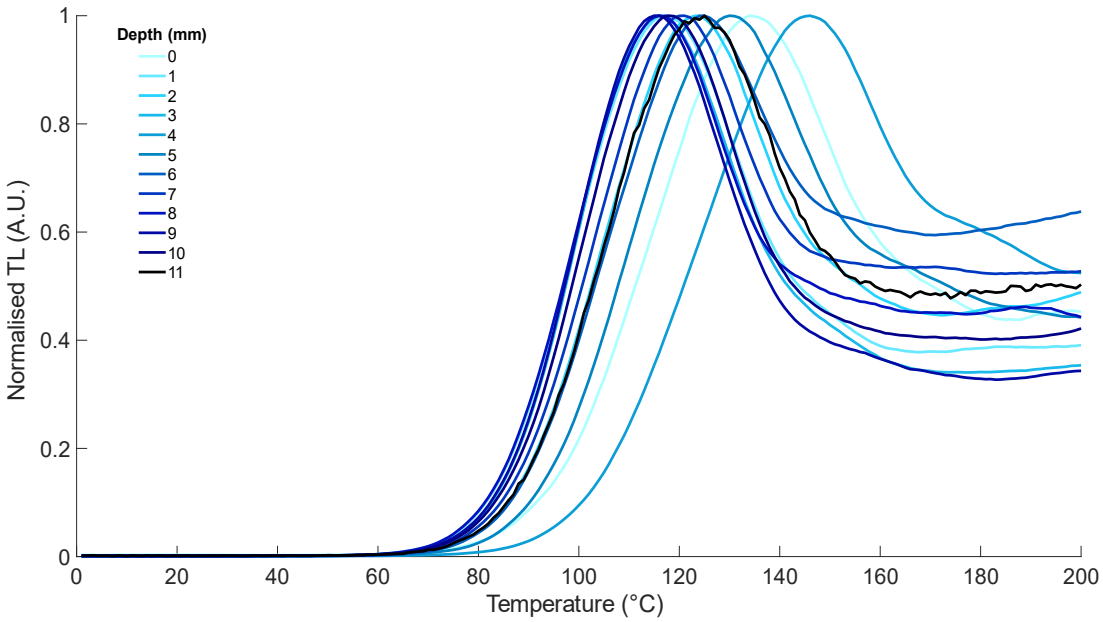

Figure 4.11: Bleaching profile tests for shfd21-153, measuring the natural TL emission from 1 mm thin slices from the outside edge until 11 mm deep. If bleaching were to occur systematically with depth, we would expect to see the signal peaks shifting sequentially to lower temperatures at deeper slices. There is no such systematic change present here, though significant variation in TL response was believed to be influenced by differences in minerology ratios between the slices.

4.3.3 Isothermal and SAR Treatments

As an initial investigation into the sensitivity of acquired samples to TL measurements, a small subset of samples were used to conduct isothermal decay experiments which could then be used to gain an estimate of sample age using a single aliquot regenerative (SAR) protocol.

For the isothermal experiments, a small mono layer of K feldspar was sprinkled onto a single cup per sample. First, the natural TL signal was measured by heating the aliquot up to 450 °C at a rate of 5 °C/s. Then, following each TL measurement a dose of 8 Gy was given to repopulate the traps before the sample was held at a specific temperature for a specific time, these being: T = 50, 100, 150, 200, 250 °C, t = 10, 32, 100, 320, 1000 s. Comparison of the subsequent TL glow curves from each isothermal treatment to the natural signal indicated the appropriate T and t combination to use in the pre-heat procedure for the following SAR protocol (Figure 4.12a).

In the SAR protocol, the sample was repeatedly irradiated and measured across a range of doses from 16.2 Gy up to 1,620 Gy. The resulting TL data was then used to construct a dose-response curve from which the sample's natural geologic dose could be determined by extrapolating the natural TL intensity (Figure 4.12b-c). Dividing the determined dose by the dose rate (from ICP data, Table 4.2) then yielded an estimation of sample age.

The results from this initial SAR testing are presented next in the following section, followed by the main results from the MAAD method.

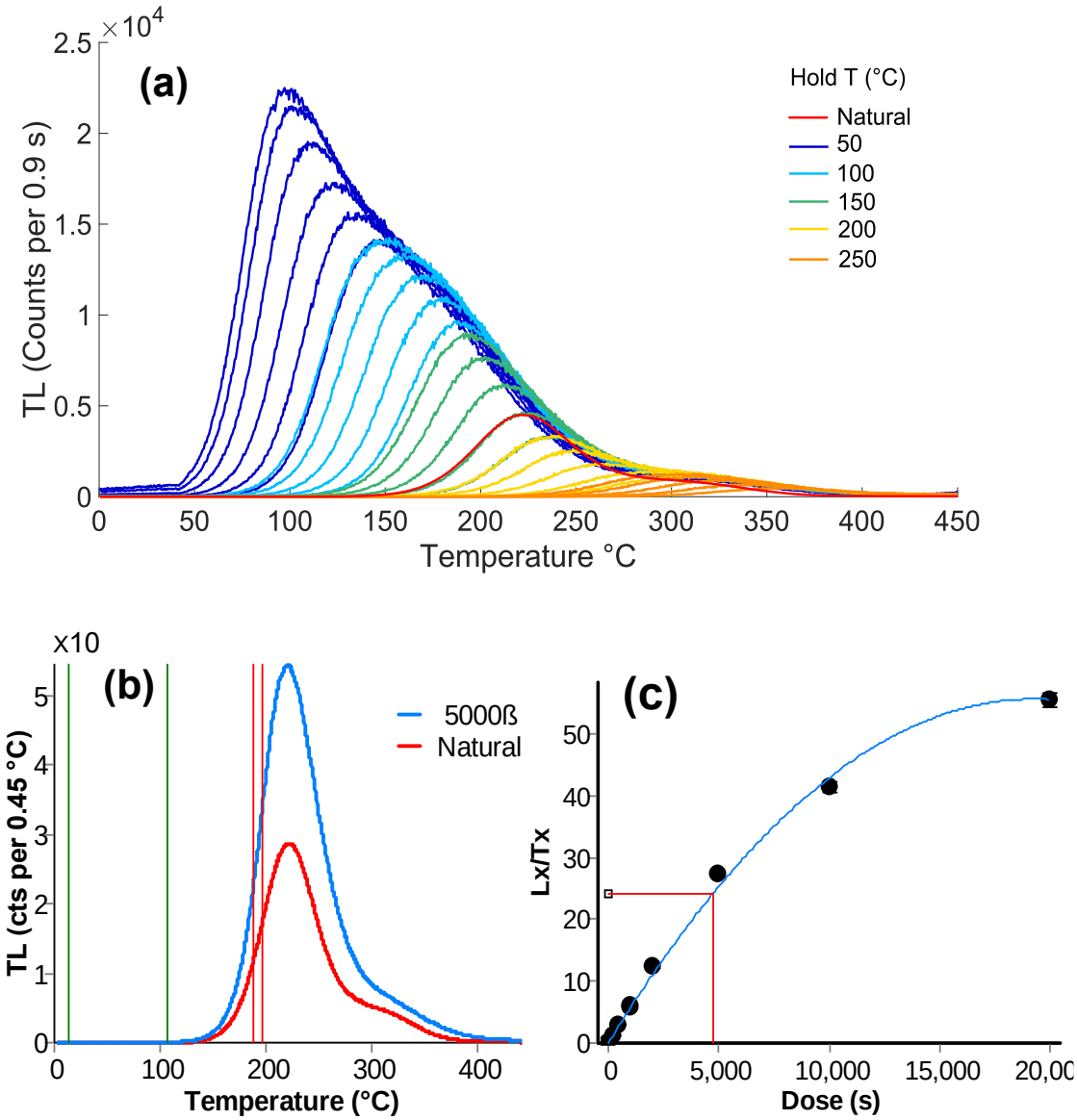

Figure 4.12: Example outputs from the isothermal and SAR procedures, here with sample shfd21-135. **(a)** Isothermal treatment across the five different temperatures and at hold times 10, 32, 100, 320 & 1000 s, with initial 50°C set also held for 3200 s. The red natural data is scaled down to the TL counts of the isothermal data to find the best fit *t*-*T* combination, in this case 320 s at 150 °C. **(b)** TL from the natural signal and closest laboratory Beta dose, $T_{1/2}$ region of interest shown between the red lines, background signal for sensitivity correction shown by the green lines in the low temperature region. **(c)** Dose response curve of sensitivity corrected luminescence (Lx/Tx) according to lab doses. Red line indicates TL of the natural signal, which is interpolated to a dose of just below 5000 s.

4.4 Results

4.4.1 Determined Ages from SAR Protocol

Out of the 11 samples used in the final MAAD protocol, 5 were also fully measured in the initial isothermal and SAR treatments. The equivalent dose of each sample at the $T_{1/2}$ position was used along with their respective environmental dose rate (Table 4.2) to determine an estimated age (Table 4.5). Since the TL signal accumulates up the leading edge of the glow curve, the $T_{1/2}$ position represents a region of traps stable at the current ambient temperature. As such, these estimated ages should be interpreted as the maximum possible time spent at the current temperature (Brown, 2017).

An interesting range of ages has been determined across the samples (Table 4.5). The first four samples are from Triftgletscher, with samples shfd21-146 and 150 situated on the large riegel wall giving similar ages of ~90 ka. A substantial contrast between samples shfd21-134 and 135, situated just metres apart on the crest of the icefall, is hypothesised to be the result of the uniquely different lithology of 134 (see Figure 4.6c, Figure 4.7), as the age of ~240 ka is so far removed from the age of ~80 ka for 135 and indeed the aforementioned other samples from the catchment. Whether this difference can be prescribed to a divergent geologic cooling history or discrepancy in kinetic behaviour between the different rock types is unclear and difficult to determine under the SAR procedure. The intricacies of these two samples will be explored further with results from the MAAD protocol.

Table 4.5: Determined equivalent dose and estimated ages for 5 samples measured using the SAR protocol.

Sample	De (Gy)	Estimated Age (ka)
Shfd21-134	1509.8 ± 88.6	238.9 ± 14
Shfd21-135	425.5 ± 12.6	79.4 ± 2.4
Shfd21-146	451.5 ± 13.7	92.9 ± 2.8
Shfd21-150	520.3 ± 52	91.4 ± 9.1
Shfd21-163	156 ± 10.9	22.8 ± 1.6

The final sample measured here is shfd21-163, the only one from Otemma, which gives a significantly younger age of ~20 ka. At first glance this would appear to be an indication of more rapid exhumation, but once again this cannot be determined without examination of the kinetic behaviour, hence the need for the more advanced methodology afforded by the MAAD procedure.

Ultimately, no further measurements using the SAR protocol were made as the MAAD procedure proved to be far more suitable to constraining the kinetic parameters needed to unlock the full cooling and exhumation history (cf. Figure 4.8).

4.4.2 MAAD TLT Data from Triftgletscher

Using the Monte Carlo simulation approach outlined earlier in section 4.3.1.2, the best fit 5th percentile values were acquired for the kinetic parameters (Table 4.6). These values are consistent with those reported in previous studies for different samples and regions (Biswas et al., 2018; Bouscary & King, 2022; Brown & Rhodes, 2022). They were then used in the inverse model to determine the full cooling and exhumation history. Due to a systematic behaviour intrinsic to the current approach, any data from the most recent 10 ka and beyond 100 ka were deemed unreliable in these samples and discarded (Brown, pers. com.). Hence, the final data is presented on an axis between 10 ka and 100 ka (Figure 4.13). The results are also presented on the catchment map for easier interpretation of the data according to each sample and its context in the landscape (Figure 4.14).

Table 4.6: Kinetic parameters determined for the Triftgletscher samples.

Sample	D_0 (Gy)	ΔE (eV)	N (log10)	ρ (log10)
Shfd21-134	566 ± 217	1.10 ± 0.04	4.33 ± 0.15	26.00 ± 0.20
Shfd21-135	874 ± 494	1.08 ± 0.07	4.45 ± 0.27	26.28 ± 0.22
Shfd21-139	1137 ± 808	1.07 ± 0.07	4.30 ± 0.23	26.17 ± 0.22
Shfd21-143	794 ± 491	1.05 ± 0.07	4.32 ± 0.16	25.92 ± 0.23
Shfd21-146	1607 ± 679	1.05 ± 0.07	4.58 ± 0.18	25.91 ± 0.22
Shfd21-150	1261 ± 698	1.04 ± 0.07	4.62 ± 0.16	25.96 ± 0.21

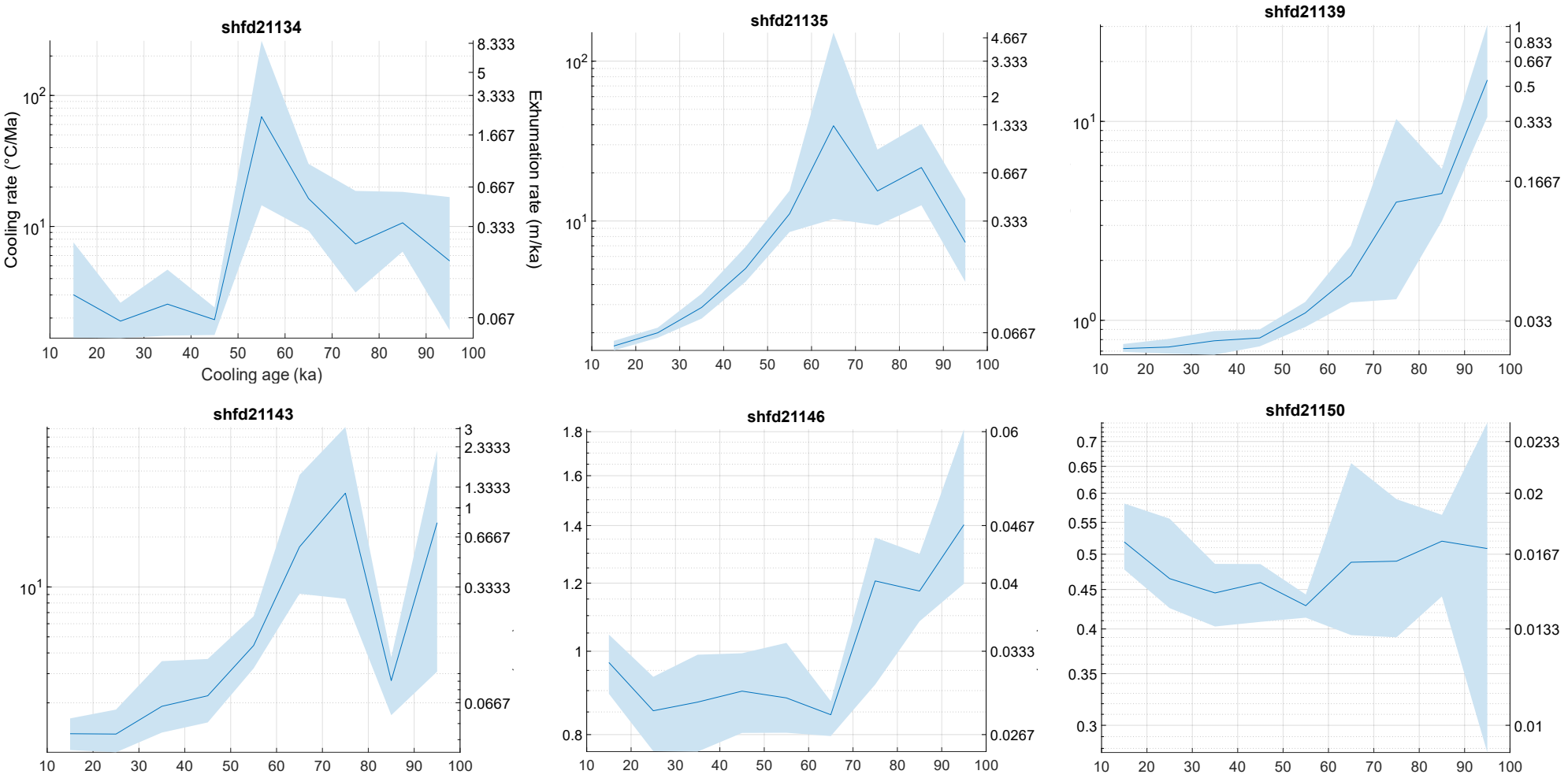

Figure 4.13: Cooling and exhumation rate histories between 10 and 100 ka for the samples from Triftgletscher. Blue shaded area represents the 95% confidence interval bounds. Note that both Y axes are on a log scale.

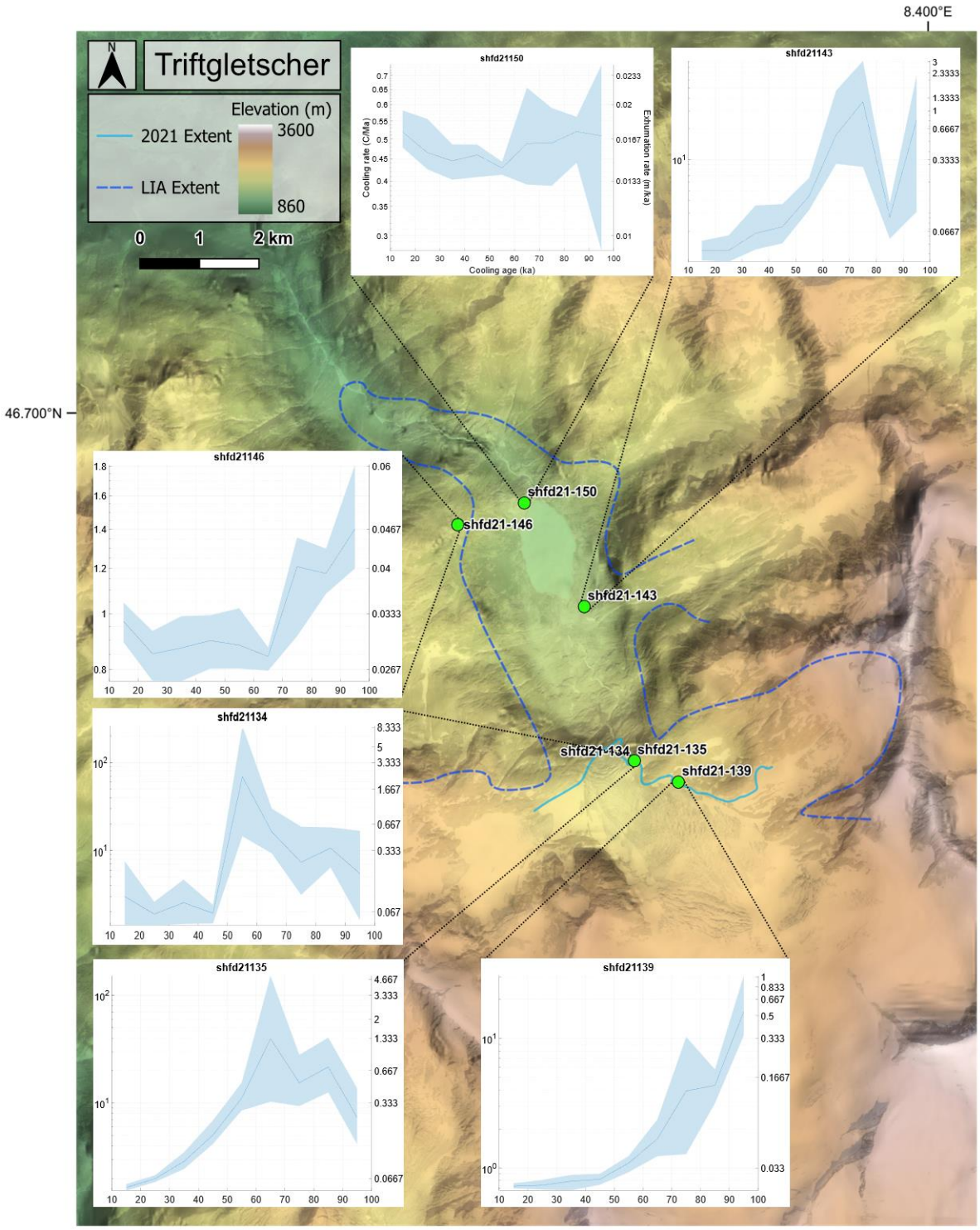

Figure 4.14: TLT data for Triftgletscher in the context of each sample's position in the catchment. Glacier flow direction is from the bottom right to the top left of the map. A substantial contrast in exhumation rates is present between the two lower samples on the riegel ridge (146 & 150) and those higher up near the present-day ice extent.

A wide range of exhumation rates is present across Triftgletscher, the lowest being down towards a possible 0.01 mm a^{-1} at shfd21-150 on the riegel ridge and the highest potentially in excess of 2 mm a^{-1} at samples shfd21-134 & 135 on the icefall crest. The broad trend across the data is a general decrease in exhumation rate moving forwards through time from 100 to 10 ka, though there is significant internal variability between the samples, demonstrating that the decreasing trend is unlikely to be any sort of systematic artefact from the measuring approach.

The trend of the two riegel samples (146 & 150) remain at very low rates of exhumation throughout the determined cooling history, suggesting a very inactive zone of erosion on this landform. Note that the log scale gives the appearance of a large decrease in rates for 146, but the actual change in values is very small from ~0.05 to 0.03 mm a^{-1} (See Appendix 4.7.1 for the data presented on normal linear axes).

Remarkably, the pattern and magnitude of exhumation for the two icefall samples (134 & 135) is highly similar, starting at ~0.3 mm a^{-1} with a high peak in the mid-glacial before decreasing down to values less than 0.1 mm a^{-1}. This correspondence would be expected given the proximity of the two samples, but perhaps not after the aforementioned differences in lithology which resulted in substantial differences in TL sensitivity (e.g. Table 4.5, Figure 4.15). Measured TL response of the two samples can be seen in Figure 4.15 where the MAAD and fading curves for sample 134 contain a high degree of noise and overlap indicative of much lower sensitivity. This is in stark contrast to the neat and uniform response of sample 135 shown below on the same figure.

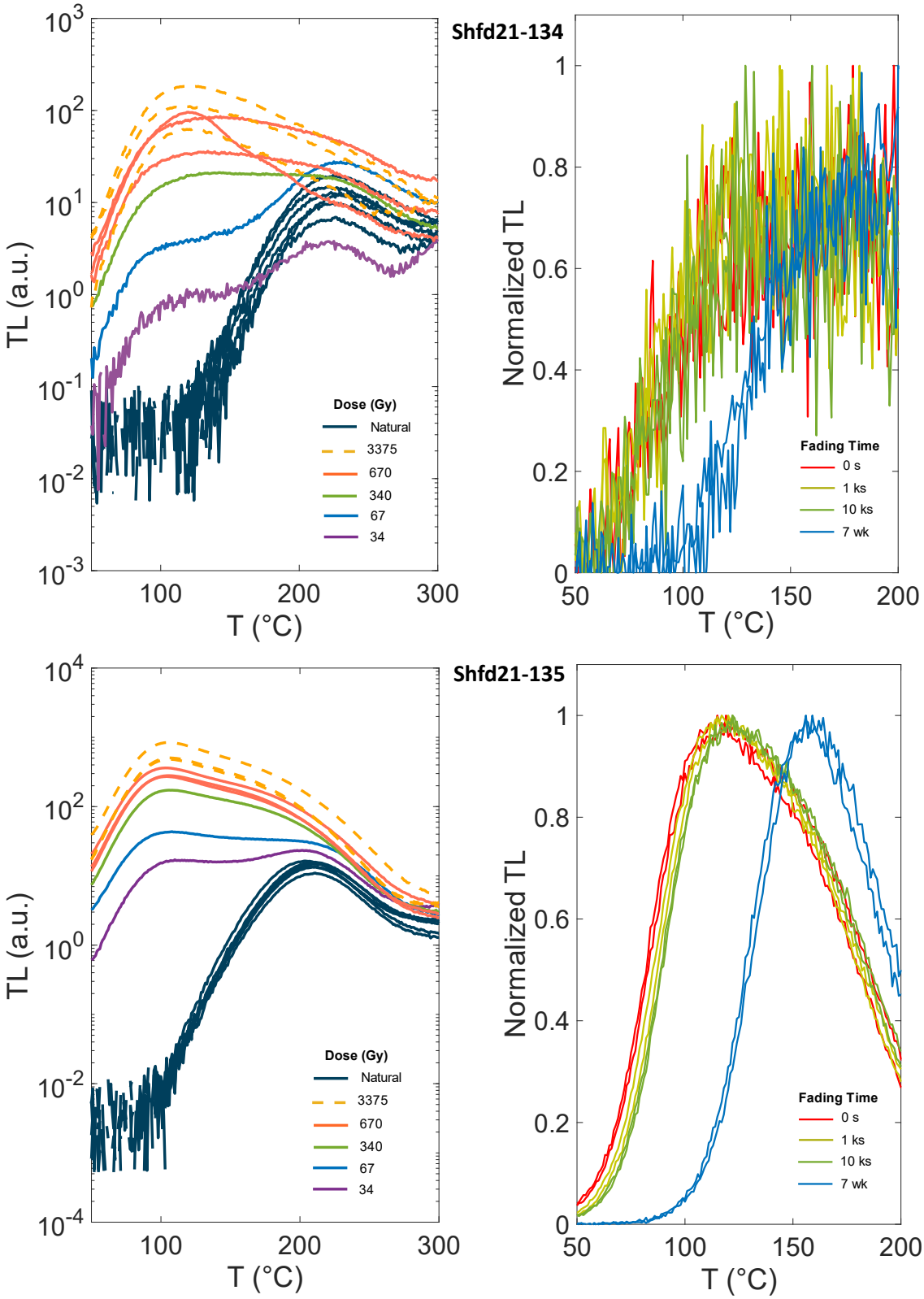

Figure 4.15: MAAD **(left)** and fading **(right)** curves for samples shfd21-134 **(top)** and 135 **(bottom)**. Sample 134 clearly has a much lower degree of sensitivity. The long 7 week hold period has still produced a noticeable fading signal, but the trend is far less clear on the shorter timescales, particularly due to the noisy data from low TL values.

4.4.3 MAAD TLT Data for Otemma

The kinetic parameters determined for the Glacier d'Otemma samples were very consistent with those from Triftgletscher (Table 4.7). Likewise, the derived exhumation rates are of similar magnitude, towards 0.01 mm a^{-1} at the lower end (sample shfd21-159) and towards 2 mm a^{-1} or more at the upper end (sample shfd21-163 and shfd22-241) (Figure 4.16). The general pattern across the catchment is larger exhumation rates at the higher elevations and more limited rates at the lower elevation (Figure 4.17). In a similar fashion to Triftgletscher, a couple of the samples show a peak in rates around the mid-glacial and a few demonstrate a steady decrease in exhumation rate by an order of magnitude towards the late-glacial. The two lower elevation samples (shfd21-159 & 155) maintain a consistently low rate of exhumation, though 155 contains some large uncertainties suggesting potential for a decrease in exhumation rates by up to two orders of magnitude in the mid-glacial and an *increase* by up to two orders of magnitude in the late-glacial. Inspection of the raw TL data reveals a spurious region in the background subtracted signals that correlates to the mid-glacial drop (Appendix 4.7.3), which can be discounted as an error. This does not affect the reliability of the rest of the data.

A significant point of interest is the limited data available for sample shfd21-163, in that the cooling history could only be determined for the last 45 ka, implying that rapid exhumation to the surface has occurred, which is consistent with the high estimated exhumation rates and the previously determined young SAR age (Table 4.5).

Table 4.7: Kinetic parameters determined for the Otemma samples.

Sample	D_0 (Gy)	ΔE (eV)	N (log10)	ρ (log10)
Shfd21-155	819 ± 762	1.08 ± 0.06	3.51 ± 0.15	25.86 ± 0.22
Shfd21-159	1630 ± 1001	1.11 ± 0.04	4.33 ± 0.24	26.39 ± 0.20
Shfd21-163	1374 ± 716	1.09 ± 0.07	4.15 ± 0.11	25.60 ± 0.23
Shfd22-237	786 ± 546	1.08 ± 0.04	3.71 ± 0.13	25.88 ± 0.14
Shfd22-241	1071 ± 765	1.09 ± 0.06	4.06 ± 0.16	25.77 ± 0.22

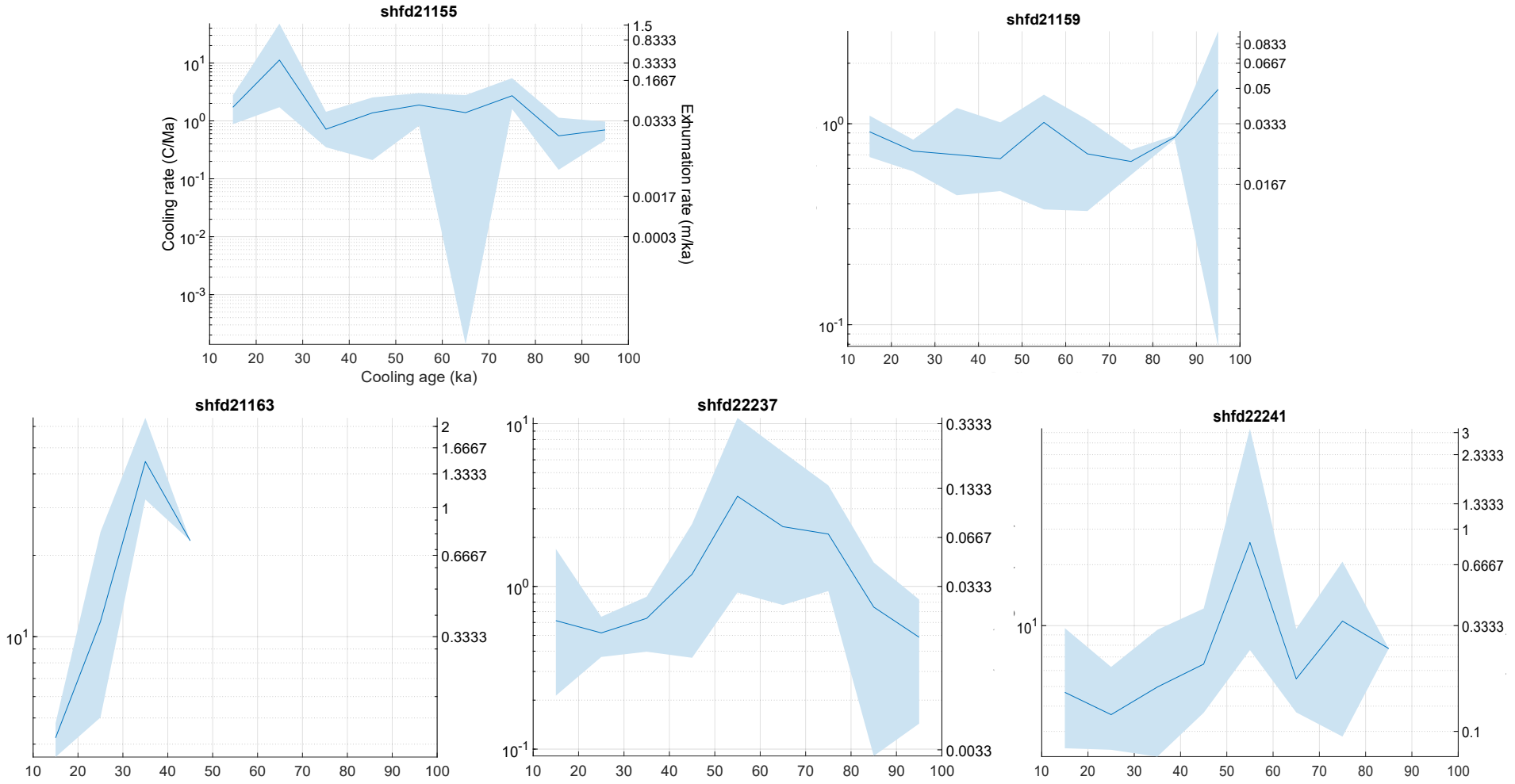

Figure 4.16: Cooling and exhumation rate histories between 10 and 100 ka for the samples from Glacier d'Otemma. Blue shaded area represents the 95% confidence interval bounds. Note that both Y axes are on a log scale.

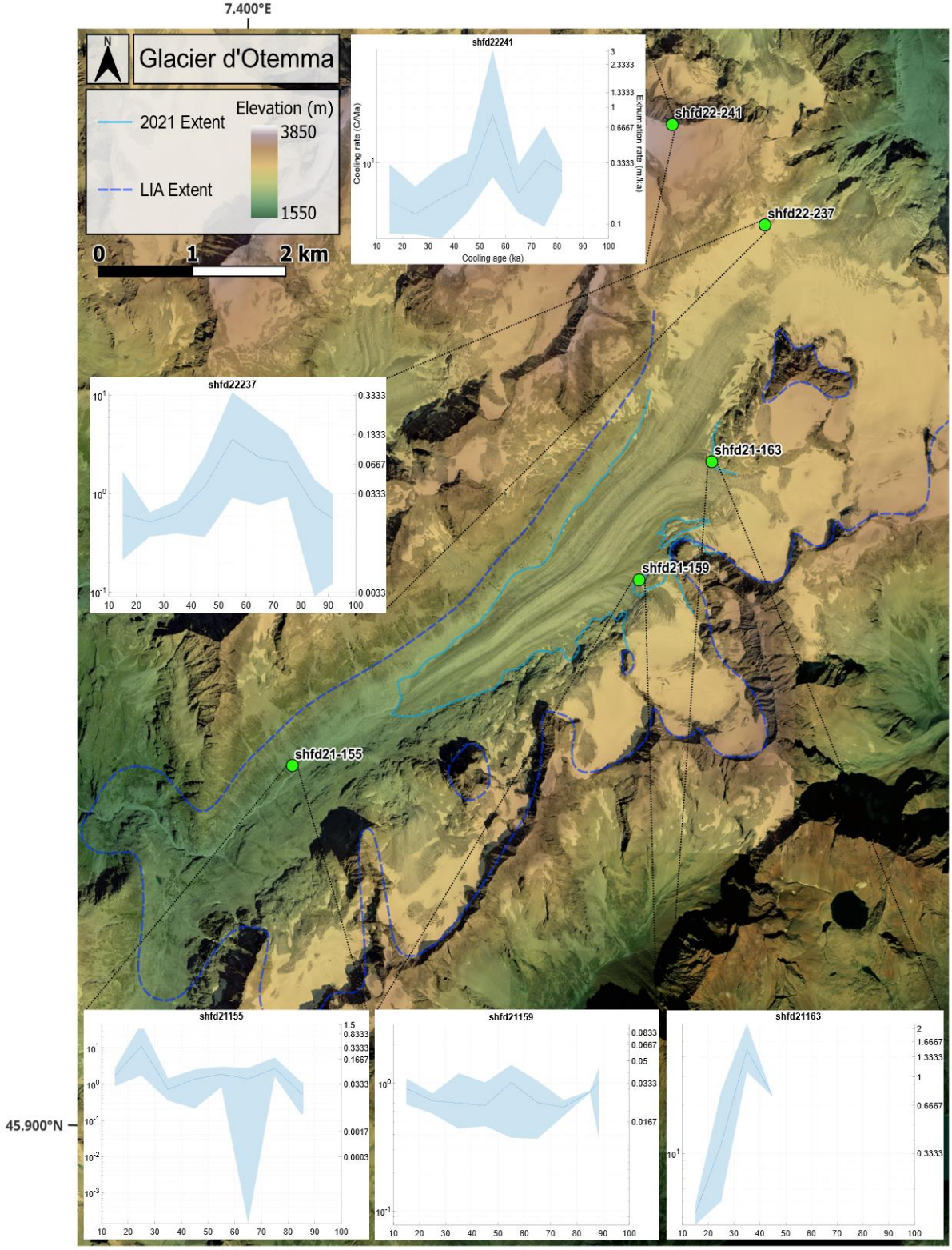

Figure 4.17: TLT data for Glacier d'Otemma in the context of each sample's position in the catchment. Glacier flow direction is from the top right to the bottom left of the map.

4.5 Discussion

4.5.1 MAAD TLT Performance and Accuracy of Results

The MAAD TLT protocol, though a more time-intensive method requiring more sample material and longer measurement sequences than a SAR approach, has successfully unlocked a detailed history of exhumation not previously possible to achieve using more traditional methods of thermochronometry as outlined in section 4.1.2.

It is important to note that the results derived from the MAAD TLT method are, strictly speaking, and as with all thermochronometry, measurements of a cooling rate assumed to represent exhumation – the uplift of rocks relative to the Earth surface. It is therefore not a direct measure of erosion rates, however, the rate of exhumation occurs as an isostatic response equal to the amount of rock removed from the local surface (Molnar & England, 1990) so can be equivalently interpreted as the erosion rate. Thermochronometry alone is also not capable of resolving the specific processes responsible for the erosion: this is left to sensible interpretation given the geomorphic context and history. In this case, given the two study catchments were fully glaciated over the last glacial cycle period covered by the resolution of the measurements (e.g. see Chapter 3), it is reasonable to assign the derived exhumation rates as a response to, and therefore measure of, glacial erosion processes.

A number of assumptions and uncertainties are also integrated to the current methodological approach. Notably, assumptions are made for some of the kinetic parameters used in the model, such as the tunnel and escape frequency factors (P_0, s), which likely vary in magnitude in reality (Jain et al., 2015), but are assigned the same value in this instance for the sake of simplicity and model stability (Brown et al., 2017). Moreover, the use of a simple 1D model and single geothermal gradient to extrapolate the thermal history may result in a systematic bias in interpretation of data into the final results, particularly in settings/samples of more rapid exhumation (Huntington et al., 2007; Furlong et al., 2021). Use of more sophisticated 1D or 3D models to account for lateral variation in thermal pathways and the influence of topography on isotherms has the potential to improve the accuracy of results, but there is a balance to be struck given that more complex models will themselves be reliant on an equally complex set of assumptions (Huntington et al., 2007; Fox & Carter, 2020).

Despite the assumptions and uncertainties involved, the determined exhumation rates in the ranges of <0.1 to >2 mm a^{-1} are consistent with previously reported values of glacial

erosion for contemporary alpine glaciers (e.g. Hallet et al., 1996; Cook et al., 2020) and within the ranges derived from the numerical modelling of the same catchments in Chapter 3. Further, whilst the two samples atop the icefall at Trift (shfd21-134 & 135) were situated just metres apart and thus expected to have undergone very similar exhumation histories over the past 100 ka, they displayed highly different characteristics from ICP data (Table 4.2), SAR analysis (Table 4.5) and TL sensitivity (Figure 4.15), which is hypothesised to be a result of differences in lithology. That the final results do indeed yield the expected similar thermochronology with correlations in kinetic parameters (Table 4.6) and exhumation rates (Figure 4.13) suggests the model is highly adept to appropriately resolving and interpreting cooling histories despite the initial discordance in sample characteristics, demonstrating the value of the MAAD TLT approach compared to more traditional SAR and/or OSL approaches.

4.5.2 Interpretation of Erosion Patterns at Triftgletscher

To aid interpretation of the spatial variation in erosion rates the results were simplified into a relative scale according to the magnitude of erosion at the start (100 ka) and end (10 ka) of the measured time period and broadly interpolated to create a heatmap of erosion for the sampled catchment area (Figure 4.18).

Immediately obvious is the dramatic contrast in erosion between the two riegel samples (shfd21-146 & 150) and the rest of the catchment. These two samples maintain very low rates throughout the whole measured period, demonstrating how this large riegel has sustained such prominence, over 100 m in height (Figure 4.6a), without being smoothed out like the rest of the valley. This poses something of a 'chicken or egg' question – was the riegel formed from persistently low erosion in this zone, or does the presence of the riegel pre-condition the landscape and ice dynamics to minimal erosion through time? The answer is likely an element of both scenarios. A thorough analysis of the area by Steinemann et al. (2021) attributed the formation of the overdeepening at Trift to a zone of enhanced erosion from the confluence of glaciers during larger ice extents (see Chapter 3 section 3.4.1) and the presence of fault zones in this region of the valley. Excavation of the overdeepening here (where the present-day lake now lies), therefore left behind the prominent riegel ridge downstream. Under normal circumstances, high basal water pressures in an overdeepening permits water to ascend the adverse slope of a riegel and

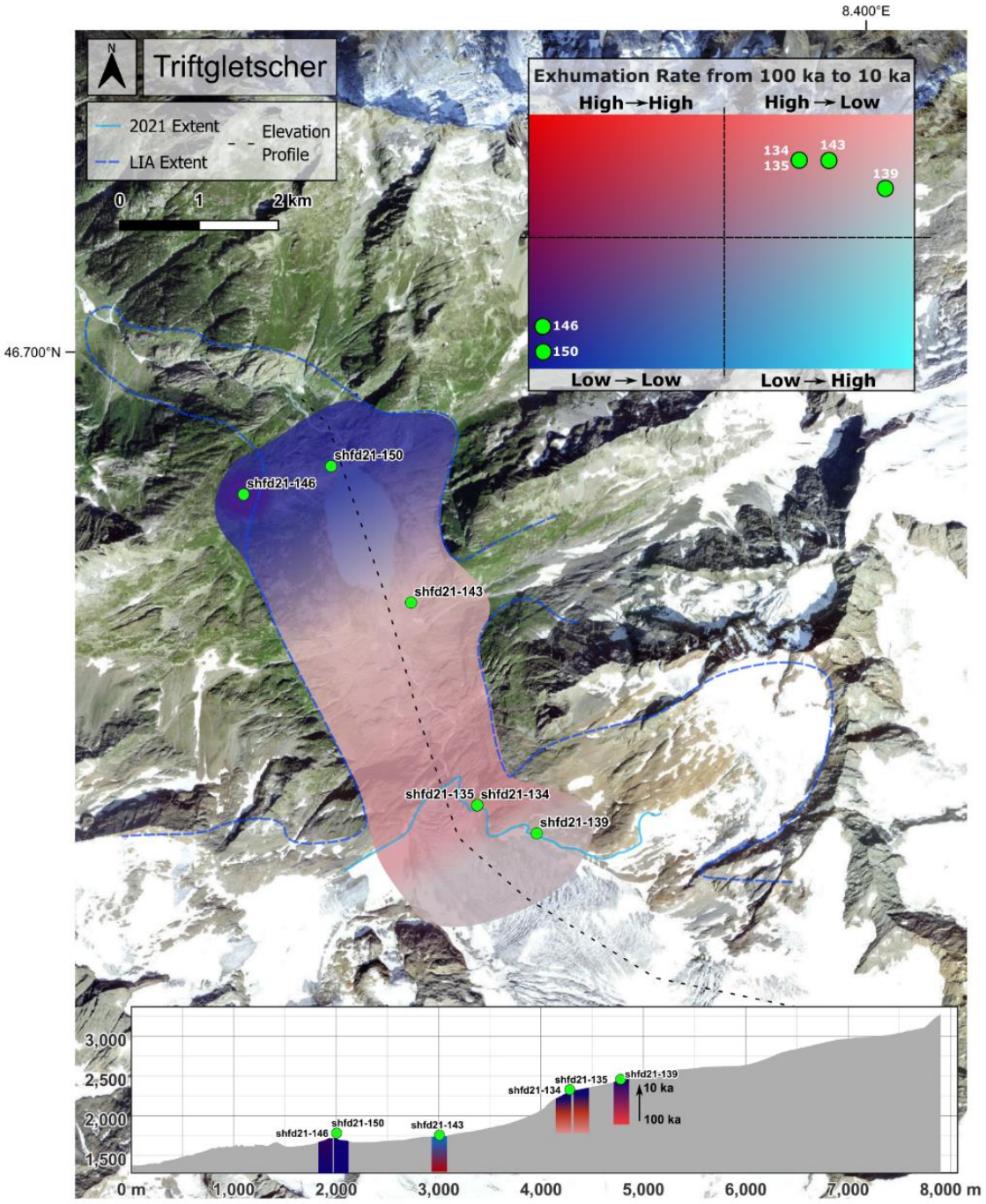

Figure 4.18: Heatmap of erosion for the Triftgletscher catchment, interpolated from TLT exhumation data according to relative magnitude of rates from 100 to 10 ka – see plot in the top right for colour guide. Relative exhumation columns for each sample also displayed on the elevation profile from 100 ka (deeper) to 10 ka (shallower), more rapid rates represented by warmer colours, slower rates by cooler colours.

can lead to rapid extrusion flow of the ice (Hooke et al., 1987). Maintaining high flow velocities and sediment transport in this manner allows erosion of a riegel to take place and keep it from growing in prominence. Further feedback mechanisms exist to prevent the overdeepening from continuously excavating deeper such as loss of water pressure, sediment accumulation and subglacial ponding of meltwater which will occur at a critical threshold of bed slope (Hooke, 1991; Cook & Swift, 2012; Swift et al., 2021a). Fluctuation between these two states should keep both the riegel and overdeepening in a state of dynamic equilibrium and prevent either from growing too large. However, as Steinemann et al. (2021) hypothesise, the development of a deep gorge incised into the riegel at Trift provided a low-threshold avenue for subglacial water and sediment evacuation, dynamically decoupling the overdeepening and riegel from one another and thus allowing each to continue growing to their present abnormally large size.

The TLT data here (Figure 4.18) fits Steinemann et al.'s hypothesis well, as the overdeepened region proximal to sample 143 continues to erode at a more rapid rate, unabated by negative feedbacks, whilst the loss of pressurised water substantially retards ice flow over the large riegel wall, reducing erosional potential. Interestingly, the erosion rate calculated by Steinemann et al. (2021) using TCN analysis for their sample 'Trift-06' is approximately 1 mm a^{-1}, two orders of magnitude greater than the equivalent sample here (shfd21-150) which varies around 0.015 mm a^{-1}. The main difference between these two approaches, though, is that the TCN from Steinemann et al. (2021) could only resolve erosion over the Holocene period (~11 ka), whilst the MAAD TLT approach here does not currently produce reliable results during this latter timeframe. As such, this points towards a dramatic switch in erosion rates between these two time periods, brought about by a substantial change in climate and thus glacier dynamics (see section 4.5.4 for further discussion on this), as well as frequent deglaciation exposing the surface to potentially intense weathering processes.

Further up the catchment, the strong signal of erosion from the two icefall lip samples (shfd21-134 & 135) is a clear indication of the importance of icefalls as glacial landforms. The magnitude of erosion here is substantial, potentially a factor of 5 greater than the next most rapidly exhumed sample – shfd21-143 located in the overdeepening below. This demonstrates the significance of icefall influences on ice dynamics, as the rapid extensional flow of ice as it is brought into this sudden steepened zone locally enhances abrasion and quarrying processes. The data here lacks the spatial or temporal resolution needed to provide more assertive evidence for the questions posed by Chapter 2 on how icefalls might

evolve over time – fixed in-situ, or dynamically retreating headward – but it does support the hypothesis that icefalls can be regions of high rather than low erosion, complimenting the outcomes of the numerical modelling in Chapter 3.

Approximately 500 m upstream of the icefall, the final sample from Trift (shfd21-139) returns to somewhat average rates of erosion for the catchment and decreases steadily through time. The lack of any major landform influence here means this may be a simple dependence of ice dynamics coupled to the cooling climate over the last glacial cycle – which will be discussed later in section 4.5.4.

4.5.3 Interpretation of Erosion Patterns at Otemma

As with Trift, a heatmap of relative erosion rates over the measured period was produced for the data at Otemma (Figure 4.19). In concordance with the numerical modelling in Chapter 3, the smoother, flatter profile of Otemma has generally resulted in lower erosion rates than those at Trift, though some significant patterns have still emerged.

At the lower end of the catchment, sample shfd21-155 situated on the presently deglaciated proglacial plain maintains a steady low rate of approximately 0.03 mm a^{-1}, potentially indicative of slow sliding rates experienced in this region. The suggested sudden increase by an order of magnitude to ~0.3 mm a^{-1} around the LGM period (~25 ka) is difficult to explain unless an increase in ice thickness and flux was sufficient to induce some greater response – e.g. by bringing the basal regime into the pressure melting point. However, given none of the other samples across either catchment display this LGM uptick behaviour it could well be an artefact of uncertainties in the data and by instead following the lower edge of the confidence interval bounds, a steady rate of 0.03 mm a^{-1} is maintained, as is the case for shfd21-159 further upstream (Figure 4.16).

Similarly, low rates are present at shfd22-237 on the flat-topped accumulation plateau of Otemma, which both starts and ends the period below 0.03 mm a^{-1}. There is a small increase in rates for this sample during the mid-glacial though, which may potentially be explained by the proximity of the large icefall of the Bas Glacier d'Arolla to the immediate north-east, which drains the same accumulation plateau as Otemma. As such, relatively warmer conditions during this mid glacial period (Ivy-Ochs et al., 2008) may have been sufficient to briefly increase the sliding rate here to raise erosion slightly.

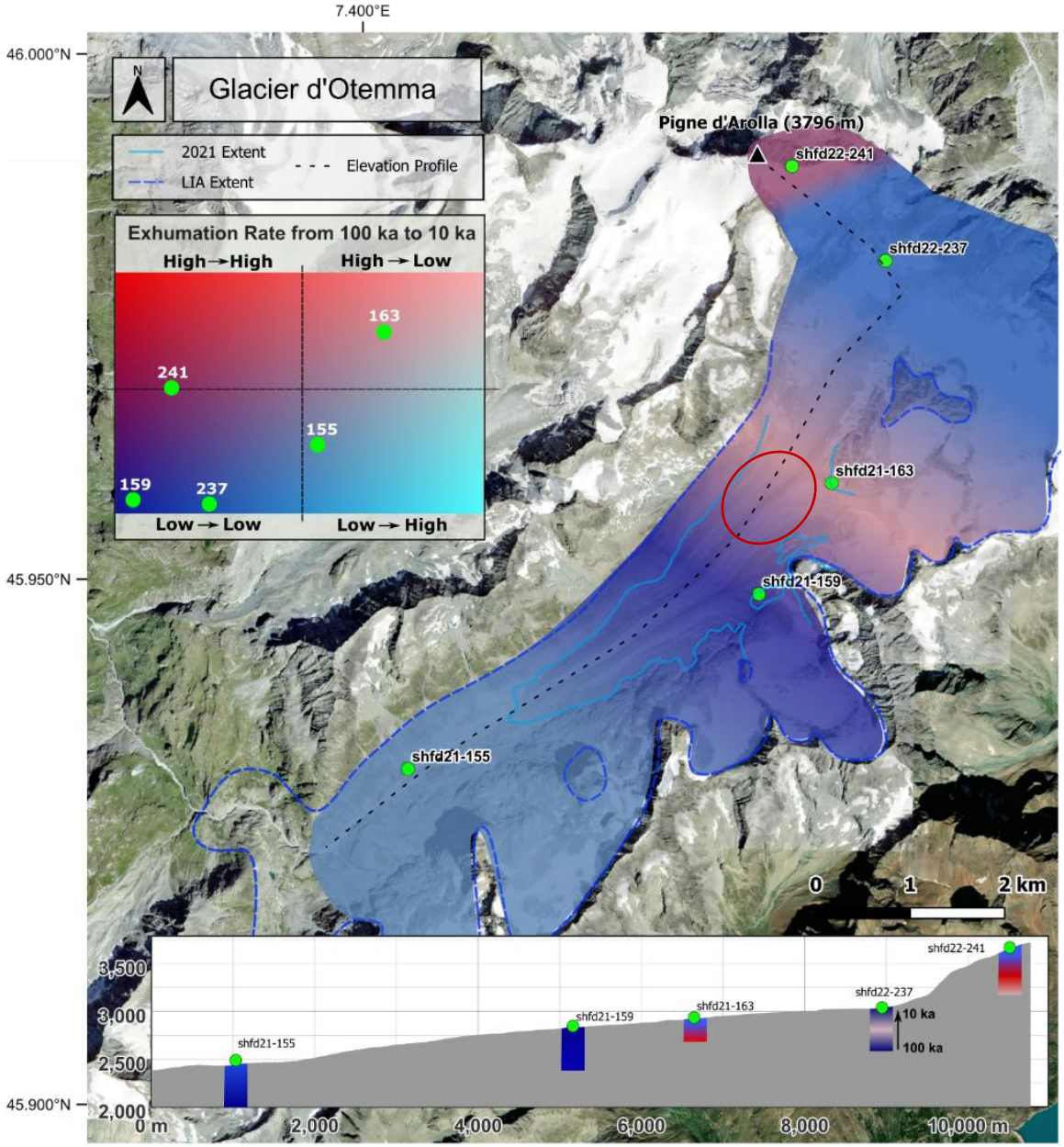

Figure 4.19: Heatmap of erosion for the Glacier d'Otemma catchment, interpolated from TLT exhumation data according to relative magnitude of rates from 100 ka to 10 ka – see plot in the top left for colour guide. Relative exhumation columns for each sample also displayed on the elevation profile from 100 ka (deeper) to 10 ka (shallower), more rapid rates represented by warmer colours, slower rates by cooler colours. Dark red circle indicates approximate position of possible bed overdeepening according to GPR data from Grab et al. (2021).

The highest erosion rates at Otemma, towards 2 mm a^{-1}, are achieved by shfd21-163, though the temporal resolution of this data is limited to 45 ka. The sample is situated at the confluence of the two accumulation areas of the glacier, on the edge of the small mountain of Petit Mont Collon. The increase in ice flux from this confluence could be a driver of higher erosion rates here, a mechanism that has previously been modelled and advocated (e.g. MacGregor et al., 2000; Anderson et al., 2006) as well as suggested to contribute to the overdeepening at Trift (Steinemann et al., 2021). Indeed, a significant bed overdeepening (>70 m) is indicated to be present at this confluence next to sample 163 according to the ground-penetrating radar surveys of Grab et al. (2021) (Figure 4.19). The higher erosion rates of the sample here are therefore consistent with this theory, possibly evidencing enhanced erosion driven by ice flux. Alternatively, the prominence of the Petit Mont Collon meant the peak was likely uncovered above the LGM ice surface as a nunatak (Bini et al., 2009), exposing it to extra-glacial processes of erosion as well as glacial incision from below. TCN analysis of supraglacial debris derived from this peak by Wetterauer et al. (2022) suggests increasing headwall erosion rates over the last couple of centuries, demonstrating the propensity for higher erosion under warmer conditions. Thus, the area may indicate higher exhumation rates due to the added process of extra-glacial erosion attacking this summit during slightly warmer intervals in the mid-glacial.

The final sample at Otemma, shfd22-241, also indicates relatively high rates of erosion compared to the rest of the catchment – around 0.3 mm a^{-1} with a possible peak up to 3 mm a^{-1} in the mid-glacial. The situation of this sample, located on the drainage divide just 100 m below the locally highest peak, is the steepest region of the profile in this catchment and therefore conducive to greater sliding velocities (Figure 4.19). The high rates may also be indicative of effective headward erosion and joint attack of the ridgeline on both sides from the neighbouring Glacier de Pièce and Tsijiore Nouve, as well as the exposure possibly permitting extra-glacial processes as just described for sample 163.

4.5.4 Links with Climate and Implications for Landscape Evolution

The previous two sections showed how there is great variability, both spatially and temporally, in erosion rates across both catchments. At Trift, patterns of erosion appear to be primarily driven by the presence of major landforms, whilst the less heterogeneous topography at Otemma suggests more subtle differences potentially caused by climate driven changes in ice dynamics.

A noticeable trend across the two catchments is a significant reduction in exhumation rates through time towards the LGM period (~25 ka). On average, rates decrease by 73% from their peak down to the LGM value, or -86% if accounting for the bounds of the confidence intervals. The late Würmian period associated with the expansion of glaciers to the LGM in the Alps was characterised by the coldest conditions of the last glacial cycle (Ivy-Ochs et al., 2008; Jouvet et al., 2023). Consequently, numerical modelling has suggested cold-based thermal regimes dominate the upper mountain catchments during this time (Cohen et al., 2018; Seguinot et al., 2018; Jouvet et al., 2023). These cold basal conditions, where the ice is effectively frozen onto the bed, inhibits basal sliding such that glacier movement is predominantly controlled by internal deformation at very slow rates and thus subglacial erosion is likely to be much diminished (Godon et al., 2013). There is no substantial geomorphic evidence for widespread cold-based ice conditions in the Alps, however, so the alternative consideration could be a reduction in sliding velocities due to decreased surface slopes from thicker ice, as evident from the modelled scenarios of Chapter 3.

Conversely, many of the samples also display an uptick in exhumation rate around the mid-glacial (50 – 60 ka) which could coincide with interstadial periods of MIS 3, where relatively warmer conditions in the Alps meant ice likely retreated back from the lowlands (Ivy-Ochs et al., 2008). An increase in summer temperatures may well have raised the elevation at which production and routing of meltwater occurred, increasing sliding velocities and promoting more effective erosion in some regions.

Overlaying reconstructed mean annual air temperature data for Glacier d'Otemma over the last glacial cycle from Jouvet et al. (2023) with the exhumation rates from sample shfd22-241 shows a remarkable correlation between the two (Figure 4.20). This suggests that rates of glacial erosion at some sample locations may be strongly coupled to changes in climate and possibly basal thermal regimes, providing supporting field evidence for

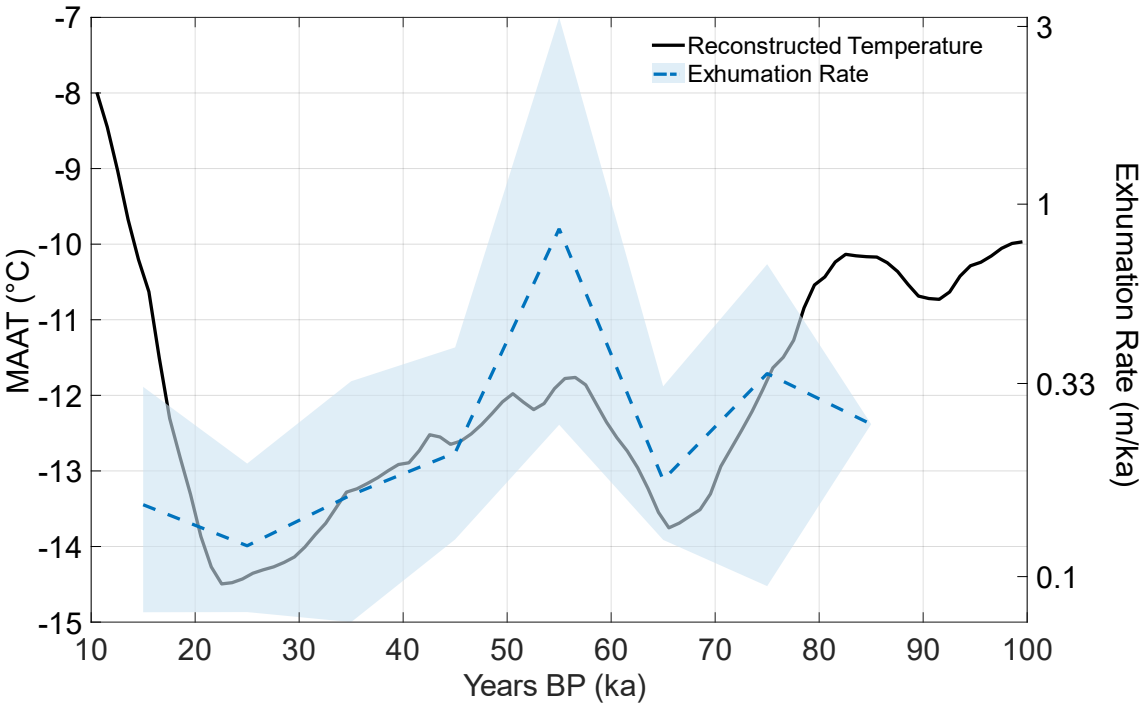

Figure 4.20: Exhumation rate of sample shfd22-241 compared with the reconstructed mean annual air temperature for the Glacier d'Otemma over the last glacial cycle by Jouvet et al. (2023). The trend in exhumation rate mimics the patterns of temperature change over the period, suggesting changes in climate have a strong influence on glacial erosion.

hypotheses previously solely derived from numerical modelling (e.g. Lai & Anders, 2021). Variability in basal thermal regimes influenced by differences in precipitation and accumulation as well as local influences of topography (e.g. the large riegel at Trift) are possible explanations for why some of the samples do not demonstrate similarly strong sensitivity to climate, either remaining steady at low rates, or decreasing monotonically towards the LGM. Moreover, glacier re-equilibration to changes in climate can take time and may be more rapid in some regions of the catchment than others according to the local ice dynamics (Cuffey & Paterson, 2010).

Another notable trend across both studied catchments is the tendency towards higher rates of exhumation at the higher elevation samples, a finding that would seem to support the glacier buzzsaw hypothesis that rapid glacial and peri-glacial erosion at high elevations limits the altitude and relief of topography (e.g. Brozović et al., 1997; Whipple et al., 1999). However, TCN analysis from the Pyrenees suggested much lower rates of denudation for

exposed ridgetops, which likely remained ice free over Pleistocene glaciations (Crest et al., 2017). Whilst many of the summits and large ridgelines around Otemma are believed to have been exposed during the LGM (Kelly et al., 2004; Bini et al., 2009), all of the samples extracted for the MAAD TLT were no more than a few metres above the present day ice surface and hence likely to have been covered during greater extents. As such, the samples themselves are unlikely to have experienced any peri-glacial weathering over the measured period, though may have undergone a similar exhumation due to removal of exposed features close by.

It is also important to note that samples were only acquired from these upper catchment regions near the present-day ice extent, with no measurement from further down valley towards or below the LGM ELA where modelling work (Sternai et al., 2013; Seguinot & Delaney, 2021) and evidence from detrital thermochronometry in Patagonia has suggested most erosion to have occurred (Falkowski et al., 2021). As such, it would be prudent not to over-interpret these results as evidence of the glacial buzzsaw in action, since the wider landscape context has not been accounted for.

Ultimately, the results here have shown glacial erosion to be significantly influenced by the pre-existing topography and landforms as well as large changes in climate. This has led to a highly variable pattern of erosion both spatially and temporally and gives us some insight as to how major landforms have been able to develop and/or persist over time, with minimal rates on the riegel and high exhumation on the icefall that outpace the surrounding landscape being two very clear examples.

4.6 Summary

In this chapter I have used a novel application of thermoluminescence thermochronometry to unlock a unique dataset of erosion rates spanning the last glacial cycle, providing a resolution of information previously unachievable using traditional methods of geochronology.

The findings provide further evidence towards hypotheses that glacial erosion varies substantially across the catchment, which were observationally apparent from alpine landscapes and from analysis of major landforms (e.g. icefalls – Chapter 2). Substantial changes in exhumation rate according to climate trends are also a primary finding of the data, demonstrating the importance of changes in ice dynamics and possibly basal thermal regime brought about by broad cycles in temperature, as has been posited from numerical modelling (e.g. Chapter 3; Lai & Anders, 2021; Magrani et al., 2021). In this respect the data has supported some of the key outcomes from the numerical modelling, though it also presents some conflicting findings (e.g. erosion at the higher elevations), all of which will be discussed in the following, final chapter.

Despite the novelty of this dataset, additional sampling, measurement and development of the technique in the future could further improve the spatial and temporal resolution of the data to provide even greater insights and constraints on how the landscape evolves under glacial activity. For example, more samples from the full length of the icefall and around cirque and headwall regions would permit analysis of the rates and feasibility of substantial headward retreat.

This chapter has addressed Objective 3 of the thesis and Questions 1 & 2, as well as providing crucial empirical data that can be used to address Questions 3 & 4. It is the last results chapter of the thesis and in the next, final chapter, I will bring together the results from the previous three chapters to culminate in a discussion of the main findings and implications, before addressing each of the research questions in turn.

4.7 Appendices

4.7.1 Triftgletscher MAAD TLT Data on Normal Axes

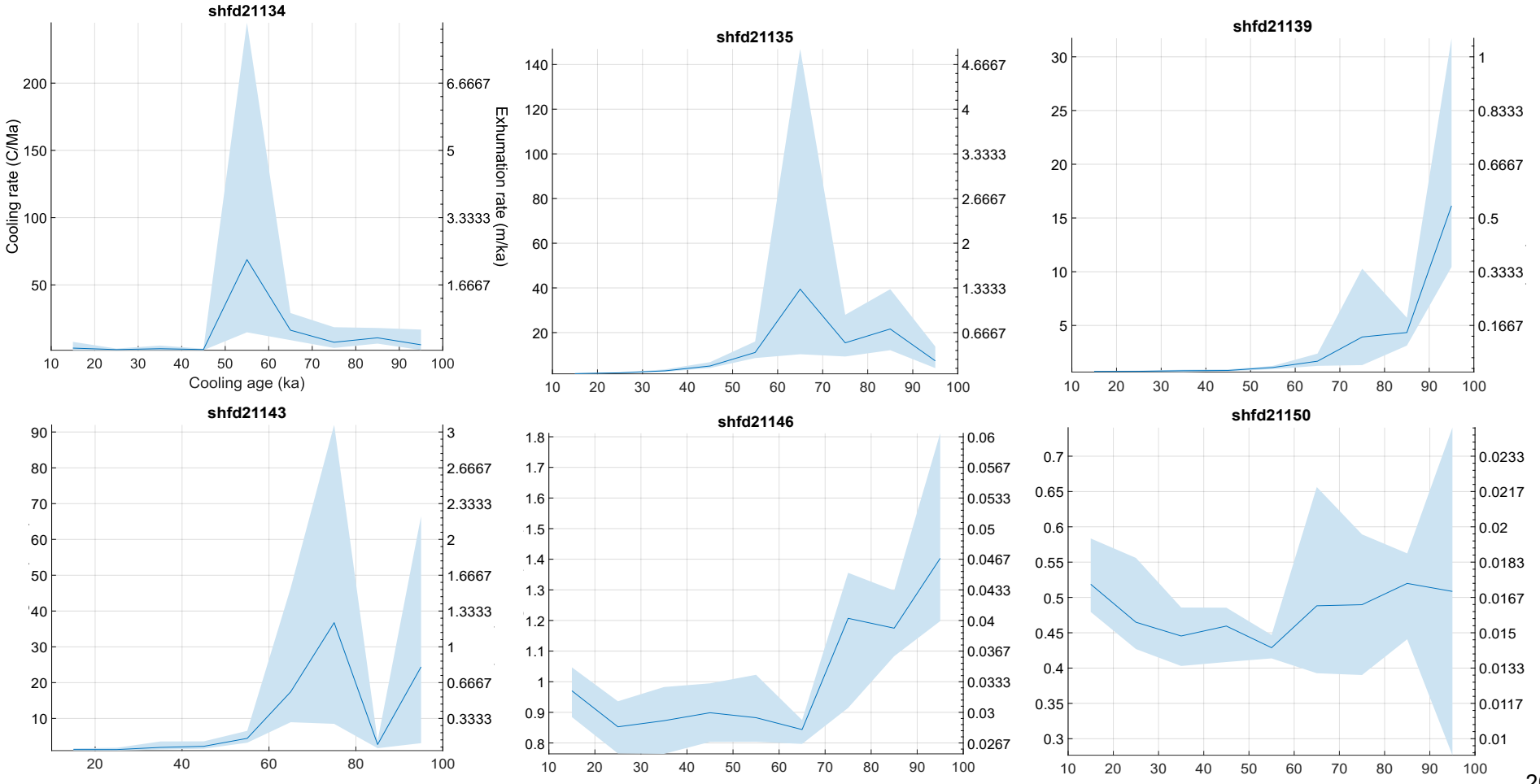

4.7.2 Otemma MAAD TLT Data on Normal Axes

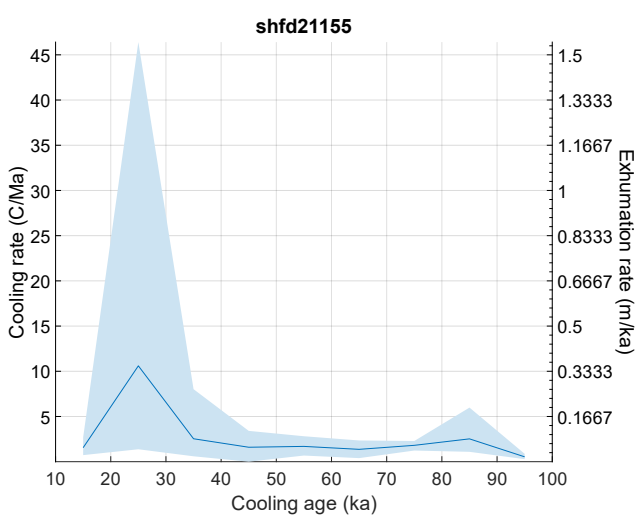

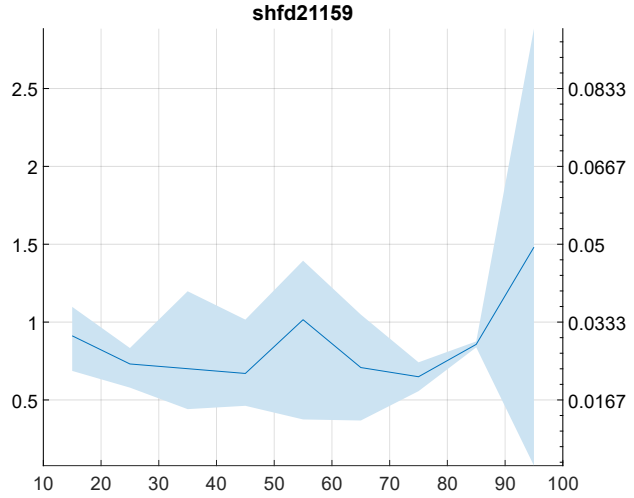

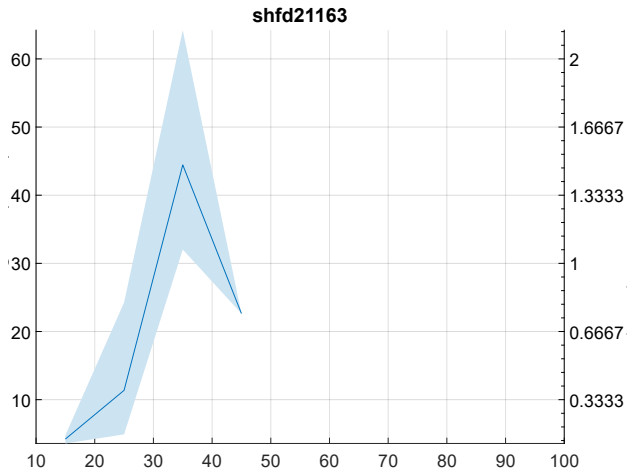

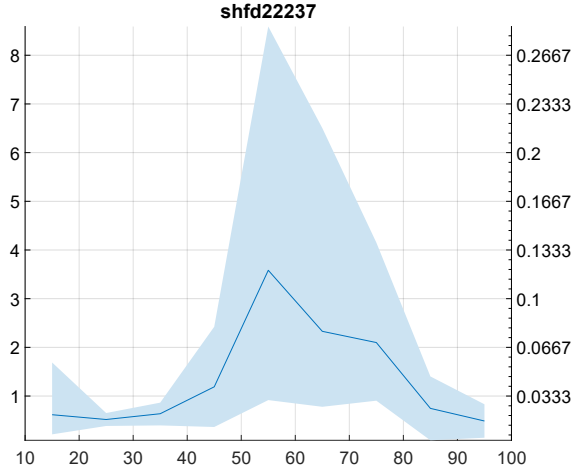

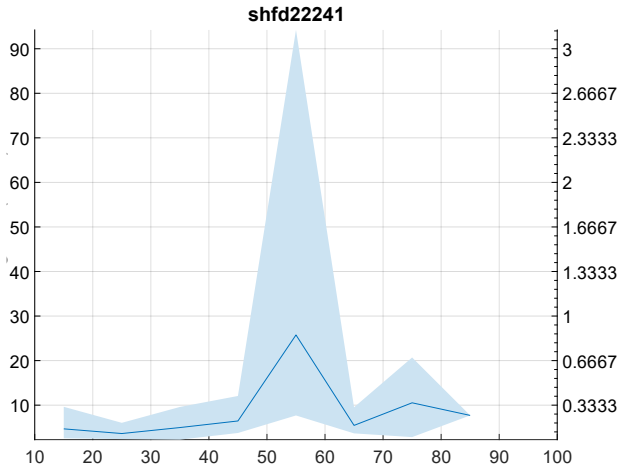

4.7.3 Spurious data for Sample shfd21-155

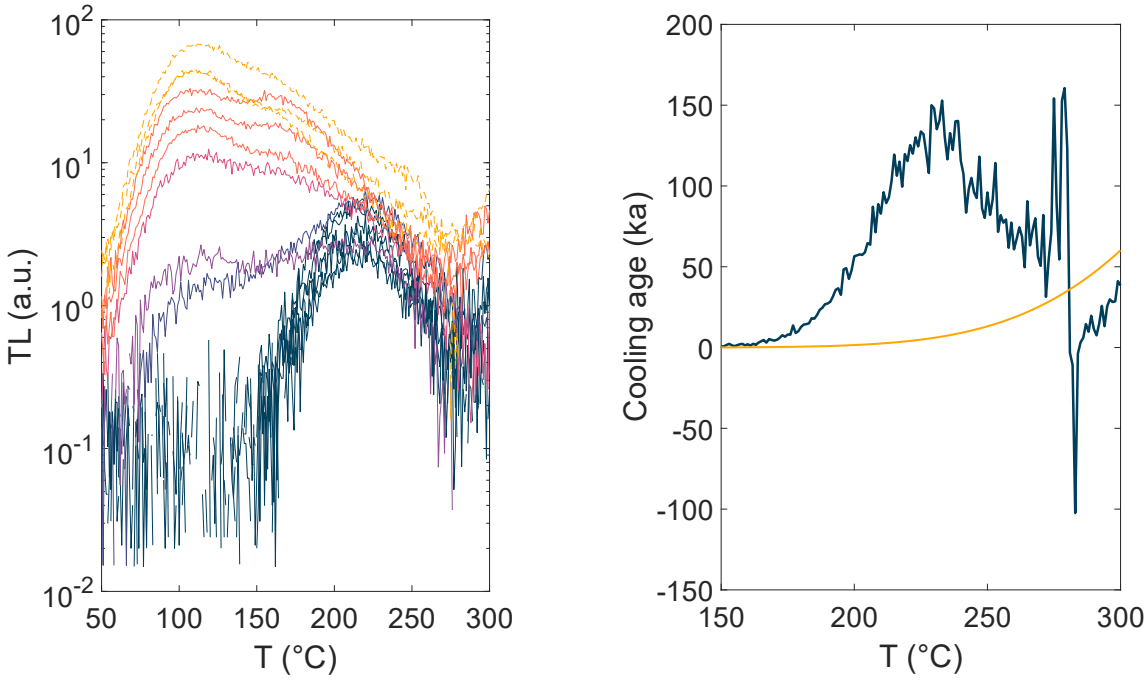

Appendix 4.7.3: Raw data for sample shfd21-155 which displayed an anomalously large drop in exhumation during the mid-glacial. On the sensitivity corrected natural and additive dose curves (left plot) there is a large and sudden decrease in TL around the 280°C region due to spuriously high background values. This translate into an erroneous, negative cooling age in the same temperature region (blue line, right plot) which is inconsistent with the synthetic simulated sample response (orange line). Consequently, this large error can be ignored and the interpolated trend put out by the model code should be followed.

Chapter 5

Discussion & Conclusions

5.1 Chapter Overview

The overall aim of this thesis was 'To improve our understanding of the dynamism of glacial erosion operating at the sub-catchment scale under a range of glacier conditions'. In this chapter I bring together the outcomes of the previous three results chapters (2 - 4) to critically review and discuss the findings, which together form valuable information in this wider context and are required to be discussed collectively in order to answer the main research questions of the thesis.

Firstly, I start by briefly summarising the key findings of each results chapter (section 5.2). The discussion then follows, starting by piecing together the data into a picture of the patterns and rates of erosion in high alpine catchments (section 5.3.1). Then, I discuss and evaluate the numerical glacial erosion law within the context of the data and results of the thesis (section 5.3.2). Following from this, I compare the derived rates of erosion to contemporary equivalents for the Alps and discuss the potential biases involved in the interpretation of both, which directly addresses the fourth research question of the thesis (section 5.3.3). Finally, I discuss how the results from these chapters fit into the context of wider theories and implications for the impact of glacial erosion on landscape evolution, particularly in high alpine catchments (section 5.3.4).

Following the discussion, I return to the main research questions set out in Chapter 1, section 1.3, to provide a brief overview of where and how each of these have been addressed (section 5.4). I then set out recommendations for future research directions (section 5.5) before finally concluding the thesis by summarising the key findings and contributions (section 5.6).

5.2 Summary of Chapter Results

The first results from this thesis presented in Chapter 2 investigated the prevalence and positioning of icefalls in contemporary alpine glacier catchments, teasing out some insights from the landscape on the dynamical nature of glacial erosion in these high alpine regions. The regular pattern that emerged with icefalls able to be categorised into distinct geomorphological groups and a notably strong correlation to climate gradients within the most common of these groups (i.e. cirque lip and plateau types) suggested a substantial spatial contrast in glacial erosion to have occurred, largely driven by climate forcings, in order for prominent landforms to be produced. Since climate varies considerably over geologic timeframes and glaciation responds in turn, the temporal dynamics of icefalls was questioned, specifically how they evolve in response to substantial changes in glacier extent and conditions, and how the higher accumulation area regions are able to maintain a balance with signals of strong erosion around and below the icefall – elements that are discussed further in a later section (5.3.4).

The topographic approach to analysis of icefalls presented an initial case for a strong spatio-temporal variation in glacial erosion but lacked specificity in terms of quantifiable rates of change over time. Whilst some previous studies have used topographic analysis alone to infer quantitative rates of denudation (e.g. Brocklehurst & Whipple, 2002; Naylor & Gabet, 2007), such determinations are somewhat crude and can only be measured as a broad time and space-averaged rate. Consequently, the dual approach of numerical modelling and thermoluminescence thermochronometry (TLT) used in Chapters 3 and 4 provided more intricate detail on just how much glacial erosion can vary within high elevation contemporary catchments over the scale of the last glacial period.

In Chapter 3, numerical modelling showed the impact of both different parameterisation of a simple erosion law and different climate and glacier setups on the spatio-temporal dynamics of simulated glacial erosion across two contrasting catchments. Choice of value of l and K_G in the simple numeric law critically impact the scaling of erosion with sliding velocity and the specific magnitude of that erosion, respectively. A sub-linear l (i.e. 0.65) works towards a more homogenous landscape, whilst non-linear values (i.e. 2) accentuate the existing heterogeneity. A simple linear l of 1 is a balance between the two but can produce very deep, likely unrealistic erosion with commonly employed couplings of K_G. The value of K_G has received little prior attention and is difficult to constrain but enacts a strong influence on the overall denudation and evolution of the catchment domain.

Under different simulated climate scenarios and glacier extents, erosion patterns change according to ice thickness impacting sliding velocity through altered surface gradients, and ice residency time impacting the overall cumulative denudation of portions of the catchment. In both cases, the pre-existing topography of the basin strongly influences these outcomes, with the shallower and more isolated catchment of Otemma showing little change in erosion rates between glacial and interglacial states, whilst the steeper catchment of Trift proximal to the main trunk valleys underwent substantially different patterns and rates of erosion between glacier states.

In Chapter 4, the use of a novel method of TLT on bedrock samples acquired from the field unlocked a time-series of exhumation rates over the past 10-100 ka. Inferred as approximately equivalent to rates of glacial erosion, the data empirically demonstrates strong spatio-temporal variation across the catchment, particularly in relation to major features and landforms like the icefall and riegel at Trift, or confluence and summit region at Otemma. The exhumation history of some samples also exhibit a strong correlation to trends in reconstructed climate over the past 100 ka, which can be inferred as the efficacy of glacial erosion changing according to ice dynamics through time, as indicated by the prior modelling data.

5.3 Discussion

5.3.1 Inferred Patterns and Rates of Erosion in High Alpine Catchments

This section compares the outputs of the model and TLT data to infer some of the overall patterns and rates of erosion in the study catchments by exploring the similarities and differences in the data, starting with the temporal scale before examining the spatial aspect.

Plotting a timeseries of catchment-averaged erosion rates for the modelled glacial period scenarios and the TLT data permits analysis of the temporal changes to erosion found in these study catchments (Figure 5.1). The dramatic reduction in erosion seen at Trift part way through the model is also present within the TLT data which drops by a similar magnitude, though in the latter this occurs some 30 ka later. In the model the cause of this change was a sudden increase in ice volume from rapidly cooling temperatures, which inundated the Trift basin and reduced the surface slope and subsequent basal shear stress in regions of previously high erosion like the icefall (Chapter 3, section 3.4.3). The highly simplified idealised climate forcing of this model means a lot of shorter-term temperature variability from the last glacial reconstructions was not included (Chapter 3, Figure 3.4). This likely forced the large change in ice volume too soon, as the low rates captured by the TL from 45 – 25 ka coincide with periods of greatest advance for the Aare valley trunk glacier in this region (Jouvet et al., 2023).

The situation at Otemma is complex as the modelled erosion maintains low rates throughout the period, whilst TLT data implies a generally increasing rate of erosion until just before the LGM. The mean TLT rates at Otemma are skewed considerably though by two samples (shfd21-163, shfd22-241) which yield substantially higher rates than the other samples during the period 35 - 55 ka, possible reasons for which will be examined shortly with the aid of further figures.

Aside from differences in the specific magnitude of erosion between modelled and measured data (which will be discussed in the next section), the measured TLT rates are far more variable over the time period than the modelled equivalent. Standard deviations of the whole TL data were 0.41 for Trift and 0.29 for Otemma, compared to just 0.065 and 0.0003 in the model data. This again speaks to the simplifications imposed by numerical modelling,

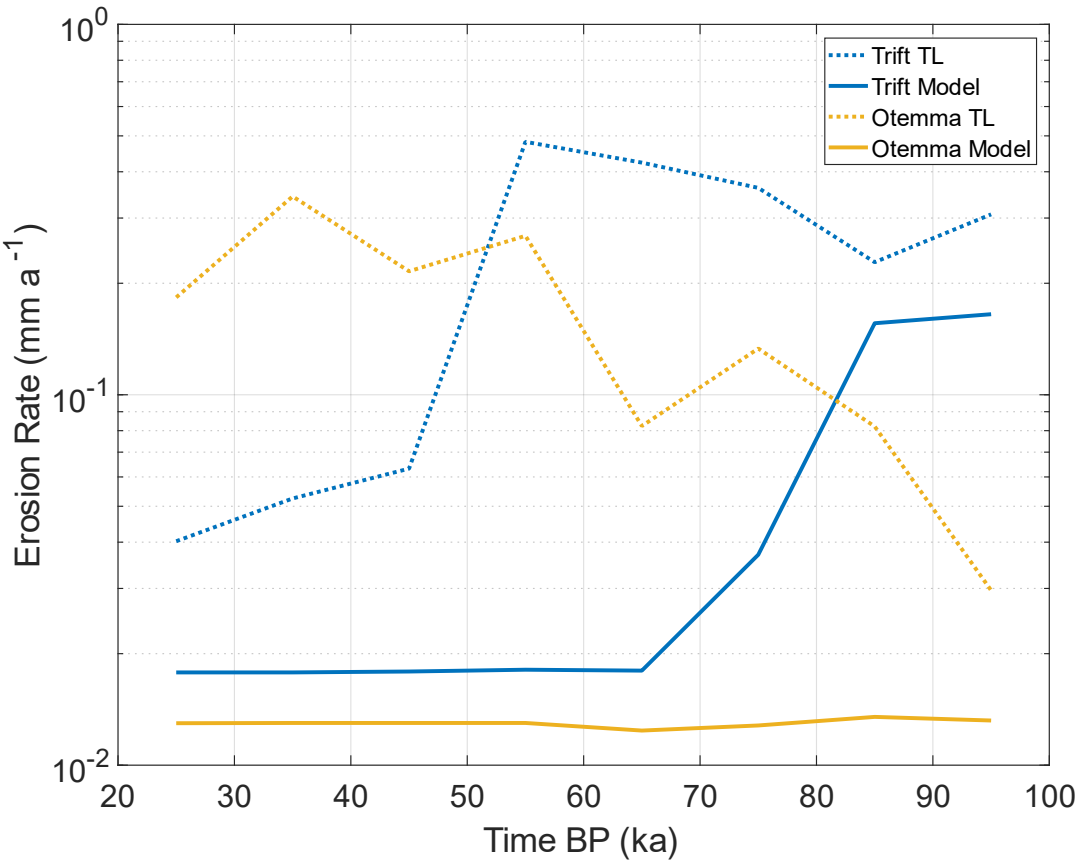

Figure 5.1: Time-series catchment-averaged erosion rates over the last glacial period for the Trift and Otemma sites at 10 ka intervals, as derived from the numerical modelling and thermoluminescence thermochronometry. Model data was converted back to chronological time BP from its raw format of model run time as presented in Chapter 3. An increasing trend toward younger ages is present in the TLT data for Otemma due to high values for two samples during the mid-glacial (c. 45-55 ka) and an anomalously high LGM value at one sample skewing the mean rates.

specifically the climate forcing as just discussed, as well as the use of simple erosion laws coupled to sliding velocity. It is therefore no great surprise that the empirical data from the field, which encompasses all natural processes responsible for sample exhumation, displays a greater degree of variance. Moreover, it is worth reiterating the point made at the start of Chapter 4's discussion (section 4.5.1): that thermochronometry is a measurement of a sample's cooling history, which is inferred to be proportional to exhumation and erosion, but therefore may also encompass elements such as isostatic responses to lithospheric loading or unloading elsewhere in the wider basin (Champagnac et al., 2009; Anderson & Anderson, 2010) which could contribute to the overall variability of the sample's history.

Switching now to compare the spatial distribution of erosion across both catchments by time-averaging the model and TLT data, there is generally broad agreement, though with some notable exceptions (Figure 5.2). At Trift (Figure 5.2a), the highest TLT rates are located in the region of highest modelled erosion, at the top of the icefall. Likewise, the lowest TLT rates from the two samples on the riegel (shfd21-146, 150) are similarly regions of very low erosion rates in the model. A notable outlier is the TLT sample from the overdeepened basin (shfd21-143), which is measured to have undergone an average rate of exhumation that is almost as high as those at the icefall, yet the model produces very low rates for the same region. This may be a result of the difficulty in accurately modelling overdeepenings, as the specific mechanisms that lead to formation are still largely unknown, though differences in lithology and bedrock erodibility is believed to be an important control (Preusser et al., 2010; Cook & Swift, 2012; Haeberli et al., 2016; Magrani et al., 2020), which is not accounted for in the model. Alternatively, since the present day topography (with lakes and ice removed) was used for the model bed, it may be that this basin has currently reached an equilibrium form not conducive to further excavation (Cook & Swift, 2012) and as such this is reflected in the low erosion rates produced by the model.

At Otemma (Figure 5.2b), a few of the TLT sample rates are in broad agreement with the modelled pattern, though shfd22-241 at the summit region is outside of the model domain (which is set below the watershed for stability reasons). This was one of the aforementioned samples responsible for skewing the catchment mean during the 35-55 ka period in Figure 5.1. The summit slope region proximal to this sample experienced an isostatic uplift in the model in response to large volumes of ice and erosion in the main Val de Bagnes confluence

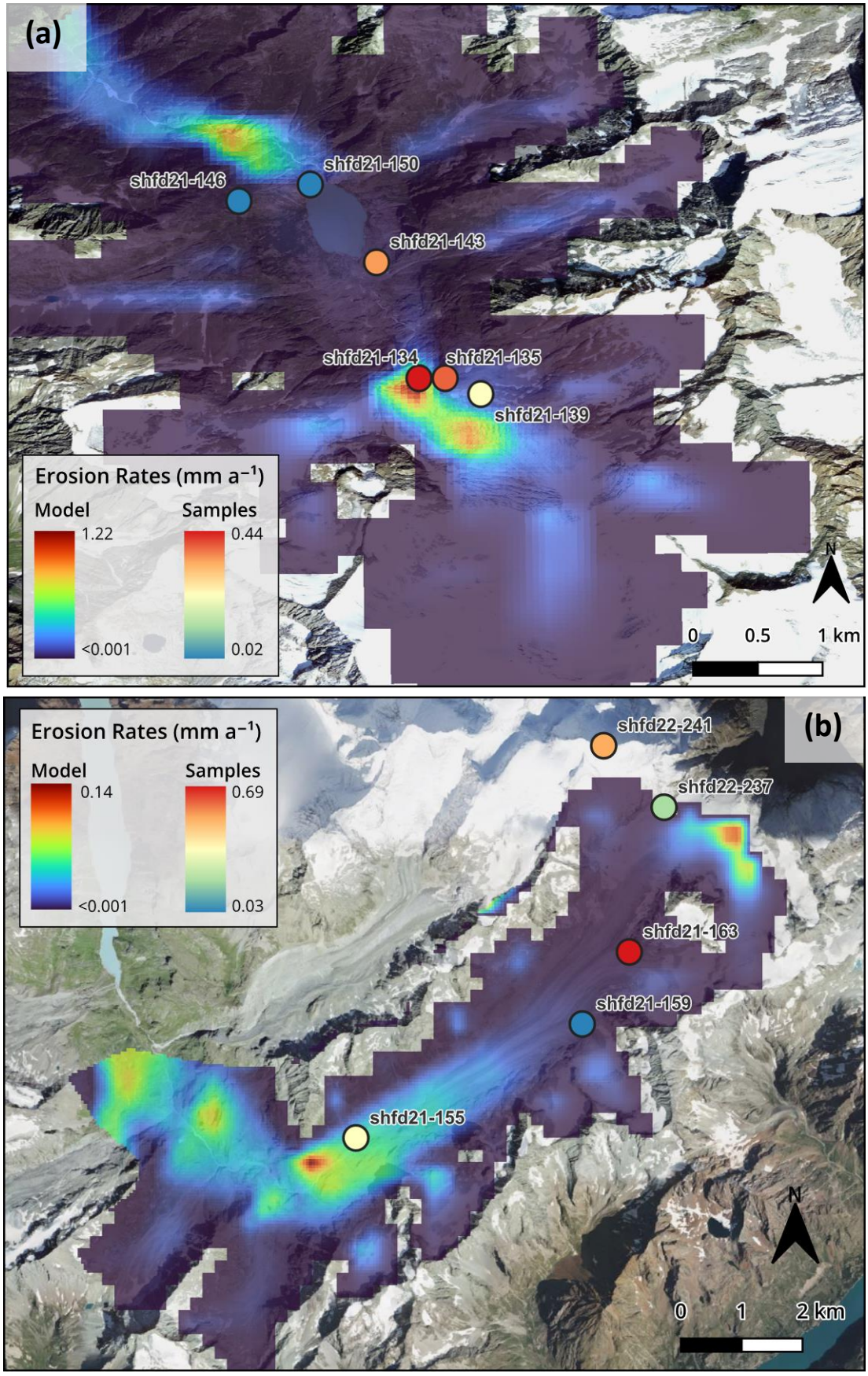

Figure 5.2: Time-averaged erosion rates from 25 – 90 ka as derived from the model (overlaid colour gradient) and each TLT sample (coloured dots) at Trift **(a)** and Otemma **(b).**

valley, as such this may be one possible explanation for the higher measured exhumation rates here. Alternatively, it may reflect higher erosion on the watershed here due to steep slopes on either side that maintain greater sliding velocities than the flatter profile of Otemma below. The main peak in erosion at this sample towards 1 mm a^{-1} occurred at 55 ka, coinciding with a warmer interstadial period during MIS 3 that may have been more conducive to more effective erosion at higher elevations (Ivy-Ochs et al., 2008).

Similar to Trift, an outlier of high measured rates in a modelled region of low erosion is present with sample shfd21-163 at Otemma. In Chapter 4 this sample, which yields the highest exhumation rates at Otemma, was theorised to be in a region of high erosion due to the confluence of the glacier's two major flow units as well as the proximity of a large overdeepening. The model again may be underestimating erosion in this overdeepened region as per the reasons outlined above for Trift. The sample is also situated at the base of a large bedrock step descending off the Petit Mont Collon summit, where a presently small glacier would have flowed down in the form of an icefall to join Otemma during larger ice extents. This summit and glacier are not modelled accurately (visible as a hole in the data to the right of sample shfd21-163 in Figure 5.2b) due to the imposed 200 m resolution and so the potential enhancement of erosion here would not be reflected in the model outputs.

Overall, the model and TLT data largely complement each other, showing that erosion varies temporally in line with climate forcings, generally towards lower rates under colder conditions with thicker ice masses, and is strongly controlled spatially by pre-existing topography and landforms which influence ice dynamics.

5.3.2 Empirically Evaluating Numerical Erosion Laws

The field data acquired through the TLT technique also enables a critical examination of the performance of the different erosion laws used in the numerical modelling. Catchment-averaged rates are listed in Table 5.1, along with the standard deviations for each measurement which indicates how widely the data varied across the measured timeframe. Over the last glacial period, the model using the non-linear law where l = 2 is underestimating both the magnitude and variance of erosion by an order of magnitude or greater when compared to TLT. Things are slightly different under the modelled steady-state LGM scenario where all three erosion laws were tested. Here, the field data from Trift matches closely to the non-linear erosion law, whilst TLT rates at Otemma are closer to the

Table 5.1: Catchment-averaged rates of erosion (mm a^{-1}) for TLT and model data over the full last glacial period and under LGM conditions only.

	Trift		Otemma	
Last Glacial (25 – 95 ka)				
TLT	0.22	σ 0.41	0.17	σ 0.29
Model (l = 2)	0.06	σ 0.06	0.01	σ 0.0003
LGM (25 ka)				
TLT	0.04	σ 0.02	0.18	σ 0.18
Model l = 0.65	0.24	σ 0.48	0.2	σ 0.27
l = 1	0.59	σ 1.67	0.44	σ 0.73
l = 2	0.01	σ 0.06	0.004	σ 0.01

sub-linear law of l = 0.65, as the non-linear law vastly underestimates erosion by two orders of magnitude.

The non-linear law was proposed by Herman et al. (2015) from measurements at Franz Josef glacier in New Zealand, where sliding rates were a factor of five or greater than the highest rates modelled here at the Trift icefall and far in excess of the sliding rates at Otemma (Figure 5.3). The rapid scaling of erosion over a large range of sliding velocities determined at Franz Josef means the non-linear law is therefore not particularly well constrained for the limited range of low sliding velocities present in the upper alpine catchments studied here and thus generally leads to underestimation across the catchment, or overestimation in specific high velocity regions (e.g. the icefall). This scaling is also apparent in the spatial distribution of erosion in Figure 5.2 of the previous section, where a higher range of sliding velocities at Trift result in modelled erosion that is both too low and too high compared with the field data. At Otemma, the very low sliding velocities confine modelled erosion to very low rates that are far below that of the field data. A comparison of thermochronometric erosion data and low modelled sliding velocities at a wide scale (100's km) and coarse resolution (700 m) over two glacial-interglacial cycles for the southern Coast Mountains of Canada by Yanites & Ehlers (2016) suggested a similar strength in relationship

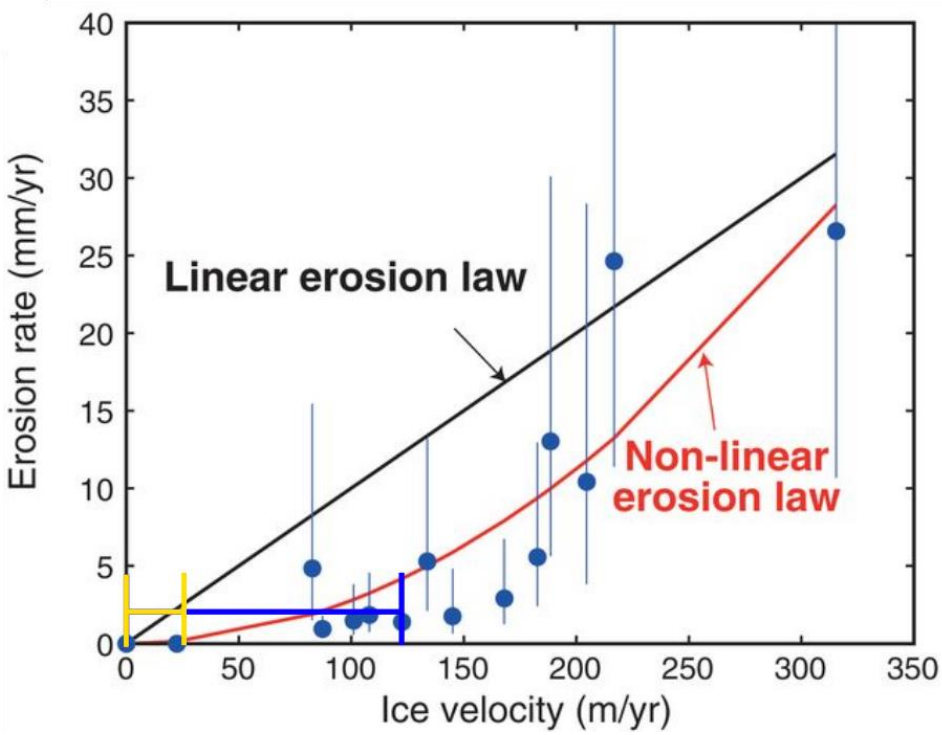

Figure 5.3: Determination of the non-linear erosion law by Herman et al. (2015) based off data from Franz Josef Glacier in New Zealand. The majority of data points are situated at high ice velocities, whereas Otemma (yellow line) and Trift (blue line) are at the lower end of this trend which is poorly constrained with fewer datapoints. Figure adapted from Herman et al. (2015).

between a linear and non-linear power fit to the data, demonstrating the difficulty in constraining erosion at such low sliding rates.

In all cases the use of the simple linear law (l = 1) is found to be wholly inadequate, eroding at rates that greatly exceed the TLT data during the LGM period, as well as the early glacial (i.e. 110 – 70 ka, no data thereafter due to model instability) where average modelled rates were 1.23 mm a^{-1} for Trift and 1.37 mm a^{-1} for Otemma compared to TLT averages of 0.3 and 0.08 mm a^{-1} respectively.

The sub-linear law was not tested in the model over the full glacial period, though given that it yields average rates below that of the linear and far above the non-linear laws under the steady-state scenarios, it could be inferred that it would be a more suitable fit to producing erosion similar to the TLT data over full glacial scenarios. Non- or sub-linear values of l are therefore likely to be a more suitable application at these catchment scales,

as they could tacitly reflect the strong spatial variability in erosion along the glacier profile, as is evident from the TLT data, which may be a consequence of spatially-variable dynamic feedback mechanisms that are not coupled simply to sliding velocity – e.g. the storage or flushing of till at the bed (Alley et al., 2019). The strength of this variability, and therefore specific choice of l value, likely changes between catchments depending on the prevalence of such feedback mechanisms. The coupled value of K_G is also of crucial importance to simulate realistic rates of change.

As discussed previously in Chapter 3 (section 3.5.1), the choice of K_G value in the numerical erosion law is critical to the magnitude of erosion produced by the model. In section 3.4.1 of Chapter 3, a series of model runs were conducted over different K_G for a steady-state Otemma (Figure 3.9). Comparing these outcomes to the equivalent LGM TLT data can enable greater constraints on the value of K_G needed to reproduce the same magnitude of erosion in this specific catchment – i.e. slightly lower for the linear and sub-linear laws and over an order of magnitude higher for the non-linear law (Figure 5.4). However, such determinations using catchment-averaged rates are still problematic given the considerable spatial variation in erosion present within the TLT data, which point towards the need for spatially-variable K_G to accurately reflect this in numerical models, particularly for features like overdeepenings where lithological weakness is believed to be an important catalyst for formation, as mentioned prior in section 5.3.1.

Ultimately, K_G is currently lacking in sufficient empirical constraints considering the large impact it has on model outcomes. Recommendations for future research on this aspect are presented later in section 5.5.2.

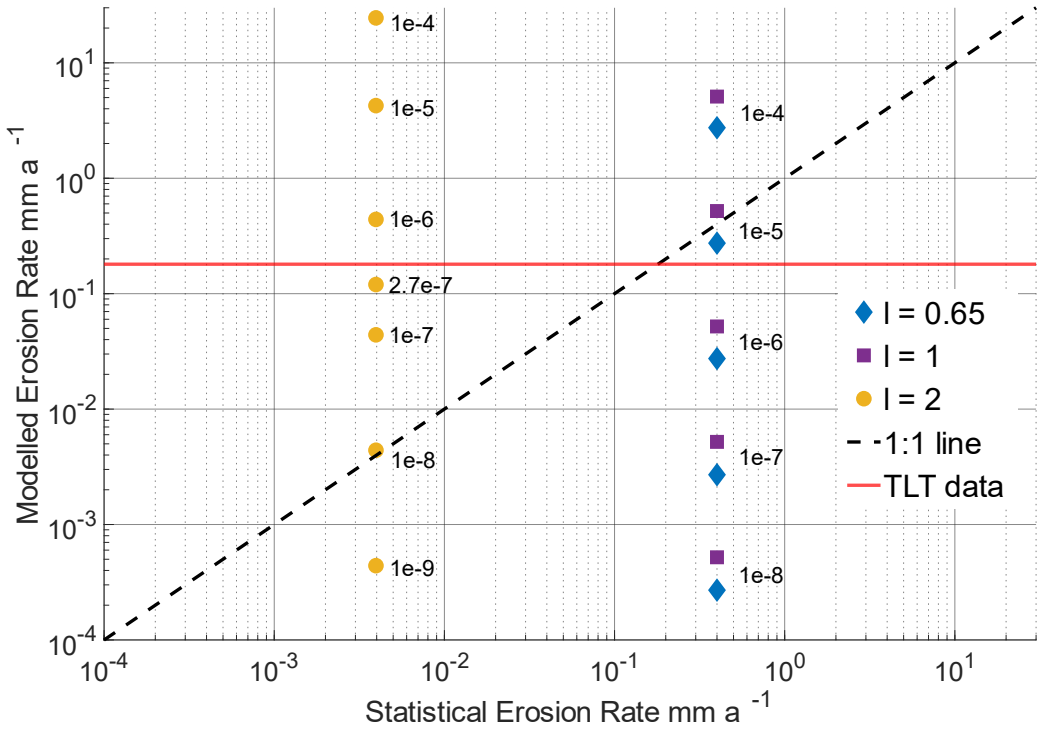

Figure 5.4: Calibration of the K_G parameter in Chapter 3, where modelled sliding velocity at Otemma was used to calculate statistical rates of erosion that were then compared to modelled erosion over a range of K_G values to determine the best fit. The TLT value (red line) essentially shows the empirical field fit, suggesting a slightly lower K_G for the linear and sub-linear laws and a much greater value for the non-linear law.

5.3.3 Comparisons to Contemporary Estimates of Erosion

Contemporary estimates of glacial erosion have often been shown to be far greater than those averaged over longer glacial-interglacial periods in regions such as Alaska and Patagonia (Koppes & Montgomery, 2009). In the Alps, contemporary rates are generally not excessively high when measured predominantly by the common method of suspended sediment concentration gauging of proglacial meltwater streams, which provides an average rate for the whole catchment (Table 5.2). At Otemma, recent meltwater gauging data from Mancini et al. (2023b) yields an erosion rate that changes by 30% between melt seasons and is far lower than that of neighbouring Haut Glacier d'Arolla from 1990, despite both glaciers having highly similar gradient and ice velocity (Gabbud et al., 2016). Such inter-annual and decadal-scale differences have been reported elsewhere in Switzerland and are likely due to changing meltwater input and hydrological conditions flushing more or less sediment from the subglacial system, rather than a genuine change in bedrock erosion (Delaney et al., 2018). The location of the gauging station may also have a substantial impact on the calculated rates as the proglacial forefield can act as a significant sediment source or sink depending on the hydrological conditions at the time (Guillon et al., 2018; Mancini et al., 2023a; Delaney et al., 2024).

The derived contemporary rates at Otemma of ~0.1 mm a^{-1} (Table 5.2) are generally consistent with the catchment-averaged rates determined from the TLT over the last glacial period and LGM at ~0.17 mm a^{-1} (Table 5.1), suggesting average erosion during present extent and glacial periods may be broadly similar here. Indeed, this was suggested to be the case from steady-state LIA and LGM models of Otemma (Chapter 3, section 3.4.2), though not under variable climate where mean interglacial rates were an order of magnitude lower than those of the glacial period due to significant amounts of time under highly diminished ice thickness and extent (section 3.4.3). Contemporary erosion rates at Otemma may, however, be potentially *overestimated* due to increased meltwater flux flushing out regions of stored sediment (Delaney & Adhikari, 2020) and/or an increasing contribution of extra-glacial sources of material from heightened periglacial processes under warming climate conditions, as has been measured to occur at Otemma (Wetterauer et al., 2022). On the other hand, measurements of suspended sediment flux may *underestimate* the total glacial erosion rate as bedload is not considered, which may contribute approximately an additional 40% of the total flux (Riihimaki et al., 2005).

Table 5.2: A sample of estimated contemporary erosion rates for glaciers across the Alps, with Otemma and Trift highlighted in blue at the bottom. Majority of estimates are derived from meltwater gauging of suspended sediment concentration (SSC) and a couple from terrestrial cosmogenic nuclide (TCN) analysis.

Glacier	Erosion Rate (mm a^{-1})	Method	Time Period	Source
Bossons	0.39 ±0.33	TCN of evacuated material	~2013	Guillon et al. (2015)
"	1.28	SSC meltwater gauging	Unknown contemporary	Cook et al. (2020) & refs. therein
Gornergletscher	1.11	"	1970-80	"
Haut Glacier d'Arolla	2.26	"	1989-90	"
St Sorlin	2.2	"	Unknown contemporary	"
Tsanfleuron	0.5	Englacial sediment samples	2007	"
Tsidjore Nouve	0.56	SSC meltwater gauging	~1980's	Hallet et al. (1996) & refs. therein
"	1.17	"	~1980's	"
Ferpècle	0.47	"	~1980's	"
Gornergletscher	0.25	"	2016-17	Delaney et al. (2018)
Aletsch	0.4	"	2016-17	"
Otemma	0.079	"	2020	Mancini et al. (2023b)
"	0.103	"	2021	"
Triftgletscher	0.2 - 2	TCN on Riegel	Holocene	Steinemann et al. (2021)

At Trift there are currently no published estimated contemporary erosion rates, but the cosmogenic nuclide analysis of Steinemann et al. (2021) gives a range of 0.2 – 2 mm a^{-1} across the riegel over the Holocene period. This is within the range of steady-state LIA modelled rates (Chapter 3, section 3.4.2) as well as the overall catchment mean from the TLT data (Table 5.1). However, the riegel specific TLT samples give a time-averaged rate of 0.02 and 0.03 mm a^{-1}, suggesting erosion on the riegel itself was an order of magnitude lower over the last glacial period than during the Holocene.

Estimates of glacial erosion using contemporary sediment yields should only ever be interpreted in the context of the glacier extent and ice dynamics at the time the measurements were made, with particular attention paid to the fact present-day glaciers are significantly out of balance with climate and undergoing large transient adjustments (Koppes & Montgomery, 2009). The data from this thesis suggests the applicability of these contemporary rates to longer term average erosion over previous glacial/interglacial cycles may be uniquely dependent on the characteristics of the catchment in question. At Otemma, the topography of the catchment permitted similar erosion rates to be achieved under modelled LIA and LGM scenarios (Chapter 3, section 3.4.2) and subsequently there is little difference between contemporary and long-term rates from the meltwater gauging and TLT data. Conversely, at Trift there was a substantial reduction of erosion under LGM conditions in the modelled scenarios, which is supported by a mis-match in rates on the riegel between the TCN of Steinemann et al. (2021) over the Holocene and the TLT data in this study over the last glacial period. Admittedly, a sample size of two catchments is rather insufficient to make such a claim confidently, though what is clear is that methods yielding a simple average rate are blind to substantial variation in erosion both spatially and temporally as revealed by the TLT and model data, which may have significant impacts on landscape evolution, as will be discussed in the following section.

5.3.4 Implications for Landscape Evolution

Whilst the contemporary sediment and erosion yields discussed in the previous section contain some regional and inter-annual variation, they are not dissimilar in magnitude to erosion rates averaged over much longer 1-2 Ma timescales from thermochronometric data, which give rates on the order of ~1 km/Ma (i.e. 1 mm a^{-1}) (Valla et al., 2011; Fox et al., 2016), suggesting the landscape exists in a broad sense of topographic steady-state over

such timeframes (Burbank, 2002). The combined modelling and TLT approach in this thesis has demonstrated a great deal of variability over a single glacial cycle between these timeframes. Erosion in these high alpine catchments is generally outpaced by the lower trunk valleys during periods of greater ice extent, where > 1000 m of erosional potential is present in some regions (Seguinot & Delaney, 2021). However, the TLT data has revealed that exhumation (which can likely be interpreted as denudation) is very much still present in these high elevation regions under even the coldest, maximum ice conditions when many have suggested them to be predominantly cold-based and largely inactive (Cohen et al., 2018; Seguinot & Delaney, 2021; Jouvet et al., 2023).

Diminished erosion in the high elevation areas during larger glacial extents is balanced out somewhat by increased rates in these areas under less extensive ice, such that the landscape may sustain a dynamic equilibrium when patterns are integrated over a sufficiently long timescale (Hack, 1975). Significant spatial changes in the patterns of erosion within high alpine catchments also occur between glacier extents, such as that seen on the icefall at Trift (Chapter 3, Figure 3.18), where glacial conditions act to maintain or enhance icefall relief whereas interglacial erosion acts to remove the step and smooth the profile. In such cases the overall time spent under certain climatic conditions will dictate the dominant process that will drive local topographic evolution.

While the frequent assumption that glacial erosion is most effective around the position of the ELA (e.g. MacGregor et al., 2000; Anderson et al., 2006; Fox et al., 2016) may well be the case during the initial glacial occupation of fluvial landscapes (Sternai et al., 2013), or idealised models with simplistic profiles (MacGregor et al., 2000; Anderson et al., 2006; Prasicek et al., 2018, 2020), this is not found to hold true under the steady-state LIA or variable interglacial modelling scenarios presented in Chapter 3. The findings here, supported by the TLT field data (Figure 5.2), show the pre-existing glacially influenced topography to be the dominant control on patterns of erosion, as has been suggested elsewhere at larger scales (Headley et al., 2012; Pedersen et al., 2014; Yanites & Ehlers, 2016).

The glacier buzzsaw hypothesis further implies erosion to be most effective at elevations above the long-term ELA (Brozović et al., 1997; Mitchell & Montgomery, 2006; Egholm et al., 2009), which is yet again not supported by rates from modelling and TLT data, as these are far below those indicated from modelled cumulative erosion of the lower alpine trunk valleys (Seguinot & Delaney, 2021). Moreover, as presented in Chapter 2, the presence of major topographic steps which manifest as contemporary icefalls are as strongly correlated

to climatic gradients as cirque and peak elevations are, which form the basis of the buzzsaw hypothesis (Mitchell & Montgomery, 2006; Anders et al., 2010; Mitchell & Humphries, 2015) despite the former being contrarily indicative of erosion in the lower reaches outpacing that of the upper regions.

How these upper regions are then kept in balance with the rest of the landscape returns to the notion of a dynamic equilibrium, whereby they are subjected to stronger erosion during warmer periods when the lower regions are mostly ice-free – as seen by the up-valley shifting of cumulative erosion between steady-state LIA and variable interglacial model scenarios in Chapter 3. In this respect, the glacier buzzsaw hypothesis is more a mechanism of discriminating the regions of longest ice residency with steady, slow-varying erosion rates that act to keep the landscape in balance over time, rather than a zone of particularly strong or effective erosion. Further down the profile the landscape is subjected to comparatively shorter but stronger pulses of glacial erosion that produces the high relief features of deep U-shaped valleys and large steps/icefalls.

Several modelling studies have indicated the lower elevation regions of intense erosion may propagate headwards up-valley (Shuster et al., 2011; Sternai et al., 2013; Liebl et al., 2021), which was suggested in Chapter 2 as a mechanism by which icefalls may evolve over time. Such studies have found these responses to occur over timeframes longer than a single glacial/interglacial cycle and particularly during initial glacial occupation as fluvial valleys are progressively transformed into glacial landscapes. As such the lack of any evidence of a similar process in the modelling or TLT data of this thesis may well be a result of both the long glacial history of the Alps and the smaller temporal scope of a single glacial cycle, indicating the landscape is at present in a state of broadly long-term dynamic equilibrium.

5.4 Addressing the Thesis Questions

In Chapter 1, section 1.3, four research questions were outlined to achieve the main aim of the thesis. Here, I will state where and how each research question was addressed, along with briefly summarising the key findings.

Question 1: How do rates of exhumation vary along high alpine glacial profiles that include complex features and landforms unique to glacial erosional processes?

Question 1 was addressed across all three results chapters (2-4). In Chapter 2 I showed the positioning of contemporary icefalls in glacial catchments to be coupled with climate and indicative of a landform created from a long-term bi-modal gradient in glacial erosional efficacy between upper and lower regions of the profile due to the unique spatial variability in glacial activity over time. In Chapter 3 I expanded on this by using numerical modelling to show the spatial variability in glacial erosion according to a simple sliding-erosion law, which was strongly influenced by topographic forcing from features and landforms in the catchment (including icefalls), as well as great temporal variation under changing climate conditions. In Chapter 4 I used a novel method of luminescence thermochronometry that provided empirical field evidence to support the findings of the previous two chapters, by showing variation in exhumation rates by several orders of magnitude throughout the two study catchments, both spatially according to major landforms and temporally over the last glacial period.

Collectively, results from the three chapters demonstrate rates of exhumation vary significantly along high alpine glacial profiles, influenced heavily by the complex features contained within them due to their impact on local ice dynamics.

Question 2: How does glacial erosion vary spatially through time and is dynamic behaviour such as headward migration of features like icefalls or cirques plausible?

Both Chapter 3 and Chapter 4 provided data towards this question. The modelling in Chapter 3 revealed changing ice dynamics (e.g. extent, volume, meltwater) under variable climate scenarios had a significant impact on the response of glacial erosion through time. During interglacial scenarios the longer ice residency time of higher elevation portions of the catchment enabled a balancing of total erosion through time, despite otherwise lower rates of denudation. During glacial conditions, erosional efficacy generally decreases under thicker ice during colder climates which is supported by the TLT data of Chapter 4, with many samples showing a decrease in exhumation rates towards the LGM. Dynamic headward erosion was not explicitly detectable in either the modelling or TLT data. However, the modelling did show a difference in the spatial focusing of erosion on the Trift icefall between glacial and interglacial states, implying a certain degree of dynamism of the feature. The work on icefalls in Chapter 2 also provides a plausible case of headward migration in the cases of large glaciers that lack icefalls but contain steeply graded cirques. It is likely that dynamic headward erosion requires timeframes longer than a single glacial/interglacial cycle (see end of previous section), in which case it would not be detectable in the data here which focused on a single glacial period. In this respect, while the results here are not strictly supportive of the concept of dynamic headward erosion of key features like icefalls and cirques, I do not feel it can be plausibly denied with certainty and should be explored further in future research (see next section).

Question 3: Which erosion law is most applicable at the individual catchment scale and over a variety of timescales?

The use of different erosion law parameters in the modelling work of Chapter 3 demonstrated the significant impact the choice of l and K_G have on the outcome of simulated glacial erosion. The TLT data in Chapter 4 also provided crucial empirical field evidence to help constrain these modelled outcomes, which is often lacking in numerical modelling studies. Earlier in this chapter (section 5.3.2) I discussed the collective findings. The use of l = 1, despite being amongst the most common in previous modelling studies, is found to be wholly inadequate as it greatly over exaggerates erosion throughout the catchment. The use of the non-linear (l = 2) and sub-linear (l = 0.65) exponents were found

to be differently suitable according to the catchment and glacier conditions. Notably, the non-linear exponent appears to greatly underestimate erosion at lower sliding velocities, where the sub-linear law likely provides a better representation. The most accurate choice of l likely depends on the degree to which feedback mechanisms along the glacier are present to spatially limit or enhance erosion, which can be difficult to empirically constrain. The value of K_G was also found to be of critical importance for determining the overall magnitude of erosion, yet remains poorly constrained and likely needs to be varied spatially, necessitating further research (see next section).

Question 4: What is the magnitude of potential bias in using contemporary sediment yields to estimate longer-term glacial cycle erosion rates?

This final question was specifically addressed earlier in this chapter within section 5.3.3, where estimates of erosion from contemporary sediment yields of catchments across the Alps were compared to the data from Chapter 3 and 4. At Otemma, the contemporary estimate is close to the catchment-averaged TLT rate for the last 100 ka, as the modelling work showed little difference between average erosion rates under interglacial or glacial conditions. At Trift, Holocene-averaged rates on the riegel are far greater than TLT rates for the same region, implying this catchment differs greatly between longer-term glacial cycle and more recent rates. It was therefore suggested that the potential bias involved in extrapolating contemporary estimates to longer-term rates of erosion may be dependent on the specific dynamics of the catchment in question – i.e. hypsometry, position within the wider basin structure – that will influence glacier response to climatic forcing, but a wider sample size across more catchments is needed to accept such a hypothesis with confidence.

5.5 Recommendations for Future Research Directions

The results of this thesis have improved our understanding of just how variable glacial erosion is within smaller high alpine catchments, yet a number of methodological limitations were encountered along the way, which if addressed, could provide even further insight into some of the topics raised. Here I will provide some key recommendations for future research that would build upon the findings of the thesis, presented in a chronological order of the topics in each results chapter.

5.5.1 Icefalls and Dynamic Migratory Erosion

The regional inventory of Swiss icefalls in Chapter 2 was the first of its kind to present a detailed view of icefall metrics and their potential importance in the glacial landscape. The chosen methodological approach limited the dataset to current, actively glaciated icefalls only. During compilation of the inventory, it was clear that there were many cases of large topographic steps being present much further down the valley profile that would have only been ice covered during larger ice extents such as the LGM. Under which specific glacier extents these features would have been of sufficient relief to enact a dynamical ice response in the form of an icefall is unclear, though it would be very interesting to see if their correlation with climate is strong enough such that they could be used as a proxy for delineating LGM ELAs. Mapping such features in the future would require a joint topographic-modelling data approach to identify appropriately sized features and ice dynamics under past glacial conditions in the same way as it was done here for the contemporary features further up the profile.

The case for a potential dynamic headward evolution of icefalls akin to fluvial knickpoint retreat was also made here, but the later evidence from Chapters 3 and 4 were ultimately insufficient to satisfactorily resolve the likelihood of such phenomena occurring. Recent developments in producing 1D models of steady-state glacial long-profiles have been used to test the interplay of glacial erosion in balancing tectonic uplift over long geologic timescales > 1 Ma (Prasicek et al., 2018, 2020; Deal & Prasicek, 2021). Adapting such models to include more complex heterogenous profiles with variably effective glacial

erosion according to elevation or changes in lithology could enable a wide range of icefall formation and evolution hypotheses to be tested, including that of headward migration.

In the fluvial domain, a method has been developed using the stream power incision model to numerically represent the steady-state elevation of channels along the profile, which when compared across river basins can determine the state of landscape disequilibrium and give a direction and intensity of divide migration (Willett et al., 2014). Application of such a method to the glacial domain is difficult due to the highly non-linear nature of glacial erosion along the profile, though the development of an equivalent 'sliding ice incision model' by Deal & Prasicek (2021) may allow similar methods to be tested in an attempt to understand where glacial catchments are most out of balance with the surrounding landscape and therefore where erosion may be focused for dynamic re-equilibration (e.g. potentially around icefalls).

Future higher-order modelling work (e.g. with iSOSIA) could use simple synthetic domains to test hypotheses of formation (e.g. lithology, confluences, QELA) and evolution (static vs. headward) developed in Chapter 2 to provide further analysis of these landforms.

Finally, empirical data will always be needed to test the accuracy of model outputs such as those described above and therefore, obtaining more samples from cirques, headwalls and on/around icefalls to apply to TLT and/or other thermochronometric techniques would prove highly valuable.

5.5.2 Numerical Erosion Laws

The discussions earlier in this chapter demonstrated that the simple numeric erosion law coupled to sliding velocity is capable of yielding rates and patterns of erosion that are highly similar to the independent TLT data from the field. A number of uncertainties are still present though, notably the poor performance of the non-linear exponent at lower sliding velocities which demonstrate it may not simply be suitable to all model scenarios. More empirical data on both sliding velocities and erosion rates are required to improve constraints on the linearity exponent, both at the sub-catchment scale as explored here, and at the wider multi-glacier scale (e.g. Cook et al., 2020).

The lack of constraints on K_G is a large hindrance on being able to model accurate magnitudes of glacial erosion. This calls for further empirical testing on the specific erodibility of different lithologies in the vein of Boulton (1979), which may then permit a

more reliable method of spatially varying K_G within model domains according to catchment geology, or dynamically through time according to bed responses to simulated behaviour (e.g. crevassing, air exposure or hydrological pressure weaking lithology over time). This would improve model accuracy in simulating the spatial patterns of glacial erosion across real landscapes and the investigation of the formation of key features like overdeepenings and icefalls beyond simply imposing a single step-change in K_G to force a response (e.g. Prasicek et al., 2018).

The development of more complex numerical erosion laws to separate the processes of quarrying and abrasion (Ugelvig et al., 2016; Ugelvig & Egholm, 2018) could also improve model accuracy, particularly when coupled with advancements in extra-glacial particle generation and tracking (Bernard et al., 2020). However, such laws lack an empirical constraint due to the difficulty of reliably determining the relative contribution of quarrying and abrasion processes in the field. Consequently, they require careful consideration over a range of model parameters, whose outputs need to be combined and compared with real catchment data.

5.5.3 Thermoluminescence Thermochronometry

The TLT method employed in Chapter 4 of this thesis represents a significant step forward in the application of thermochronometry to geomorphological applications, as the ability to extract a meaningful timeseries of exhumation data across sample histories spanning 100 ka is unrivalled by other geochronology techniques. The method is still in its infancy, however, this being only the second main study to which it was used and the first in an actively glaciated landscape, following Nathan Brown's initial development and use of the technique in the postglacial landscapes of the San Bernardino mountains of California and in Yellowstone, Montana (Brown, 2017; Brown & Rhodes, 2022). As such, there are some simplifications and uncertainties that can be improved on with future development.

Firstly, the current method employs a simplistic thermal model with a fixed geothermal gradient across the landscape. The reality of nature is of course far more complex, as the surface topography can warp the regularity of isotherms, potentially up to a depth twice that of the total surface relief (Anderson & Anderson, 2010), which would influence the inferred rate of exhumation. More sophisticated models can be employed to account for such topographic variation (Fox & Carter, 2020), though these carry their own set of

assumptions and ideally would be forced with empirical field data from the likes of measured borehole temperatures (e.g. Guralnik et al., 2015).

Secondly, exhumation history for the most recent 10 ka time period was unable to be reliably resolved, as a systematic deviation to higher rates occurs across all samples regardless of geologic history (including samples from Brown's aforementioned studies). The exact reasonings behind this are currently unknown but a matter of future investigation (Brown, pers. comm., 2023).

Overall, the technique is highly promising and the main desire for future research is its application to more samples, not only to those collected in this study which were unable to be processed due to time constraints, but also to further sample sites to resolve histories of cirques and icefalls as mentioned prior, or indeed any landscape and geomorphological question worthy of investigation.

5.6 Thesis Conclusions

In this thesis I have presented work that improves our understanding of glacial erosion operating at the sub-catchment scale under a range of glacier conditions. Through application of three distinctly different methodologies I have produced complimentary datasets that demonstrate a strong spatio-temporal variability to glacial erosion within the small high elevation alpine catchments occupied by today's glaciers.

Mapping of contemporary icefalls across Switzerland in Chapter 2 brings attention to these unique glacial landforms through improved definition according to empirically constrained characteristics (e.g. gradient, ice velocity, thickness) and a previously unreported coupling to climatic gradients. The latter has potentially significant implications for our understanding of the processes of glacial landscape evolution, as it contradicts the oft-cited glacial buzzsaw hypothesis (Brozović et al., 1997; Egholm et al., 2009) which uses a similar climatic correlation to cirque and summit elevations to imply glacial erosion is more effective above the long-term ELA. Instead, I suggest the buzzsaw mechanism to be a signal highlighting the regions of longest ice-residency time, which slowly but steadily enable a dynamic equilibrium of the landscape.

Use of numerical modelling in Chapter 3 showed the substantial impact that choice of erosion law parameters can have on simulated patterns and magnitudes of erosion. A commonly employed forcing where erosion scales linearly with sliding speed was found to dramatically over-exaggerate denudation of the landscape when compared to field data in this final chapter, whilst non-linear or sub-linear exponents were found to be more appropriate, though likely differently applicable according to the catchment in question. The constant for bedrock erodibility (K_G) has significant impacts on the magnitude of simulated erosion and requires further attention and study in the future. Simulated glacial erosion was found to vary substantially both spatially across catchments and temporally across changing climate conditions. Spatial patterns are dominantly controlled by the pre-existing topography which influences rates of basal sliding and shear stress, whilst the temporal changes are influenced by catchment-specific ice dynamical responses to shifts in climate, such that catchment hypsometry and proximity to larger trunk valleys will impact the rapidity to which erosion is dampened or enhanced under cooling or warming climates.

Application of a novel method of thermoluminescence thermochronometry in Chapter 4 provided a unique timeseries of exhumation rates across the last glacial period, which can be inferred to represent rates of glacial erosion. The spatial and temporal patterns revealed

from this field data is in broad agreement with those found in the numerical modelling and shows major landforms like icefalls and riegels to be regions of significantly different erosional intensity. Further development of the technique and application to more samples in the future would permit an even more detailed analysis of the history of alpine landscape evolution and empirically-test key hypotheses like the glacial buzzsaw mechanism of summit and headwall denudation, and headward migration of icefalls.

Together, the data demonstrates that the unique heterogenous signature of glacial long-profiles and high relief catchments that contain different landforms, are a result of substantially variable glacial erosion both spatially and temporally according to topographic and climate forcings, a complexity that is lost under models that imply cold-based conditions over the last glacial period or time-averaged rates of erosion that suggests the landscape to be in a long-term steady-state.

6. References

Adamiec, G. & Aitken, M. J. (1998). Dose-Rate Conversion Factors: Update. *Ancient TL*, 16(2), 37–50.

Aitken, M. J. (1985). *Thermoluminescence Dating*. Academic Press Inc. Retrieved January 6, 2021,

Alley, R. B., Cuffey, K. M. & Zoet, L. K. (2019). Glacial Erosion: Status and Outlook. *Annals of Glaciology*, 60(80), 1–13.

Anders, A. M., Mitchell, S. G. & Tomkin, J. H. (2010). Cirques, Peaks, and Precipitation Patterns in the Swiss Alps: Connections among Climate, Glacial Erosion, and Topography. *Geology*, 38(3), 239–242.

Anderson, R. S. (2005). Teflon Peaks: The Evolution of High Local Relief in Glaciated Mountain Ranges, AGU Fall Meeting Abstracts, 2005. H33F-04

Anderson, R. S. (2014). Evolution of Lumpy Glacial Landscapes. *Geology*, 42(8), 679–682.

Anderson, R. S. & Anderson, S. P. (2010). *Geomorphology: The Mechanics and Chemistry of Landscapes*. Cambridge University Press.

Anderson, R. S., Molnar, P. & Kessler, M. A. (2006). Features of Glacial Valley Profiles Simply Explained. *Journal of Geophysical Research: Earth Surface*, 111(1), 1–14.

Armstrong, W. H., Anderson, R. S. & Fahnestock, M. A. (2017). Spatial Patterns of Summer Speedup on South Central Alaska Glaciers. *Geophysical Research Letters*, 44(18), 9379–9388.

Atkins, C. B., Barrett, P. J. & Hicock, S. R. (2002). Cold Glaciers Erode and Deposit: Evidence from Allan Hills, Antarctica. *Geology*, 30(7), 659–662.

Baral, D. R., Hutter, K. & Greve, R. (2001). Asymptotic Theories of Large-Scale Motion, Temperature, and Moisture Distribution in Land-Based Polythermal Ice Sheets: A Critical Review and New Developments. *Applied Mechanics Reviews*, 54(3), 215–256.

Barr, I. D., Ely, J. C., Spagnolo, M., Evans, I. S. & Tomkins, M. D. (2019). The Dynamics of Mountain Erosion: Cirque Growth Slows as Landscapes Age. *Earth Surface Processes and Landforms*, 44(13), 2628–2637.

Barr, I. D. & Spagnolo, M. (2014). Testing the Efficacy of the Glacial Buzzsaw: Insights from the Sredinny Mountains, Kamchatka. *Geomorphology*, 206, 230–238.

Barr, I. D. & Spagnolo, M. (2015). Glacial Cirques as Palaeoenvironmental Indicators: Their Potential and Limitations. *Earth-Science Reviews*, 151, 48–78.

Bateman, M. D. (Ed.). (2019). *Handbook of Luminescence Dating*. Dunbeath, Caithness, Scotland, UK: Whittles Publishing.

Beaud, F., Venditti, J. G., Flowers, G. E. & Koppes, M. (2018a). Excavation of Subglacial Bedrock Channels by Seasonal Meltwater Flow. *Earth Surface Processes and Landforms*, 43(9), 1960–1972.

Beaud, F., Flowers, G. E. & Venditti, J. G. (2018b). Modeling Sediment Transport in Ice-Walled Subglacial Channels and Its Implications for Esker Formation and Proglacial Sediment Yields. *Journal of Geophysical Research: Earth Surface*, 123(12), 3206–3227.

Benn, D. & Evans, D. J. A. (2010). *Glaciers and Glaciation, 2nd Edition*. Routledge.

Berlin, M. M. & Anderson, R. S. (2007). Modeling of Knickpoint Retreat on the Roan Plateau, Western Colorado. *Journal of Geophysical Research: Earth Surface*, 112(F3)

Bernard, M., Steer, P., Gallagher, K. & Egholm, D. L. (2020). Modelling the Effects of Ice Transport and Sediment Sources on the Form of Detrital Thermochronological Age Probability Distributions from Glacial Settings. *Earth Surface Dynamics*, 8(4), 931–953.

Bindschadler, R. (1982). A Numerical Model of Temperate Glacier Flow Applied to the Quiescent Phase of a Surge-Type Glacier. *Journal of Glaciology*, 28(99), 239–265.

Bini, A., Buoncristiani, J. F., Couterrand, S., Ellwanger, D., Felber, M., Florineth, D., Graf, H. R., Keller, O., Kelly, M., Schlüchter, C. & Schoeneich, P. (2009). *Die Schweiz Während Des Letzteiszeitlichen Maximums (LGM)*. Bundesamt für Landesto-pografie swisstopo.

Bishop, P., Hoey, T. B., Jansen, J. D. & Artza, I. L. (2005). Knickpoint Recession Rate and Catchment Area: The Case of Uplifted Rivers in Eastern Scotland. *Earth Surface Processes and Landforms*, 30(6), 767–778.

Biswas, R. H., Herman, F., King, G. E. & Braun, J. (2018). Thermoluminescence of Feldspar as a Multi-Thermochronometer to Constrain the Temporal Variation of Rock Exhumation in the Recent Past. *Earth and Planetary Science Letters*, 495, 56–68.

Bogen, J. (1996). Erosion Rates and Sediment Yields of Glaciers. *Annals of Glaciology*, 22, 48–52.

Bohleber, P., Hoffmann, H., Kerch, J., Sold, L. & Fischer, A. (2018). Investigating Cold Based Summit Glaciers through Direct Access to the Glacier Base: A Case Study Constraining the Maximum Age of Chli Titlis Glacier, Switzerland. *The Cryosphere*, 12(1), 401–412.

Bohleber, P., Schwikowski, M., Stocker-Waldhuber, M., Fang, L. & Fischer, A. (2020). New Glacier Evidence for Ice-Free Summits during the Life of the Tyrolean Iceman. *Scientific Reports*, 10(1), 20513.

Boulton, G. S. (1979). Processes of Glacier Erosion on Different Substrata. *Journal of Glaciology*, 23(89), 15–38.

Boulton, G. S. (1982). Processes and Patterns of Glacial Erosion, in: Coates, D. R. (Ed.), *Glacial Geomorphology*, (pp. 41–87). Dordrecht: Springer Netherlands. Retrieved November 1, 2023, from http://link.springer.com/10.1007/978-94-011-6491-7_2

Bouscary, C. & King, G. E. (2022). Luminescence Thermochronometry of Feldspar Minerals: Optimisation of Measurement Conditions for the Derivation of Thermal Kinetic Parameters Using Isothermal Holding Experiments. *Quaternary Geochronology*, 67, 101240.

Brædstrup, C. F., Egholm, D. L., Ugelvig, S. V. & Pedersen, V. K. (2016). Basal Shear Stress under Alpine Glaciers: Insights from Experiments Using the iSOSIA and Elmer/Ice Models. *Earth Surface Dynamics*, 4(1), 159–174.

Brocklehurst, S. H. & Whipple, K. X. (2002). Glacial Erosion and Relief Production in the Eastern Sierra Nevada, California. *Geomorphology*, 42(1–2), 1–24.

Brocklehurst, S. H. & Whipple, K. X. (2007). Response of Glacial Landscapes to Spatial Variations in Rock Uplift Rate. *Journal of Geophysical Research*, 112(F2), F02035.

Brown, G. H., Sharp, M. & Tranter, M. (1996). Subglacial Chemical Erosion: Seasonal Variations in Solute Provenance, Haut Glacier D'Arolla, Valais, Switzerland. *Annals of Glaciology*, 22, 25–31.

Brown, N. D. (2017). Using Luminescence Signals from Bedrock Feldspars for Low-Temperature Thermochronology. PhD Thesis, UCLA.

Brown, N. D. (2020). Which Geomorphic Processes Can Be Informed by Luminescence Measurements? *Geomorphology*, 367, 107296.

Brown, N. D. & Rhodes, E. J. (2022). Developing an Internally Consistent Methodology for K-Feldspar MAAD TL Thermochronology. *Radiation Measurements*, 153, 106751.

Brown, N. D., Rhodes, E. J. & Harrison, T. M. (2017). Using Thermoluminescence Signals from Feldspars for Low-Temperature Thermochronology. *Quaternary Geochronology*, 42, 31–41.

Brozović, N., Burbank, D. W. & Meigs, A. J. (1997). Climatic Limits on Landscape Development in the Northwestern Himalaya. *Science*, 276(5312), 571–574.

Budd, W. F., Keage, P. L. & Blundy, N. A. (1979). Empirical Studies of Ice Sliding. *Journal of Glaciology*, 23(89), 157–170.

Bueler, E. & Brown, J. (2009). Shallow Shelf Approximation as a "Sliding Law" in a Thermomechanically Coupled Ice Sheet Model. *Journal of Geophysical Research: Earth Surface*, 114(F3), 2008JF001179.

Burbank, D. W. (2002). Rates of Erosion and Their Implications for Exhumation. *Mineralogical Magazine*, 66(1), 25–52.

Campani, M., Mulch, A., Kempf, O., Schlunegger, F. & Mancktelow, N. (2012). Miocene Paleotopography of the Central Alps. *Earth and Planetary Science Letters*, 337–338, 174–185.

Castillo, M., Bishop, P. & Jansen, J. D. (2013). Knickpoint Retreat and Transient Bedrock Channel Morphology Triggered by Base-Level Fall in Small Bedrock River Catchments: The Case of the Isle of Jura, Scotland. *Geomorphology*, 180–181, 1–9.

Champagnac, J. D., Schlunegger, F., Norton, K., von Blanckenburg, F., Abbühl, L. M. & Schwab, M. (2009). Erosion-Driven Uplift of the Modern Central Alps. *Tectonophysics*, 474(1–2), 236–249.

Clark, J. M. & Lewis, W. V. (1951). Rotational Movement in Cirque and Valley Glaciers. *The Journal of Geology*, 59(6), 546–566.

Cohen, D., Gillet-Chaulet, F., Haeberli, W., Machguth, H. & Fischer, U. H. (2018). Numerical Reconstructions of the Flow and Basal Conditions of the Rhine Glacier, European Central Alps, at the Last Glacial Maximum. *The Cryosphere*, 12(8), 2515–2544.

Cohen, D., Hooyer, T. S., Iverson, N. R., Thomason, J. F. & Jackson, M. (2006). Role of Transient Water Pressure in Quarrying: A Subglacial Experiment Using Acoustic Emissions. *Journal of Geophysical Research: Earth Surface*, 111(F3), 2005JF000439.

Colgan, W., Rajaram, H., Abdalati, W., McCutchan, C., Mottram, R., Moussavi, M. S. & Grigsby, S. (2016). Glacier Crevasses: Observations, Models, and Mass Balance Implications. *Reviews of Geophysics*, 54(1), 119–161.

Cook, S. J. & Swift, D. A. (2012). Subglacial Basins: Their Origin and Importance in Glacial Systems and Landscapes. *Earth-Science Reviews*, 115(4), 332–372.

Cook, S. J., Swift, D. A., Kirkbride, M. P., Knight, P. G. & Waller, R. I. (2020). The Empirical Basis for Modelling Glacial Erosion Rates. *Nature Communications*, 11(1), 1–7.

Crest, Y., Delmas, M., Braucher, R., Gunnell, Y. & Calvet, M. (2017). Cirques Have Growth Spurts during Deglacial and Interglacial Periods: Evidence from 10Be and 26Al Nuclide Inventories in the Central and Eastern Pyrenees. *Geomorphology*, 278, 60–77.

Crosby, B. T. & Whipple, K. X. (2006). Knickpoint Initiation and Distribution within Fluvial Networks: 236 Waterfalls in the Waipaoa River, North Island, New Zealand. *Geomorphology*, 82(1–2), 16–38.

Cuffey, K. M. & Paterson, W. S. B. (2010). *The Physics of Glaciers*. Academic Press.

Dalban Canassy, P., Faillettaz, J., Walter, F. & Huss, M. (2012). Seismic Activity and Surface Motion of a Steep Temperate Glacier: A Study on Triftgletscher, Switzerland. *Journal of Glaciology*, 58(209), 513–528.

Davies, B., Bendle, J., Carrivick, J., McNabb, R., McNeil, C., Pelto, M., Campbell, S., Holt, T., Ely, J. & Markle, B. (2022). Topographic Controls on Ice Flow and Recession for Juneau Icefield (Alaska/British Columbia). *Earth Surface Processes and Landforms*, esp.5383.

Deal, E. & Prasicek, G. (2021). The Sliding Ice Incision Model: A New Approach to Understanding Glacial Landscape Evolution. *Geophysical Research Letters*, 48(1).

Delaney, I. & Adhikari, S. (2020). Increased Subglacial Sediment Discharge in a Warming Climate: Consideration of Ice Dynamics, Glacial Erosion, and Fluvial Sediment Transport. *Geophysical Research Letters*, 47(7), 1–11.

Delaney, I. & Anderson, L. (2022). Debris Cover Limits Subglacial Erosion and Promotes Till Accumulation. *Geophysical Research Letters*, 49.

Delaney, I., Bauder, A., Werder, M. A. & Farinotti, D. (2018). Regional and Annual Variability in Subglacial Sediment Transport by Water for Two Glaciers in the Swiss Alps. *Frontiers in Earth Science*, 6(October), 1–17.

Delaney, I., Werder, M. A., Felix, D., Albayrak, I., Boes, R. M. & Farinotti, D. (2024). Controls on Sediment Transport From a Glacierized Catchment in the Swiss Alps Established Through Inverse Modeling of Geomorphic Processes. *Water Resources Research*, 60(4), e2023WR035589.

Derksen, C., Adler, C., Collins, M. & Sebesvari, Z. (2022). Editorial: Knowledge Gaps from the IPCC Special Report on the Ocean and Cryosphere in a Changing Climate and Recent Advances (Volumes I and II). *Frontiers in Climate*, 4, 983144.

Dieleman, C., Christl, M., Vockenhuber, C., Gautschi, P., Graf, H. R. & Akçar, N. (2022). Age of the Most Extensive Glaciation in the Alps. *Geosciences*, 12(1), 39.

Dodson, M. H. (1973). Closure Temperature in Cooling Geochronological and Petrological Systems. *Contributions to Mineralogy and Petrology*, 40(3), 259–274.

Dowling, T. P. F., Spagnolo, M. & Möller, P. (2015). Morphometry and Core Type of Streamlined Bedforms in Southern Sweden from High Resolution LiDAR. *Geomorphology*, 236, 54–63.

Dühnforth, M., Anderson, R. S., Ward, D. & Stock, G. M. (2010). Bedrock Fracture Control of Glacial Erosion Processes and Rates. *Geology*, 38(5), 423–426.

Duller, G. A. T. (1994). Luminescence Dating of Sediments Using Single Aliquots: New Procedures. *Quaternary Science Reviews*, 13(2), 149–156.

Duller, G. A. T. (2008). *Luminescence Dating: Guidelines on Using Luminescence Dating in Archaeology*. English Heritage.

Dürst Stucki, M. & Schlunegger, F. (2013). Identification of Erosional Mechanisms during Past Glaciations Based on a Bedrock Surface Model of the Central European Alps. *Earth and Planetary Science Letters*, 384, 57–70.

Egholm, D. L., Jansen, J. D., Brædstrup, C. F., Pedersen, V. K., Andersen, J. L., Ugelvig, S. V., Larsen, N. K. & Knudsen, M. F. (2017). Formation of Plateau Landscapes on Glaciated Continental Margins. *Nature Geoscience*, 10(8), 592–597.

Egholm, D. L., Knudsen, M. F., Clark, C. D. & Lesemann, J. E. (2011). Modeling the Flow of Glaciers in Steep Terrains: The Integrated Second-Order Shallow Ice Approximation (iSOSIA). *Journal of Geophysical Research: Earth Surface*, 116(F2).

Egholm, D. L., Nielsen, S. B., Pedersen, V. K. & Lesemann, J. E. (2009). Glacial Effects Limiting Mountain Height. *Nature*, 460(7257), 884–887.

Egholm, D. L., Pedersen, V. K., Knudsen, M. F. & Larsen, N. K. (2012a). Coupling the Flow of Ice, Water, and Sediment in a Glacial Landscape Evolution Model. *Geomorphology*, 141–142, 47–66.

Egholm, D. L., Pedersen, V. K., Knudsen, M. F. & Larsen, N. K. (2012b). On the Importance of Higher Order Ice Dynamics for Glacial Landscape Evolution. *Geomorphology*, 141–142, 67–80.

Erb, M. P., McKay, N. P., Steiger, N., Dee, S., Hancock, C., Ivanovic, R. F., Gregoire, L. J. & Valdes, P. (2022). Reconstructing Holocene Temperatures in Time and Space Using Paleoclimate Data Assimilation. *Climate of the Past*, 18(12), 2599–2629.

Evans, I. S. (2021). Glaciers, Rock Avalanches and the 'Buzzsaw' in Cirque Development: Why Mountain Cirques Are of Mainly Glacial Origin. *Earth Surface Processes and Landforms*, 46(1), 24–46.

Evans, I. S., Hall, A. M. & Kleman, J. (2015). Glacial Cirques and the Relationship between Equilibrium Line Altitudes and Mountain Range Height: COMMENT. *Geology*, 43(6), e366–e366.

Fabel, D., Ballantyne, C. K. & Xu, S. (2012). Trimlines, Blockfields, Mountain-Top Erratics and the Vertical Dimensions of the Last British–Irish Ice Sheet in NW Scotland. *Quaternary Science Reviews*, 55, 91–102.

Falkowski, S., Ehlers, T. A., Madella, A., Glotzbach, C., Georgieva, V. & Strecker, M. R. (2021). Glacial Catchment Erosion From Detrital Zircon (U-Th)/He Thermochronology: Patagonian Andes. *Journal of Geophysical Research: Earth Surface*, 126(10).

Federal Office of Topography swisstopo. (2022). GeoCover Dataset. *Bundesamt für Landestopografie swisstopo*. Retrieved May 6, 2022, from https://www.swisstopo.admin.ch/de/geodata/geology/maps/geocover.html

Federal Office of Topography swisstopo. (2024). Digital Dufour card. Retrieved March 15, 2024, from https://www.swisstopo.admin.ch/de/digitale-dufourkarte

Fischer, U., Bebiolka, A., Brandefelt, J., Follin, S., Hirschorn, S., Jenson, M., Keller, S., Kennell, L., Naslund, J., Normani, S., Selroos, J. & Vidstrand, P. (2014). Radioactive Waste Under Conditions of Future Ice Ages, in: Haeberli, W., Whiteman, C., and Shroder, J. (Eds.), *Snow and Ice-Related Hazards, Risks, and Disasters*, (pp. 345–385). Waltham, MA: Academic Press.

Fitzsimons, S. J. & Veit, H. (2001). Geology and Geomorphology of the European Alps and the Southern Alps of New Zealand: A Comparison. *Mountain Research and Development*, 21(4), 340–349.

Forbes, J.D. (1859). *Occasional Papers on the Theory of Glaciers*. Salzwasser-Verlag. Retrieved from https://books.google.fr/books?id=ICmKEAAAQBAJ

Forbes, James David. (1859). *Occasional Papers on the Theory of Glaciers Now First Collected and Arranged*. A & C Black.

Foster, D., Brocklehurst, S. H. & Gawthorpe, R. L. (2008). Small Valley Glaciers and the Effectiveness of the Glacial Buzzsaw in the Northern Basin and Range, USA. *Geomorphology*, 102(3–4), 624–639.

Fox, M. & Carter, A. (2020). Heated Topics in Thermochronology and Paths towards Resolution. *Geosciences*, 10(9), 375.

Fox, M., Herman, F., Willett, S. D. & Schmid, S. M. (2016). The Exhumation History of the European Alps Inferred from Linear Inversion of Thermochronometric Data. *American Journal of Science*, 316(6), 505–541.

Furlong, K. P., Kirby, E., Creason, C. G., Kamp, P. J. J., Xu, G., Danišík, M., Shi, X. & Hodges, K. V. (2021). Exploiting Thermochronology to Quantify Exhumation Histories and Patterns of Uplift Along the Margins of Tibet. *Frontiers in Earth Science*, 9, 688374.

Gabbud, C., Micheletti, N. & Lane, S. N. (2016). Response of a Temperate Alpine Valley Glacier to Climate Change at the Decadal Scale. *Geografiska Annaler: Series A, Physical Geography*, 98(1), 81–95.

Gabet, E. J., Burbank, D. W., Pratt-Sitaula, B., Putkonen, J. & Bookhagen, B. (2008). Modern Erosion Rates in the High Himalayas of Nepal. *Earth and Planetary Science Letters*, 267(3–4), 482–494.

Gagliardini, O., Zwinger, T., Gillet-Chaulet, F., Durand, G., Favier, L., de Fleurian, B., Greve, R., Malinen, M., Martín, C., Råback, P., Ruokolainen, J., Sacchettini, M., Schäfer, M., Seddik, H. & Thies, J. (2013). Capabilities and Performance of Elmer/Ice, a New-Generation Ice Sheet Model. *Geoscientific Model Development*, 6(4), 1299–1318.

Gilbert, G. K. (1910). *Harriman Alaska Series: Glaciers and Glaciation*. Washington D.C.: Smithsonian Institution. Retrieved from https://books.google.co.uk/books?id=TsOuwAEACAAJ

GLAMOS. (2018). Yearbook No 1-138The Swiss Glaciers 1880-2016/17. Retrieved March 13, 2024, from https://doi.glamos.ch/pubs/glrep/glrep_series.html

Godon, C., Mugnier, J. L., Fallourd, R., Paquette, J. L., Pohl, A. & Buoncristiani, J. F. (2013). The Bossons Glacier Protects Europe's Summit from Erosion. *Earth and Planetary Science Letters*, 375, 135–147.

Goodsell, B., Hambrey, M. J. & Glasser, N. F. (2002). Formation of Band Ogives and Associated Structures at Bas Glacier d'Arolla, Valais, Switzerland. *Journal of Glaciology*, 48(161), 287–300.

Grab, M., Mattea, E., Bauder, A., Huss, M., Rabenstein, L., Hodel, E., Linsbauer, A., Langhammer, L., Schmid, L., Church, G., Hellmann, S., Délèze, K., Schaer, P., Lathion, P., Farinotti, D. & Maurer, H. (2021). Ice Thickness Distribution of All Swiss Glaciers Based on Extended Ground-Penetrating Radar Data and Glaciological Modeling. *Journal of Glaciology*, (May), 1–19.

Greene, A. M., Broecker, W. S. & Rind, D. (1999). Swiss Glacier Recession since the Little Ice Age: Reconciliation with Climate Records. *Geophysical Research Letters*, 26(13), 1909–1912.

Guillon, H., Mugnier, J. & Buoncristiani, J. (2018). Proglacial Sediment Dynamics from Daily to Seasonal Scales in a Glaciated Alpine Catchment (Bossons Glacier, Mont Blanc Massif, France). *Earth Surface Processes and Landforms*, 43(7), 1478–1495.

Guillon, H., Mugnier, J. L., Buoncristiani, J. F., Carcaillet, J., Godon, C., Prud'homme, C., vander Beek, P. & Vassallo, R. (2015). Improved Discrimination of Subglacial and Periglacial Erosion Using 10Be Concentration Measurements in Subglacial and Supraglacial Sediment Load of the Bossons Glacier (Mont Blanc Massif, France). *Earth Surface Processes and Landforms*, 40(9), 1202–1215.

Guinness World Records. (2024). Fastest Glacier Retreat on Land. *Guinness World Records*. Retrieved March 13, 2024, from https://www.guinnessworldrecords.com/world-records/724741-fastest-glacier-retreat-on-land

Guralnik, B., Jain, M., Herman, F., Ankjærgaard, C., Murray, A. S., Valla, P. G., Preusser, F., King, G. E., Chen, R., Lowick, S. E., Kook, M. & Rhodes, E. J. (2015). OSL-Thermochronometry of Feldspar from the KTB Borehole, Germany. *Earth and Planetary Science Letters*, 423, 232–243.

Guralnik, B., Jain, M., Herman, F., Paris, R. B., Harrison, T. M., Murray, A. S., Valla, P. G. & Rhodes, E. J. (2013). Effective Closure Temperature in Leaky and/or Saturating Thermochronometers. *Earth and Planetary Science Letters*, 384, 209–218.

Hack, J. T. (1957). *Studies of Longitudinal Stream Profiles in Virginia and Maryland*. US Government Printing Office.

Hack, J. T. (1975). Dynamic Equilibrium and Landscape Evolution. *Theories of landform development*, 1, 87–102.

Haeberli, W., Linsbauer, A., Cochachin, A., Salazar, C. & Fischer, U. H. (2016). On the Morphological Characteristics of Overdeepenings in High-Mountain Glacier Beds: Morphology of Glacier-Bed Overdeepenings. *Earth Surface Processes and Landforms*, 41(13), 1980–1990.

Haefeli, R. (1951). Some Observations on Glacier Flow. *Journal of Glaciology*, 1(9), 496–500.

Hählen, N. & Keusen, H. (2022). Susten, Berner Oberland, Felsstürze Steigletscher 2019/2020. *Bulletin fuer Angewandte Geologie*, 26(2), 21–29.

Hall, A. M. & Kleman, J. (2014). Glacial and Periglacial Buzzsaws: Fitting Mechanisms to Metaphors. *Quaternary Research (United States)*, 81(2), 189–192.

Hallet, B. (1979). A Theoretical Model of Glacial Abrasion. *Journal of Glaciology*, 23(89), 39–50.

Hallet, B. (1981). Glacial Abrasion and Sliding: Their Dependence on the Debris Concentration in Basal Ice. *Annals of Glaciology*, 2, 23–28.

Hallet, B. (1996). Glacial Quarrying: A Simple Theoretical Model. *Annals of Glaciology*, 22, 1–8.

Hallet, B., Hunter, L. & Bogen, J. (1996). Rates of Erosion and Sediment Evacuation by Glaciers: A Review of Field Data and Their Implications. *Global and Planetary Change*, 12(1–4), 213–235.

Hambrey, M. J., Milnes, A. G. & Siegenthaler, H. (1980). Dynamics and Structure of Griesgletscher, Switzerland. *Journal of Glaciology*, 25(92), 215–228.

Hansen, K. (2020). Inlet's Iceberg Maker Is Nearly Gone. *NASA Earth Observatory*. Retrieved November 9, 2023, from https://earthobservatory.nasa.gov/images/147171/inlets-iceberg-maker-is-nearly-gone

Harbor, J. M. (1989). Early Discoverers XXXVI: W.J. McGee On Glacial Erosion Laws and the Development of Glacial Valleys. *Journal of Glaciology*, 35(121), 419–425.

Harbor, J. M. (1992). Numerical Modeling of the Development of U-Shaped Valleys by Glacial Erosion. *Geological Society of America Bulletin*, 104(10), 1364–1375.

Headley, R., Hallet, B., Roe, G., Waddington, E. D. & Rignot, E. (2012). Spatial Distribution of Glacial Erosion Rates in the St. Elias Range, Alaska, Inferred from a Realistic Model of Glacier Dynamics. *Journal of Geophysical Research: Earth Surface*, 117(F3), 2011JF002291.

Heimsath, A. M. & McGlynn, R. (2008). Quantifying Periglacial Erosion in the Nepal High Himalaya. *Geomorphology*, 97(1–2), 5–23.

Herman, F., Beaud, F., Champagnac, J. D., Lemieux, J. M. & Sternai, P. (2011). Glacial Hydrology and Erosion Patterns: A Mechanism for Carving Glacial Valleys. *Earth and Planetary Science Letters*, 310(3–4), 498–508.

Herman, F., Beyssac, O., Brughelli, M., Lane, S. N., Leprince, S., Adatte, T., Lin, J. Y. Y., Avouac, J. P. & Cox, S. C. (2015). Erosion by an Alpine Glacier. *Science*, 350(6257), 193–195.

Herman, F. & Braun, J. (2008). Evolution of the Glacial Landscape of the Southern Alps of New Zealand: Insights from a Glacial Erosion Model. *Journal of Geophysical Research: Earth Surface*, 113(2).

Herman, F., Braun, J., Deal, E. & Prasicek, G. (2018). The Response Time of Glacial Erosion. *Journal of Geophysical Research: Earth Surface*, 123(4), 801–817.

Herman, F., De Doncker, F., Delaney, I., Prasicek, G. & Koppes, M. (2021). The Impact of Glaciers on Mountain Erosion. *Nature Reviews Earth & Environment*, 2009(75), 31–47.

Herman, F., Rhodes, E. J., Braun, J. & Heiniger, L. (2010). Uniform Erosion Rates and Relief Amplitude during Glacial Cycles in the Southern Alps of New Zealand, as Revealed from OSL-Thermochronology. *Earth and Planetary Science Letters*, 297(1–2), 183–189.

Herman, F., Seward, D., Valla, P. G., Carter, A., Kohn, B., Willett, S. D. & Ehlers, T. A. (2013). Worldwide Acceleration of Mountain Erosion under a Cooling Climate. *Nature*, 504(7480), 423–426.

Hicks, D. M., Mcsaveney, M. J. & Chinn, T. J. H. (1990). Sedimentation in Proglacial Ivory Lake, Southern Alps, New Zealand. *Arctic and Alpine Research*, 22(1), 26–42.

Holzhauser, H., Magny, M. & Zumbuühl, H. J. (2005). Glacier and Lake-Level Variations in West-Central Europe over the Last 3500 Years. *The Holocene*, 15(6), 789–801.

Hooke, R. Leb. (1991). Positive Feedbacks Associated with Erosion of Glacial Cirques and Overdeepenings. *Geological Society of America Bulletin*, 103, 1104–1108.

Hooke, R. Leb., Holmlund, P. & Iverson, N. R. (1987). Extrusion Flow Demonstrated by Bore-Hole Deformation Measurements Over a Riegel, Storglaciären, Sweden. *Journal of Glaciology*, 33(113), 72–78.

Humphrey, N. F. & Raymond, C. F. (1994). Hydrology, Erosion and Sediment Production in a Surging Glacier: Variegated Glacier, Alaska, 1982–83. *Journal of Glaciology*, 40(136), 539–552.

Hunter, L. E., Powell, R. D. & Lawson, D. E. (1996). Flux of Debris Transported by Ice at Three Alaskan Tidewater Glaciers. *Journal of Glaciology*, 42(140), 123–135.

Huntington, K. W., Ehlers, T. A., Hodges, K. V. & Whipp, D. M. (2007). Topography, Exhumation Pathway, Age Uncertainties, and the Interpretation of Thermochronometer Data. *Tectonics*, 26(4), 2007TC002108.

Huss, M. (2022). Worse than 2003: Swiss Glaciers Are Melting More than Ever Before. *Swiss Academy of Sciences (SCNAT)*. Retrieved February 1, 2023, from https://scnat.ch/en/id/qPn2w

Huss, M., Dhulst, L. & Bauder, A. (2015). New Long-Term Mass-Balance Series for the Swiss Alps. *Journal of Glaciology*, 61(227), 551–562.

Hutter, K. (1983). The Application of the Shallow-Ice Approximation, in: *Theoretical Glaciology*, (pp. 256–332). Dordrecht: Springer Netherlands.

Iken, A. (1981). The Effect of the Subglacial Water Pressure on the Sliding Velocity of a Glacier in an Idealized Numerical Model. *Journal of Glaciology*, 27(97), 407–421.

Iken, A. & Bindschadler, R. A. (1986). Combined Measurements of Subglacial Water Pressure and Surface Velocity of Findelengletscher, Switzerland: Conclusions about Drainage System and Sliding Mechanism. *Journal of Glaciology*, 32(110), 101–119.

IPCC. (2019). *The Ocean and Cryosphere in a Changing Climate: Special Report of the Intergovernmental Panel on Climate Change* (H.-O. Pörtner, D. C. Roberts, V. Masson-Delmotte, P. Zhai, M. Tignor, E. Poloczanska, K. Mintenbeck, A. Alegría, M. Nicolai, A. Okem, J. Petzold, B. Rama, and N. M. Weyer, Eds.). Cambridge University Press.

Iverson, N. R. (2012). A Theory of Glacial Quarrying for Landscape Evolution Models. *Geology*, 40(8), 679–682.

Iverson, N. R., Helanow, C. & Zoet, L. K. (2019). Debris-Bed Friction during Glacier Sliding with Ice–Bed Separation. *Annals of Glaciology*, 60(80), 30–36.

Ivy-Ochs, S. (2015). Glacier Variations in the European Alps at the End of the Last Glaciation. *Cuadernos de Investigación Geográfica*, 41(2), 295.

Ivy-Ochs, S., Kerschner, H., Kubik, P. W. & Schlüchter, C. (2006). Glacier Response in the European Alps to Heinrich Event 1 Cooling: The Gschnitz Stadial. *Journal of Quaternary Science*, 21(2), 115–130.

Ivy-Ochs, S., Kerschner, H., Maisch, M., Christl, M., Kubik, P. W. & Schlüchter, C. (2009). Latest Pleistocene and Holocene Glacier Variations in the European Alps. *Quaternary Science Reviews*, 28(21–22), 2137–2149.

Ivy-Ochs, S., Kerschner, H., Reuther, A., Preusser, F., Heine, K., Maisch, M., Kubik, P. W. & Schlüchter, C. (2008). Chronology of the Last Glacial Cycle in the European Alps. *Journal of Quaternary Science*, 23(6–7), 559–573.

Ivy-Ochs, S., Schäfer, J., Kubik, P. W., Synal, H.-A. & Schlüchter, C. (2004). Timing of Deglaciation on the Northern Alpine Foreland (Switzerland). *Eclogae Geologicae Helvetiae*, 97(1), 47–55.

Jain, M., Sohbati, R., Guralnik, B., Murray, A. S., Kook, M., Lapp, T., Prasad, A. K., Thomsen, K. J. & Buylaert, J. P. (2015). Kinetics of Infrared Stimulated Luminescence from Feldspars. *Radiation Measurements*, 81, 242–250.

Jenkins, G. T. H., Duller, G. A. T., Roberts, H. M., Chiverrell, R. C. & Glasser, N. F. (2018). A New Approach for Luminescence Dating Glaciofluvial Deposits - High Precision Optical Dating of Cobbles. *Quaternary Science Reviews*, 192, 263–273.

Jiskoot, H., Fox, T. A. & Van Wychen, W. (2017). Flow and Structure in a Dendritic Glacier with Bedrock Steps. *Journal of Glaciology*, 63(241), 912–928.

Joerin, U. E., Nicolussi, K., Fischer, A., Stocker, T. F. & Schlüchter, C. (2008). Holocene Optimum Events Inferred from Subglacial Sediments at Tschierva Glacier, Eastern Swiss Alps. *Quaternary Science Reviews*, 27(3–4), 337–350.

Joerin, U. E., Stocker, T. F. & Schlüchter, C. (2006). Multicentury Glacier Fluctuations in the Swiss Alps during the Holocene. *The Holocene*, 16(5), 697–704.

Jorge, M. G. & Brennand, T. A. (2017). Semi-Automated Extraction of Longitudinal Subglacial Bedforms from Digital Terrain Models – Two New Methods. *Geomorphology*, 288, 148–163.

Jouvet, G., Cohen, D., Russo, E., Buzan, J., Raible, C. C., Haeberli, W., Kamleitner, S., Ivy-Ochs, S., Imhof, M. A., Becker, J. K., Landgraf, A. & Fischer, U. H. (2023). Coupled Climate-Glacier Modelling of the Last Glaciation in the Alps. *Journal of Glaciology*, 1–15.

Jouvet, G., Picasso, M., Rappaz, J. & Blatter, H. (2008). A New Algorithm to Simulate the Dynamics of a Glacier: Theory and Applications. *Journal of Glaciology*, 54(188), 801–811.

Kelly, M. A., Buoncristiani, J.-F. & Schlüchter, C. (2004). A Reconstruction of the Last Glacial Maximum (LGM) Ice-Surface Geometry in the Western Swiss Alps and Contiguous Alpine Regions in Italy and France. *Eclogae Geologicae Helvetiae*, 97(1), 57–75.

King, C. a. M. & Lewis, W. V. (1961). A Tentative Theory of Ogive Formation. *Journal of Glaciology*, 3(29), 912–939.

King, G. E., Guralnik, B., Valla, P. G. & Herman, F. (2016a). Trapped-Charge Thermochronometry and Thermometry: A Status Review. *Chemical Geology*, 446, 3–17.

King, G. E., Herman, F. & Guralnik, B. (2016b). Northward Migration of the Eastern Himalayan Syntaxis Revealed by OSL Thermochronometry. *Science*, 353(6301), 800–804.

King, G. E., Herman, F., Lambert, R., Valla, P. G. & Guralnik, B. (2016c). Multi-OSL-Thermochronometry of Feldspar. *Quaternary Geochronology*, 33, 76–87.

Kirchner, N., Ahlkrona, J., Gowan, E. J., Lötstedt, P., Lea, J. M., Noormets, R., Von Sydow, L., Dowdeswell, J. A. & Benham, T. (2016). Shallow Ice Approximation, Second Order Shallow Ice Approximation, and Full Stokes Models: A Discussion of Their Roles in Palaeo-Ice Sheet Modelling and Development. *Quaternary Science Reviews*, 147, 136–147.

Koppes, M., Hallet, B., Rignot, E., Mouginot, J., Wellner, J. S. & Boldt, K. (2015). Observed Latitudinal Variations in Erosion as a Function of Glacier Dynamics. *Nature*, 526(7571), 100–103.

Koppes, M. N. & Hallet, B. (2002). Influence of Rapid Glacial Retreat on the Rate of Erosion by Tidewater Glaciers. *Geology*, 30(1), 47–50.

Koppes, M. N. & Montgomery, D. R. (2009). The Relative Efficacy of Fluvial and Glacial Erosion over Modern to Orogenic Timescales. *Nature Geoscience*, 2.

Kühni, A. & Pfiffner, O. A. (2001). The Relief of the Swiss Alps and Adjacent Areas and Its Relation to Lithology and Structure: Topographic Analysis from a 250-m DEM. *Geomorphology*, 41(4), 285–307.

Lague, D. (2014). The Stream Power River Incision Model: Evidence, Theory and Beyond. *Earth Surface Processes and Landforms*, 39(1), 38–61.

Lai, J. & Anders, A. M. (2020). Tectonic Controls on Rates and Spatial Patterns of Glacial Erosion through Geothermal Heat Flux. *Earth and Planetary Science Letters*, 543.

Lai, J. & Anders, A. M. (2021). Climatic Controls on Mountain Glacier Basal Thermal Regimes Dictate Spatial Patterns of Glacial Erosion. *Earth Surface Dynamics*, 9, 845–859.

Langhammer, L., Rabenstein, L., Bauder, A. & Maurer, H. (2017). Ground-Penetrating Radar Antenna Orientation Effects on Temperate Mountain Glaciers. *GEOPHYSICS*, 82(3), H15–H24.

Le Meur, E., Gagliardini, O., Zwinger, T. & Ruokolainen, J. (2004). Glacier Flow Modelling: A Comparison of the Shallow Ice Approximation and the Full-Stokes Solution. *Comptes Rendus. Physique*, 5(7), 709–722.

Lehmann, B., Valla, P. G., King, G. E. & Herman, F. (2018). Investigation of OSL Surface Exposure Dating to Reconstruct Post-LIA Glacier Fluctuations in the French Alps (Mer de Glace, Mont Blanc Massif). *Quaternary Geochronology*, 44, 63–74.

Leighton, F. B. (1951). Ogives of the East Twin Glacier, Alaska Their Nature and Origin. *The Journal of Geology*, 59(6), 578–589.

Liebl, M., Robl, J., Egholm, D. L., Prasicek, G., Stüwe, K., Gradwohl, G. & Hergarten, S. (2021). Topographic Signatures of Progressive Glacial Landscape Transformation. *Earth Surface Processes and Landforms*, (December 2020), 1–17.

Liebl, M., Robl, J., Hergarten, S., Egholm, D. L. & Stüwe, K. (2023). Modeling Large-scale Landform Evolution with a Stream Power Law for Glacial Erosion (OpenLEM V37): Benchmarking Experiments against a More Process-Based Description of Ice Flow (iSOSIA v3.4.3). *Geoscientific Model Development*, 16(4), 1315–1343.

Linsbauer, A., Huss, M., Hodel, E., Bauder, A., Fischer, M., Weidmann, Y., Bärtschi, H. & Schmassmann, E. (2021). The New Swiss Glacier Inventory SGI2016: From a Topographical to a Glaciological Dataset. *Frontiers in Earth Science*, 9.

Lliboutry, L. (1968). General Theory of Subglacial Cavitation and Sliding of Temperate Glaciers. *Journal of Glaciology*, 7(49), 21–58.

Louvat, P., Gislason, S. R. & Allegre, C. J. (2008). Chemical and Mechanical Erosion Rates in Iceland as Deduced from River Dissolved and Solid Material. *American Journal of Science*, 308(5), 679–726.

Lukas, S., Spencer, J. Q. G., Robinson, R. A. J. & Benn, D. I. (2007). Problems Associated with Luminescence Dating of Late Quaternary Glacial Sediments in the NW Scottish Highlands. *Quaternary Geochronology*, 2(1–4), 243–248.

MacGregor, K. R., Anderson, R. S., Anderson, S. P. & Waddington, E. D. (2000). Numerical Simulations of Glacial-Valley Longitudinal Profile Evolution. *Geology*, 28(11), 1031–1034.

MacGregor, K. R., Anderson, R. S. & Waddington, E. D. (2009). Numerical Modeling of Glacial Erosion and Headwall Processes in Alpine Valleys. *Geomorphology*, 103(2), 189–204.

Magrani, F., Valla, P. G. & Egholm, D. (2021). Modelling Alpine Glacier Geometry and Subglacial Erosion Patterns in Response to Contrasting Climatic Forcing. *Earth Surface Processes and Landforms*, esp.5302.

Magrani, F., Valla, P. G., Gribenski, N. & Serra, E. (2020). Glacial Overdeepenings in the Swiss Alps and Foreland: Spatial Distribution and Morphometrics. *Quaternary Science Reviews*, 243, 106483.

Mahan, S. & DeWitt, R. (2019). Principles and History If Luminescence Dating, in: Bateman, M. D. (Ed.), *Handbook of luminescence dating*. Dunbeath, Caithness, Scotland, UK: Whittles Publishing.

Mancini, D., Dietze, M., Müller, T., Jenkin, M., Miesen, F., Roncoroni, M., Nicholas, A. P. & Lane, S. N. (2023a). Filtering of the Signal of Sediment Export From a Glacier by Its Proglacial Forefield. *Geophysical Research Letters*, 50(21), e2023GL106082.

Mancini, Davide, Dietze, M., Jenkins, M., Miesen, F. & Lane, S. N. (2023b). Suspended Sediment Load and Bedload Flux from the Glacier d'Otemma Proglacial Forefield (Summers 2020 and 2021). Retrieved April 12, 2024, from https://zenodo.org/record/8380814

Mancini, D. & Lane, S. N. (2020). Changes in Sediment Connectivity Following Glacial Debuttressing in an Alpine Valley System. *Geomorphology*, 352, 106987.

Mariotti, A., Blard, P.-H., Charreau, J., Toucanne, S., Jorry, S. J., Molliex, S., Bourlès, D. L., Aumaître, G. & Keddadouche, K. (2021). Nonlinear Forcing of Climate on Mountain Denudation during Glaciations. *Nature Geoscience*, 14(1), 16–22.

Maussion, F., Butenko, A., Champollion, N., Dusch, M., Eis, J., Fourteau, K., Gregor, P., Jarosch, A. H., Landmann, J., Oesterle, F., Recinos, B., Rothenpieler, T., Vlug, A., Wild, C. T. & Marzeion, B. (2019). The Open Global Glacier Model (OGGM) v1.1. *Geoscientific Model Development*, 12(3), 909–931.

McKeever, S. W. S. (1985). *Thermoluminescence of Solids*. Cambridge(GB) New York New Rochelle [etc.]: Cambridge university press.

MeteoSwiss. (2024). The Climate of Switzerland - MeteoSwiss. Retrieved March 14, 2024, from https://www.meteoswiss.admin.ch/climate/the-climate-of-switzerland.html

Michel, J.-B., Shen, Y. K., Aiden, A. P., Veres, A., Gray, M. K., The Google Books Team, Pickett, J. P., Hoiberg, D., Clancy, D., Norvig, P., Orwant, J., Pinker, S., Nowak, M. A. & Aiden, E. L. (2011). Quantitative Analysis of Culture Using Millions of Digitized Books. *Science*, 331(6014), 176–182.

Millan, R., Mouginot, J., Rabatel, A. & Morlighem, M. (2022). Ice Velocity and Thickness of the World's Glaciers. *Nature Geoscience*, 15(2), 124–129.

Mîndrescu, M. & Evans, I. S. (2014). Cirque Form and Development in Romania: Allometry and the Buzzsaw Hypothesis. *Geomorphology*, 208, 117–136.

Mitchell, S. G. & Humphries, E. E. (2015). Glacial Cirques and the Relationship between Equilibrium Line Altitudes and Mountain Range Height. *Geology*, 43(1), 35–38.

Mitchell, S. G. & Montgomery, D. R. (2006). Influence of a Glacial Buzzsaw on the Height and Morphology of the Cascade Range in Central Washington State, USA. *Quaternary Research*, 65(1), 96–107.

Molnar, P. & England, P. (1990). Late Cenozoic Uplift of Mountain Ranges and Global Climate Change: Chiken or Egg? *Nature*, 346(5 July), 29–34.

Montgomery, D. R. (2002). Valley Formation by Fluvial and Glacial Erosion. *Geology*, 30(11), 1047–1050.

Montgomery, D. R., Balco, G. & Willett, S. D. (2001). Climate, Tectonics, and the Morphology of the Andes. *Geology*, 29(7), 579.

Montgomery, D. R. & Korup, O. (2011). Preservation of Inner Gorges through Repeated Alpine Glaciations. *Nature Geoscience*, 4(1), 62–67.

Muller, B. (1999). Paraglacial Sedimentation and Denudation Processes in an Alpine Valley of Switzerland. An Approach to the Quantification of Sediment Budgets. *Geodinamica Acta*, 12(5), 291–301.

Naylor, S. & Gabet, E. J. (2007). Valley Asymmetry and Glacial versus Nonglacial Erosion in the Bitterroot Range, Montana, USA. *Geology*, 35(4), 375–378.

Nye, J. F. (1952). The Mechanics of Glacier Flow. *Journal of Glaciology*, 2(12), 82–93.

Nye, J. F. (1958). A Theory of Wave Formation in Glaciers, in: *International Union of Geodesy and Geophysics*, (pp. 134–154).

Nye, J. F. (1959). The Deformation of a Glacier Below an Ice Fall. *Journal of Glaciology*, 3(25), 386–408.

Nye, J. F. (1972). Water at the Bed of a Glacier, in: *International Glaciological Society*, (pp. 189–194).

Oerlemans, J. (1984). Numerical Experiments on Glacial Erosion. *Zeitschrift für Gletscherkunde und Glazialgeologie*, 20, 107–126.

Oskin, M. & Burbank, D. W. (2005). Alpine Landscape Evolution Dominated by Cirque Retreat. *Geology*, 33(12), 933–936.

Patton, H., Swift, D. A., Clark, C. D., Livingstone, S. J. & Cook, S. J. (2016). Distribution and Characteristics of Overdeepenings beneath the Greenland and Antarctic Ice Sheets: Implications for Overdeepening Origin and Evolution. *Quaternary Science Reviews*, 148, 128–145.

Pattyn, F. et al. (2008). Benchmark Experiments for Higher-Order and Full-Stokes Ice Sheet Models (ISMIP–HOM). *The Cryosphere*, 2(2), 95–108.

Pedersen, V. K., Huismans, R. S., Herman, F. & Egholm, D. L. (2014). Controls of Initial Topography on Temporal and Spatial Patterns of Glacial Erosion. *Geomorphology*, 223, 96–116.

Penck, A. (1905). Glacial Features in the Surface of the Alps. *The Journal of Geology*, 13(1), 1–19.

Planet Team. (2017). Planet Application Programme Interface: In Space for Life on Earth. Retrieved from https://api.planet.com

Poolton, N. R. J., Kars, R. H., Wallinga, J. & Bos, A. J. J. (2009). Direct Evidence for the Participation of Band-Tails and Excited-State Tunnelling in the Luminescence of Irradiated Feldspars. *Journal of Physics: Condensed Matter*, 21(48), 485505.

Poolton, N. R. J., Nicholls, J. E., B□tter-Jensen, L., Smith, G. M. & Riedi, P. C. (2001). Observation of Free Electron Cyclotron Resonance in NaAlSi3O8 Feldspar: Direct

Determination of the Effective Electron Mass. *physica status solidi (b)*, 225(2), 467–475.

Porter, S. C. (1989). Some Geological Implications of Average Quaternary Glacial Conditions. *Quaternary Research*, 32(3), 245–261.

Posamentier, H. W. (1978). Thoughts on Ogive Formation. *Journal of Glaciology*, 20(82), 218–220.

Pralong, A. & Funk, M. (2006). On the Instability of Avalanching Glaciers. *Journal of Glaciology*, 52(176), 31–48.

Prasicek, G., Hergarten, S., Deal, E., Herman, F. & Robl, J. (2020). A Glacial Buzzsaw Effect Generated by Efficient Erosion of Temperate Glaciers in a Steady State Model. *Earth and Planetary Science Letters*, 543, 116350.

Prasicek, G., Herman, F., Robl, J. & Braun, J. (2018). Glacial Steady State Topography Controlled by the Coupled Influence of Tectonics and Climate. *Journal of Geophysical Research: Earth Surface*, 123(6), 1344–1362.

Preusser, F., Reitner, J. M. & Schlüchter, C. (2010). Distribution, Geometry, Age and Origin of Overdeepened Valleys and Basins in the Alps and Their Foreland. *Swiss Journal of Geosciences*, 103(3), 407–426.

Putkinen, N., Eyles, N., Putkinen, S., Ojala, A. E. K., Palmu, J.-P., Sarala, P., Väänänen, T., Räisänen, J., Saarelainen, J., Ahtonen, N., Rönty, H., Kiiskinen, A., Rauhaniemi, T. & Tervo, T. (2017). High-Resolution LiDAR Mapping of Glacial Landforms and Ice Stream Lobes in Finland. *Bulletin of the Geological Society of Finland*, 89(2), 64–81.

Rabatel, A., Dedieu, J.-P. & Vincent, C. (2005). Using Remote-Sensing Data to Determine Equilibrium-Line Altitude and Mass-Balance Time Series: Validation on Three French Glaciers, 1994–2002. *Journal of Glaciology*, 51(175), 539–546.

Rabatel, A., Letréguilly, A., Dedieu, J.-P. & Eckert, N. (2013). Changes in Glacier Equilibrium-Line Altitude in the Western Alps from 1984 to 2010: Evaluation by Remote Sensing and Modeling of the Morpho-Topographic and Climate Controls. *The Cryosphere*, 7(5), 1455–1471.

Raming, L. W. & Whipple, K. X. (2019). Lithologic Controls on the Formation and Retreat of Waterfalls. AGU Fall Meeting Abstracts, 2019, EP53F-2220.

Ramsay, A. C. (1862). XLIX. *The Excavation of the Valleys of the Alps*. *The London, Edinburgh, and Dublin Philosophical Magazine and Journal of Science*, 24(162), 377–380.

Rhodes, E. J. (2015). Dating Sediments Using Potassium Feldspar Single-Grain IRSL: Initial Methodological Considerations. *Quaternary International*, 362, 14–22.

Riihimaki, C. A., MacGregor, K. R., Anderson, R. S., Anderson, S. P. & Loso, M. G. (2005). Sediment Evacuation and Glacial Erosion Rates at a Small Alpine Glacier. *Journal of Geophysical Research: Earth Surface*, 110(3), 1–17.

Rippin, D. M., Sharp, M., Van Wychen, W. & Zubot, D. (2020). 'Detachment' of Icefield Outlet Glaciers: Catastrophic Thinning and Retreat of the Columbia Glacier (Canada). *Earth Surface Processes and Landforms*, 45(2), 459–472.

Robl, J., Prasicek, G., Hergarten, S. & Salcher, B. (2015). Glacial Cirques and the Relationship between Equilibrium Line Altitudes and Mountain Range Height: COMMENT. *Geology*, 43(6), e365–e365.

Rootes, C. M. & Clark, C. D. (2020). Glacial Trimlines to Identify Former Ice Margins and Subglacial Thermal Boundaries: A Review and Classification Scheme for Trimline Expression. *Earth-Science Reviews*, 210, 103355.

Röthlisberger, H. (1972). Water Pressure in Intra- and Subglacial Channels. *Journal of Glaciology*, 11(62), 177–203.

Rowan, A. V., Egholm, D. L., Quincey, D. J. & Glasser, N. F. (2015). Modelling the Feedbacks between Mass Balance, Ice Flow and Debris Transport to Predict the Response to Climate Change of Debris-Covered Glaciers in the Himalaya. *Earth and Planetary Science Letters*, 430, 427–438.

Rowan, A. V., Egholm, D. L., Quincey, D. J., Hubbard, B., King, O., Miles, E. S., Miles, K. E. & Hornsey, J. (2021). The Role of Differential Ablation and Dynamic Detachment in Driving Accelerating Mass Loss From a Debris-Covered Himalayan Glacier. *Journal of Geophysical Research: Earth Surface*, 126(9).

Röthlisberger, H. & Iken, A. (1981). Plucking as an Effect of Water-Pressure Variations at the Glacier Bed. *Annals of Glaciology*, 2, 57–62.

Scherler, D. (2014). Climatic Limits to Headwall Retreat in the Khumbu Himalaya, Eastern Nepal. *Geology*, 42(11), 1019–1022.

Scherler, D. & Egholm, D. L. (2020). Production and Transport of Supraglacial Debris: Insights From Cosmogenic 10Be and Numerical Modeling, Chhota Shigri Glacier, Indian Himalaya. *Journal of Geophysical Research: Earth Surface*, 125(10), 1–26.

Schimmelpfennig, I., Schaefer, J. M., Akçar, N., Koffman, T., Ivy-Ochs, S., Schwartz, R., Finkel, R. C., Zimmerman, S. & Schlüchter, C. (2014). A Chronology of Holocene and Little Ice Age Glacier Culminations of the Steingletscher, Central Alps, Switzerland, Based on High-Sensitivity Beryllium-10 Moraine Dating. *Earth and Planetary Science Letters*, 393, 220–230.

Schlüchter, C. (2004). The Swiss Glacial Record – a Schematic Summary, in: *Developments in Quaternary Sciences*, (pp. 413–418). Elsevier.

Schmidt, W. & Joshi, R. (1982). Simulation Of Glacier Flow Using The Finite Element Method. *International Journal of Modelling and Simulation*, 2(3), 183–187.

SCNAT (2020). Glaciers Are Retreating Unabated. Retrieved April 20, 2023, from https://scnat.ch/en/id/YYqFt

Seddik, H., Greve, R., Zwinger, T. & Sugiyama, S. (2017). Regional Modeling of the Shirase Drainage Basin, East Antarctica: Full Stokes vs. Shallow Ice Dynamics. *The Cryosphere*, 11(5), 2213–2229.

Seguinot, J. & Delaney, I. (2021). Last Glacial Cycle Glacier Erosion Potential in the Alps. *Earth Surface Dynamics*, 9(4), 923–935.

Seguinot, J., Ivy-Ochs, S., Jouvet, G., Huss, M., Funk, M. & Preusser, F. (2018). Modelling Last Glacial Cycle Ice Dynamics in the Alps. *Cryosphere*, 12(10), 3265–3285.

Seong, Y. B., Owen, L. A., Caffee, M. W., Kamp, U., Bishop, M. P., Bush, A., Copland, L. & Shroder, J. F. (2009). Rates of Basin-Wide Rockwall Retreat in the K2 Region of the Central Karakoram Defined by Terrestrial Cosmogenic Nuclide 10Be. *Geomorphology*, 107(3–4), 254–262.

Service topographique fédéral (1955). *Arolla*. Wabern-Berne.

Shuster, D. L., Cuffey, K. M., Sanders, J. W. & Balco, G. (2011). Thermochronometry Reveals Headward Propagation of Erosion in an Alpine Landscape. *Science*, 332(6025), 84–88.

Simond, L. (1823). Travels in Switzerland. *The Atheneum; or Spirit of the English Magazines*, 12, 169–183.

Six, D. & Vincent, C. (2014). Sensitivity of Mass Balance and Equilibrium-Line Altitude to Climate Change in the French Alps. *Journal of Glaciology*, 60(223), 867–878.

Smedley, R. K. & Skirrow, G. K. A. (2020). Luminescence Dating in Fluvial Settings: Overcoming the Challenge of Partial Bleaching, in: Herget, J. and Fontana, A. (Eds.), *Palaeohydrology*, (pp. 155–168). Geography of the Physical Environment. Springer International Publishing.

Spooner, C., Scheck-Wenderoth, M., Cacace, M., Götze, H.-J., Luijendijk, E., (2020). The 3D thermal field across the Alpine orogen and its forelands and the relation to seismicity. *Global and Planetary Change* 193, 103288.

Steinemann, O., Ivy-Ochs, S., Hippe, K., Christl, M., Haghipour, N. & Synal, H.-A. (2021). Glacial Erosion by the Trift Glacier (Switzerland): Deciphering the Development of Riegels, Rock Basins and Gorges. *Geomorphology*, 375, 107533–107540.

Sternai, P., Herman, F., Fox, M. R. & Castelltort, S. (2011). Hypsometric Analysis to Identify Spatially Variable Glacial Erosion. *Journal of Geophysical Research: Earth Surface*, 116(3), 1–17.

Sternai, P., Herman, F., Valla, P. G. & Champagnac, J.-D. (2013). Spatial and Temporal Variations of Glacial Erosion in the Rhône Valley (Swiss Alps): Insights from Numerical Modeling. *Earth and Planetary Science Letters*, 368, 119–131.

Sternai, P., Sue, C., Husson, L., Serpelloni, E., Becker, T. W., Willett, S. D., Faccenna, C., Di Giulio, A., Spada, G., Jolivet, L., Valla, P., Petit, C., Nocquet, J.-M., Walpersdorf, A. & Castelltort, S. (2019). Present-Day Uplift of the European Alps: Evaluating Mechanisms and Models of Their Relative Contributions. *Earth-Science Reviews*, 190, 589–604.

Stroeven, A. P. & Swift, D. A. (2008). Glacial Landscape Evolution - Implications for Glacial Processes, Patterns and Reconstructions. *Geomorphology*, 97(1–2), 1–4.

Swift, D. A., Cook, S., Heckmann, T., Moore, J., Gärtner-Roer, I. & Korup, O. (2015). *Ice and Snow as Land-Forming Agents*.

Swift, D. A., Nienow, P. W., Hoey, T. B. & Mair, D. W. F. (2005). Seasonal Evolution of Runoff from Haut Glacier d'Arolla, Switzerland and Implications for Glacial Geomorphic Processes. *Journal of Hydrology*, 309(1–4), 133–148.

Swift, D. A., Nienow, P. W., Spedding, N. & Hoey, T. B. (2002). Geomorphic Implications of Subglacial Drainage Configuration: Rates of Basal Sediment Evacuation Controlled by Seasonal Drainage System Evolution. *Sedimentary Geology*, 149(1–3), 5–19.

Swift, D. A., Persano, C., Stuart, F. M., Gallagher, K. & Whitham, A. (2008). A Reassessment of the Role of Ice Sheet Glaciation in the Long-Term Evolution of the East Greenland Fjord Region. *Geomorphology*, 97(1–2), 109–125.

Swift, D. A., Tallentire, G. D., Farinotti, D., Cook, S. J., Higson, W. J. & Bryant, R. G. (2021a). The Hydrology of Glacier-bed Overdeepenings: Sediment Transport Mechanics, Drainage System Morphology, and Geomorphological Implications. *Earth Surface Processes and Landforms*, 46(11), 2264–2278.

Swift, D. A., Tallentire, G. D., Farinotti, D., Cook, S. J., Higson, W. J. & Bryant, R. G. (2021b). The Hydrology of Glacier-bed Overdeepenings: Sediment Transport Mechanics, Drainage System Morphology, and Geomorphological Implications. *Earth Surface Processes and Landforms*, 46(11), 2264–2278.

The Himalayan Database, The Expedition Archives of Elizabeth Hawley. Retrieved December 30, 2023, from https://www.himalayandatabase.com/Online/peakdead.html

Tomkin, J. H. (2007). Coupling Glacial Erosion and Tectonics at Active Orogens: A Numerical Modeling Study. *Journal of Geophysical Research: Earth Surface*, 112(2), 1–14.

Tyndall, J. (1864). XXX. *On the Conformation of the Alps*. *The London, Edinburgh, and Dublin Philosophical Magazine and Journal of Science*, 28(189), 255–271.

Ugelvig, S. V. & Egholm, D. L. (2018). The Influence of Basal-Ice Debris on Patterns and Rates of Glacial Erosion. *Earth and Planetary Science Letters*, 490, 110–121.

Ugelvig, S. V., Egholm, D. L., Anderson, R. S. & Iverson, N. R. (2018). Glacial Erosion Driven by Variations in Meltwater Drainage. *Journal of Geophysical Research: Earth Surface*, 123(11), 2863–2877.

Ugelvig, S. V., Egholm, D. L. & Iverson, N. R. (2016). Glacial Landscape Evolution by Subglacial Quarrying: A Multiscale Computational Approach. *Journal of Geophysical Research: Earth Surface*, 121(11), 2042–2068.

Unsworth, W. (1982). *Everest*. Harmondsworth, Middlesex, England ; New York, N.Y., U.S.A: Penguin Books.

Valla, P. G., Shuster, D. L. & Van Der Beek, P. A. (2011). Significant Increase in Relief of the European Alps during Mid-Pleistocene Glaciations. *Nature Geoscience*, 4(10), 688–692.

Valla, P. G., Sternai, P. & Fox, M. (2021). How Climate, Uplift and Erosion Shaped the Alpine Topography. *Elements*, 17(1), 41–46.

Višnjević, V., Herman, F. & Prasicek, G. (2020). Climatic Patterns over the European Alps during the LGM Derived from Inversion of the Paleo-Ice Extent. *Earth and Planetary Science Letters*, 538, 116185.

Waddington, E. D. (1986). Wave Ogives. *Journal of Glaciology*, 32(112), 325–334.

Wallinga, J., Murray, A. & Wintle, A. (2000). The Single-Aliquot Regenerative-Dose (SAR) Protocol Applied to Coarse-Grain Feldspar. *Radiation Measurements*, 32(5–6), 529–533.

Ward, D. J., Anderson, R. S. & Haeussler, P. J. (2012). Scaling the Teflon Peaks: Rock Type and the Generation of Extreme Relief in the Glaciated Western Alaska Range. *Journal of Geophysical Research: Earth Surface*, 117(F1), 2011JF002068.

Weertman, J. (1957). On the Sliding of Glaciers. *Journal of Glaciology*, 3(21), 33–38.

Wetterauer, K., Scherler, D., Anderson, L. S. & Wittmann, H. (2022). Temporal Evolution of Headwall Erosion Rates Derived from Cosmogenic Nuclide Concentrations in the Medial Moraines of Glacier d'Otemma, Switzerland. *Earth Surface Processes and Landforms*, 47(10), 2437–2454.

Whipple, K. X., Kirby, E. & Brocklehurst, S. H. (1999). Geomorphic Limits to Climate-Induced Increases in Topographic Relief. *Nature*, 401(6748), 39–43.

Willett, S. D., McCoy, S. W., Perron, J. T., Goren, L. & Chen, C.-Y. (2014). Dynamic Reorganization of River Basins. *Science*, 343(6175), 1248765.

Wintle, A. G. (1973). Anomalous Fading of Thermo-Luminescence in Mineral Samples. *Nature*, 245(5421), 143–144.

Wirsig, C., Zasadni, J., Ivy-Ochs, S., Christl, M., Kober, F. & Schlüchter, C. (2016). A Deglaciation Model of the Oberhasli, Switzerland. *Journal of Quaternary Science*, 31(1), 46–59.

Yanites, B. J. & Ehlers, T. A. (2016). Intermittent Glacial Sliding Velocities Explain Variations in Long-Timescale Denudation. *Earth and Planetary Science Letters*, 450, 52–61.

Ye, F.-Y., Barriot, J.-P. & Carretier, S. (2013). Initiation and Recession of the Fluvial Knickpoints of the Island of Tahiti (French Polynesia). *Geomorphology*, 186, 162–173.

Žebre, M., Colucci, R. R., Giorgi, F., Glasser, N. F., Racoviteanu, A. E. & Del Gobbo, C. (2021). 200 Years of Equilibrium-Line Altitude Variability across the European Alps (1901−2100). *Climate Dynamics*, 56(3–4), 1183–1201.

Zoet, L. K. & Iverson, N. R. (2015). Experimental Determination of a Double-Valued Drag Relationship for Glacier Sliding. *Journal of Glaciology*, 61(225), 1–7.